New Organic Chromophores for Metal Complexation: Investigations into the Synthesis and Photophysics of Thioindigo Diimines, AzaDIMEs, and their Metal Complexes

by

Geneviève Nicole Boice
B.A., Mount Holyoke College, 2000
M.Sc., University of Washington, 2011

A Dissertation Submitted in Partial Fulfillment of the
Requirements for the Degree of

DOCTOR OF PHILOSOPHY

in the Department of Chemistry

University of Victoria

New Organic Chromophores for Metal Complexation: Investigations into the Synthesis and Photophysics of Thioindigo Diimines, AzaDIMEs, and their Metal Complexes

by

Geneviève Nicole Boice
B.A., Mount Holyoke College, 2000
M.Sc., University of Washington, 2011

Supervisory Committee

Dr. Robin G. Hicks, Supervisor
(Department of Chemistry, University of Victoria)

Dr. Cornelia Bohne, Departmental Member
(Department of Chemistry, University of Victoria)

Dr. Thomas Fyles, Departmental Member
(Department of Chemistry, University of Victoria)

Dr. Geoff Steeves, Outside Member
(Department of Physics, University of Victoria)

Abstract

Supervisory Committee

Dr. Robin G. Hicks, Supervisor
(Department of Chemistry, University of Victoria)

Dr. Cornelia Bohne, Departmental Member
(Department of Chemistry, University of Victoria)

Dr. Thomas Fyles, Departmental Member
(Department of Chemistry, University of Victoria)

Dr. Geoff Steeves, Outside Member
(Department of Physics, University of Victoria)

The synthesis and comprehensive characterization of diamine and diimine derivatives of thioindigo are reported. X-ray crystal structures demonstrate a planar structure for the diimine derivatives and a twisted conformation for the diamines. The diamine compounds absorb in the UV (λ_{max} 324 nm - 328 nm), and exhibit moderate fluorescence (Φ_F = 0.25, 0.045). A transient triplet state is observed in laser flash photolysis (LFP) experiments, with lifetimes an order of magnitude longer than those of the triplet state of thioindigo. The diimine compounds absorb at longer wavelengths than the diamines (λ_{max} 495 nm - 510 nm), but are still slightly blue-shifted from thioindigo. The diimines have molar extinction coefficients 17 – 70% higher than thioindigo. The diimine compounds are not emissive, and LFP studies show transient species with microsecond lifetimes. The transient absorption spectra and quenching experiments of the diimines are consistent with *trans-cis* isomerisation about the central double bond.

Mono- and diruthenium hexafluoroacetylacetonate (hfac) complexes of thioindigo-*N,N′*-diphenyldiimine have been prepared. The monoruthenium complex was isolated as a racemic mixture and the diruthenium complexes were isolated as the *meso* (ΔΛ) and *rac* (ΔΔ and ΛΛ) diastereomers. Extensive structural characterization of the compounds revealed intrinsic diastereomeric differences in the X-ray crystal structures, cyclic voltammograms, and NMR spectra. Variable temperature NMR experiments demonstrated that the *rac* diastereomer undergoes conformational exchange with a rate constant of 8700 sec^{-1} at 298 K, a behavior that is not observed in the *meso* diastereomer. Ground state optical properties of the complexes were examined, showing that all the complexes possess metal-to-ligand charge transfer (MLCT) absorption bands in the near-infrared (λ_{max} 689 nm – 783 nm). The compounds do not display photoluminescence in room temperature solution-phase experiments or in experiments at 77 K. Ultrafast transient absorption spectroscopy measurements revealed excited states with picosecond lifetimes. Unexpectedly, the transient absorption measurements revealed differences in the transient spectra and disparate time constants for the excited state decay of the diastereomers, which are linked to the conformational changes observed in the NMR experiments.

Investigations into the synthesis of azaDIMEs and azaDicarbazolyls are described. Examination of the Buchwald-Hartwig amination produced reaction conditions that enabled preparation of amino-diindoles. Oxidation of the amino-diindoles to azaDIMEs was complicated by concomitant oligomerization of the substrates. Substitution of the reactive positions of the amino-diindole afforded increased stability towards oxidative oligomerization. Scalable synthetic routes to azaDicarbazolyl precursors were identified and optimized, and preparation of amino and azaDicarbazolyl compounds was explored.

Table of Contents

List of Schemes

List of Tables

List of Figures

List of Numbered Compounds

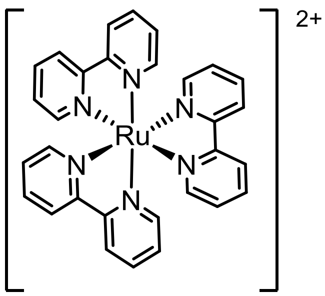
1.1

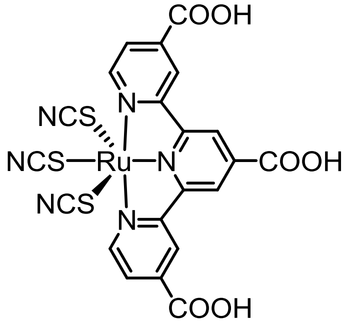
1.2

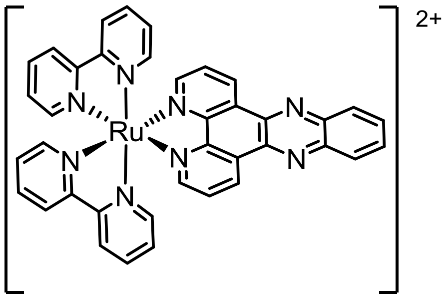
1.3

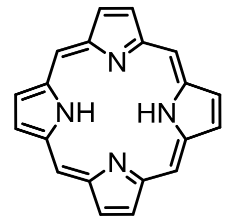
1.4

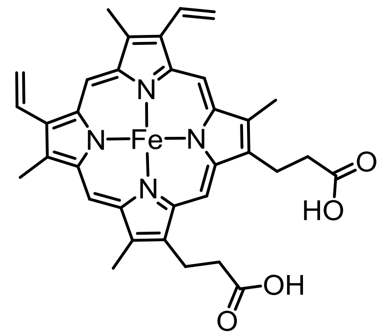
1.5

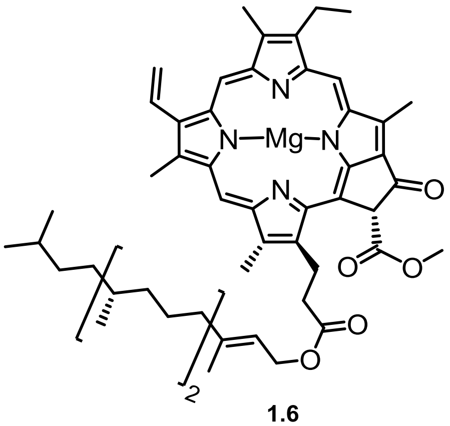
1.6

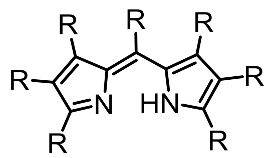
1.7

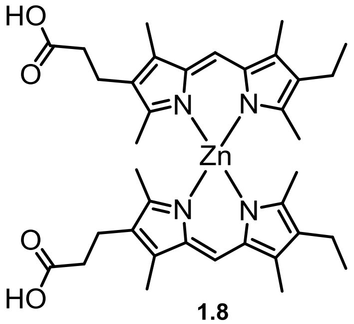
1.8

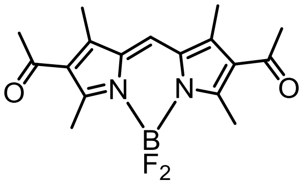
1.9

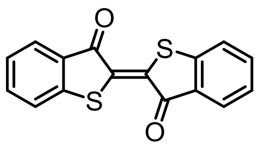

2.1

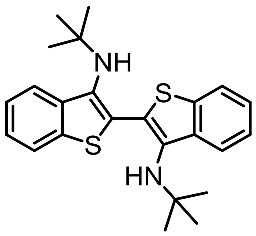

2.2a

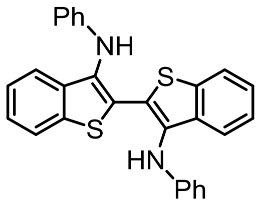

2.2b

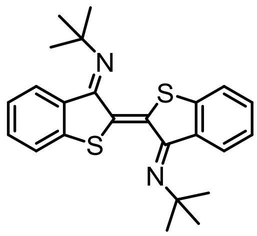

2.3a

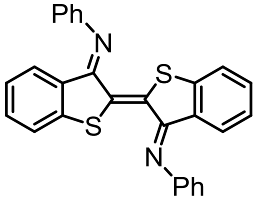

2.3b

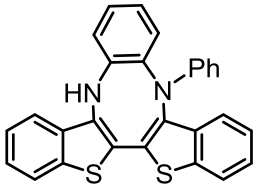

2.4b

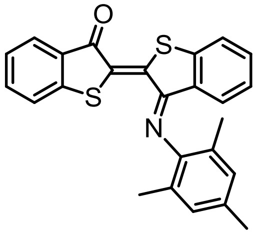

2.5c

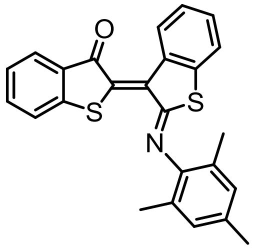

2.6c

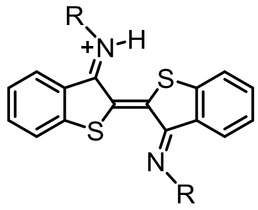

2.7

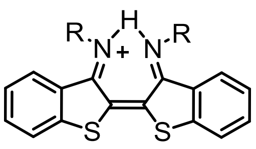

2.8

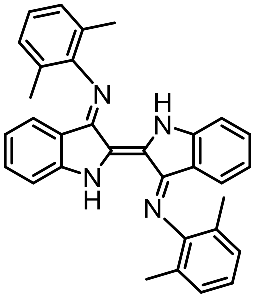

2.9

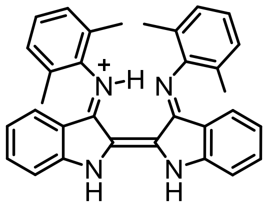

2.10

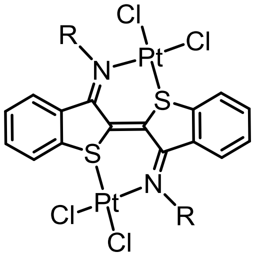

3.1

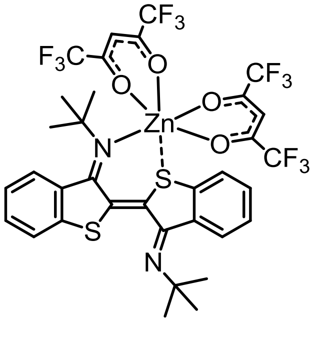

3.2

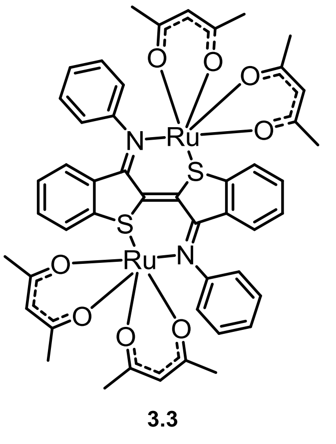

3.3

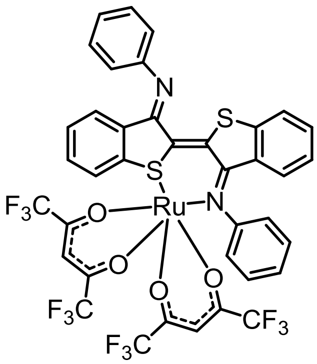

3.4

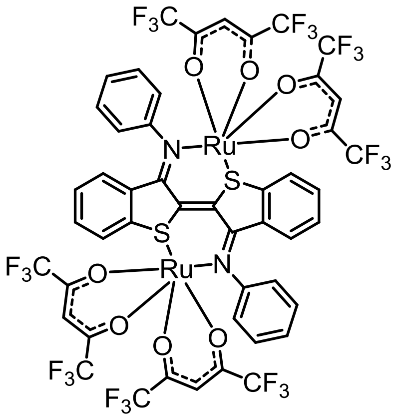

3.5a ΔΛ (*meso*)
3.5b ΔΔ/ΛΛ (*rac*)

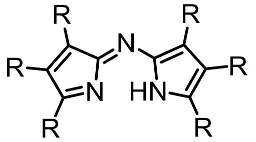

4.1

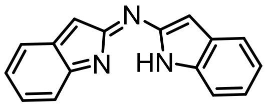

4.2

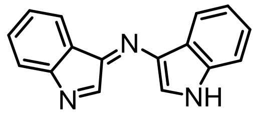

4.3

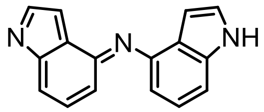

4.4

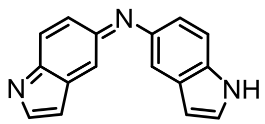

4.5a

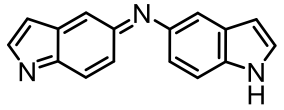

4.5b

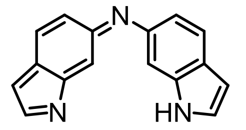

4.6a

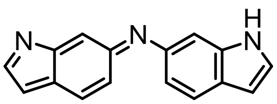

4.6b

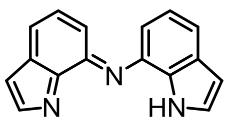

4.7

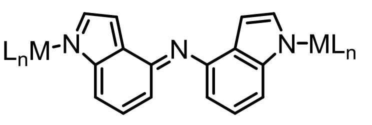

4.8

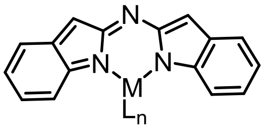

4.9

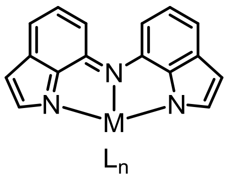

4.10

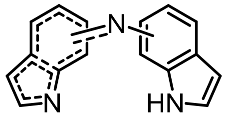

4.11

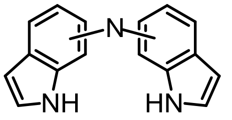

4.12

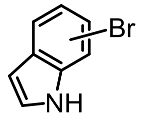

4.13

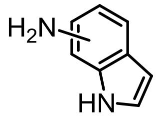

4.14

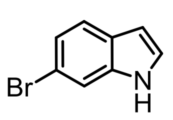

4.15a

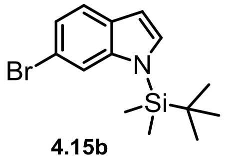

4.15b

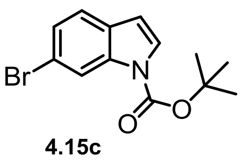

4.15c

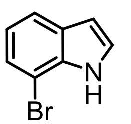

4.16a

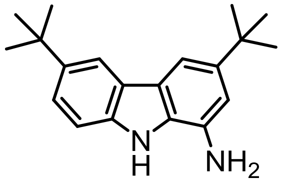

4.37

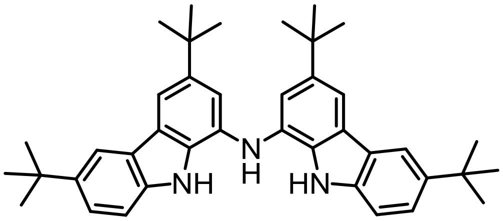

4.38

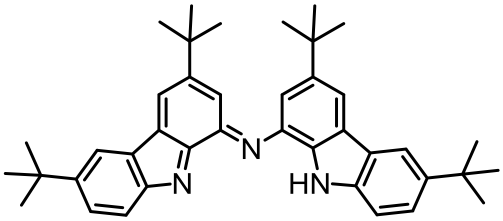

4.39

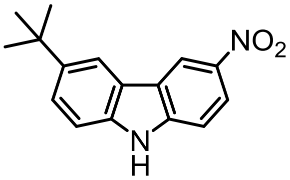

4.40

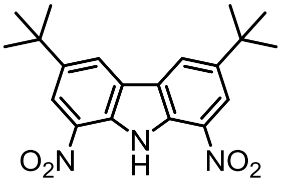

4.41

List of Abbreviations

bpy		2,2′- bipyridyl
NIR		near infrared
IR		infrared
EM		electromagnetic
MLCT		metal to ligand charge transfer
TA		transient absorption
DDQ		2,3-dichloro-5,6-dicyano-1,4-benzoquinone
DABCO		diazabicyclooctane
Pyr		pyridine
BODIPY		Boron dipyrromethene
BHA		Buchwald-Hartwig amination
DSSC		dye sensitized solar cell
PDT		photodynamic therapy
azaDIME		Aza diindolyl methene
LFP		laser flash photolysis
hfac		hexafluoroacetylacetonate
acac		acetylacetonate
PET		photoinduced electron transfer
TFAA		trifluoroacetic acid

List of Publications

Research presented in this dissertation has appeared in the following publications:

Boice, G.; Patrick, B. O.; McDonald, R.; Bohne, C.; Hicks, R. Synthesis and Photophysics of Thioindigo Diimines and Related Compounds. *The Journal of Organic Chemistry* **2014,** 79 (19), 9196-9205 DOI: 10.1021/jo501630f.

Boice, G. N.; Garakyaraghi, S.; Patrick, B. O.; Sanz, C. A.; Castellano, F. N.; Hicks, R. G. Diastereomerically Differentiated Excited State Behavior in Ruthenium(II) Hexafluoroacetylacetonate Complexes of Diphenyl Thioindigo Diimine. *Inorganic Chemistry* **2018,** 57 (3), 1386-1397 DOI: 10.1021/acs.inorgchem.7b02803.

Acknowledgements

I would like to thank the following people for their contributions to this work: Brian O. Patrick, Bob McDonald, and Corey Sanz who collected the crystallography data and solved the X-ray crystal structures; Sophia Garakyaraghi who performed the ultrafast transient absorption and spectroelectrochemical experiments in chapter 3; Nicole Poy who worked with me on the early stages of the aza-dicarbazolyl project; Yun Ling and the UBC Mass Spectrometry Center who collected the high resolution mass spectrometry data; and the folks at Canadian Microanalytical who ran the elemental analyses.

I would also like to thank the many people who have lent me their ear and their expertise: Chris Barr for all things NMR; Luis Netter for help with computers and lasers; Lars Yunker for all things mass spec; the Hicks group members past and present for all things inorganic –Emma Davy, Cooper Johnston, Corey Sanz, Dillon Hofsommer, Sean MacLean, Nick Richard, and Erica Hong; the Bohne group members past and present for all things photophysics – Hao Tang, Subhasree Banerjee, Suma Susan-Thomas, Mehraveh Seyedalikhani, Karol Valente, Kevin Voss, Jessy Oake, and Sree Gayathri; and Aiko Kurimoto for her insight into multiple areas of photophysics, organic and inorganic chemistry. I would especially like to thank Cornelia Bohne for her guidance and mentorship throughout this project, and most of all, my supervisor Robin Hicks for providing an academic environment that allowed me to grow as an independent scientist.

Last but not least, I would like thank all of the people who have supported and encouraged me through this process and throughout my chemistry career, especially professors Sean Decatur, Jan Smith, and Julie Kovacs; my high school chemistry teacher Mr. Gaylord (whose first-day demo I will never forget);

Jennifer Albaneze-Walker and Kristen McCaleb who I am lucky to call both mentors and friends; Yinka Oyeyemi, Katie Mar, Rhonda Stoddard, Cindy Wang, and Dennis Zed, who have all done this before and remind me that there is a world beyond school; and Brianna Cook-Coates who tells me that the mountains are still out there. Finally, I would like to thank my parents Sylvia and Jack, my siblings Jocelyn, Christina, and Lonny, and my grandfather Lee for their unwavering support and love. I could not have done this without you.

In Loving Memory of Jacqueline H. Smitrovich, Mary Collins Boice, and Helen Johnson Person

Chapter 1

Introduction

Optical properties of chemical compounds hold a particular fascination for many inorganic chemists. Aside from the aesthetically pleasing rainbow of colors displayed by inorganic complexes, the interplay of ligand and metal orbitals that occurs upon coordination can provide the metal-organic complex with unique optical and photophysical features that neither the metal nor the organic ligand possess. Partly because of this, the optical, photophysical, and photochemical characteristics of metal-organic coordination compounds form the basis for many technologies currently in use, and many technologies currently being developed.

The impacts of the practical applications of metal-organic complexes on society are readily apparent, from solar energy to light emitting devices to biomedical imaging and beyond. The fundamental studies underpinning these advances, however, are often less obvious to the casual observer, and the importance of basic research to the development of such technologies can be difficult to evaluate and communicate. Nevertheless, without curiosity-driven studies into the photophysical and photochemical phenomena associated with metal-organic complexes and the principles that control them, the optical technologies we rely on would not have come into being. Indeed, the viability of this kind of fundamental approach to technological advances is demonstrated by the historical literature records of metal-organic complexes like the prototypical transition metal complex $[Ru(bpy)_3]^{2+}$ and the dipyrromethene class of coordination compounds.

The following dissertation is one set of such curiosity-driven studies into the essential nature of transition metal-organic complexes. Collectively, the aim of these investigations is to add to the fundamental knowledge of the interactions between structure, electrochemical properties, and excited state behavior of transition metal complexes by the introduction and comprehensive characterization of previously unexplored organic chromophores and transition metal-organic complexes.

1.1 A Photophysical and Photochemical Consideration of Transition Metal Complexes

Various organic and inorganic compounds have found applications in optical technologies, but transition metal complexes are of special interest in technologies that require the absorption and/or emission of light in the visible and near IR spectral regions.[1] Transition metal complexes of organic ligands are more apt to absorb or emit light in the visible and NIR wavelengths than unbound organic molecules because they possess the ability to undergo charge transfer reactions to and from the metal and ligand, as well as between the coordinated ligands themselves. These transitions are often low energy and are symmetry allowed, resulting in intense long wavelength absorptions that are ideal for applications that require absorption between ~400 and 1000 nm.

Kasha's rule governing the radiative decay of excited states requires that the emission of light from a molecular excited state (for example a triplet or singlet state) occur from the lowest energy level for the given multiplicity.[2] In general, this means that the wavelength of light emitted during fluorescence or phosphorescence, (be it photoluminescence or electroluminescence), must not be higher in energy than the lowest energy absorption band of the emitting molecule. Therefore, the advantageous low energy visible and NIR absorption properties of inorganic complexes also make them potentially suited to technologies requiring NIR and visible light production.

The emission of light from a transition metal-organic complex can be either fluorescence or phosphorescence. Depending on the optical application, a preference for one type of emission may exist. Although exceptions exist,[3] luminescence usually occurs when a molecule emits light as a result of the movement of an electron from an excited state to the ground state of the molecule. In the case of fluorescence, the excited state and the ground state involved in the transition have the same spin state. Phosphorescence, however, occurs when the transition of the electron is between energy levels of different spin states. Therefore, fluorescence is spin-allowed and phosphorescence is spin-forbidden, which typically leads to shorter lifetimes for fluorescence and longer lifetimes for phosphorescence. Longer excited state lifetimes (hundreds of ns and greater), while theoretically not imperative, are considered advantageous for intermolecular processes such as electron and energy transfer, which may also lead to a preference for phosphorescent compounds in some applications.

Unlike organic compounds, where fluorescence is common and phosphorescence is rare,[4] in transition metal complexes it is possible to design compounds to favor a particular type of emission. The choice of metal is a crucial component in this process. First row transition metals often lead to complexes that are not luminescent because of destabilizing low-energy d to d* transitions that can result in ligand dissociation.[5] However, in the case of first row metals with full d orbitals (Zn^{2+}, Cu^{1+}), or inaccessible d orbitals (square planar Ni^{2+}), those d to d* transitions are not possible. This leads to an increased observation of fluorescence in complexes containing these metals.[6] In contrast, transition metal complexes of second and third row metals often have low-energy charge transfer transitions rather than d to d* transitions (if the redox potentials of metal and ligand are well matched), which can enhance their luminescent ability.[7] Second and third row metals possess large spin-orbit coupling constants, which enables their metal-organic complexes to undergo efficient intersystem crossing between spin states. In practice, this often leads to short-lived singlet states that undergo intersystem crossing to long-lived triplet states which can relax via phosphorescence to the singlet ground state. Coordination of an organic compound to a metal can induce luminescence when the ligand itself does not emit. The coordination can restrict the molecular motion of the ligand, reducing non-radiative decay pathways such as internal conversion that proceed through rotational and vibrational action in the molecule.

In addition to the photophysical attributes, like luminescence, that make transition metal complexes useful, photochemical processes are also of interest in optical applications. Photochemical processes are chemical transformations that occur in the excited state, ultimately resulting in a change in the molecule in the ground state. In the case of transition metal complexes this encompasses photoinduced ligand dissociation, ligand substitution and isomerization, as well as photoredox reactions involving electron transfer. Photochemical processes often compete with photophysical processes in an excited state molecule.[8] It is possible to tune transition metal-organic complexes to increase the quantum yield of a particular process. For instance, the choice of a first-row metal for a complex could encourage ligand dissociation as described above. Yet, careful selection of the ligands is also important. The steric bulk, ligand field strength, coordinative ability, redox characteristics, structure, absorption features, and monodentate or chelating nature of the ligands can all impact the excited state behavior of the transition metal complex.

1.2 Optical Applications Using Transition Metal Complexes

The photophysical and photochemical properties of transition metal complexes are used in a diverse range of fields and technologies, including solar energy conversion, medicine and environmental testing, and electronics. In solar energy conversion, dye sensitized solar cells (DSSC)[9] and photocatalyzed water splitting[10] are two technologies that have relied heavily on metal complexes. DSSCs are a type of photoelectrochemical cell that generates electricity from photons. In these cells, charge generation is produced by electron transfer from a photoexcited molecule (the dye) into a nanocrystalline oxide layer.

In order for the cells to be efficient and durable, several photophysical and photochemical characteristics must be present in the dye molecule.[11] The dye must absorb in regions that overlap with the most intense output of solar irradiation, which at sea level is the visible and NIR region of the spectrum. The dye must have an excited state lifetime long enough to favor intermolecular processes, and it must be redox active to allow for electron transfer and regeneration of the dye upon reduction by the cell's electrolyte. These traits are common among transition metal complexes, which therefore find widespread use in DSSCs.

Photocatalyzed water splitting is the reduction and oxidation of water into H_2 and O_2, respectively, using solar irradiance to generate the necessary potential for electrolysis, or, alternatively, to directly initiate the redox reactions.[10] Photoelectrochemical cells are one type of device that performs this function. The cells consist of and anode and a cathode at which O_2 and H_2 generation take place with the aid of catalysts. At least one of the electrodes is a semiconductor which is the source of current for the cell. In order to increase efficiency and avoid the use of external current, dyes may be appended to the semiconductor, as they are in DSSCs. The requirements for the dye are the same as in a DSSC, with the caveat that the charge regeneration may be from the oxidation catalyst, not an electrolyte.

The use of a homogeneous photoactive catalyst to directly initiate reduction or oxidation (or both) of water is a less well – developed, but very active, area of research in this field. The properties needed for a robust catalyst make a transition metal-organic complex well-matched for the task. In addition to the absorption overlap with the solar spectrum, the compounds must have redox potentials (photoinduced or otherwise) capable of performing the reduction and oxidation half reactions of water. The compounds must also be able to undergo electron transfer and/or association and dissociation reactions to enable the reaction of water and the release of O_2 and H_2. The former may be enhanced in the excited state, and the latter step could be facilitated through photoinduced ligand dissociation.

In biomedical applications, transition metal-organic complexes are being investigated as optical probes for cellular imaging and as potential cancer treatments in photodynamic therapy. Luminescence-based cellular imaging relies on the probe molecule having distinct absorption and emission profiles, with minimal overlap between them.[9] This allows the imaging agent to be excited at a one wavelength and monitored at a second wavelength with negligible interference from self-quenching. Luminescence from biological fluorophores within the cell can also obstruct detection of the emission from the probe. For in vivo imaging, low concentration of the probe can also be beneficial, but requires intense emission for good image resolution. Thus, the relatively large Stokes shifts, long lifetimes, and low energy absorption and emission wavelengths featured by many transition metal complexes (in comparison to organic molecules) make them attractive for imaging applications.[9]

Photodynamic therapy (PDT) is the targeted delivery of drugs via the activation of molecules by light. Oncology is the largest research area in PDT because of the potential for minimizing the side-effects of chemotherapy.[12] In this paradigm, the spatially selective generation of cytotoxic compounds to a tumor is controlled by the irradiation of "prodrug" molecules by light. Currently, the photoinduced cytotoxicities of these prodrugs occur via one of three general mechanisms: singlet oxygen generation via energy transfer from an excited state molecule, reactive oxygen species generation (for example superoxide and hydroxyl radicals) through electron transfer from an excited state molecule, and oxygen-independent DNA modification though intercalation, covalent binding and cleavage-inducing oxidation.[13]

The photophysical and photochemical attributes of transition metal-organic complexes make them ideal prodrug candidates for PDT. Maximum penetration of tissue by light occurs in the 600 – 900 nm range, which is well-suited to the intense low energy charge transfer absorption bands of transition metal complexes. Production of singlet oxygen requires an intermolecular energy transfer from an excited triplet state of the electron donor to the triplet ground state of O_2. The efficient intersystem crossing and subsequent long triplet lifetimes of many transition metal complexes means that a large quantum yield of singlet oxygen is possible for these complexes.[13] Likewise, these same features, along with photoinduced enhancement in redox ability, can promote generation of reactive oxygen species through electron transfer from the excited state transition metal complex. The excited state redox properties of transition metal complexes can also be applied to DNA cleavage. Covalent binding to DNA requires the prodrug to break or form bonds, but only under illumination. In transition metals this can be accomplished through photoinduced ligand dissociation and substitution.

Electronic devices have incorporated transition metal complexes in several capacities, the most notable of which is in light emitting devices.[14] These optical displays use the electroluminescence of molecules to produce light. The color of light produced depends on both the absorption maximum and the profile of the molecule's emission spectrum. Some colors are produced by using a mixture of molecules such that the overall impression upon combination of the light output is one of the desired color. Thus, structurally tunable emission maxima that occur in the visible region and high luminescence quantum yields are two important properties for this application that make transition metal complexes appealing for these applications.

1.3 Fundamental Research Gives Rise to Technological Applications: Two Case Studies

The next pages aim to highlight, by the examination of selected transition metal-organic complexes, how fundamental studies into the complexes' photophysical and photochemical properties have elucidated important underlying principles of transition metal complex excited state behavior and enabled the complexes' widespread use in optical applications. Furthermore, the use of these compounds in medical, energy, electronic, and chemical applications has in turn resulted in the development of entire families of transition metal-organic complexes with highly tunable characteristics that use the progenitor complexes as structural templates.

1.3.1 Ruthenium (II) trisbipyridine: $[Ru(bpy)_3]^{2+}$

The transition metal-organic complex $[Ru(bpy)_3]^{2+}$ (and derivatives thereof) is arguably the most omnipresent transition metal coordination complex in optical applications. 2,2′-Bipyridine (bpy), the organic ligand in this complex, is a colorless compound that does not luminesce at room temperature in non-aqueous solutions.[15] The compound coordinates readily to metal centers through the pyridine nitrogens, and the resulting metal complexes have been shown to exhibit properties that are quite distinct from those of the ligand. Despite the widespread use of $[Ru(bpy)_3]^{2+}$ in optical applications, it was not a purpose-built compound.

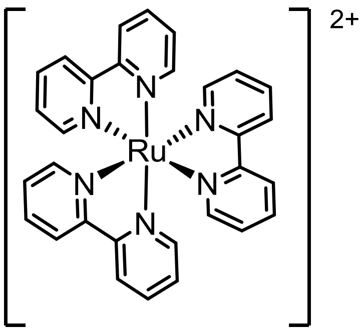

1.1

Figure 1.1 The structure of ruthenium (II) trisbipyridine ($[Ru(bpy)_3]^{2+}$).

$[Ru(bpy)_3]^{2+}$ was initially reported in the literature in 1936, as the first example of chiral resolution and optical activity (specific rotation) for Δ, Λ enantiomers in a cationic metal-organic complex.[16] The complex was reported to exhibit luminescence in 1959 [17] and several studies debating the excited state nature of the luminescence were subsequently published.[18] It wasn't until 1966, however, that a broader interest in the excited state properties of $[Ru(bpy)_3]^{2+}$ began, with the observation of chemiluminescence upon reduction of $[Ru(bpy)_3]^{3+}$ to $[Ru(bpy)_3]^{2+}$ in aqueous solution.[19] Comparison of the emission spectrum of $[Ru(bpy)_3]^{2+}$ and the chemiluminescence spectrum from the reduction reaction revealed the spectra to be identical, indicating that the ruthenium 2+ complex was the source of the luminescence. Following this report, further studies determined the luminescence lifetime, assigned the MLCT nature of the lowest energy absorption, and identified the luminescence as triplet to singlet phosphorescence enabled by the large spin-orbit coupling constant of ruthenium.

In the 1970s, experiments with $[Ru(bpy)_3]^{2+}$ and the electron acceptors and donors methyl viologen and provided the first examples of photoinduced electron transfer from metal complexes.[20, 21] These experiments demonstrated an increase in the reduction and oxidation ability of the photoinduced excited state over the ground state of $[Ru(bpy)_3]^{2+}$, however it was some time before the magnitude of this increase was measured.[22, 23] Up to this time, the primary interest in this molecule was in the basic, scientific discoveries associated with the photophysics and photochemistry of $[Ru(bpy)_3]^{2+}$. However, the realization that, facilitated by the excited state change in redox potential, $[Ru(bpy)_3]^{2+}$ (and therefore possibly other transition metal-organic complexes) could undergo photoinduced intermolecular electron transfer, opened up the possibility of performing otherwise energetically unfavorable chemical reactions and charge generation. This led, through the work of numerous research groups pursuing both applied and fundamental science, to the development of dye sensitized solar cells[22] and the ultimately the ongoing exploration of transition metal complex-based photocatalysis, in pursuit of both water splitting for energy storage and organic synthesis.[24, 25]

The photophysical features that have made $[Ru(bpy)_3]^{2+}$ attractive for a wide variety of optical applications include the placement of the lowest energy MLCT absorption band in the visible spectrum (456 nm/451 nm in acetonitrile and water, respectively),[26] the relatively large molar absorptivity of the MLCT band (14,000/16,000 M^{-1} cm^{-1} in acetonitrile and water, respectively),[26] and the long-lived phosphorescence in the visible region (λ_{em} = 610 nm, τ_T = 920 ns in acetonitrile)[26] which is facilitated by rapid intersystem crossing (τ_{isc} = 25 fs, k_{isc} = 40 ps^{-1}) enabled by the relatively large spin-orbit coupling constant (1200 cm^{-1}).[26] Collectively, these characteristics have made $[Ru(bpy)_3]^{2+}$ a prototype compound for medical imaging[9] and light emitting devices. Likewise, $[Ru(bpy)_3]^{2+}$ and its derivatives have found widespread use in DSSCs[27] because of these properties in addition to the compounds' excited state electron transfer capabilities.

$[Ru(bpy)_3]^{2+}$ has also been studied extensively for possible use in photodynamic therapy. The efficient intersystem crossing from the ^{1}MLCT to the ^{3}MLCT excited state allows for a large quantum yield of singlet oxygen generation, making it an attractive compound. $[Ru(bpy)_3]^{2+}$ has also been investigated because of the ligand dissociation that occurs upon population of antibonding σ^* orbitals, resulting in DNA binding and intercalation.[12]

However, $[Ru(bpy)_3]^{2+}$ does have some drawbacks for certain optical technologies. The phosphorescence quantum yield is relatively low ($\Phi_P = 0.06$ in acetonitrile), which is not ideal for imaging or light emitting device applications. The lowest energy absorption maximum occurs at a fairly high-energy wavelength in the visible region. Absorbance in the lower energy visible region or NIR is desirable for PDT applications in which the light source must penetrate tissue to reach the metal complex. For solar energy applications, the absorption spectrum would ideally cover most of the visible and NIR to better overlap with the solar spectrum and increase the efficiency of solar devices. Efforts to modify these properties have led to the development of innumerable polypyridyl metal-organic complexes based on the $[Ru(bpy)_3]^{2+}$ scaffold (Figure 1.2) and a vast collection of literature on the ground and excited state characteristics of those compounds. In a sense, the research on $[Ru(bpy)_3]^{2+}$ has come full circle, since to date, thousands of fundamental studies have been undertaken, in part because of the technological applications of $[Ru(bpy)_3]^{2+}$ and its polypyridyl derivatives, that have resulted in advances in the understanding of the excited state behavior, photophysical, and photochemical properties of transition metal-organic complexes.

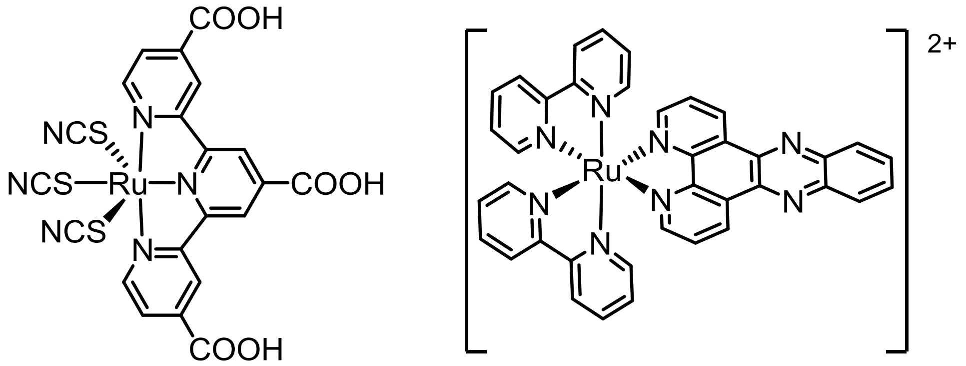

1.2 **1.3**

Figure 1.2 Selected polypyridyl transition metal complexes based on the $[Ru(bpy)_3]^{2+}$ scaffold. The "Black Dye" (left) has been used in DSSCs[28] and the "DNA Lightswitch" (right) has been extensively studied for the luminescence enhancement it exhibits upon DNA intercalation.[12]

1.3.2 Dipyrrins and their Coordination Complexes

The origin of dipyrrin coordination complexes begins with the discovery of, and investigation into, the structure and characterization of the related porphyrin compounds. Porphyrins are naturally occurring cyclic molecules consisting of four pyrrolic units connected by methene carbons (Figure 1.3). The compounds are highly colored, owing to the extended conjugation around the macrocyclic ring. Absorption spectra of porphyrins exhibit two main bands in the visible region, one at approximately 400–500 nm (the B band) and one at approximately 550–750 nm (the Q band). The molar extinction coefficients of both bands are relatively large, with the B band generally possessing a molar extinction coefficient an order of magnitude greater than that of the Q band (10^5 M^{-1} cm-1 and 10^4 M^{-1} cm^{-1}, respectively).[29] Porphyrins are also fluorescent, a property recorded as early as 1867.[30]

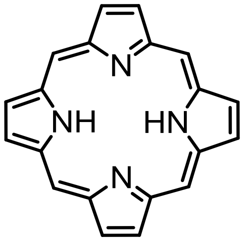

1.4

Figure 1.3 Porphin, the unsubstituted porphyrin skeleton.

The structure of the porphyrin's macrocyclic pocket provides an exceptional coordination environment for a wide variety of metals including nickel, zinc, copper, cobalt, manganese, and cadmium. Two of the best known examples of metalloporphyrins are heme and chlorophyll, porphyrins bound to iron and magnesium, respectively. The chemical efforts to identify and elucidate the structure of the highly colored substance in blood (heme) began in the late 1830s and early 1840 with reports of the extraction of hemin from blood and of the isolation of iron-free heme.[30, 31] In 1871, porphyrin was reported to contain pyrrole units[32] and by the end of the decade, the structural similarity of heme and chlorophyll had been ascertained. It wasn't until 1912,[33] however, that the correct structure of the tetrapyrrolic core of heme was known.[30] Interest in synthesizing the newly defined porphyrin chromophore gave rise to the dipyrrin ligand.

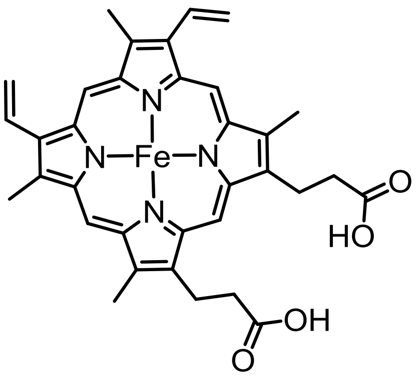

1.5

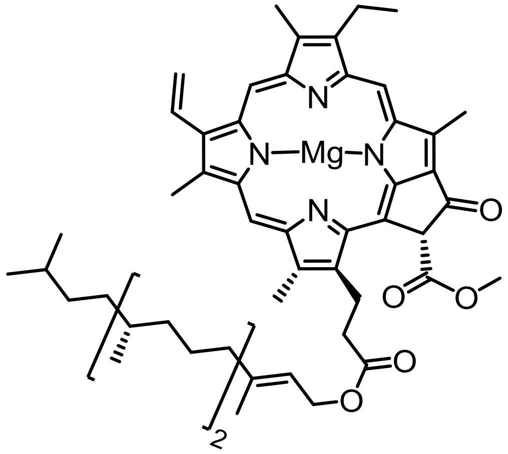

1.6

Figure 1.4 The structures of heme B and chlorophyll A.

The 2,2′-dipyrrin compounds were originally created for use as intermediates in the synthesis of porphyrins.[34] They contain the structural elements of one half of the porphyrin macrocyclic ring (Figure 1.5). The two pyrrolic units are connected by a methene bridge, and conjugation extends over the two pyrrolic units. A key feature of these structures is that it is possible to derivatize the compounds at every peripheral carbon, with much of the synthetic chemistry used to access these derivative being developed by Fischer and coworkers in the first four decades of the twentieth century.[35]

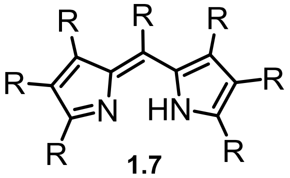

1.7

Figure 1.5 The structure of 2,2′-dipyrrin

The first metal dipyrrin complexes were reported in 1924[36] by Fischer as part of his studies into "blood-dye cleavage products" (i.e porphyrins and related compounds). Several complexes of Zn, Co, Ni, and Cu are presented as containing one metal to two dipyrrin units, and are most likely the homoleptic metal complexes (Figure 1.6). The dipyrrin metal complexes seem to have attracted little attention over the next decades,[37] but reemerge in the 1960s with a handful of reports on metal complexes similar to those described in 1924.[37-40] However, the metal dipyrrin complexes were subsequently overshadowed by the rise of boron complexes of dipyrrins.

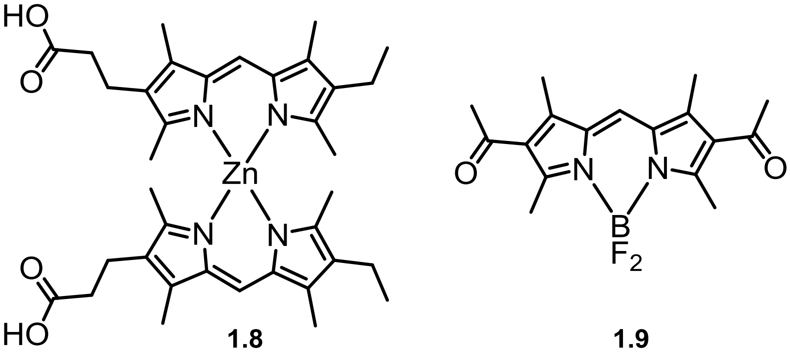

1.8 **1.9**

Figure 1.6 Presumed structure of one group of transition metal-dipyrrin complexes reported in 1924 and one of the boron-dipyrrin (BODIPY) complexes first reported in 1968.

In 1968 the first boron complexes of dipyrrins (BODIPYs) appeared in the literature. [41] This series of complexes were reported to be highly colored in the visible region (appearing yellow to red) and to be intensely fluorescent. Over the next two decades a relatively small number of studies were published investigating the optical properties of BODIPYs[42] and the possibility of using BODIPYs as fluorescent probes[43] and in laser applications.[42]

The advent of using of a BODIPY as a fluorescent probe within a biological system was reported in the literature in 1989,[44] but a patent covering the same use was published the previous year.[45] These publications prompted a flood of investigations into the synthesis, photophysical properties, and biological compatibility of boron dipyrrin dyes. This brought about the ubiquity of boron dipyrrin complexes in biological imaging applications (including their commercial development[46]) by revealing their highly desirable photophysical properties. BODIPYs have highly tunable absorption and emission profiles which range from approximately 500 nm to 900 nm[47] depending on the amount of conjugation appended to the dipyrrin core (this tunability is enabled by the diverse structures available in the dipyrrin substitution). The compounds possess quantum yields nearing unity, even in aqueous solution, and the emission profiles are pH independent.[48] The structural variability of the dipyrrin also allows manipulation of singlet and triplet excited states, and tuning of the complexes to yield accessible triplet states has prompted their use in photodynamic therapy applications.[48, 49]

However, boron dipyrrin complexes have drawbacks for some optical applications. The stokes shift of boron dipyrrin complexes is generally small, causing challenges in their use in optoelectronics.[50] These issues, along with the recognition of the possibility of longer wavelength absorption, have led to a renewed interest in the metal complexes of dipyrrins. While the fluorescence quantum yields of most dipyrrin metal complexes do not rival those of their boron counterparts,[51] a larger stokes shift is often observed, along with an overall red-shift toward the NIR, even without the use of extended pi conjugation. Improvements in fluorescence intensity have been made through the design of particular substitution of the dipyrrin backbone.[34, 52] These improvements have resulted in the investigation of metal dipyrrin complexes for optical applications involving electron and energy transfer.[53]

Without a doubt, the emergence of dipyrrin coordination complexes has caused advances in the technology of optical imaging, and may eventually do the same in other areas of optical technology. However, it is important to remember that none of this would have been possible except for the centuries of basic research that ultimately began with the fundamental question "why is blood red?"

1.4 Research Objectives

Broadly, the objective of the research presented in this thesis is to add to the body of fundamental work related to inorganic transition metal complexes and their excited state behavior. More specifically, this research centers on three primary goals: 1) creation of new organic dyes suitable for transition metal coordination, 2) formation of their corresponding coordination complexes and 3) complete structural, electrochemical, and photophysical characterization of both the dyes and metal complexes. Within this general scope, the focus of this work is synthesis of organic chromophores and their transition metal complexes with reasonably intense ground state absorption in the visible and near IR regions of the EM spectrum. Because absorption in the NIR is a desirable property in several wide-ranging areas of practical application, including solar energy conversion and photodynamic therapy, this provides a principal starting point for our design of new ligands for metal complexation.

The ideal organic chromophores are small-molecule chelating ligands, capable of coordination to metal centers in bidentate, bridging, or tridentate geometries. Small molecules with low-energy absorption maxima in the visible or NIR region and large molar extinction coefficients require either extended pi systems or a donor-acceptor structural motif. In the following chapters, both options are explored. In chapter 2, the classic dye thioindigo is used as a template for the creation of diimine ligands that maintain the donor-acceptor H-chromophore responsible for the parent molecule's absorption in the green portion of the visible spectrum. This approach preserves the absorption properties of thioindigo yet facilitates transition metal complexation of the new dye through the replacement of carbonyl groups with imines, producing a potential bridging ligand capable of chelating metals through an imine-and-thioether moiety. In chapter 4, the synthesis of two new chromophore classes, the aza diindolylmethenes (azaDIME) and aza dicarbazolylmethenes is examined. The design and construction of these chromophores relies on the formation of a fully conjugated pi system that extends across two polycyclic halves of the molecules, which is predicted to imbue the chromophores with absorption in the visible to NIR region of the spectrum. The azaDIME and azadicarbazolyl classes of ligands provide diverse opportunities for metal complexation through neutral and anionic nitrogen donors with a variety of coordination architectures.

Because one the primary aims in developing these new molecules lies in examining the excited state behavior of their transition metal complexes, metals that are known to be compatible with the generation of longer-lived excited states are desirable for the construction of coordination complexes. In chapter 3, investigations into the formation of coordination complexes of the thioindigo diimines using some second and third row transition metals, as well as photophysically compatible first row metals are considered.

Careful characterization of the structural properties of both the free organic ligand and the metal complex and a thorough examination of the photophysics and photochemistry of the molecules is necessary to enhance our fundamental understanding of the relationships between structure, optical properties, and excited state behavior in transition metal complexes, which is an essential goal of this research. To this end, chapters 2 and 3 describe the photophysical, electrochemical, and structural inspection of the thioindigo diimines and their ruthenium hexafluoroacetylacetonate complexes. This inspection revealed sometimes surprising (but always illuminating) differences in photophysical activity between thioindigo and the thioindigo diimines, and highly unusually diastereomeric variation in the excited state behavior of the ruthenium complexes that may advance a new avenue in fundamental photophysical research involving transition metal complexes.

Chapter 2

Thioindigo Diimines and Related Compounds

2.1 Introduction

Trans-thioindigo, the sulfur analog of the well-known dye indigo, is a highly fluorescent compound. Like indigo, thioindigo is a commercially available dye used in pigments and coatings.[54] The spectral and photophysical properties of the two molecules, however, differ significantly, which in the 1950s led to extensive studies of the excited state behaviour of thioindigo.[55-57] More recently, indigo has also become the subject of photophysical investigation.[58-61] Because of its intense fluorescence, thioindigo has been explored as a dye for fluorescent solar collectors.[62, 63] Thioindigos have also been investigated as organic semiconductors and charge generation devices.[64, 65] Additionally, thioindigo is a photochromic compound, undergoing photoinduced *trans-cis* isomerisation. The photoinduced isomerization has been studied in solution,[66-68] monolayers[69] and thin films,[70, 71] and on solid support.[72] The application of the *trans-cis* isomerization in liquid crystals[73, 74] and ion transport[75] has also been investigated.

Research aimed at understanding and controlling the physical and photophysical properties of thioindigo has been advanced through the synthesis, characterization, and application of thioindigo derivatives. These studies have largely focussed on thioindigos with substituents on the carbon atoms of the peripheral benzene rings.[76-80] Analogs made by modification of the ketone moiety are rare; the most commonly synthesized and examined is the leuco form of thioindigo.[81, 82] Isolated examples exist of thioether,[83] amine,[84] and primary imine[85] replacement of the thioindigo ketone.

Substituted imine derivatives represent an unexplored avenue in thioindigo chemistry. This work was undertaken with the objective of expanding the scope of thioindigo derivatives by taking advantage of the carbonyl-to-imine transformation (which has been recently used to make diimine derivatives of indigo)[86] and examining the properties of the products. Synthetic efforts toward the diimines led to the isolation of several unexpected products, some of which we identified as potentially interesting. Herein the spectroscopic, electrochemical, and photophysical characteristics of some 2,2′-diiminothioindigos **2.3** and related diamine compounds **2.2** are presented (Figure 2.1).

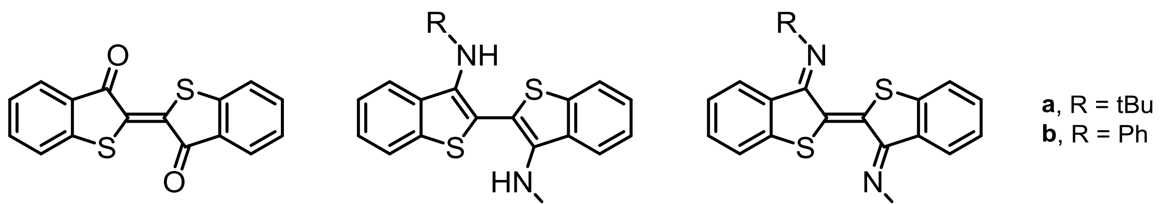

Thioindigo
2.1

2.2a, b

2.3a, b

Figure 2.1 The chemical structures of thioindigo, thioindigo diimines **2.3**, and related amino derivatives **2.2** are shown.

2.2 Synthesis and Photophysics of Thioindigo Diimines (2.3), Amino Derivatives (2.2), and Related Compounds

2.2.1 Synthesis

Imines are commonly prepared by nucleophilic attack of an amine at a carbonyl carbon and subsequent elimination of water. For thioindigo, however, a survey of standard nucleophilic reaction conditions did not lead to product, instead resulting in recovery of starting material. Reaction conditions included addition of a variety of acids, both Bronsted and Lewis (to increase the nucleophilicity of the ketone), and drying agents such as molecular sieves and the use of Dean Stark apparatus (to reduce the back-reaction involving water). Less conventional approaches, including the use of montmorillonite clay were also employed, but did not result in the desired transformation. The failure of amines to react with thioindigo under nucleophilic substitution conditions is likely caused by a combination of factors: the low solubility of thioindigo in most solvents and the increased electron density of the carbonyl carbon due to donation from the sulfur atom which deactivates the carbonyl to nucleophilic attack.

Procedures for making imines using a metal-mediated method in which titanium tetrachloride acts as a coordinating intermediate (not as a Lewis acid) are less common, but have precedent in conjugated systems including anthraquinone and indigo.[87, 88] In these cases a pre-formed titanium-imide species is refluxed in a high boiling solvent (bromobenzene) with the ketone and DABCO, affording the imine. However, when applied to thioindigo, these conditions resulted in the isolation of different products, the nature and distribution of which depend on the starting amine (Scheme 2.1 and Table 2.1).

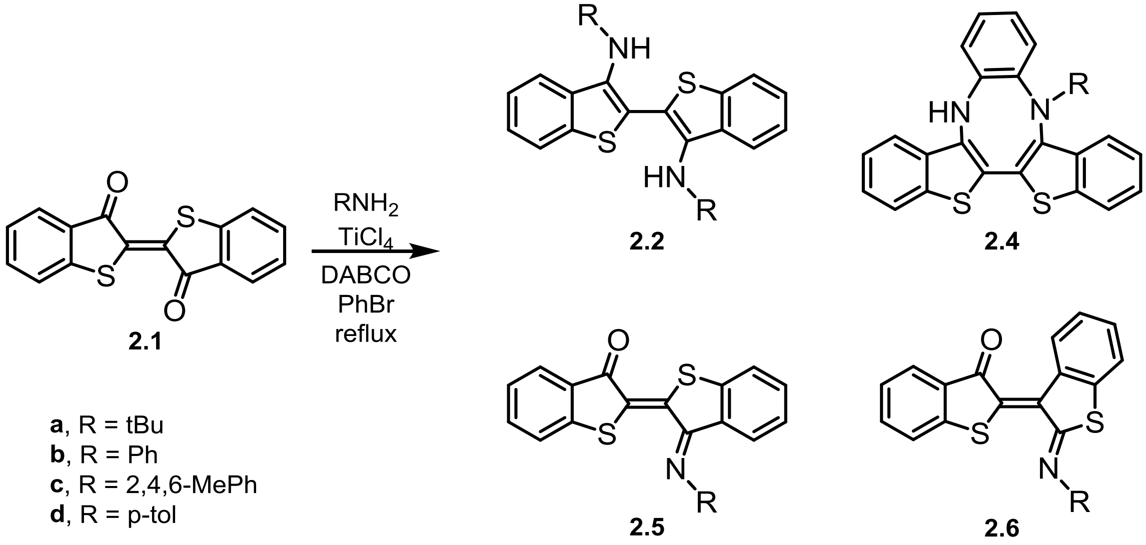

Scheme 2.1 Products from $TiCl_4$ mediated amine condensation reactions with thioindigo.

The reaction also appears to be sensitive to water content, with differences observed in product distribution when the solvent is dried over molecular sieves versus dried in a still. Adding a small amount of water (10-20 μL on a 5 mM scale reaction) to molecular-sieve-dried solvent resulted in product distribution identical to still-dried solvent (which suggests that distilled solvent is not completely dry[89, 90]). Table 2.1 reports product distribution for reactions conducted in still-dried solvents.

Table 2.1 Isolated yields of products observed in Titanium tetrachloride mediated reactions.

Amine	Products				
		2.2	**2.4**	**2.5**	**2.6**
*t*BuNH$_2$	**a**	54%	0%	Trace	Trace
PhNH$_2$	**b**	39%	35%	0%	0%
MesNH$_2$	**c**	0%	0%	9%	33%

The synthesis of the *N,N′*-diphenyldiimine derivative **2.3b** (Scheme 2.2) was attempted, and a yellow compound was obtained following column chromatography. NMR spectroscopy showed lower symmetry than expected, and a single exchangeable proton was confirmed by a D_2O shake. Mass spectrometry data indicated a molecular formula identical to that expected for **2.3b**. Single crystal x-ray analysis elucidated the structure, wherein the thioindigo diimine is reduced and substitution of one amine at the ortho position on a neighbouring phenyl ring has occurred, giving rise to the polycyclic product **2.4b**. By replacing the ortho-hydrogens of the aniline with methyl groups, we hoped to avoid the cyclization reaction. 2,4,6-trimethylaniline was chosen as the replacement amine and was submitted to the reaction conditions. No cyclized product was observed, but neither was desired diimine. Instead, two major products, separable by column chromatography, were each found to incorporate a single amine. Proton NMR and single crystal x-ray analysis (Appendix Figures A1 and A2) revealed one of the compounds to be a monoimine derivative of thioindigo, **2.5c,** while the other was thioindirubin derivative **2.6c**. Lengthening the reaction time did not provide addition of a second amine. Another amine chosen to avoid cyclization, *t*-butylamine, gave yet a different product, a diamine, **2.2a**, which was isolated in 54% yield. Minor products isolated were the monoimine and thioindirubin derivatives (identified by NMR comparison with the trimethylaniline products).

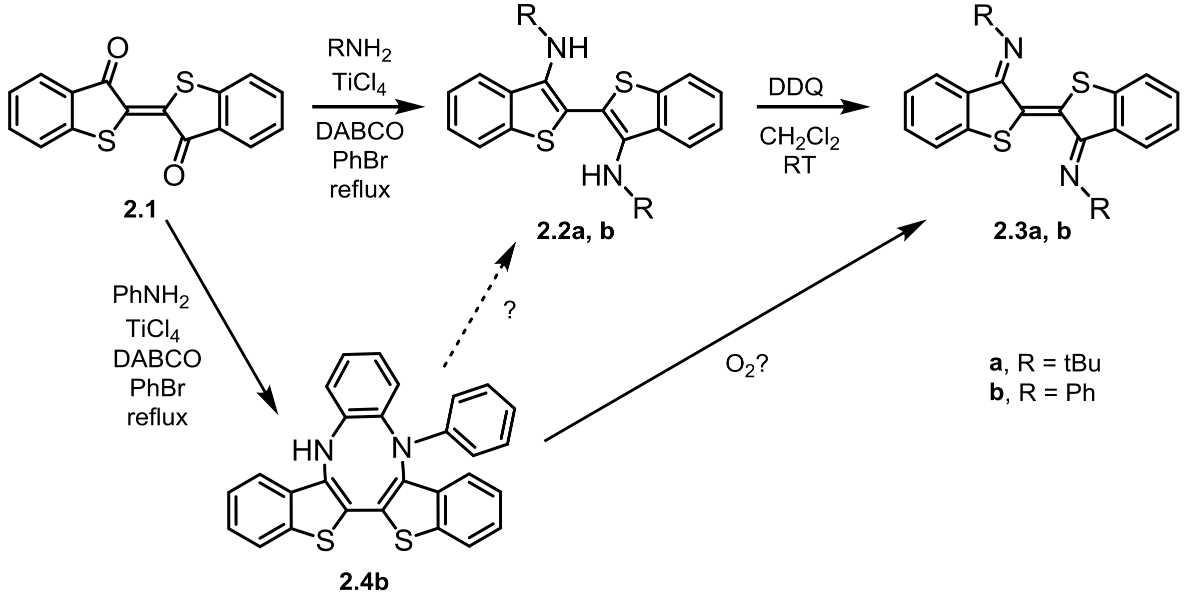

Scheme 2.2 Synthesis of diamines **2.2a,b** and diimines **2.3a, b** from thioindigo.

In the metal-mediated reaction, there are significant differences in reactivity between indigo and thioindigo. The titanium tetrachloride reaction with indigo consistently yields the desired diimine[86, 88] but thioindigo products vary. Formation of cyclized product **2.4** was initially thought to be aided by the known photo-induced isomerisation of thioindigo. However, **2.4** was the major product even when the reaction was run in the dark. Standard conditions for the reaction used an excess of amine (3.1 eq.) and DABCO (9 eq.), both of which could be active in reduction of the imine, and as a source of H^+ in the amine formation. (DABCO is used to remove the HCl generated by reaction of the amine and titanium tetrachloride). Reducing the number of equivalents of aniline to 2.2 did not prevent formation of compound **2.4** or otherwise change the outcome of the reaction. Exchanging DABCO for a base with a higher pK_a could potentially promote formation of diimine over diamine, but the options are limited because a bridgehead nitrogen is necessary to avoid reduction of the titanium and formation of polymeric amine byproduct.[87]

The isolation of thioindirubin derivative **2.6** is striking. Its formation as a major product in the case of the sterically hindered 2,4,6-trimethylaniline, a very minor product in the case of *tert*-butylaniline, and its absence in the case of aniline may suggest a steric component to the formation. Thioindirubins can be made by reaction of thioquinone and thioindoxyl.[91] One explanation for the formation of **2.6** (albeit unlikely, given the air-free reaction conditions) is that thioquinone and thioindoxyl are formed, react with each other to give thioindirubin, and then imine formation occurs (Scheme 2.3). Formation of thioindoxyl from thioindigo is reasonable, as the reverse reaction (oxidative coupling of the enol tautomer of thioindoxyl) is an established method for making thioindigo. Formation of the thioquinone is more problematic, as the second oxygen must come from another thioindigo molecule or dissolved O_2. Dissolved O_2 is an unlikely oxygen source since the reaction is run under N_2. Thioindigo is a possible oxygen source (the combined 42% yield of the products allows it), but an exact mechanism is difficult to envision. An alternative mechanistic possibility invokes a titanium-mediated metathesis pathway in which imine formation and cleavage of the central double bond occur simultaneously, followed by a second metathesis reaction giving the thioindirubin **4.6** and titanium dioxide. This pathway is attractive because it does not necessitate the use of thioindigo as an oxygen source, and relies on established metathesis mechanisms.

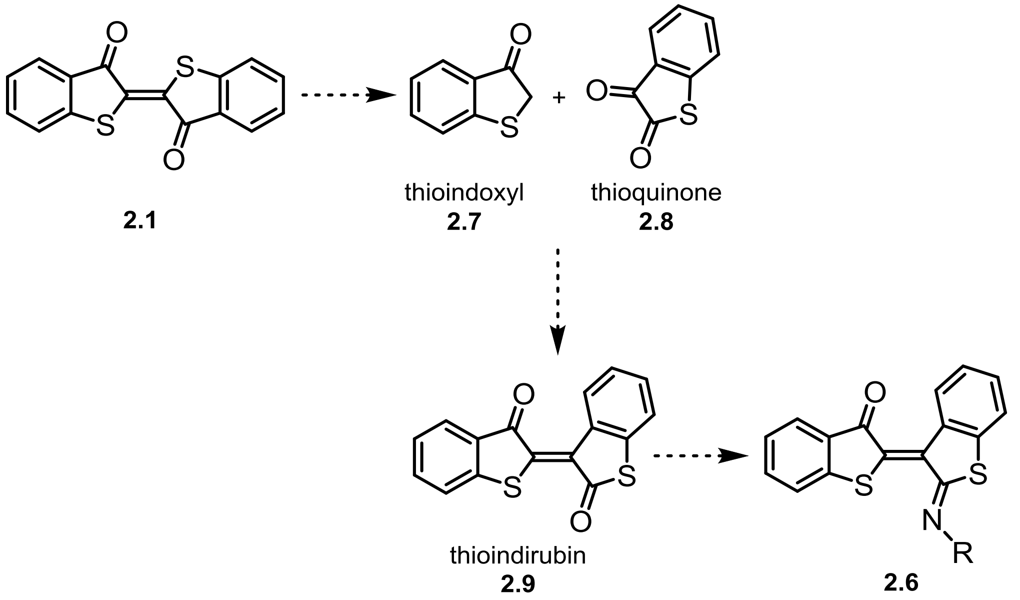

Scheme 2.3 Possible mechanism for formation of thioindirubin derivatives **2.6**.

Formation of the diimines **2.3** was accomplished via two different synthetic pathways. Diamine **2.2a** was converted to the desired diimine **2.3a** (78% yield) by oxidation with 2,3-dichloro-5,6-dicyano-1,4-benzoquinone (DDQ). The diimine **2.3b** was obtained in an unorthodox manner – by subjecting the filtered reaction mixture containing cyclized product **2.4b** to an air or oxygen atmosphere. This slowly results in formation of the diimine and disappearance of **2.4b,** presumably through an oxidative mechanism. Diamine **2.2b** has been isolated from this solution, and may be an intermediate in the synthesis of **2.3b**, although the formation of **2.2b** by reduction of **2.4b** seems unlikely given the oxidizing conditions. Diamine **2.2b** has been subjected to oxidation with DDQ and forms **2.3b** in high yields.

2.2.2 X-ray Analysis

The single crystal X-ray structures of **2.3a** and **2.3b** are shown in Figure 2.2. The π-conjugated core of both derivatives is, within experimental error, planar as expected. Compounds **2.3a** and **2.3b** have C1-C1′ bond lengths of 1.361(4) and 1.350(4) Å, C1-C2 bond lengths of 1.486(3) and 1.481(5) Å, and C2-N1 bond lengths of 1.280(2) and 1.286(5) Å, respectively, in agreement with their assignment as the diimines. The C1-S1 bond lengths for **2.3a–b** are 1.743 and 1.747Å. The C9 of the substituents is almost in plane with the core structure of the diimines; the torsion angles around C9-N1-C2-C1 are 178.75(18)° and 175.5(4)° in the *tert*-butyl and phenyl compounds. The orientation of the phenyl ring of **2.3b** is almost perpendicular to the core, with a torsion angle of 88.85° around C2′-N1′-C9′-C10′. The C1-C1′, C1-C2, and C-S bond lengths of the diimines are comparable to those found in thioindigo derivatives.[65]

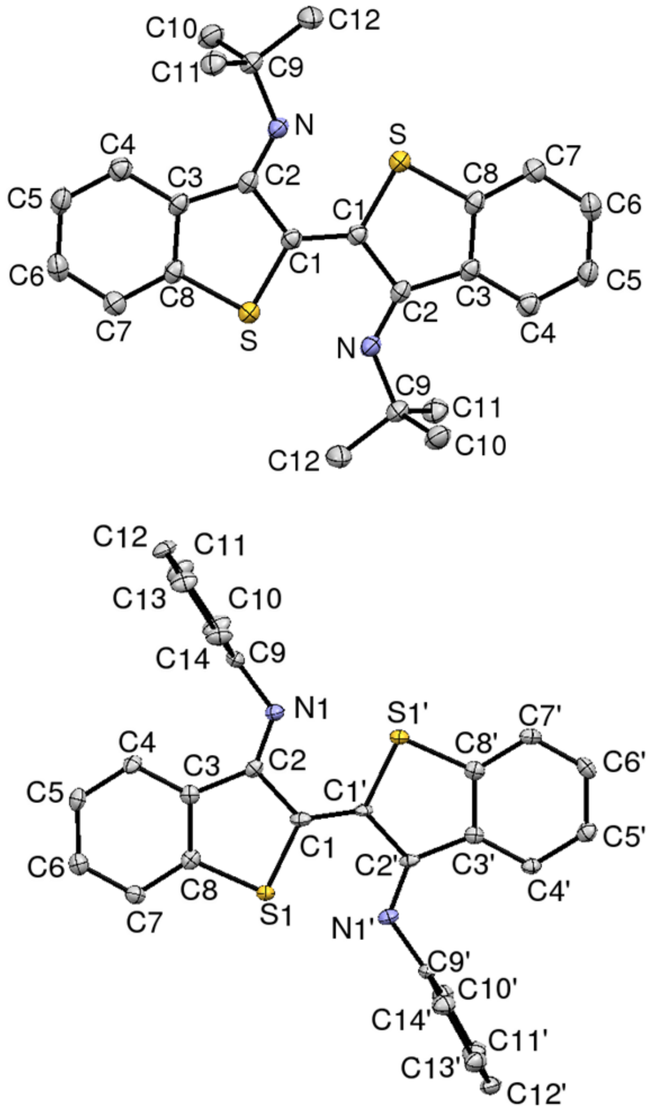

Figure 2.2 X-ray crystal structures of di-*tert*-butyl diimine **2.3a** (top) and diphenyl diimine **2.3b** (bottom). Hydrogen atoms have been removed for clarity. Thermal ellipsoids are presented at 50% probability.

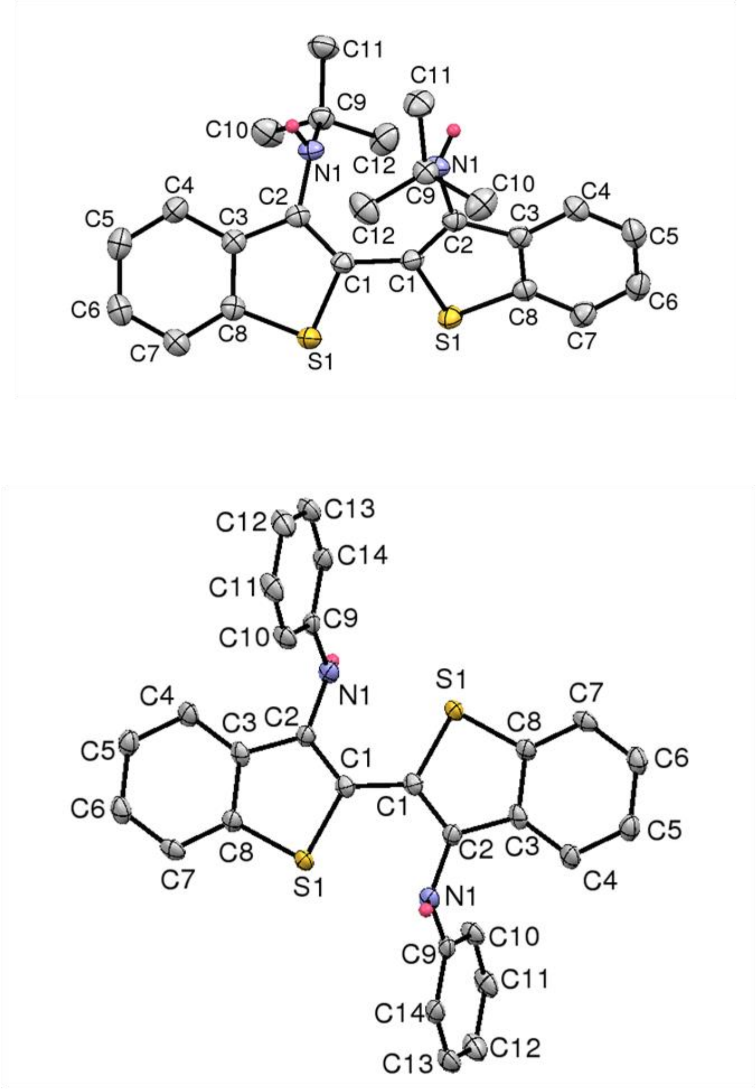

Figure 2.3. X-ray structures of di-*tert*-butyl diamine **2.2a** (top) and diphenyl diamine **2.2b** (bottom). Hydrogen atoms, with the exception of the NH protons, have been removed for clarity. Thermal ellipsoids are presented at 50% probability.

The structures of diamines **2.2a** and **2.2b** are shown in Figure 2.3. Diamines **2.2a,b** have bond lengths consistent with their canonical representations. The C1-C1′ bond lengths are 1.460(3) and 1.454(9) Å and indicate a central single bond while the C1-C2 bond lengths of 1.371(2) and 1.369(7) Å signify double bonds. The C2-N1 bond lengths 1.416(2) and 1.416(6) Å stipulate an amine. In the solid state, the two diamines adopt different configurations in regard to rotation around the central C1-C1′bond. In the *tert*-butyl derivative **2.2a**, the S1-C1-C1′-S1′ torsion angle is 46.5(2)° while in the phenyl derivative **2.2b** the angle is 180.0°. The substituents in the diamines are out-of-plane with the central rings, as evidenced by the C9-N1-C2-C1 torsion angles, 91.87(19)° for **2.2a** and -113.2(6)° for **2.2b**. Additionally, the phenyl substituent in **2.2b** is twisted with regard to the core, with a C2-N1-C9-C10 torsion angle of 19.39°.

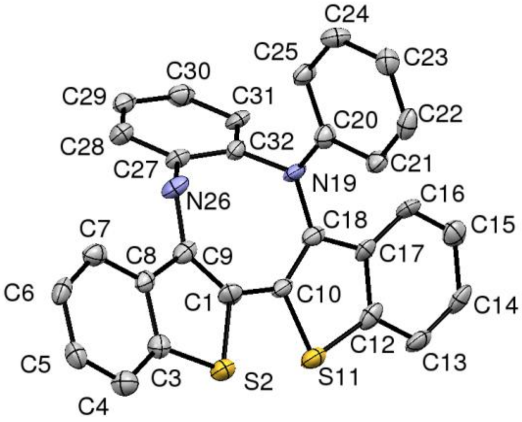

Figure 2.4. X-ray structure of cyclized diazocine product **2.4b**. Hydrogen atoms have been removed for clarity. Thermal ellipsoids are represented at 50% probability.

The x-ray crystal structure of compound **2.4b** was determined (Figure 2.4). The structure identified the new connectivity between N19-C32, the single bond at C1-C10 (1.453(10) Å), and the single bond at C9-N26 (1.408(9) Å). The slightly twisted conformation around the central C1-C10 bond is evidenced by the S2-C1-C10-C18 torsion angle of -159.7(7)°.

2.2.3 Photophysical Studies

Compounds **2.2a,b** and **2.3a,b** were studied by absorption spectroscopy, fluorescence, and laser flash photolysis to determine their excited state behaviour. Comparisons of the photophysical properties of **2.2a,b** and **2.3a,b** to those of thioindigo are provided: the structural similarities between diimines **2.3a,b** and thioindigo are apparent and, while the structures of **2.2a,b** are markedly different, the juxtaposition of their properties with those of **2.3a,b** and thioindigo is provided as context for readers interested in potential photophysical or materials applications of these compounds. The results of preliminary photophysical examinations of diazocine **2.4b** are also presented.

2.2.3.1 Diamines (2.2a,b)

Diamine **2.2a** absorbs in the ultraviolet region with a maximum at 324 nm and an extinction coefficient at this wavelength of $(1.75 \pm 0.04) \times 10^{4}\ M^{-1}\ cm^{-1}$ in methanol (Figure 2.5 and Table 2.2). The compound is fluorescent, and has a fluorescence maximum at 451 nm in methanol. The Stokes shift in methanol is 8690 cm^{-1} (Figure 2.7). The fluorescence maximum is red-shifted slightly with increasing solvent polarity, e.g., by 14 nm on changing solvents from cyclohexane to acetonitrile (Figure 2.6), indicating a weakly polarized excited state. Upon cooling to 77 K in ethanol, the emission maximum is blue-shifted approximately 50 to 60 nm (Figure 2.8), concomitant with an increase in fine structure. The emission intensity decreases at 77 K compared to room temperature, which suggests that aggregation may be occurring at low temperatures.

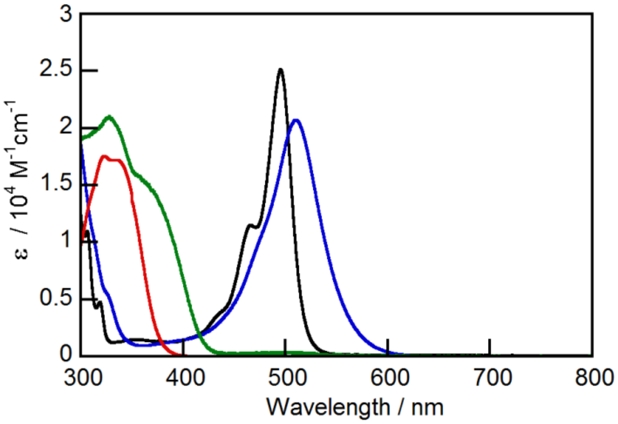

Figure 2.5 Ground state absorption spectra of **2.2a** (red) and **2.2b** (green) in methanol, **2.3a** (black) and **2.3b** (blue) in toluene.

The fluorescence quantum yield of **2.2a** at room temperature is 0.25 ± 0.01 in methanol (three independent experiments). The fluorescence lifetimes in varying solvents were measured in the presence and absence of air. The decays were found to be single exponential and the lifetimes in deaerated solvents range from 1.23 ns in cyclohexane to 2.13 ns in acetone (Appendix Table A1). The fluorescence excitation spectrum and the absorption spectrum show good overlap.

Table 2.2 Absorption and Emission Properties of Thioindigo Derivatives.

	λ_{max}^{abs} / nm	ε^{a} / 10^4 $M^{-1}cm^{-1}$	λ_{max}^{em} / nm	$\Phi_F{}^{a}$	τ_F / ns^{b}	**Solvent**
2.2a	324	1.75±0.04	451	0.25 ± 0.01	1.81 ± 0.06	Methanol
2.2b	328	2.1±0.2	449	0.045 ± 0.004	0.5 ± 0.1	Methanol
2.3a	495	2.4±0.1	N/A	N/A	N/A	Toluene
2.3b	510	2.1±0.1	N/A	N/A	N/A	Toluene

[a]The errors in the molar extinction coefficients and fluorescence quantum yields correspond to the standard deviation of three independent experiments. [b] The errors in the lifetimes correspond to the average errors for two independent experiments.

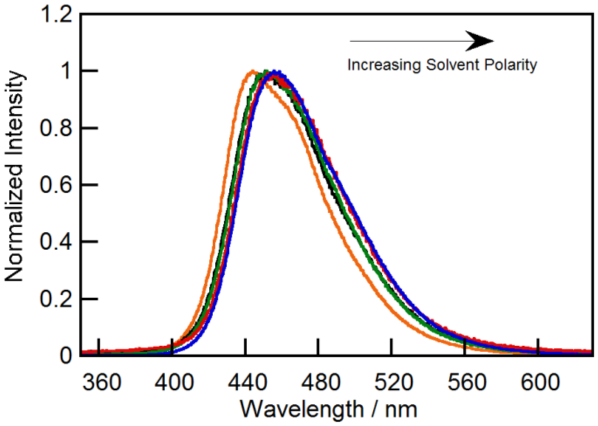

Figure 2.6 Normalized fluorescence spectra of **2.2a** in varying solvents (left to right: cyclohexane, methanol, ethanol, acetone, acetonitrile). The excitation wavelength is 320 nm.

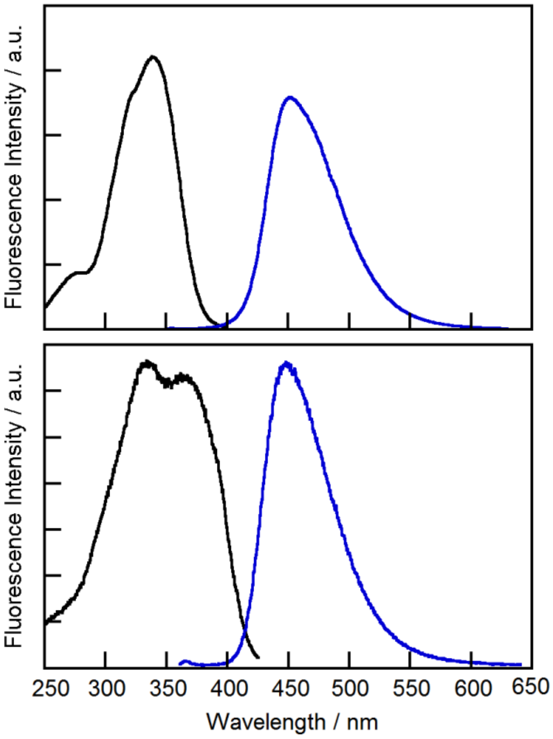

Figure 2.7 Top panel: fluorescence excitation (black line) and emission (blue line) spectra of **2.2a** in methanol at room temperature. Bottom panel: fluorescence excitation (black line) and emission (blue line) spectra of **2.2b** in methanol at room temperature.

Diamine **2.2b** has similar absorbance and emission profiles to **2.2a** (Table 2.2 and Figure 2.5). The absorbance maximum is red-shifted by 4 nm to 328 nm compared to **2.2a**, but prominent shoulder is observed for **2.2b**. The emission maximum is almost identical, at 449 nm (versus 451 nm for **2.2a**). The Stokes shift is still large (8220 cm^{-1}), but slightly more overlap is observed between the excitation and emission spectra (Figure 2.7). The fluorescence lifetime was found to be 0.5 ns in methanol and the quantum yield is correspondingly lower than **2.2a**: 0.045 ± 0.004 at room temperature. The differences observed between **2.2a** and **2.2b** for the lifetimes and fluorescence quantum yields can be ascribed to the different amine substituents. Based on the slight red shift in absorption maxima of **2.2b** relative to **2.2a,** the phenyl substituent in **2.2b** provides some additional degree of conjugation with the rest of the molecule. Therefore, in the excited state the rotation of the phenyl ring can lead to an additional deactivation pathway through internal conversion, consequently shortening the excited state lifetime.[8] The roughly threefold increase in fluorescence intensity for **2.2b** at 77 K compared to room temperature (Figure 2.8) is consistent with this argument. The 77 K emission maximum of **2.2b** is blue-shifted 18 nm relative to the room temperature maximum.

The large blue-shift observed in the ground state absorption spectra for the lowest energy absorption band of diamines **2.2a,b** compared to thioindigo and diimines **2.3a,b** is consistent with the destruction of planarity coincident with diimine reduction and rotation around the resulting central single bond. The loss of planarity is also demonstrated in the crystal structure of **2.2a** (see above). The molar extinction coefficient for **2.2a** is higher than that of thioindigo, but lower than the diimines. The large Stokes shift for **2.2a,b** reveals a substantial change in geometry between the S_0 and S_1 states, while the small red-shift in emission maxima found in solvents of increasing polarity suggests a relatively non-polar excited state.

Compared to reported fluorescence lifetime values of 12.3 ns[57] or 13.4 ns[56] for thioindigo in toluene, the fluorescence lifetimes of **2.2a** and **2.2b** (1.81 ns and 0.5 ns, respectively) are substantially shorter than that of thioindigo. (Both diamines show kinetics corresponding to single exponential decays). Similarly, the quantum yields are much lower for **2.2a** (0.25) and **2.2b** (0.045) than for thioindigo (0.70 to 0.73 depending on solvent).[57]

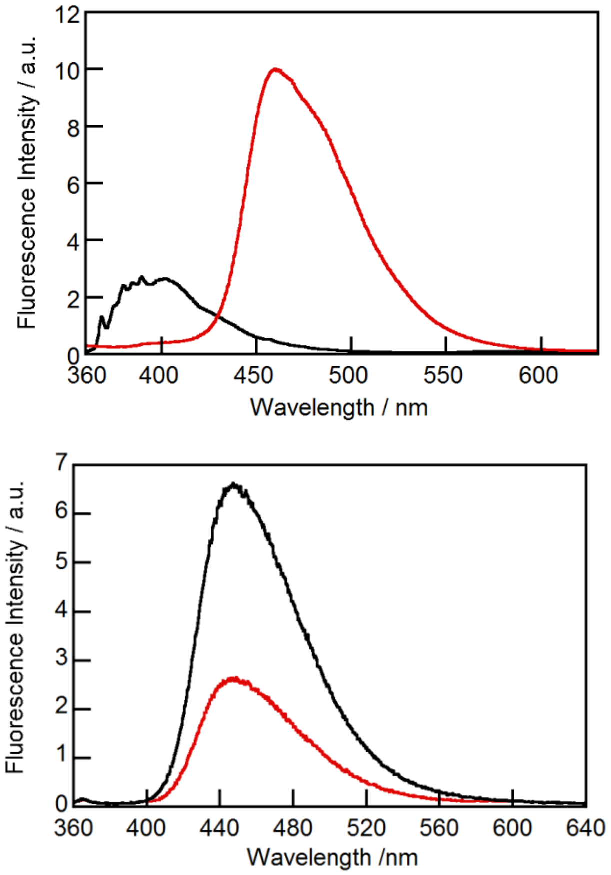

Figure 2.8 Fluorescence emission spectra of diamines **2.2a,b** at 77 K (black line) and at room temperature (red line) in ethanol. The top panel displays the spectrum of **2.2a** (excitation wavelength 320 nm) while the bottom panel displays the spectrum of **2.2b** (excitation wavelength 328 nm).

Transient absorption spectroscopy experiments on **2.2a** show a triplet excited state with an 18 μs lifetime and a single exponential decay. The transient absorption spectrum (Figure 2.9) shows a ground state bleaching at 340 nm and a positive transient absorption at 440 nm.

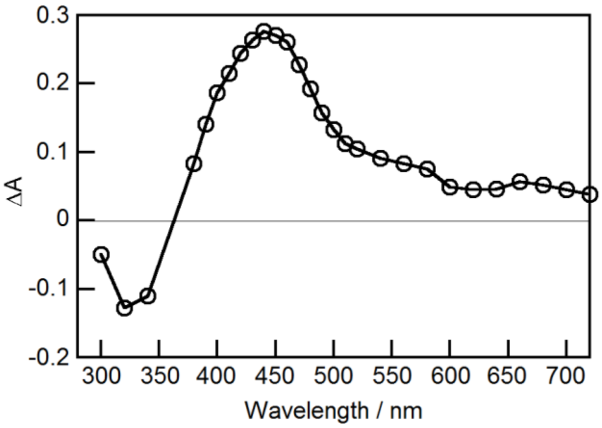

Figure 2.9 Transient absorption spectrum of **2.2a** in toluene (7.8 × 10^{-5} M) integrated between 1.0 and 2.0μs after the laser pulse. Laser excitation is at 355 nm.

Oxygen quenching experiments were carried out to confirm the triplet state, giving a quenching rate constant, k_q, of (3.24 ± 0.04) × 10^9 M^{-1} s^{-1} (one independent experiment; the error is from the fitting software used for equation 2.2), Appendix Figure A3. The energy of the ground state to first excited state transition for oxygen is 94 kJ/mol.[92] Because this energy is low, and the ground state of oxygen is a triplet, most triplet states of organic molecules can be quenched by oxygen. Because the measured quenching rate constant of **2.2a** by oxygen is (3.24 ± 0.04) × 10^9 M^{-1} s^{-1}, the quenching is close to the diffusion limit. (The diffusion rate constant for toluene is 1.1 × 10^{10} L mol^{-1} s^{-1}.)[92] Together, these results indicate that the transient observed in the laser flash photolysis studies is a triplet excited state. By performing a series of quenching experiments on **2.2a** using triplet quenchers with sequentially higher triplet energies, the E_T of **2.2a** was determined to be approximately 220 kJ mol^{-1} with an upper limit of 240 kJ mol^{-1} (Table 2.3 and Appendix Figures A3–A6).

Table 2.3 Rate constants for the quenching of the triplet state of **2.2a** by various quenchers and triplet excited state energies of the quenchers.

Quencher	E_T **(kJ/mol)**[a]	E_T **(kcal/mol)**[a]	k_q **(M^{-1} s^{-1})**[b]
Oxygen	94	22.4	$(3.24 \pm 0.04) \times 10^9$
Ferrocene	159	38.0	$(1.16 \pm 0.05) \times 10^9$
1,3-cyclohexadiene	219	52.4	$(3.1 \pm 0.2) \times 10^8$
1,3-pentadiene (E/Z)	247/240	59.0/57.4	0

[a]Triplet energies from Murov, S.L.; Carmichael, I.; Hug, G.L. *Handbook of Photochemistry, 2nd Edition*, Marcel Dekker, Inc., 1993. [b]One independent experiment, quenching rate constant errors were calculated by the Kaleidagraph software used to fit the quenching plots.

Similar to **2.2a**, **2.2b** exhibits a transient absorption spectrum with a ground state bleaching at approximately 340 nm and a positive transient absorption at 460 nm (Figure 2.10). The transient species has a 22μs lifetime, a single exponential decay (Appendix Figure A7), and exhibits an oxygen quenching rate constant consistent with a triplet state ($(3.1 \pm 0.1) \times 10^9$ M^{-1} s^{-1}), analogous to the transient spectroscopy of **2.2a**.

The triplet excited state species observed in the transient absorption spectra of **2.2a** and **2.2b** have significantly longer lifetimes (18 and 22μs) than the triplet state observed for thioindigo, which is reported as 135 to 428 ns depending on the solvent.[57, 93-95] The k_q of 3.24×10^9 $M^{-1}s^{-1}$ and 3.1×10^9 $M^{-1}s^{-1}$ found in oxygen quenching experiments (for **2.2a** and **2.2b**, respectively) are on par with those found for thioindigo (3.2×10^9 $M^{-1}s^{-1}$, 2.12×10^9 $M^{-1}s^{-1}$ depending on solvent).[57, 93]

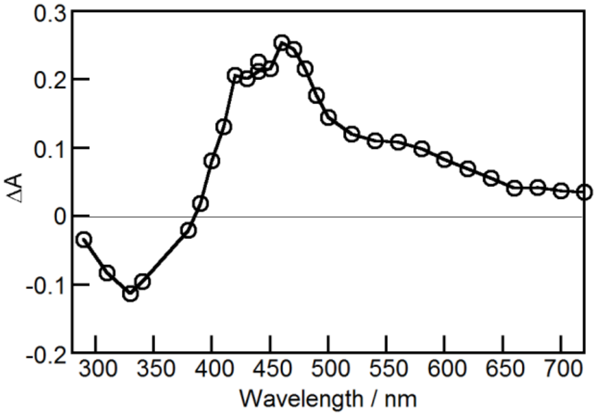

Figure 2.10 Transient absorption spectrum of **2.2b** in toluene (8 × 10^{-5} M) integrated between 2.0 and 4.4 μs after the laser pulse. Laser excitation is at 355 nm.

2.2.3.2 Diimines (2.3a–b)

Diimines **2.3a** and **2.3b** absorb in the visible region (Figure 2.5), with absorption maxima in toluene at 495 and 510 nm, respectively, corresponding to their lowest energy bands. Molar extinction coefficients at the lowest energy absorption maxima are (2.4 ± 0.1) × 10^4 M^{-1} cm^{-1} and (2.1 ± 0.1) × 10^4 M^{-1} cm^{-1} (**2.3a**, **2.3b**). No emission is observed at room temperature or 77 K for either molecule. The spectral data are shown in Table 2.2.

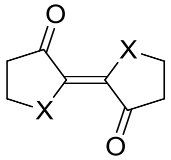

Figure 2.11 The "H-chromophore"of thioindigo (X = S) and indigo (X = NH).

The absorbance maxima of diimines **2.3a,b** are blue-shifted by 47 and 32 nm from thioindigo. The relatively low energy absorption maximum of thioindigo (542 nm in toluene)[57] is due to the central cross-conjugated sulfur-to-oxygen structural motif, or “H-chromophore”[96] (Figure 2.11). X-ray crystal structures show that the planar structure of the central thioindigo scaffold is maintained in **2.3a,b**. The solid state planarity is most likely conserved in solution, suggesting that the blue-shift is caused by a disruption of the H-chromophore due to the weaker electronegativity of the imine nitrogen. Because of the out-of-plane geometry of the substituents relative to the core of the molecule, the nature of the imine substituent only mildly affects the wavelength of the absorption maxima. The ε values of **2.3a,b** are between 17% and 70% higher than that of thioindigo, which in toluene has reported molar extinction coefficients of (1.4 and 1.8) × $10^4 M^{-1}cm^{-1}$.[57, 97] Fine structure is observed in the absorbance spectrum of **2.3a**. In contrast, **2.3b** is broadened and lacks fine structure.

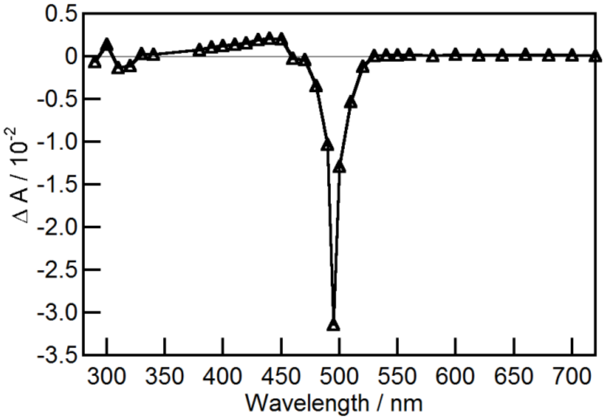

Figure 2.12 Transient absorption spectrum of **2.3a** in toluene (5.7 × 10^{-5} M) integrated between 132 and 391 ns after the laser pulse. Laser excitation is at 355 nm.

The transient absorption spectrum of **2.3a** (Figure 2.12) shows a ground state bleaching at 495 nm and a positive transient absorption at 440 nm. A 1.5 μs transient lifetime is observed in both toluene and acetonitrile (laser excitation at 355 nm and 266 nm, respectively). The lifetime is unchanged when oxygen is removed from the solution. The transient absorption spectrum in acetonitrile (Appendix Figure A8) has an identical shape, but the features are blue-shifted approximately 5 nm from the toluene spectrum. This is consistent with the blue shift observed in the ground state absorption spectrum.

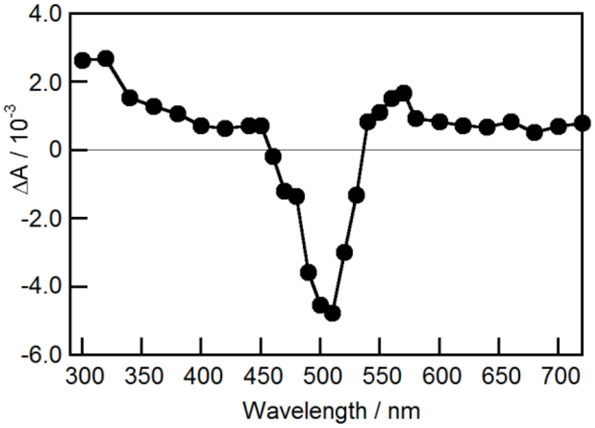

Figure 2.13 Transient absorption spectrum of **2.3b** in dichloromethane (2.2×10^{-5} M) integrated between 852 ns and 3.70 μs after the laser pulse. Laser excitation is at 266 nm.

Because of poor solubility in acetonitrile and very low ground state absorbance at 355 nm, LFP experiments on **2.3b** were performed in dichloromethane with laser excitation at 266 nm. These experiments reveal a transient species with a 29 μs lifetime. As we observed with **2.3a**, the lifetime is unchanged when oxygen is removed from the solution. The transient spectrum shows a ground state bleaching at approximately 510 nm (Figure 2.13).

The lack of emission from the diimines was unexpected based on the known emissive properties of thioindigo. (Originally, the reformation of the central double-bond and planarization of the core structure in the diimines was hypothesized to increase fluorescence intensity compared to the diamines). Thioindigo is highly emissive, with a fluorescence quantum yield of 0.70 to 0.73 depending on solvent.[56, 57] *Trans-cis* isomerisation competes with fluorescence as a decay pathway in thioindigo. This photoisomerization is media dependent, with an upper limit of $\Phi_{trans \rightarrow cis}$ = 0.11, and occurs via intersystem crossing to a triplet state.[56, 93, 95] *cis*-Thioindigo exhibits a blue-shifted absorption maximum at 485 nm[98] and is metastable.[99] The lifetimes of the transient species observed for diimines **2.3a**,**b** are unchanged in oxygen quenching experiments, ruling out triplet states or radical species. However, the lack of sensitivity to oxygen in the quenching experiments is consistent with the formation of a *cis*-thioindigo-type isomer (i.e. isomerism about the central C=C bond). The bleaching of the $S_0 \rightarrow S_1$ absorption (495 nm) and blue-shifted positive absorption (440 nm) in the transient absorption spectrum further supports the assignment of the transient to a *cis* isomer. Together, these features indicate that isomerism may be responsible, at least in part, for the diimines' lack of fluorescence. Nevertheless, we cannot completely rule out the possibility that *imine* (C=N) isomerism could be occurring instead, although confirmed examples of this are quite rare due to the very fast reversion of the photoexcited *cis* form of the imine back to the *trans*.[100, 101]

Another possible cause for the lack of emission must also be considered. Recent mechanistic studies have shown that intramolecular photoinduced electron transfer (PET) can quench fluorescence in compounds that contain imine moieties.[102, 103] The diimines **2.3a,b** contain the structural motifs that make this quenching mechanism possible. However, the complete lack of emission from the diimines hinders further evaluation of this mechanism because of the requirement for the energy difference between the ground and excited states in the Rehm-Weller equation.

2.2.3.3 Diazocine (2.4b)

The ground state absorption spectrum of **2.4b** exhibits a profile that is intermediate between the diamine **2.2b** and the diimine **2.3b**. The diazocine has absorption bands in the UV region of the spectrum, with a λ_{max} at 275 nm, and a low energy absorption band in the visible region of the spectrum with an absorption maximum at 416 nm in ethanol (Figure 2.14). The molar extinction coefficient of the low energy band is approximately 7.3×10^3 M^{-1} cm^{-1} (single data point measurement), which is significantly lower than the extinction coefficients of both the corresponding diamine and diimine (2.1×10^4 M^{-1} cm^{-1}).

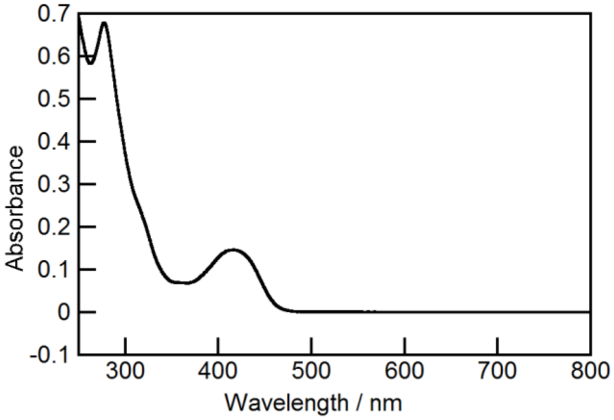

Figure 2.14 Ground state absorption spectrum of diazocine **2.4b**, 20 μM in ethanol.

The intermediate wavelength of the low energy absorption band makes sense in terms of the structures of **2.2b**, **2.3b**, and **2.4b**. The polycyclic nature of the diazocine prevents rotation about the central bond that connects the two halves of the thioindigo moiety, and imparts a relatively planar structure to the molecule, providing more contribution from conjugation than is found for diamine **2.2b**. However, as can be seen in the X-ray crystal structure, the molecule is not perfectly planar (Figure 2.4), and the H-chromophore pattern that imparts the lower energy absorption bands to diimine **2.3b** is absent in the diazocine.

Diazocine **2.4b** is not fluorescent in room temperature solutions, but does display luminescence when examined at 77 K in an ethanol glass. The emission maximum is at approximately 480 nm (Figure 2.15), and the spectral shape is similar to the emission spectrum of **2.2b**, with a sharp onset of luminescence at short wavelengths and a trailing edge at longer wavelengths. The low temperature luminescence turn-on observed for diazocine **2.4b** is analogous to the increase in fluorescence intensity observed for diamine **2.2b** at low temperature. Rotation about the N-C bond connecting the "free" phenyl ring to the polycycle provides an internal conversion deactivation pathway at room temperature that is not available to the molecule when frozen in a glass at 77 K.

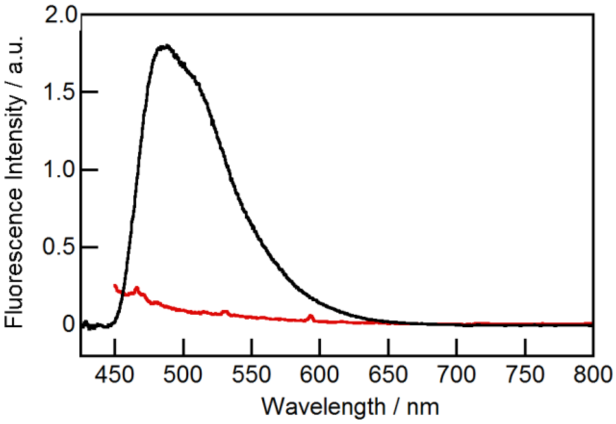

Figure 2.15 Fluorescence emission spectrum of **2.4b**, 2.2 μM in ethanol at 77K (black line) and room temperature (red line). The excitation wavelength is 400 nm.

2.2.4 Redox Properties of Diimines (2.3a,b)

Cyclic voltammetry was used to characterize the redox behaviour of the diimines **2.3a,b** and for comparison thioindigo was also analyzed. (Only one report on the electrochemistry of thioindigo exists in the literature; the experiments were performed in DMF).[104] Because of solubility considerations, the experiments were performed in dichloromethane.

The *tert*-butyl diimine **2.3a** exhibits a quasi-reversible one-electron oxidation peak at E_1^{O} = 0.66 V vs. Ferrocene (Figure 2.16). An irreversible two-electron reduction peak is observed at -1.91 V. Scanning to higher potentials leads to additional irreversible processes and the 0.66 V oxidation also becomes irreversible. Like **2.3a**, diphenyl diimine **2.3b** has two one electron oxidation peaks. The first is at 0.87 V vs. Ferrocene and the second appears at the edge of the solvent window at approximately 1.3 V (Appendix Figure A9). The oxidation peaks at the edge of the dichloromethane solvent window for **2.3a,b** could not be further investigated because of compound insolublility in appropriate solvents (*e.g.* acetonitrile). Unlike the first oxidation in the *tert*-butyl diimine, the oxidation of **2.3b** at 0.87 V is irreversible, even if the switching potential is set before the onset of the second oxidation. A two-electron reduction at -1.55 V is noted for diimine **2.3b**. The more facile nature of the reduction in **2.3b**, compared to **2.3a,** is accounted for by the greater ability of the phenyl substituent to delocalize the negative charge. The reduction and oxidation processes for **2.3b** are more closely spaced than for **2.3a**.

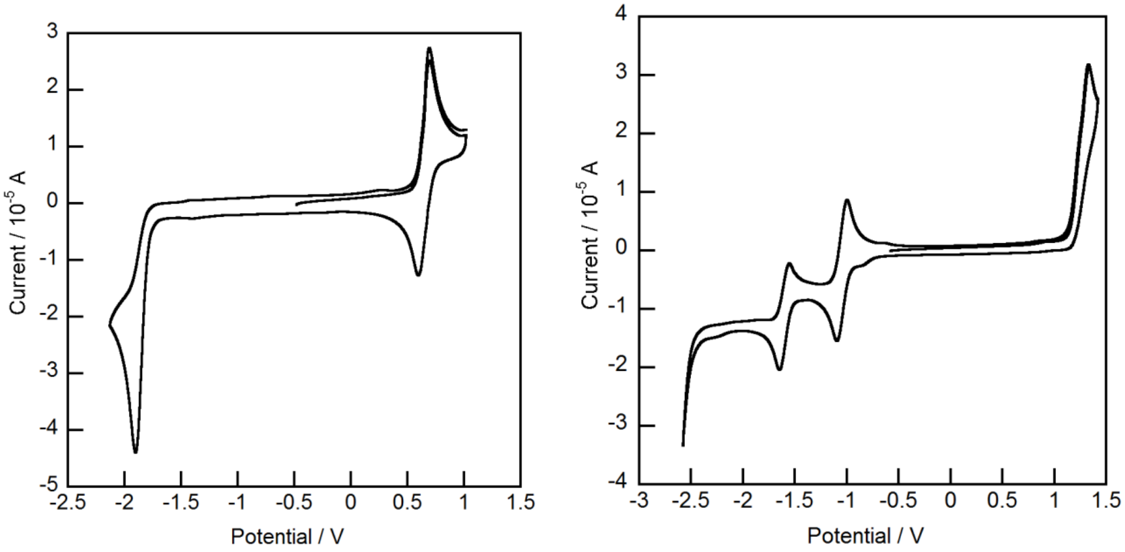

Figure 2.16 Cyclic voltammograms of diimine **2.3a** in dichloromethane (left panel), and thioindigo in dichloromethane (right panel). The concentration of analyte in dichloromethane is ~1 mM. The standard is Fc/Fc$^+$, the electrolyte is 0.1 M Bu_4NBF_4 and the scan rate is 100 mV s^{-1}.

In contrast with the diimines, thioindigo has two one-electron reversible reduction processes (E_1^O = -1.1 V; E_2^O = -1.6 V vs. Fc/Fc$^+$). An irreversible two-electron oxidation process is visible at the edge of the solvent window (Figure 2.16). The less positive potential of the oxidation peaks in the diimines can be explained in terms of the lower electronegativity of the imine nitrogen atoms compared to the thioindigo oxygen atoms. Likewise, the thioindigo reduction peaks occur at more positive potentials than the diimines because of the more electronegative nature of the oxygen atoms.

2.3 Protonation of thioindigo diimines (2.3a,b)

Protonation of the thioindigo diimines was undertaken with the aim of further investigating the possibility that intramolecular PET was responsible for the diimine's lack of fluorescence. Protonation of the imine functional group in molecules that experience fluorescence quenching by an intramolecular PET mechanism has been shown to inhibit the PET and increase the fluorescence quantum yields of those molecules.[102] Treatment of the diimines **2.3a,b** with trifluoroacetic acid (TFAA) resulted in protonation, however the diimines were found to be weakly basic, with the presence of water leading to deprotonation and reformation of the starting species. Careful drying of the solvents and reagents combined with measurement of water content by Karl Fisher apparatus allowed closer examination of the protonation.

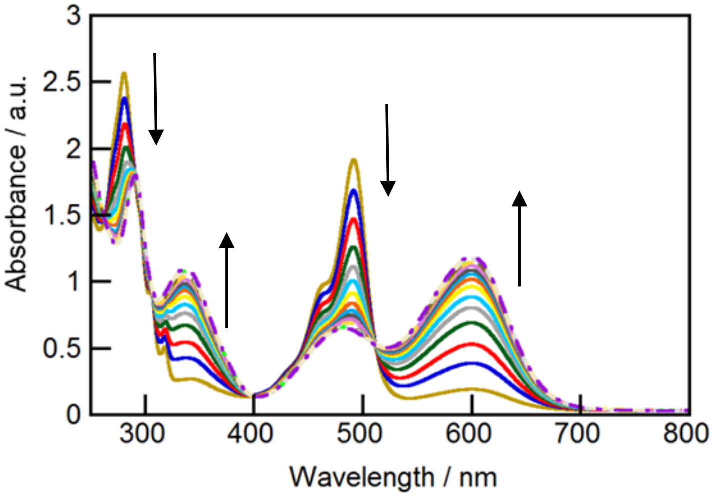

Figure 2.17 Titration of diimine **2.3a** with trifluoroacetic acid in dichloromethane, from 1 equiv. of TFAA (tan line) to 33 equiv. of TFAA (dashed purple line).

Titration of the diimine **2.3a** with TFAA in dichloromethane was monitored using UV-visible absorption spectroscopy and revealed that the protonation was an equilibrium reaction (Figure 2.17). After the addition of 32 equivalents of TFAA, an endpoint for the titration was reached. A pronounced red-shift in the absorption spectrum was observed for the protonated species relative to the neutral diimine, with the lowest energy maxima upon protonation occurring at 599 nm compared with 491 nm for the neutral species. This is similar to the red-shift in the lowest energy absorption maximum reported for thioindigo in sulfuric acid.[105] The clean isosbestic points in the absorption spectrum imply that protonation of only one imine is occurring, although theoretically two protonations are possible.

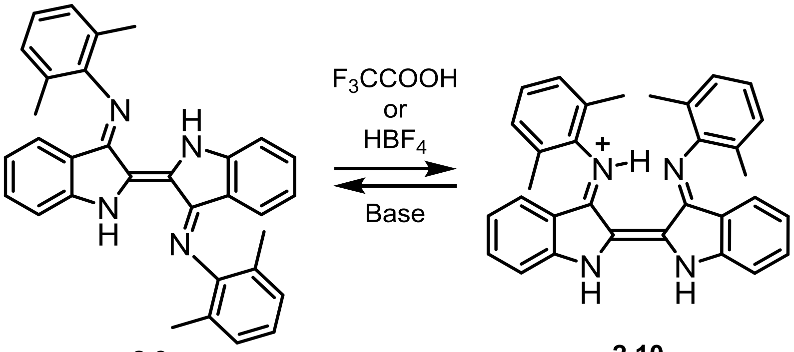

2.9 **2.10**

Scheme 2.4 Protonation of *trans* Nindigo **2.9** induces isomerization to the *cis* product **2.10**.

Mono-protonation of the related Nindigo ligands has been shown to proceed with isomerization about the central double bond, resulting in a *cis* structure for the protonated Nindigo (Scheme 2.4).[106] Identification of the protonated thioindigo diimine as the *trans* or *cis* isomer (**2.7** or **2.8**, Scheme 2.5) by X-ray crystallography or NMR spectroscopy is complicated by the weak basicity and readily reversible nature of the protonation. Isolation of solid samples of the protonated diimine were unsuccessful, and ^1H NMR experiments demonstrate that exchange between protonated and unprotonated species is occurring much faster than the NMR timescale at room temperature (i.e. only one set of peaks is observed, with chemical shifts that are an average of the two species in solution) (Appendix figure A23). Unfortunately, low temperature ^{1}H NMR spectra were not instructive; spectra obtained at 183 K using solutions of **2.3a** and either one or two equivalents of TFAA were uniformly broadened. The spectra appeared to show the presence of two species, but lacked the detail necessary for structure elucidation (Appendix Figure A24). ^{1}H NMR spectra acquired at higher concentrations of TFAA were obscured by the presence of a large, broad signal in the aromatic region of the spectrum that was assigned to the TFAA proton.

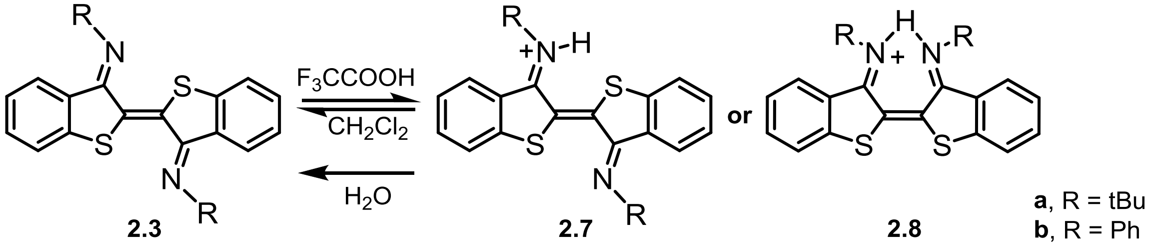

Scheme 2.5 Protonation of diimines **2.3a,b** with trifluoroacetic acid. The protonation is reversed by the addition of water.

Room temperature solutions of diimine **2.3a** and TFAA were examined for fluorescence, but were not emissive. However, this lack of luminescence cannot be used to dismiss intramolecular PET as a quenching mechanism in the neutral species. Because the diimine is monoprotonated, one imine moiety could still be available for PET. Moreover, proton transfer could be occurring in the excited state. The introduction of a hydroxyl group at the 4-position of thioindigo has been shown to result in fluorescence quenching.[76] This quenching has been attributed to excited state intramolecular proton transfer akin to the excited state proton transfer that imbues indigo with excellent photostability.[58, 107] Some thioindigos have been reported to experience fluorescence quenching in the presence of phenols and some alcohols, with a correlation observed between increasing acidity of the alcohol and increasing quenching rate constant.[108] It is therefore possible that by protonating the diimines, another quenching pathway has been introduced.

2.4 Future Work

The role of intramolecular PET in the luminescence quenching of diimines **2.3a,b** may yet be clarified. Methylation of the diimines to create the iminium salts may be possible. The methyl iminium should not be as labile as the proton, which would remove the concerns about photoinduced proton transfer as a potential quenching mechanism. Whether methylation of one or both imines would occur is unknown, and is a drawback to further studies on the diimines.

An attractive alternative is to initiate photophysical studies on the monoimine **2.5c**. The monoimine contains only one imine moiety, retaining one of the thioindigo ketones. It should still have the ability to isomerize about the central C–C double bond, but the potential for intramolecular PET is halved. Additionally, the presence of a single imine could simplify the protonation or methylation reactions to produce iminium ions. If the neutral monoimine proves to be fluorescent under photophysical examination, the Rehm-Weller equation may be used to evaluate the likelihood of intramolecular PET in the molecule. But regardless of whether the monoimine is fluorescent, protonation and methylation of the imine nitrogen could provide useful information on role of both the intramolecular PET and proton transfer quenching mechanisms in thiodindigo-type compounds.

2.5 Conclusions

The first examples of substituted diimine and diamine derivatives of thioindigo have been synthesized in a two-step sequence, in good yields. The diamine compounds were found to retain some of the fluorescent nature of thioindigo, exhibiting moderate quantum yields. Surprisingly, the diimines were not fluorescent, despite the restoration of a rigid core-structure similar to thioindigo. Investigation into the excited state characteristics of the diimines revealed a transient species consistent with the formation of a *cis* isomer. The *trans-cis* isomerisation may be responsible for the absence of fluorescence, however intramolecular photoinduced electron transfer cannot be ruled out as a contributing factor. The diimine compounds were found to be redox-active. The redox-active nature of the diimines suggests that they are potential ligands for metal coordination complexes. Complexes where the diimines behave as bidentate ligands through nitrogen and sulfur bonds may also have the dual effect of stabilizing the central C-C double-bond and inhibiting PET with the imine, thereby restoring fluorescence.

2.6 Experimental Details

2.6.1 General Synthetic Methods

The reagents used were commercially available. With the following exceptions, reagents were used without purification. Bromobenzene was dried over calcium hydride and distilled before use. Aniline, *tert*-butyl amine, and 2,4,6-trimethylaniline were purified by vacuum distillation.

^{1}H NMR and ^{13}C NMR were recorded at ambient temperature at a frequency of 360 or 300, and 90 or 75 MHz, respectively. The data are reported as follows: proton multiplicities (s = singlet, d = doublet, t = triplet, q = quartet, m = multiplet, br = broad, app = apparent), coupling constants, and integration. Melting points are reported uncorrected. Flash chromatography was performed using the indicated solvent system on silica gel (SiO_2) 60 (70–230 mesh). CV experiments were performed using a three-electrode setup consisting of a glassy carbon working electrode, platinum electrode, and silver quasi-reference electrode. Ferrocene was used as an internal reference. Electrolyte (tetrabutylammonium tetrafluoroborate) was purified and dried prior to use.

2.6.2 General Photophysical Methods

Fluorescence measurements were made using a PTI QM-2 fluorescence spectrophotometer. Room temperature spectra were obtained using a 10 mm × 10 mm quartz fluorescence cell. Low temperature spectra were obtained using a special low-temperature fluorescence cell. The solution of compound in ethanol was placed in a 2 mm diameter quartz sample tube and frozen by immersion in a liquid-nitrogen-filled cell. The sample was inspected for homogeneity and fluorescence measurements were taken. Control measurements (ethanol alone, and sample at room temperature) were obtained using the same apparatus. The step size was 0.5 nm and the excitation and emission monochromator slits were set to 2 nm or 3 nm bandwidths. For emission spectra of **2.2a** and **2.2b**, the excitation wavelengths were 320–322 nm and 328 nm, respectively. For excitation spectra of **2.2a** and **2.2b**, the emission wavelengths were 440 or 450 nm and 430 or 450 nm, respectively. Fluorescence decays were recorded with an Edinburgh OB 920 single photon counter. Decays were recorded with 10 mm × 10 mm long-stem fluorescence cells. The excitation wavelength was 335 nm using a light emitting diode (Edinburg Instruments EPLED-330). The emission wavelength was 450 nm unless otherwise noted. Emission slits were set to achieve 16 nm in bandwidth. The number of counts in the maximum intensity channel was 2000. The instrument response function was recorded using a Ludox solution where the emission was detected at the same wavelength as the excitation wavelength. Laser flash photolysis experiments were excited with an Nd:Yag laser at either 266 or 355 nm.[109] A quartz 7 mm × 7 mm cell was used for LFP experiments. Fluorescence quantum yields were measured using quinine bisulfate in 1N sulfuric acid as the standard ($\Phi_F = 0.546$).[110] Spectrophotometric grade or higher purity solvents were used for all photophysical experiments. Reagents used in triplet quenching experiments were used as received with the exception of 1,3-cyclohexadiene which purified by vacuum distillation prior to use. 1,3-pentadiene (piperylene) was determined by NMR to be a 1.8:1 ratio of E/Z isomers and was used without further purification. Oxygen-free solutions were obtained by bubbling nitrogen gas through the sample solution in the cell for at least 20 minutes.

2.6.3 Fluorescence Quantum Yield Measurements

Standard and unknown solutions for quantum yield measurements were prepared to give matched (±0.002) absorbance values of approximately 0.1 at the excitation wavelength. The absorbance and fluorescence measurements were obtained with nitrogen purged samples.

After the solutions were matched and the fluorescence spectra recorded, two matching serial dilutions (using nitrogen purged solvent) were made to obtain a minimum of three data points. The fluorescence spectra of the dilutions were also obtained.

Each experiment was independently performed three times and each experiment yielded three quantum yield values, according to the equation[111]

$$\Phi_u = \left[\frac{A_s F_u \eta_u^2}{A_u F_s \eta_s^2}\right] \Phi_s \qquad \text{Eq. 2.1}$$

where A is the absorbance at the excitation wavelength, F is the integrated area of the emission band, η is the refractive index of the solvent, and the subscript u refers to the unknown, s to the standard.

2.6.4 Molar Absorptivity Measurements

To obtain molar absorptivities for each of the compounds, a stock solution and three serial dilutions were made and the corresponding absorbance value for the absorbance maximum of each major absorption band was recorded. (The values for at least four concentrations were measured for each absorption band). The experiment was repeated at least three times on separate days. By graphing the absorbance value of the band maximum against the concentration (Beer-Lambert law), the molar absorptivity was determined from the slope of the graph.

2.6.5 Determination of Oxygen Quenching Rate Constants and E_T

Quenching of the triplet state of **2.2a** in toluene was measured using a 355 nm laser for excitation with observation of the kinetics at 625 nm. Quenching of the triplet state of **2.2b** in toluene was measured using a 355 nm laser for excitation with observation of the kinetics at 625 nm.

Quenching rate constants were determined by plotting k_{obs} versus the concentration of the quencher, where the equation of the line fit is

$$k_{obs} = k_0 + k_q[Q] \qquad \text{Eq. 2.2}$$

and k_{obs} is the observed rate constant, k_0 is the rate constant in the absence of quencher, $[Q]$ is the concentration of quencher, and k_q is the quenching rate constant.

Oxygen quenching experiments were performed at 20 °C. Three solutions of the compound being examined were prepared and saturated with either N_2, air, or O_2. The observed rate constants for each solution were plotted against the concentration of oxygen in the solution at 20 °C and the quenching rate constant was determined using equation 2.2.

2.6.6 Synthesis

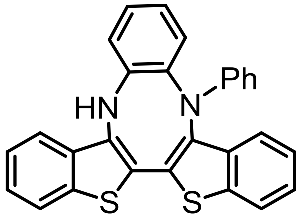

5-phenyl-5,10-dihydrobenzo[b]benzo[4,5]thieno[3,2-e]benzo[4,5]thieno[2,3-g][1,4]diazocine (2.4b) Bromobenzene (90 mL), aniline (1.4 mL, 15.8mmol), and diazabicyclooctane (5.2 g, 45.9mmol) were added to a flask. The flask was evacuated and backfilled with nitrogen three times. Titanium tetrachloride (1.0 M in toluene, 11.7 mL, 11.7 mmol) was added slowly to the clear solution. Upon addition, a brown precipitate formed and fuming occurred. After the fuming subsided, thioindigo (1.5 g, 5.1mmol) was added in portions to ensure good mixing. The reaction was heated to reflux and aged overnight. The reaction was filtered hot, rinsing the filtercake with ethyl acetate until the filtrate ran colorless. After crystallization of **2.2b** (see below), the filtrate was concentrated under vacuum. The filtrate was preabsorbed on silica gel and chromatographed using, sequentially, eluent compositions of 7:1, 5:1, and 1:1 hexanes/dichloromethane. A yellow solid was obtained (0.78 g, 35 %). Crystals suitable for x-ray analysis were grown by slow evaporation of a solution formed by layering dichloromethane and hexanes. mp 240–242 °C; ^{1}H NMR (360 MHz, $CDCl_3$) δ 7.77 (dd, *J* = 6.1, 2.7 Hz, 1 H), 7.72 – 7.65 (m, 2H), 7.55 – 7.50 (m, 2H), 7.38 – 7.29 (m, 4H), 7.20 (td, *J* = 7.7, 1.5 Hz, 1H), 7.04 (td, *J* = 7.0, 1.8 Hz, 2H), 6.95 – 6.88 (m, 2H), 6.64 (tt, *J* = 7.3, 1.0 Hz, 1H), 6.51 (dd, *J* = 8.8, 1.0 Hz), 5.81 (s, 1H) ; ^{13}C NMR (90 MHz, $CDCl_3$) δ 147.8, 142.2, 138.4, 137.8, 136.6, 135.7, 135.1, 135.0, 134.5, 133.1, 132.7, 129.2, 129.0, 125.6, 125.1, 124.9, 124.4, 123.0, 122.9, 122.7, 122.4, 121.7, 119.4, 117.8, 113.3, 110.4; IR (thin film) 3400, 3060, 1592, 1493, 1318, 906, 747, 727 cm^{-1}; Anal. Calcd for $C_{28}H_{18}N_2S_2$: C, 75.30; H, 4.06; N, 6.27. Found: C, 74.99; H, 4.01; N, 6.29.

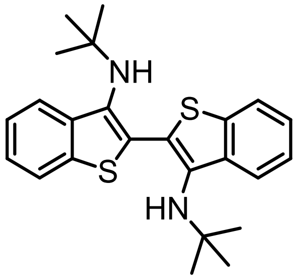

3,3′-Bis(*tert*-butylamino)-2,2′-bithianaphthene (2.2a)

Bromobenzene (60 mL), t-butylamine (1.1 mL, 10.4mmol), and diazabicyclooctane (3.4 g, 30.3mmol) were added to a flask. The flask was evacuated and backfilled with argon three times. Titanium tetrachloride (1.0 M in toluene, 7.8 mL, 7.8mmol) was added dropwise to the clear, colorless solution. Upon addition, a greenish-brown precipitate formed along with vigorous fuming. After the fuming subsided, thioindigo (1.0 g, 3.4mmol) was added in portions to ensure good mixing. The reaction was heated to reflux and aged overnight. The reaction was filtered while warm, and the filtercake was rinsed with diethyl ether until the filtrate ran colorless. The filtrate was concentrated under vacuum. The filtrate was preabsorbed on silica gel and chromatographed first using 100% dichloromethane, then switching to 1:1ethylacetate/hexanes. Chromatography afforded a tan solid (0.75g, 54%). Crystals suitable for x-ray analysis were grown by slow evaporation of a solution formed by layering acetone and hexanes. mp 196–198 °C; ^{1}H NMR (300 MHz, $CDCl_3$) δ 7.78 (dd, *J* = 6.9, 1.2 Hz, 2H), 7.73 (dd, *J* = 7.0, 1.3 Hz, 2H), 7.39 – 7.28 (m, 4H), 4.40 (s, 2H), 1.01 (s, 18H); ^{13}C NMR (75 MHz, $CDCl_3$) δ 139.3, 139.0, 136.6, 127.5, 124.6, 123.9, 122.6, 122.4, 56.0, 30.3; IR (KBr) 3318, 3228, 2961, 1441, 1364, 1225, 1202, 744, 734 cm^{-1}; HRMS (ESI-Orbitrap) m/z: [M + H]$^+$Calcd for $C_{24}H_{29}N_2S_2$ 409.1767; Found 409.1768.

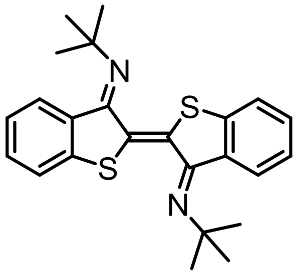

Thioindigo-*N,N′*-bis(*tert*-butyl)diimine (2.3a) Amine **2.2a** (0.50 g, 1.2 mmol) was dissolved in dichloromethane (50 mL). The solution was treated with 2,3-dichloro-5,6-dicyanobenzoquinone (0.30g, 1.3 mmol). The reaction was stirred for 3 hours, diluted with dichloromethane to dissolve the orange precipitate, and washed with 1M NaOH (2 × 30 mL) and water (2 × 30 mL). The organic layer was dried over anhydrous sodium sulfate, filtered, and concentrated to an orange solid (0.38 g, 78%). Crystals suitable for x-ray analysis were grown by slow evaporation of a solution formed by layering dichloromethane and hexanes. mp 236–239 °C; ^{1}H NMR (300 MHz, $CDCl_3$) δ 8.00 (d, *J* = 8.1 Hz, 2H), 7.44 (dd, *J* = 7.7, 1.5 Hz, 2H), 7.28 (td, *J* = 7.5, 1.0 Hz, 2H), 7.13 (td, *J* = 7.6, 1.2 Hz, 2H), 1.67 (s, 18H); ^{13}C NMR (75 MHz, $CDCl_3$) δ 159.3, 151.4, 130.7, 130.3, 129.6, 126.9, 124.1, 124.0, 57.2, 29.9; IR (KBr) 2970,1587, 1569, 1440, 1280, 1207, 1097, 865, 737 cm^{-1}; Anal. Calcd for $C_{24}H_{26}N_2S_2$: C, 70.89; H, 6.45; N, 6.89. Found: C, 71.27; H, 6.37; N, 6.87.

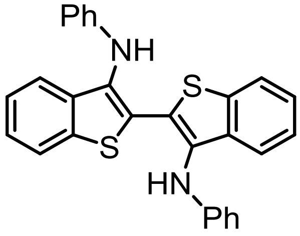

3,3′-Dianilino-2,2′-bithianaphthene (2.2b) Bromobenzene (90 mL), aniline (1.4 mL, 15.8 mmol), and diazabicyclooctane (5.2 g, 45.9 mmol) were added to a flask. The flask was evacuated and backfilled with nitrogen three times. Titanium tetrachloride (1.0 M in toluene, 11.7 mL, 11.7 mmol) was added slowly to the clear solution. Upon addition, a brown precipitate formed and fuming occurred. After the fuming subsided, thioindigo (1.5 g, 5.1 mmol) was added in portions to ensure good mixing. The reaction was heated to reflux and aged overnight. The reaction was filtered hot, rinsing the filtercake with ethyl acetate until the filtrate ran colorless. The filtrate was concentrated on a rotary evaporator until the volume remained constant. Dichloromethane (100 mL) was added to the solution via addition funnel. After ageing for 10 minutes, a fine precipitate was observed, the mixture was filtered, and the solid was collected and washed with dichloromethane, affording an off-white solid (0.46g). The filtrate was then concentrated to dryness on a high vacuum rotavap. The residue was slurried in dichloromethane (50 mL). The resulting solid was filtered and washed with dichloromethane to give a second batch off-white solid (0.43 g). A combined yield of 0.89g, 39% was obtained. Off-white solid; mp (turns red, then melts) 266–268 °C; ^{1}H NMR (300 MHz, $CDCl_3$) δ 7.76 (d, J = 7.3 Hz, 2H), 7.49 (d, J = 7.9 Hz, 2H), 7.34 (td, J = 7.5, 1.3 Hz, 2H), 7.29 – 7.24 (m, 2H), 7.18 (td, J = 7.0, 1.6 Hz, 4H), 6.85 (tt, J = 7.4, 1.0 Hz, 2H), 6.67 (dd, J = 8.6, 1.0 Hz, 4H), 5.76 (s, 2H); ^{13}C NMR (90 MHz, CDCl$_3$) δ 145.0, 138.4, 135.8, 131.6, 129.3, 126.2, 125.3, 124.3, 122.59, 122.57, 119.6, 114.9; IR (KBr) 3353, 3045, 1603, 1500, 1355, 1301, 1247, 898, 759, 696 cm^{-1}; HRMS (EI) m/z: [M]$^+$ Calcd for $C_{28}H_{20}N_2S_2$ 448.1068; Found 448.1071.

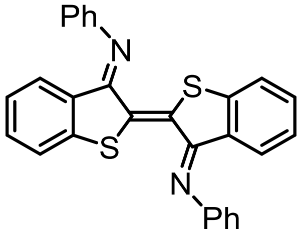

Thioindigo-*N*,*N′*-diphenyldiimine (2.3b) Method 1: Bromobenzene (30 mL), aniline (0.47 mL, 5.2 mmol), and diazabicyclooctane (1.70 g, 15.1 mmol) were added to a flask. The flask was evacuated and backfilled with argon three times. Titanium tetrachloride (1.0 M in toluene, 3.9 mL, 3.9 mmol) was added drop-wise to the clear, colorless solution. After fuming subsided, thioindigo (1.0 g, 3.4 mmol) was added in portions to the brown, heterogeneous mixture. The reaction was heated to reflux and aged overnight. The reaction was filtered hot, and the filtercakewas washed with diethyl ether until the filtrate ran colorless. The filtrate was allowed to stand open to air for 4 weeks, after which time dichloromethane (42 mL) was added, followed by hexanes (40 mL). Aged overnight with stirring and filtered to give ared solid (0.44 g, 58%); **Method 2:** Bithianaphthene **2.2b** (1.0 g, 2.3 mmol) was dissolved in dichloromethane and treated with 2,3-dichloro-5,6-dicyanobenzoquinone (0.57 g, 2.5 mmol). The reaction was stirred for 1 hour and then concentrated to a volume of approximately 30 mL by rotary evaporation. The reaction was filtered to give a red solid (0.83 g, 82%). mp 269–271 °C; ^{1}H NMR (300 MHz, CDCl3) δ 7.49 – 7.42 (m, 6H), 7.30 (td, *J* = 7.4, 1.4 Hz, 2H), 7.21 (tt, *J* = 7.4, 1.2 Hz, 2H), 7.02 (dd, *J* = 8.3, 1.1 Hz, 4H), 6.94 – 6.83 (m, 4H); ^{13}C NMR

(90 MHz, $CDCl_3$) δ 161.7, 150.1, 148.3, 131.8, 131.4, 129.6, 127.3, 127.1, 124.7, 124.1, 123.7, 118.2; IR (KBr) 3056, 1588, 1481, 1444, 1289, 1102, 734, 695 cm^{-1}; Anal. Calcd for $C_{28}H_{18}N_2S_2$: C, 75.31; H, 4.06; N, 6.27. Found: C, 75.50; H, 4.14; N, 6.24.

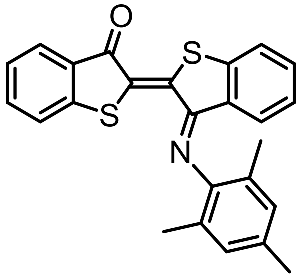

Thioindigo-*N*-(2,4,6-trimethylphenyl)imine (2.5c)

Bromobenzene (60 mL), 2,4,6-trimethyl aniline (1.4 mL, 10.4 mmol), and diazabicyclooctane (3.4 g, 30.3 mmol) were added to a flask under argon. Titanium tetrachloride (1.0 M in toluene, 7.8 mL, 7.8 mmol) was added dropwiseto the clear, colorless solution. Upon addition, a green-black precipitate formed and fuming occurred. After the fuming subsided (approximately 10 minutes), thioindigo (1.0 g, 3.4 mmol) was added in portions to ensure good mixing. The reaction was heated to reflux and aged overnight. The reaction was then filtered hot, rinsing the filtercake with diethyl ether until the filtrate ran colorless. The filtrate was concentrated under vacuum. The resulting reddish-black solid was preabsorbed on silica gel and chromatographed using 1:2 dichloromethane/hexanes. A dark reddish-purple solid was isolated (0.12 g, 9 %). Crystals suitable for x-ray analysis were grown by slow evaporation from deuterated chloroform. mp 178–181 °C; ^1H NMR (360 MHz, $CDCl_3$) δ 7.99 (d, J = 7.6 Hz, 1H), 7.59 – 7.49 (m, 3H), 7.41 (td, *J* = 7.6, 1.1 Hz, 1H), 7.32 (td, *J* = 7.4, 1.0 Hz, 1H), 7.01 (s, 2H), 6.98 (dd, *J* = 7.2, 0.9 Hz, 1H), 6.88 (d, *J* = 7.6 Hz, 1H), 2.39 (s, 3H), 2.05 (s, 6H); ^{13}C NMR (90 MHz, $CDCl_3$) δ 189.3, 162.8, 150.3, 145.4, 145.2, 138.6, 134.7, 133.5, 132.7, 130.0, 129.1, 127.4, 127.3, 126.4, 126.1, 126.0, 125.6, 124.2, 124.0, 123.8, 20.9, 18.0; IR (KBr) 2917, 1660, 1587, 1448, 1288, 1091 cm^{-1}; HRMS (EI) m/z: [M]$^+$ Calcd for $C_{25}H_{19}NOS_2$ 413.0908; Found 413.0911.

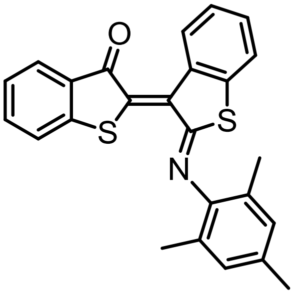

Thioindirubin-*N*-(2,4,6-trimethylphenyl)imine (2.6c) Bromobenzene (60 mL), 2,4,6-trimethyl aniline (1.4 mL, 10.4 mmol), and diazabicyclooctane (3.4 g, 30.3 mmol) were added to a flask under argon. Titanium tetrachloride (1.0 M in toluene, 7.8 mL, 7.8 mmol) was added dropwise to the clear, colorless solution. Upon addition, a green-black precipitate formed and fuming occurred. After the fuming subsided (approximately 10 minutes), thioindigo (1.0 g, 3.4 mmol) was added in portions to ensure good mixing. The reaction was heated to reflux and aged overnight. The reaction was then filtered hot, rinsing the filtercake with diethyl ether until the filtrate ran colorless. The filtrate was concentrated under vacuum. The resulting reddish-black solid was preabsorbed on silica gel and chromatographed using 1:2 dichloromethane/hexanes. A reddish-black solid was isolated (0.45g, 33%). Crystals suitable for x-ray analysis were grown by slow evaporation of a solution formed by layering dichloromethane and hexanes. mp 192–194 °C; ^{1}H NMR (360 MHz, $CDCl_3$) δ 9.59 (dd, *J* = 8.2, 1.0 Hz, 1H), 7.92 (dd, *J* = 7.6, 0.4 Hz, 1H), 7.57 (td, *J* = 7.5, 1.2 Hz, 1H), 7.44 – 7.28 (m, 5H), 6.98 (s, 2H), 2.35 (s, 3H), 2.14 (s, 6H); ^{13}C NMR (90 MHz, $CDCl_3$) δ 189.8, 166.6, 148.6, 146.7, 138.5, 137.7, 136.9, 135.3, 134.4, 132.8, 131.4, 130.2, 129.0, 128.8, 126.8, 126.0, 125.9, 125.5, 123.7, 122.8, 20.9, 17.8; IR

(KBr) 1671, 1588, 1280, 1109, 1041, 1030, 1017, 742 cm^{-1}; Anal. Calcd for $C_{25}H_{19}NOS_2$: C, 72.61; H, 4.63; N, 3.39. Found: C, 72.48; H, 4.86; N, 3.42.

Chapter 3

Coordination Complexes of Thioindigo Diimines

3.1 Introduction

The classic chromophore thioindigo was introduced as a dye in the early 1900s. The scientific appeal of thioindigo may be measured in the fact that every year following the initial patents in 1905, [112,113,114] with the exception of 1917 and 1920, has seen contributions to the scientific and patent literature detailing the synthesis, characterization, and applications of thioindigo and its derivatives. The first reports in the scientific literature focussed on the vibrant color and photostability of thioindigo (a sulfur analog of indigo),[115-117] while the synthesis of derivatives incorporating substituents on the benzene rings occupied much of the literature through the 1940s.[91, 118-123] By the 1950s, chemists had become aware of the intense fluorescence and photoinduced trans-cis isomerization that distinguish this molecule. Extensive investigation of thioindigo was carried out, most notably by Wyman and co-workers, throughout the second half of the 20th century as researchers sought a foundational understanding of thioindigo's photophysical characteristics and the mechanisms enabling them.[55, 66, 79, 94, 95, 98, 99, 124] Beginning in the 1980s, interest shifted to using thioindigo and its derivatives for materials applications. This has generated a steady flow of reports examining thioindigo-based compounds for use in organic semiconductors[64] and charge generation devices,[65] as organic electrodes for batteries,[125] sensitizers for dye sensitized solar cells[126] and fluorescent solar collectors,[62, 127] and in liquid crystals[73, 74] and ion transport.[75]

Despite the abundance of available literature on thioindigo, no examples of metal complexes featuring thioindigo or thioindigo derivatives as ligands currently exist in the literature. The coordination of organic chromophores to metals has proven to be a photophysically fruitful research strategy,[128] and we were interested in examining this previously unexplored aspect of thioindigo research. To this end, our initial research focused on preparing derivatives of thioindigo that would be amenable to metal coordination. These synthetic efforts resulted in the preparation of thioindigo diimines: N-substituted diimine derivatives of thioindigo.[129] Thioindigo diimines are potentially interesting as redox-active ligands for metal complexes. These chromophores contain both sulfur and nitrogen donors that are spatially arranged such that they could potentially form a neutral thioether-imine chelate with a metal center, yet sulfur-nitrogen chelates of this type are rare in the chemical literature.[130] The thioindigo diimines contain two such sets of potentially chelating sites, making it possible for the molecule to serve as a bridging ligand in bimetallic complexes. Like the parent thioindigo compound, thioindigo diimines absorb relatively low energy visible light despite being small molecules with limited conjugation length.[96, 129] Upon metal coordination, this may lead to absorption in the near infrared (NIR) spectral region.[131-133] Comprehensive photophysical studies of metal complexes of thioindigo diimines may provide new fundamental knowledge of the excited state behavior of transition metal complexes, leading to the design of new ligand systems with advantageous light absorption properties.

The following chapter presents investigations into the synthesis of some platinum, zinc, and ruthenium complexes of thioindigo diimines, and details the characterization and photophysical inspection of ruthenium bis hexafluoroacetylacetonate (hfac) complexes of thioindigo-*N*,*N′*-diphenyldiimine. A pair of diastereomeric diruthenium complexes **3.5a,b** are examined, along with a monoruthenium complex **3.4**. The two diruthenium diastereomers display unexpected and highly unusual diastereomeric differences in their transient absorption spectra and in the lifetimes of those transient species. These differences and their relationship to diastereomeric variances in conformational exchange observed by NMR spectroscopy are discussed.

3.2 Investigations into Metal Coordination of Thioindigo Diimines

Our desire for photophysically interesting metal complexes containing thioindigo diimine ligands dictated our choice of metals for initial screening. Luminescence-compatible metals such as Pt^{2+}, Zn^{2+}, Ru^{2+}, and Cu^{1+} were prioritized for examination in coordination reactions with thioindigo diimines **2.3a,b**. Since thioindigo diimines are neutral ligands, with the relatively unusual S and N chelating combination, most of the reported coordination chemistry of the related Nindigo ligands (neutral/anionic N,N chelation) was not transferable to the thioindigo ligands.

3.2.1 Platinum Complexes

Formation of the bis(platinumdichloride) complexes **3.1a,b** was attempted by reacting diimine **2.3a** or **2.3b** with two equivalents of $PtCl_2(PhCN)_2$ in refluxing toluene (Scheme 3.1). After approximately two hours at reflux, this resulted in the formation of medium-to-dark brown precipitates. In the case of **2.3b**, the appearance of precipitate was accompanied by a complete loss of color in the supernatant. The precipitates were isolated with yields of 49% and 100% based on the presumed structure. Unfortunately characterization of the precipitates was hampered by extremely low solubility in solvents except for DMF and, to some extent, DMSO. (It is possible that the greater solubility observed in these solvents is an effect of coordination of the solvent to the platinum complexes). ^1H NMR spectra in these solvents were not conclusive for formation of the desired product, but the aromatic regions were significantly changed from the starting diimine ligands. Low resolution mass spectrometry was also inconclusive for formation of the desired product.

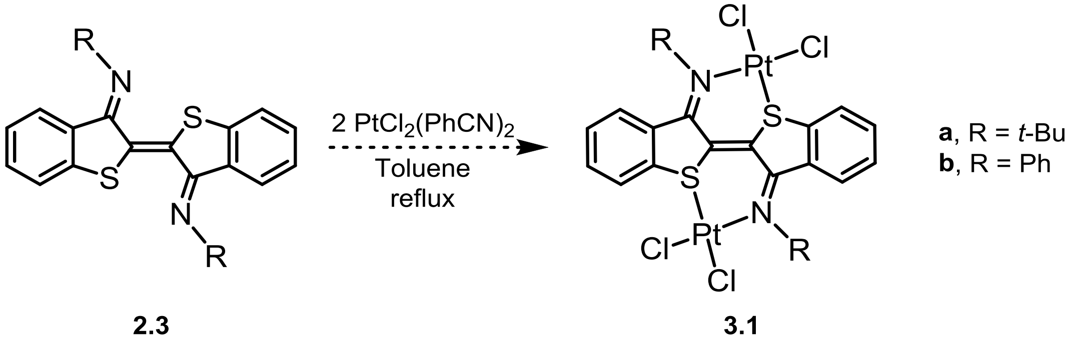

Scheme 3.1 Reaction of thioindigo diimines with platinum dichloride bis benzonitrile and possible structure of the resulting metal complexes.

The general insolubility of the compounds may be caused by Pt-Pt interactions within the crystal lattice, or may be indicative of other issues such as formation of oligomers due to chlorine acting as a briging ligand between Pt centers. Attempts at growing crystals for single crystal X-ray diffraction were necessarily limited in solvent choice and were unsuccessful.

3.2.2 Zinc Complexes

Coordination of **2.3a,b** with several different Zn^{2+} complexes was explored. $Zn(acac)_2$ in refluxing THF or toluene did not react with either **2.3a** and **2.3b**. Likewise, treating the thioindigo diimines with $Zn(OAc)_2$ or $ZnCl_2$ in acetonitrile or dichloromethane failed to produce a reaction. In the case of zinc dihexafluoroacetylacetonate dihydrate ($Zn(hfac)_2{\cdot}2H_2O$), addition of 2.1 equiv of the zinc complex to a slurry of **2.3a** in dichloromethane caused an immediate color change from orange to dark blue. A dark blue solid was isolated upon concentration of the reaction mixture, but proved to be unstable in the presence of air, rapidly reverting back to the orange free ligand **2.3a** (it is also possible that the complex was solvent stabilized and evaporation of remaining solvent caused the decomposition).

Solution-phase characterization of the diimine-$Zn(Hfac)_2$ complex by ^1H NMR spectroscopy was attempted. The reaction was carried out in an NMR tube using CD_2Cl_2 as the solvent. Room temperature experiments and experiments at 224 K exhibited broadened signals indicative of exchange on the NMR timescale (Appendix Figure A25). Lower temperature experiments (191 K) provided sharp signals that revealed the presence of uncoordinated ligand **2.3a** and a presumed zinc coordination complex (Figure 3.1).

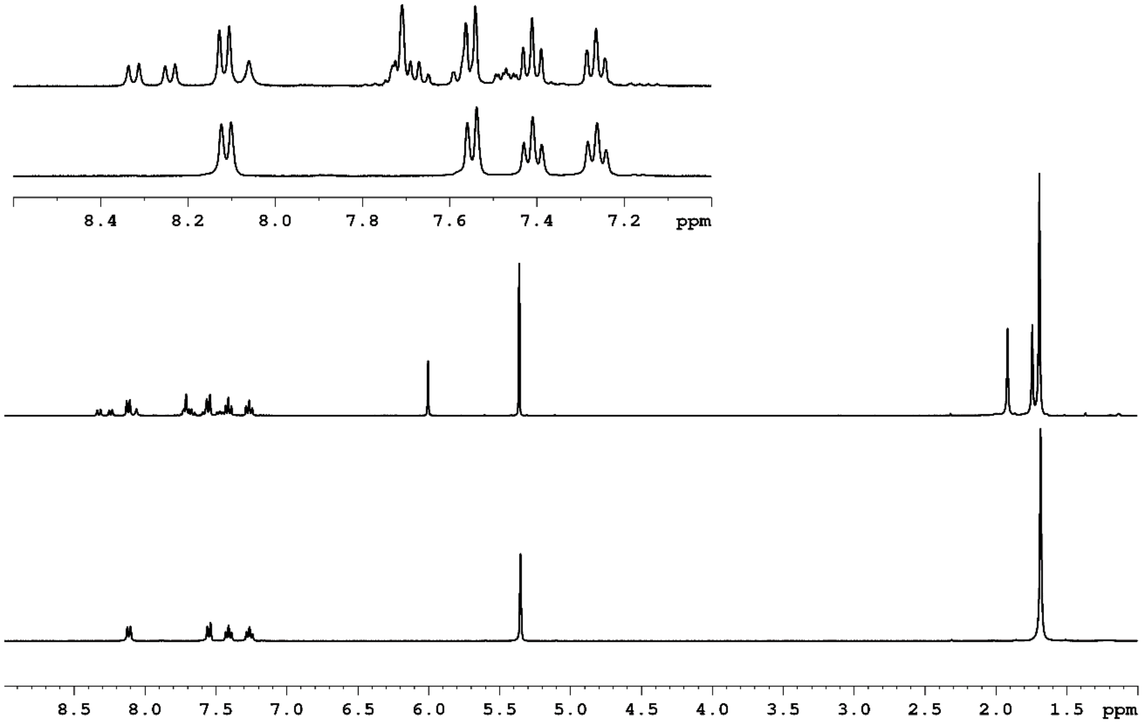

Figure 3.1 ^{1}H NMR spectra (360 MHz, CD_2Cl_2, 191 K) of the free ligand **2.3a** and of the di-*tert*-butyl thioindigodiimine **2.3a**/Zn(hfac)$_2$·2H_2O reaction mixture. The lower trace in the complete spectrum and (1.0–9.0 ppm) and the expansion (7.0–8.6 ppm) is free ligand **2.3a**. The upper trace in each spectrum is the reaction mixture.

The complex appears to be asymmetric; the existence of two product *tert*-butyl peaks with a 1:1 integration ratio and the occurrence of multiple aromatic product peaks with 1:9 integration ratios with the *tert*-butyl singlets supports the assignment of the product as a monozinc complex with a *trans* thioindigo diimine ligand (Scheme 3.2). However, the product signal for the hfac protons was not obvious. The hfac singlet at 6.00 ppm was not significantly shifted from the starting Zn(hfac)$_2$ complex, and the integration did not match the expected integration for either unbound or complexed Zn(hfac)$_2$ (although the amount of unbound Zn(hfac)$_2$ in solution may have been complicated by low solubility). A possible hfac signal was found at 7.71 ppm, but was in a region of overlapping aromatic protons and could not be verified. ^{19}F NMR spectra at 191 K displayed only one signal from the CF$_3$ groups. Given the scarcity of literature examples of zinc complexes bound to thioether ligands,[134] it is possible that the diimine **2.3a** is coordinating only through the nitrogen, which might account for the presence of a single fluorine signal. (Free rotation around the N-Zn bond would render the CF$_3$ groups equivalent, and it is possible that coordination of the complex to the imine does not alter the chemical environment of the CF$_3$ groups enough to cause a change in the chemical shift, therefore resulting in fluorine signals that overlap with those of the unbound Zn(hfac)$_2$). Brief heating (< 5 min.) of the NMR tube reaction followed by reexamination of the reaction by ^{1}H NMR spectroscopy at 191 K indicated increased product formation compared to uncoordinated ligand **2.3a**, but also appeared to show small amounts of other products beginning to form (Appendix Figure A26).

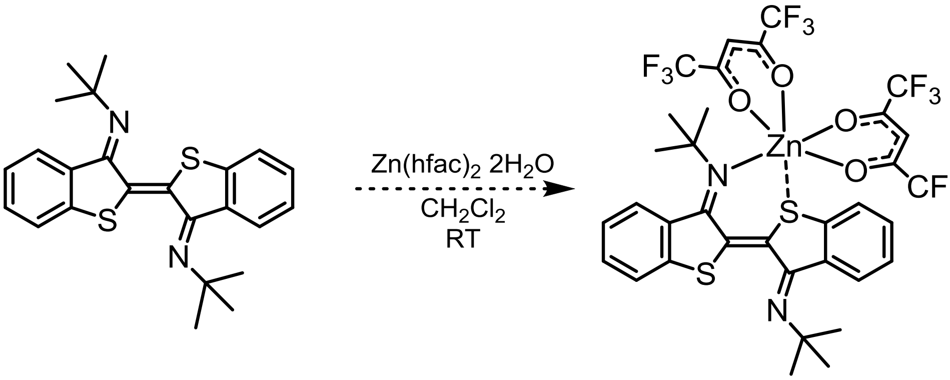

2.3a **3.2**

Scheme 3.2 Reaction of di-*tert*-butyl thioindigodiimine **2.3a** with Zn(hfac)$_2$·2H$_2$O and proposed structure of the resulting metal complex.

A survey of the reactivity of other Zn^{2+} sources with **2.3a** in dichloromethane at room temperature found that $Zn(acac)_2$, $ZnSO_4{\cdot}7H_2O$, and $Zn(NO_3)_2$ did not react, while $Zn(OCF_3)_2{\cdot}H2O$, $Zn(OTf)_2{\cdot}H2O$, and $ZnBr_2$(anhydrous) all resulted in a color change from orange to dark blue. The rate of the reaction (as monitored through the color change) was fastest with $ZnBr_2$ and slowest with $Zn(OCF_3)_2$. In the case of $ZnBr_2$, dark crystals were observed to have crystallized on top of undissolved $ZnBr_2$ after the reaction was aged overnight without stirring, which left the reaction solution a pale blue color. Unfortunately, the co-crystallization with $ZnBr_2$ prevented an X-ray crystal structure from being obtained. In the case of the zinc hydrates, overnight ageing of the reactions resulted in a color change from blue to pinkish-red consistent with hydrolysis of the diimine.

3.2.3 Ruthenium Acetylacetonate Complexes

Ruthenium complexes containing dehydronindigo ligands are known.[135, 136] The dehydronindigo ligands are neutral bridging ligands, similar to the thioindigo diimines, and therefore literature procedures for the formation of bisrutheniumdiacetylacetonate dehydronindigo complexes were used as a basis for the attempted preparation of ruthenium diacetylacetonate complexes of thioindigo diimine **2.3b**. Interestingly, reaction of diimine **2.3b** with two equivalents of $Ru(acac)_2(CH_3CN)_2$ in refluxing ethanol (with or without Et_3N) resulted in recovery of the reduced ligand, diamine **2.2b** in greater than 50% yield (Scheme 3.3). No other major products were identified from the reaction. The reduction seems likely to have happened following coordination of the ligand to the ruthenium center whereupon reduction of the ligand by Ru^{2+} to Ru^{3+}

oxidation could occur. Ethanol is the likely source of protons in the diamine formation.

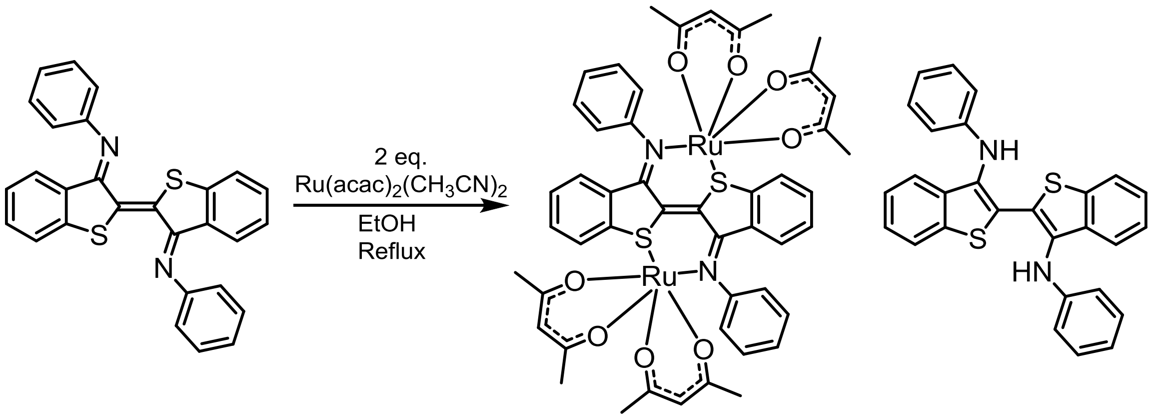

2.3b

3.3
0%

2.2b
>50%

Scheme 3.3 Attempted synthesis of ruthenium complex **3.3** leads to recovery of diamine **2.2b**.

The recovery of reduced ligand implied that coordination was likely to have occurred, and a less-electron rich ruthenium center might be less prone to oxidation, and therefore create a more stable complex. For this reason, coordination of the diimines with $Ru(hfac)_2(CH_3CN)_2$ was explored.

3.3 Ruthenium(II) Hexafluoroacetylacetonate Complexes of Diphenyl Thioindigo Diimine

3.3.1 Synthesis

The diruthenium complexes **3.5a,b**, thioindigo-*N,N′*-diphenyldiimine bisruthenium(dihexafluoroacetylacetonate), were prepared by refluxing the bridging ligand **2.3b** with an excess (2.5 equivalents) of $Ru(hfac)_2(CH_3CN)_2$ in toluene (Scheme 3.4). The reaction produces the *meso* (ΔΛ) diastereomer **3.5a** and the *rac* diastereomeric mixture of enantiomers (ΔΔ and ΛΛ) **3.5b**. Separation of the diastereomers is facilitated by solubility differences in room temperature toluene. The *meso* complex can be precipitated out of solution, leaving behind a solution that consists mainly of *rac* diastereomer. Further purification of the *meso* and *rac* complexes by column chromatography affords dark green solids in 31 and 19 percent yield, respectively.

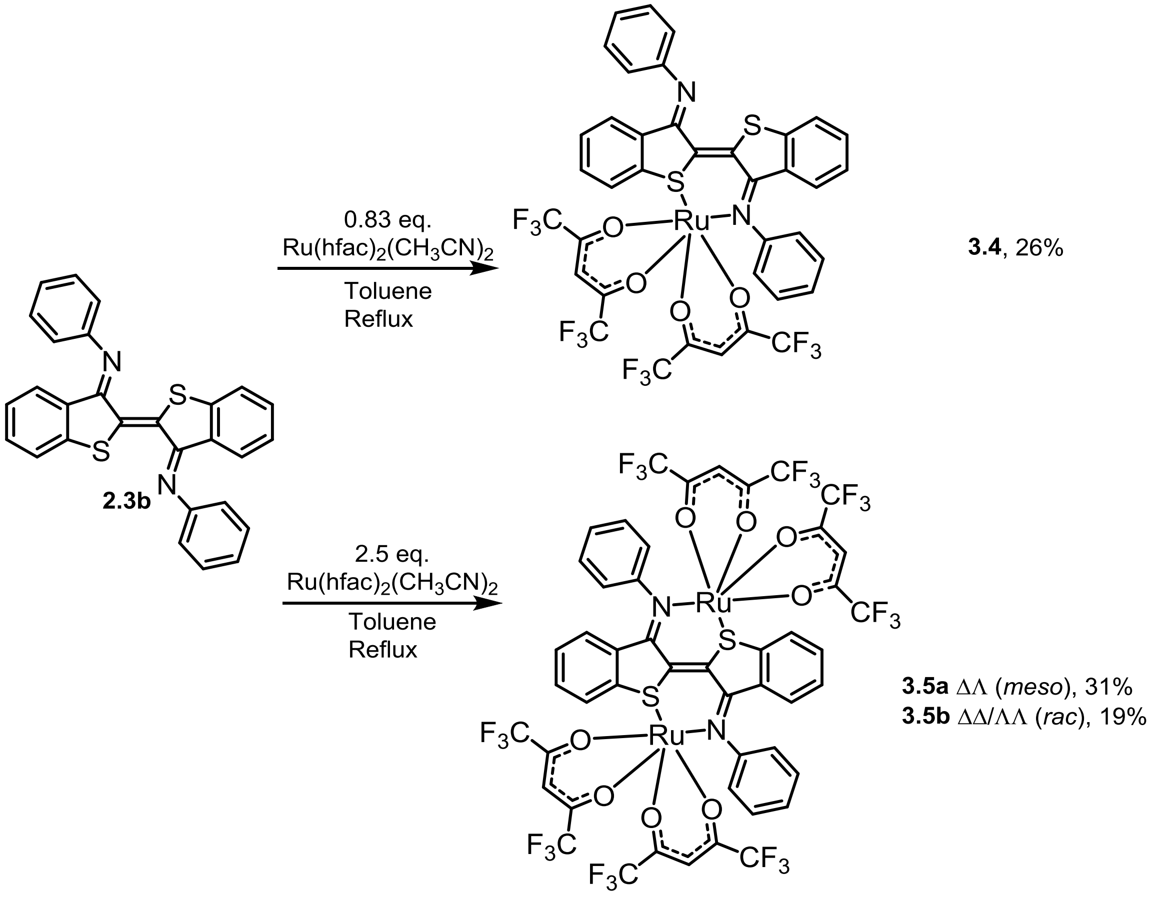

Scheme 3.4 Synthesis of Diruthenium Complexes **3.5a,b** and Monoruthenium Complex **3.4** from Diphenyl Thioindigo Diimine **2.3b**.

The thioindigo-*N,N′*-diphenyldiimine ruthenium dihexafluoroacetylacetonate complex **3.4** was also prepared for comparison to the bimetallic compounds. Separation of the monoruthenium complex from the diruthenium compounds was challenging when mixtures were present. In order to mitigate this problem, a sub-stoichiometric amount of $Ru(hfac)_2(CH_3CN)_2$ (0.83 equiv.) was used. The conditions used to prepare the monoruthenium complex were otherwise identical to the reaction conditions that afforded the diruthenium complexes. This maximized the formation of monoruthenium compound **3.4** and minimized formation of the diruthenium compounds **3.5a,b**. Despite this precaution, extensive purification was required to isolate **3.4**.

3.3.2 X-ray Analysis

The monoruthenium complex **3.4** possesses a slightly bowed thioindigo diimine ligand and a ruthenium center that lies out of the plane of the ligand (Figure 3.2 and Table 3.1). The uncoordinated half of the thioindigo diimine ligand exhibits bond lengths that are in agreement with the free ligand **2.3b** (the imine bonds are 1.286(9) Å and 1.286(5) Å in ligand 2.3b[129] and complex **3.4**, respectively; the uncoordinated C−S bonds are 1.747(3) Å and 1.760(7) Å respectively for compounds **2.3b** and **3.4**). Coordination lengthens the imine bond in the monoruthenium complex to 1.329(9) Å, but does not significantly change the C−S bond: 1.769(7) Å. The imine bond lengths in the diruthenium complexes **3.5a** and **3.5b** (Table 3.1 and Figures 3.3 and 3.4) are slightly shorter than the coordinated bond of the monoruthenium complex (1.312(9) Å and 1.315(4)/1.308(4) Å for the *meso* and *rac* compounds, respectively). The Ru−S bond in compound **3.4** is 2.2624(19) Å, which is approximately 0.02 Å shorter than the Ru−S bonds in the diruthenium complexes. The monoruthenium Ru−N bond is 2.055(6) Å, which is longer than the Ru−N bond in *rac* **3.5b**, 2.043(3)/2.039(3) Å, and is not conclusively different from the Ru−N bond in *meso* compound **3.5a** (2.050(6)/2.067(3) Å for the two molecules in the asymmetric unit). The angle of the N−Ru−S bond is smallest in the monoruthenium **3.4** (84.60(17) Å) and largest in the *rac* complex, with the angle in the *meso* complex being intermediate between the two.

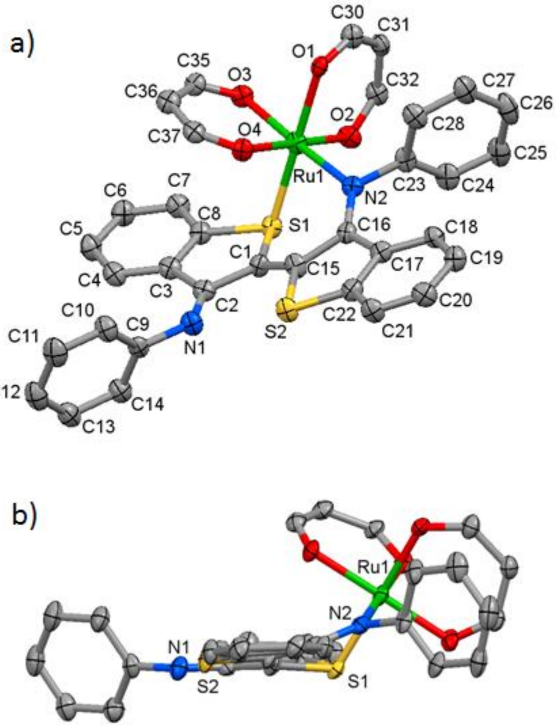

Figure 3.2 The X-ray crystal structure of monoruthenium complex **3.4** as viewed a) from above the plane of the thioindigo diimine ligand and b) down the long axis of the thioindigo diimine ligand. Ellipsoids are represented at 50% probability. Hydrogen atoms and trifluoromethyl groups of the β–diketonate ligands have been removed for clarity.

Table 3.1 Selected Bond Distances (Å), Bond Angles (deg), and Torsion Angles (deg) for Diruthenium Complexes **3.5a,b** and Monoruthenium Complex **3.4**.

	3.5a[a]	**3.5b**	**3.4**
Ru1–S1	2.285(2); 2.282(2)	2.2752(9)	2.2624(19)
Ru2–S2	N/A	2.2860(10)	N/A
Ru1–N1/Ru2–N1	2.050(6); 2.067(6)	2.043(3)	N/A
Ru1–N2	N/A	2.039(3)	2.055(6)
S1–C1	1.784(7); 1.774(8)	1.775(3)	1.769(7)
S2–C25	N/A	1.770(3)	1.760(7)
S1–C8	1.777(7); 1.777(8)	1.781(3)	1.789(8)
S2–C22	N/A	1.783(4)	1.763(8)
N1–C2	1.312(9); 1.308(10)	1.315(4)	1.286(9)
N2–C16	N/A	1.308(4)	1.329(9)
N1–C9	1.472(9); 1.449(10)	1.412(3)	1.421(9)
N2–C23	N/A	1.454(4)	1.438(10)
C1–C1–C2–N1[b]/ C1–C15–C16–N2[c]	31(1);33(1)	32.4(5)	21.3(11)
C15–C1–C2–N1	N/A	-31.5(5)	-12.1(12)
S1–C1–C1–C2[b]/ S1–C1–C15–C16[c]	-9(1); -8(1)	-7.3(5)	5.4(11)
C2–C1–C15–S2	N/A	4.0(5)	14.0(11)
C1–S1–C8–C7	173.3(7); 170.2(7)	169.4(3)	174.3(7)
C15–S2–C22–C21	N/A	-168.0(4)	178.6(6)
C22–C17–C16–C15	N/A	-15.1(4)	-10.4(8)
C8–C3–C2–C1	13.6(8); 13.8(8)	13.7(4)	5.2(9)
N–Ru–S	85.56(17); 86.57(18)	86.17(8);88.34(8)	84.60(17)

[a] Two molecules present in the asymmetric unit. [b] Compound **3.5a** only. [c] Compounds **3.5b** and **3.4**.

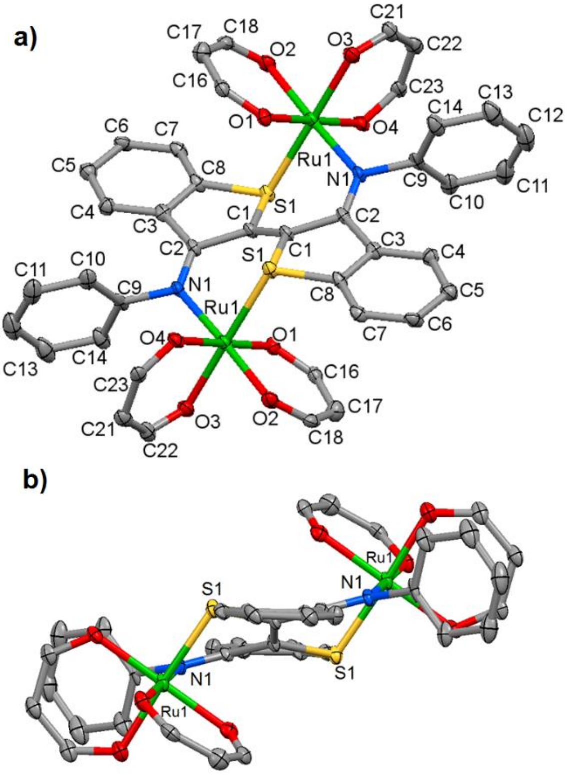

Figure 3.3 X-ray crystal structure of *meso* diruthenium complex **3.5a** viewed a) from above the plane of the thioindigo diimine ligand and b) down the long axis of the thioindigo diimine ligand, showing the chair-like structure formed by the bridging ligand and ruthenium atoms. The overlap of each phenyl ring with the neighboring hfac ligand is evident. Ellipsoids are represented at 50% probability. Hydrogen atoms and trifluoromethyl groups of the β–diketonate ligands have been removed for clarity.

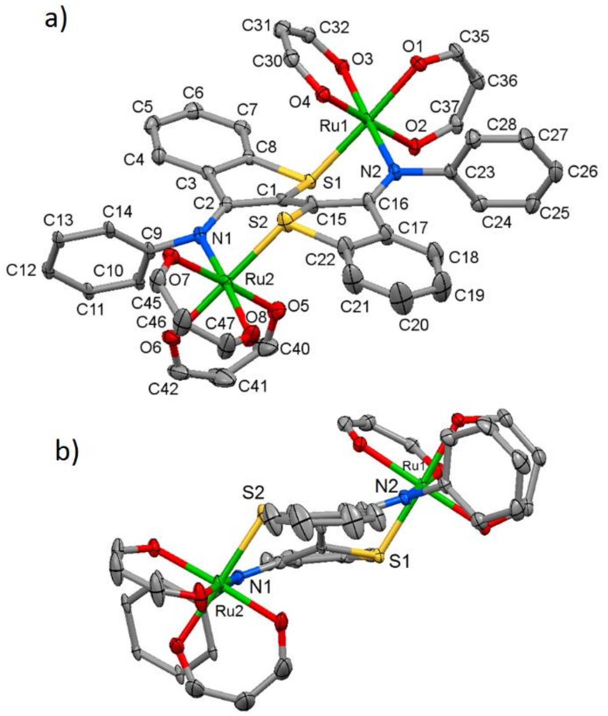

Figure 3.4 X-ray crystal structure of *rac* diruthenium complex **3.5b** viewed a) from above the plane of the thioindigo diimine ligand and b) down the long axis of the thioindigo diimine ligand, showing the chair-like structure formed by the bridging ligand and ruthenium atoms. The overlap of one hfac and one phenyl ring are evident. Ellipsoids are represented at 50% probability. Hydrogen atoms and trifluoromethyl groups of the β–diketonate ligands have been removed for clarity.

The structures of the *meso* and *rac* compounds (Figures 3.3 and 3.4) both display a chair-like conformation with the two ruthenium atoms on opposite faces of the bridging thioindigo diimine ligand. In order to accommodate this structure, the thioindigo diimine is no longer planar (unlike the free ligand).[129] When viewed down the long axis of the ligand, the two bicyclic halves of the ligand that are connected by a double bond are out of plane with each other.

This is evident in both the views of the structure, but is most recognizable in the side-on view of the molecules. The monoruthenium complex **3.4** exhibits a similar distortion but to a much lesser extent. The two halves of *meso* compound **3.5a** have identical bond lengths, and the compound as depicted in the crystal structure has a center of inversion. One feature of the structure of **3.5a** is that each phenyl ring overlaps with the neighboring hexafluoroacetylacetonate (hfac) chelate ring. Because of the greater electronegativity of fluorine and oxygen in the hfac ring, the hfac carbons have a positive electrostatic potential surface. In contrast, the phenyl ring has a negative electrostatic potential at the carbons, which strongly suggests the presence of stabilizing pi-pi interactions between the phenyl and the hfac chelate rings. Unlike the *meso* compound, the two halves of the *rac* compound **3.5b** have statistically different bond lengths and only one of the two phenyl rings overlaps with the neighboring hexafluoroacetylacetonate chelate ring. This has the possibility of destabilizing this conformation of **3.5b** relative to **3.5a** because the pi-pi interactions are halved.

Examination of the bonding arrangement of the chiral centers of diastereomers **3.5a** and **3.5b** reveals that the stereochemical differences between the compounds leads directly to the observed diastereomeric differences in overlapping phenyl rings and hfac chelates. Physical molecular models of the complexes were built and were in close agreement with the crystal structures (Appendix Figure A10). This indicates that the diastereomeric differences observed in the overlapping phenyl rings and hfac chelates is a function of the bonding in the diastereomers, not a packing effect, and is intrinsic to the chair-like conformation.

3.3.3 Redox Properties

The monoruthenium complex **3.4** and diruthenium complexes **3.5a,b** were characterized by cyclic voltammetry. Because of the relative insolubility of **3.5a** in most organic solvents, the experiments were performed in tetrahydrofuran (THF). We have previously reported the redox behavior of the ligand **2.3b** in dichloromethane.[129] For comparison with the present data, we performed cyclic voltammetry experiments on ligand **2.3b** in THF and the data is included in Table 3.2 and Figure 3.5.

Table 3.2 Electrochemical Data (V vs. Fc/Fc$^+$ in tetrahydrofuran).

	E_{pc}**(-2)**[a]	$E°$**(-1)**	E_{pa}**(+1)**[b]
3.5a	-1.50	-0.79	0.9
3.5b	-1.66	-0.91	1.0
3.4	-1.62	-1.12	0.82
2.3b	N/A	-1.57	0.83

[a]Quasi-reversible process. Cathodic peak potential reported. [b]Irreversible or quasi-reversible process. Anodic peak potential reported.

Monoruthenium complex **3.4** displays a reversible one-electron reduction process at $E°$ = -1.12 V vs. *Fc/Fc*$^+$ and a second quasi-reversible reduction at E_{pc} = -1.62 V. A quasi-reversible one-electron oxidation is observed at E_{pa} = 0.82 V. While the position of the oxidation does not change compared to the ligand **2.3b**, the first reduction potential of monoruthenium **3.4** is shifted significantly toward more positive potentials ($E°$ = -1.57 V for compound **2.3b**).

The first reduction processes of the diruthenium complexes are further shifted towards positive potentials. Likewise, the second, quasi-reversible reduction process in the diruthenium compounds is also shifted toward more positive potentials compared to the monoruthenium compound **3.4**. The trend toward more positive reduction potentials from thioindigodiimine ligand to monoruthenium to diruthenium compounds can be explained by the added electronegativity associated with the increasing number of ancillary hfac ligands in the series of molecules.

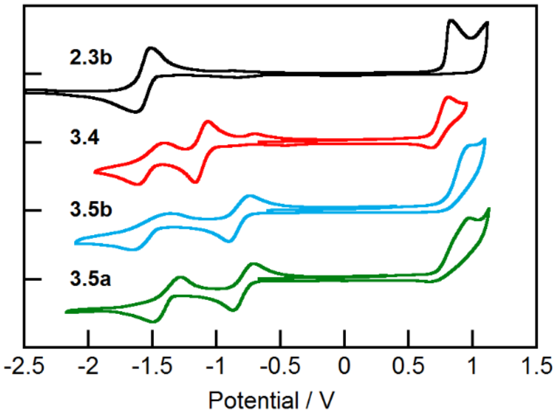

Figure 3.5 Cyclic voltammograms of diimine ligand **2.3b** (black), monoruthenium complex **3.4** (red), and diruthenium complexes **3.5a** (green) and **3.5b** (blue) in tetrahydrofuran. The scan rate is 100 mV/s for the diimine ligand and 50 mV/s for the ruthenium complexes. Concentration of analyte used is ~1.5 mM for ligand, 0.5 mM for ruthenium complexes. The standard is Fc/Fc$^+$ and the electrolyte is 0.1 M Bu_4NBF_4.

The systematic difference observed in the diastereomers **3.5a** and **3.5b** is less easily explained. The *meso* compound **3.5a** exhibits the most positively shifted reversible reduction process and the most positively shifted quasi-reversible reduction process ($E°$ = -0.79 V, E_{pc} = -1.50 V). The *rac* compound **3.5b** has a more negative potential for both of the processes ($E°$ = -0.91 V, E_{pc} = -1.66 V), and a more positively shifted oxidation process (E_{pa} = 1.0 V for **3.5b** and E_{pa} = 0.9

V for **3.5a**). The oxidations occur at the edge of the THF solvent window (approximately -3.8 to 1.5 V vs. Fc/Fc$^+$). Thus, while a second oxidation process in the diruthenium complexes is predicted (arising from an oxidation at the second of the two metal centers) it does not appear within the scanned region.

3.3.4 Dynamic Exchange Observed in Room Temperature NMR Experiments with *rac* Diruthenium Complex 3.5b

The monoruthenium compound **3.4** and *meso* diruthenium compound **3.5a** display sharp line shapes and fine structure from coupling in ambient temperature NMR spectra (i.e. have spectra consistent with single conformations or rapid conformational exchange in solution) (Appendix Figures A63–65 and A44–A46). The *rac* diruthenium compound **3.5b**, however, shows evidence of dynamic exchange between two conformations that is occurring on the NMR timescale. 1D experiments (^{1}H, ^{19}F, and ^{13}C in d8-THF) on *rac* **3.5b** each show a combination of some sharp, distinct peaks and some significantly broadened peaks in the spectra at 298 K (25 °C) (Appendix Figures A53 and A54 and A56). When the temperature of the **3.5b** sample is increased to 333 K (60 °C), the broadened peaks in the spectra (^{1}H and ^{13}C have been examined, Figure 3.6 and Appendix Figure A55) coalesce into sharper and more defined peaks, similar to the spectra obtained for the *meso* diastereomer. This is evidence of increasing exchange rate as the temperature increases. Likewise, low temperature experiments demonstrate that the rate of exchange decreases upon cooling (Figure 3.6 and Appendix Figure A66). A 1:1 ratio of conformers is observed in quantitative ^{19}F experiments.

In order to obtain rate constants and Gibbs free energy of the transition state ($\Delta G^‡$) for the conformational exchange of **3.5b**, ^{1}H NMR experiments were performed at temperatures between 208 K and 333 K (Appendix Figure A17). The line shapes of the exchanging signals were modelled to extract a rate constant of exchange at each temperature (Appendix Figure A18). An Eyring plot of the temperature dependence of the rate constant allowed calculation of the enthalpy and entropy of the exchange: $\Delta H^{\ddagger} = 11.5$ kcal mol^{-1} and $\Delta S^{\ddagger} = -1.8$ cal mol^{-1} K^{-1} (Appendix Figure A19). This revealed a $\Delta G^{\ddagger}_{298}$ value of 12.0 kcal mol^{-1} for the conformational exchange. Similarly, the rate constant of exchange at 298 K was calculated to be 8700 sec^{-1}, leading to a conformational half-life of 80 μs at 298 K.

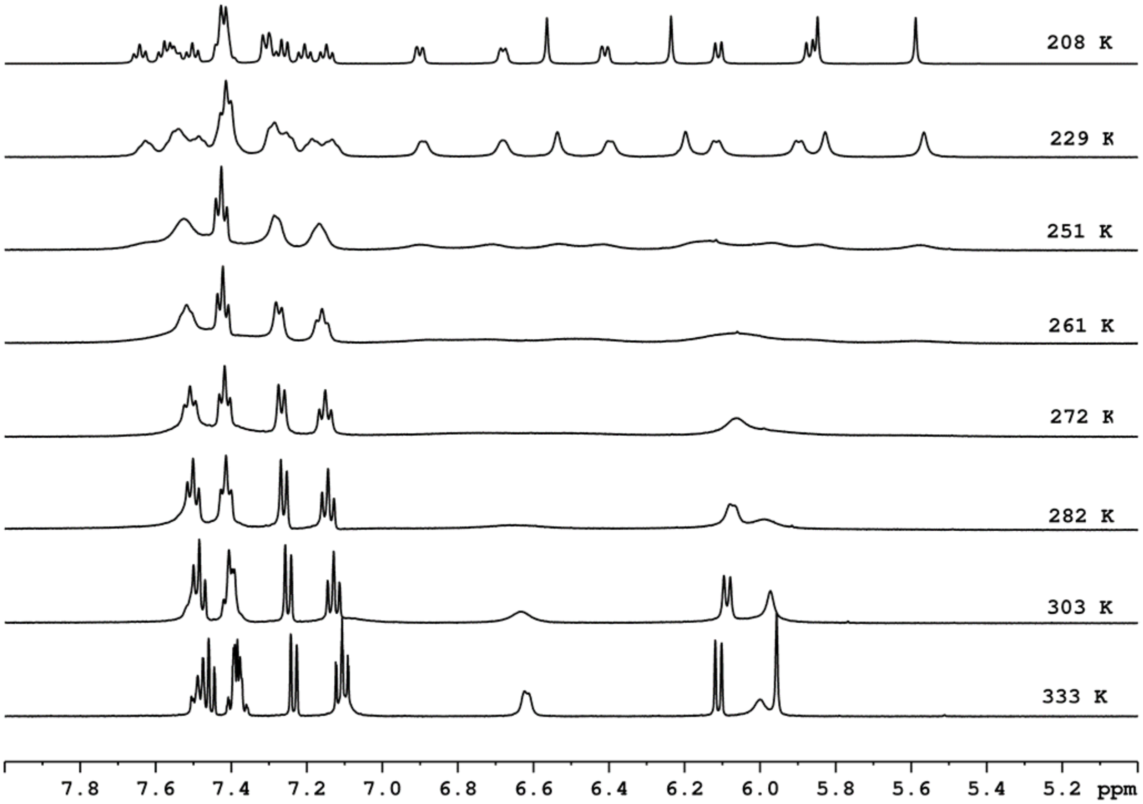

Figure 3.6 Variable temperature ^{1}H NMR spectra of *rac* diruthenium **3.5b** (500 MHz, THF-*d8*) showing the effects of temperature-dependent rates of conformational exchange. The resolved peaks of the two conformers visible at low temperatures. Broadening and coalescence of these peaks is evident at higher temperatures.

Low temperature ^{19}F and ^{1}H NMR experiments were performed on the *meso* diruthenium compound **3.5a** to determine whether a similar conformational exchange could be occurring at a different rate. The sample was cooled to a minimum temperature of 166 K, but no indication of broadening associated with conformational exchange was observed (Appendix Figures A67 and A68). This is indicative of two possibilities: either the exchange is extremely rapid even at low temperatures and thus cannot be resolved, or the *meso* diruthenium compound does not adopt a second conformation (at least in an amount detectable by NMR). Boltzmann calculations on an estimated $\Delta E = 7.5$ kJ·mol^{-1} suggest that high temperature NMR would be unlikely to show changes if a second conformation is present in amounts undetectable in 298 K NMR. ($\Delta E = 7.5$ would result in a conformer population undetectable by NMR at 298 K, while at 333 K, the population of the higher energy conformation would be ~7%, at 373 K, the population would be ~10%).

In order to assign the peaks that appeared most affected by the exchange at room temperature (i.e. the atoms with the largest difference in chemical shift between the two conformations), 2D NMR spectra at 60 °C were collected (COSY, HSQC, and HMBC, Appendix Figures A57–A62). This allowed unequivocal assignment of the proton and carbon peaks in the spectra to specific atoms in the molecule. The atoms associated with broadened peaks in the ^{13}C spectrum are found in two places: on the central thioether rings of the thioindigodiimine moiety, and on the ipso and ortho carbons of the phenyl rings (Appendix Figure A11). In the ^{1}H spectrum, the most broadened peaks are those originating from the ortho protons on the phenyl rings and the protons on the hfac ligands. In the ^{19}F spectrum, two of the four signals are broadened, but they have not been assigned to specific CF_3 groups.

The distribution of the broadened peaks throughout the molecule (Appendix Figure A11) indicates that all of the ligands are involved in the conformational change. The concentration of broadened carbon atoms in the central portion of the thioindigodiimine bridging ligand seems to suggest that the conformation interconversion involves a change of the orientation of ruthenium atoms in relation to the bridging ligand. While definitive structural information about the conformations cannot be obtained by NMR techniques, a plausible explanation is the interconversion from a chair-like conformation (as seen in the crystal structures, Figure 3.4) to a boat-like structure. In this conformation, the ruthenium atoms would be on the same face of the bridging ligand, and the ancillary hfac ligands would be in chemically different environments from the chair-like structure. Importantly, the crystal structure of a related $Pd_2(hfac)_2$Nindigo compound does have the metal atoms on the same face of the Nindigo bridging ligand.[86]

The differing numbers of pi-pi interactions apparent in the crystal structures of the diastereomers (Figures 3.3 and 3.4) may also explain the variation in conformational exchange observed in the NMR spectra. The chair-like conformation of the *meso* diastereomer possesses two pi-pi interactions between the phenyl and hfac rings while the *rac* diastereomer possesses only one interaction. This may lend added stabilization for the *meso* chair-like conformer compared to the *rac*.

Models of the proposed boat-like conformations of the diastereomers show two features that may be important – a steric interaction between the trifluoromethyl groups of the hfac rings, and a reversal of the number of stabilizing pi-pi interactions in the diastereomers. The boat-like conformer of the meso compound has only one pi-pi interaction, while the *rac* compound has two pi-pi interactions.

Considered together, this information is consistent with the NMR observations. The 1:1 ratio of conformers seen for the *rac* compound indicates similar energies for the conformers. The additional pi-pi interaction of the boat-like conformation may offset the increase in steric repulsion of the trifluoromethyl groups, leading to similar energies for the chair and boat conformations of the *rac* diastereomer. The boat-like structure of the *meso* compound, on the other hand, is higher energy than the chair conformation since it experiences both added steric repulsion from the trifluoromethyl groups and loss of one of the stabilizing pi-pi interactions. If the energy difference between the conformations is high enough, the *meso* compound may exist primarily in the chair conformation, resulting in no observation of conformational exchange in the NMR experiments.

3.3.5 Photophysical Characterization

The ground state absorption spectra of the series of complexes are presented in Figure 3.7. Monoruthenium compound **3.4** has two absorption maxima in the visible region, 689 nm and 469 nm. The lower energy absorption band tails to approximately 900 nm, and a molar extinction coefficient for this band of (5.0 ± 0.2) × 10^3 $M^{-1}cm^{-1}$ was measured in tetrahydrofuran. For comparison, the uncoordinated ligand has a lowest energy absorption maximum of 510 nm. Thus, the lowest energy absorption band of **3.4** is red-shifted almost 180 nm (Table 3.3). The absorbance spectrum of **3.4** was recorded in several solvents of varying polarity. The lowest energy absorption band was found to be solvatochromic. The band is shifted hypsochromically in solvents of increasing polarity (Appendix Figure A13 and Table A2). The observed blue-shift is 643 cm^{-1}, consistent with an MLCT transition (d to π^*) in a compound that goes from a less polar ground state to a more polar excited state. The absorption band at 469 nm exhibited no trend in absorption maximum with varying solvent polarity and is consistent with a ligand centered π to π^* transition.

Table 3.3 Ground State Absorption Properties of Ruthenium Complexes of Thioindigo Diimines.

	λ^{abs}_{max} / nm	ε / 10^3 $M^{-1}cm^{-1}$ (3)[a]	Solvent
3.5a	783	7.9±0.6	Tetrahydrofuran
3.5b	773	7.5±0.3	Tetrahydrofuran
3.4	689	5.0±0.2	Tetrahydrofuran
2.3b	510	21±1	Toluene

[a] The errors in the molar extinction coefficients correspond to the standard deviation of three independent experiments.

Diastereomers **3.5a** and **3.5b** have similar absorption profiles (Figure 3.7). Both complexes have two absorption bands, one in the near-infrared (NIR) and one on the cusp of the visible region at approximately 405 nm. *Meso* **3.5a** has the longest wavelength absorption maximum of 783 nm while the absorption maximum of *rac* **3.5b** is blue-shifted by 10 nm to 773 nm. Both compounds absorb out to approximately 1000 nm in the near-infrared, and have statistically identical molar extinction coefficients in tetrahydrofuran, $(7.9 \pm 0.6) \times 10^3$ $M^{-1}cm^{-1}$ for *meso* complex **3.5a** and $(7.5 \pm 0.3) \times 10^3$ $M^{-1}cm^{-1}$ for *rac* compound **3.5b.** The lowest energy absorption maxima of the diruthenium compounds are red-shifted 84 nm and 94 nm (**3.5b** and **3.5a**, respectively) compared to the monoruthenium complex **3.4** and have molar extinction coefficients that are fifty percent higher than **3.4**. When the absorption spectra of **3.5b** in solvents of differing polarity were examined, the lowest energy band was found to be blue-shifted by 453 cm^{-1} in the range of solvents used (Appendix Figure A12 and Table A2). This is consistent with the non-polar ground state and polar excited state arising from an MLCT transition (d to π*) in this molecule. The absorption band at 406 nm does not show a trend relating absorption maximum and solvent polarity. Assignment of this band as a ligand centered π to π* transition is consistent with this observation. A lack of solubility in a range of solvents prevented examination of the solvatochromism of *meso* compound **3.5a**.

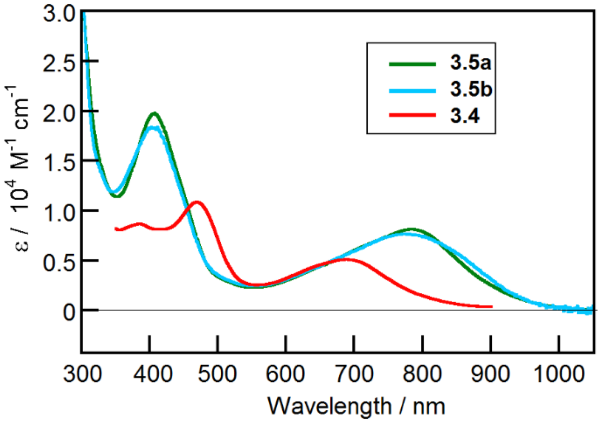

Figure 3.7 Ground state absorption spectra of **3.5a** (green), **3.5b** (blue) and **3.4** (red) in tetrahydrofuran.

Previous work on ligand **2.3b** had shown that the molecule was not fluorescent, despite the large fluorescence quantum yield of thioindigo itself.[57, 129] Fluorescence quenching of ligand **2.3b** was attributed to photoinduced trans-cis isomerization and possible intramolecular photoinduced electron transfer involving the imine moieties. Coordination to a metal may render these non-radiative decay pathways obsolete. Thus, examination of each compound for photoluminescence was carried out at room temperature in an N_2-purged tetrahydrofuran solution and at 77K in a 2-methyl tetrahydrofuran glass; however, no luminescence was detected under either condition.

Ultrafast transient absorption (TA) experiments were performed to examine the excited state dynamics of the three complexes. Following 700 nm excitation, the monoruthenium complex **3.4** displayed a strong transient signal in the UV-visible region of the spectrum, and a weaker signal spanning the NIR (Figure 3.8). The ground state bleach of the ligand centered π to π^* transitions was observed near 450 nm and positive transient absorption features were observed with maxima at approximately 525 nm and 1100 nm. Fitting procedures revealed two time constants, τ_1 = 0.8 – 1.4 ps, and τ_2 = 18 – 22 ps (Table 3.4 and Appendix Figure A14). In both the UV-visible and NIR spectral regions, the initial TA signal grows in over ~1 – 2 ps. This is followed by a blue-shift of the positive absorption maxima (from 525 to 505 nm in the UV-vis and from 1100 to 920 nm in the NIR) which is assigned to vibrational relaxation. The blue shift in the NIR is followed by decay of the signal to the ground state. After the blue-shift in the UV-visible spectrum, a dramatic change in signal shape is observed on the same timescale as the NIR signal decay. The shape change spans the visible region and is likely indicative of a state change leading to a long-lived state. Single wavelength kinetics measured identical time constants for the initial decay of both the UV-visible and NIR spectral signals, indicating that the observed transient signals originate from the same transient species.

Table 3.4 Transient Absorption Time Constants and Representative Preexponential Factors for Ruthenium Complexes of Thioindigo Diimines.

	τ_1 / ps	A_1[a]	τ_2 / ps	A_2[a]	τ_3 / ps	A_3[a]	Solvent
3.5a	2.0–4.5	-2.71	12–17	2.93	55–64	2.33	Tetrahydrofuran
3.5b	2.0–5.0	-5.14	30–37	7.54	N/A	N/A	Tetrahydrofuran
3.4	0.8–1.4	-1.62	18–22	7.36	N/A	N/A	Tetrahydrofuran

[a] Preexponential factors are × 10^{-3}. Preexponential factors for compound **3.5a**, **3.5b**, and **3.4**, respectively, are reported for transient decays recorded at 1018 nm, 1062 nm, and 1007 nm.

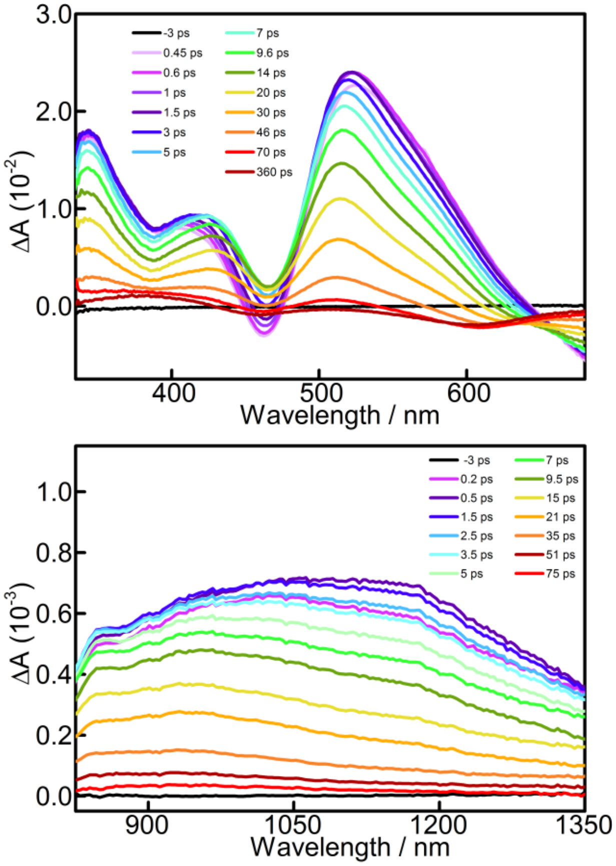

Figure 3.8 Sub-picosecond TA difference spectra of monoruthenium complex **3.4** in THF following 700 nm pulsed laser excitation (100 fs fwhm) with experimental delays indicated in the legend. The upper panel displays the UV-vis spectral region while the lower panel displays the near-IR spectral region.

The TA difference spectra of *meso* compound **3.5a** following 800 nm pulsed excitation is displayed in Figure 3.9. Excited state absorption features are observed in both the visible and near-IR spectral regions with maxima near 490 nm and 1300 nm. Ground state bleach features of the π-π* and MLCT transitions are observed between 370–425 nm and at wavelengths longer than 660 nm, respectively. Clear isosbestic points are formed during the symmetric decay of the transients in both the UV-visible (approximately 425 nm and 670 nm) and NIR spectral regions (approximate 910 nm). These isosbestic points persist through the decay of the excited state transient signals. Single wavelength kinetics were analysed using multi-exponential fits and a sum of three exponential functions was necessary to adequately fit the data (Table 3.4 and Appendix Figure A15). The obtained time constants are as follows: τ_1 = 2 – 4.5 ps, τ_2 = 12 – 17 ps, and τ_3 = 55 – 64 ps.

The TA difference spectra of the *rac* complex are qualitatively similar to those of the *meso* complex (Figure 3.10). However, several important distinctions are evident. At short timescales, the absorption feature between ~425 and 650 nm evolves a subtle shoulder to the red of the absorption maximum. This gives a broadened appearance to the signal that is not seen in the *meso* compound. Two of the isosbestic points present in the spectra of *meso* compound **3.5a** (at ~425 nm and 910 nm) are not present in the *rac* **3.5b** spectrum. At later delay times, the TA spectrum of the *rac* compound is seen to broaden in shape, accompanied by a gradual shift of the lambda max towards shorter wavelengths. Contrary to what was found for the *meso* diastereomer **3.5a**, the kinetics of the *rac* compound **3.5b** revealed only two time constants, τ_1 = 2 – 5 ps, and τ_2 = 30 – 37 ps (Table 3.4 and Appendix Figure A16). Definitive assignment of the time constants of diastereomers **3.5a** and **3.5b** to specific excited state processes is complicated by the short ps lifetimes, as the bimolecular experiments used to identify singlet or triplet excited states require nanosecond or longer lifetimes. Similarly, unequivocal assignments of excited state processes such as intersystem crossing or structural distortion cannot be made. However, certain spectral features, such as the growth and shape change observed between 0.6 and 5 ps in the UV-Vis TA spectrum of *rac* compound **3.5b**, are consistent with either intersystem crossing or structural distortion that preceeds establishment of the final excited state.

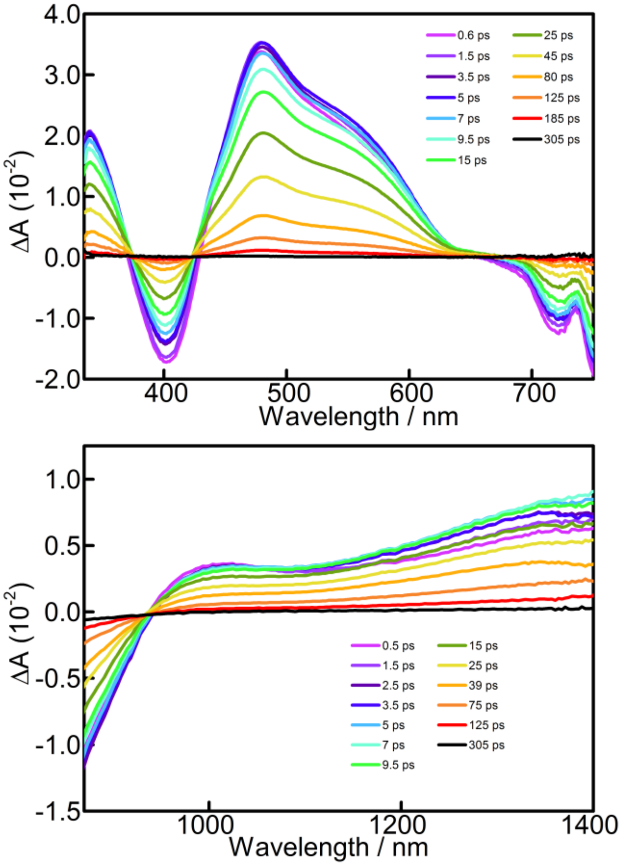

Figure 3.9 Sub-picosecond TA difference spectra of *meso* diruthenium complex **3.5a** in THF following 800 nm pulsed laser excitation. Experimental delays are indicated in the legend. The upper panel displays the UV-vis spectral region while the lower panel displays the near-IR spectral region.

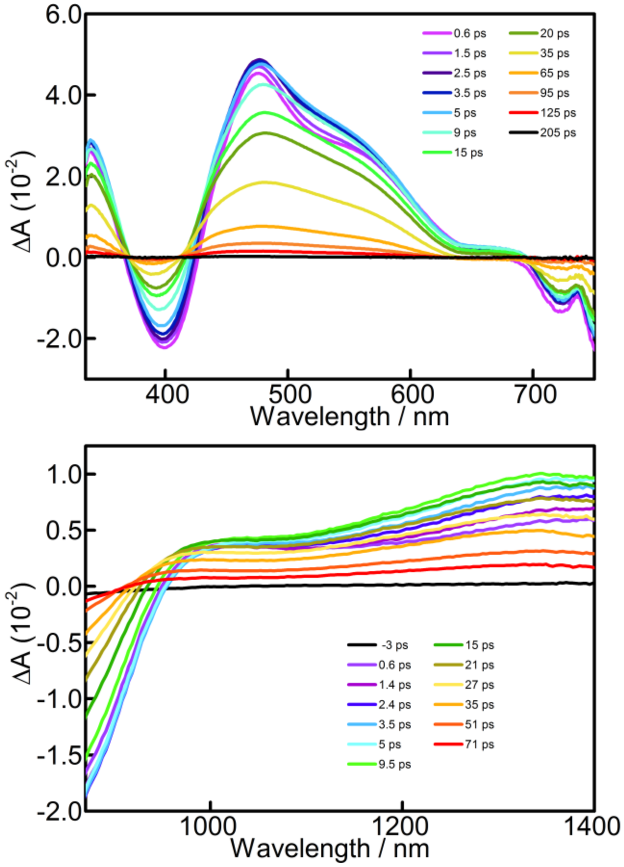

Figure 3.10 Sub-picosecond TA difference spectra of *rac* diruthenium complex **3.5b** in THF following 800 nm pulsed laser excitation with experimental delays indicated in the legend. The upper panel displays the UV-vis spectral region while the lower panel displays the near-IR spectral region.

The differences in the spectral features of the diastereomers can be interpreted in the context of the NMR experiments. The clean isosbestic points and symmetrical decay of the *meso* compound TA spectra indicate transition from one excited state species to one ground state species. This is consistent with the sharp peaks in the 166 K and room temperature NMR spectra of the *meso* compound, which indicate the presence of only one conformer in solution, or alternatively, very rapid interconversion between conformations. Either situation would result in the TA data capturing the decay of a single species. In contrast, the *rac* TA spectrum is characterized by the loss of isosbestic points and a spectral shape change over the course of the transient decay. This is suggestive of the presence of more than one transient species in the TA spectrum. Variable temperature NMR of the *rac* compound demonstrates that dynamic exchange between two conformers is occurring with a rate constant of 8700 sec^{-1} at room temperature, resulting in a conformational half-life of 80 μs. This means that interconversion between the conformers does not occur on the picosecond timescale of the transient spectroscopy. Therefore, we are indeed collecting the spectral data of two different transients, one from each conformation. This accounts for the spectral shape change and loss of isosbestic points noted in the TA difference spectrum. Importantly, the transients from each conformation have identical excited state lifetimes, as only one set of rate constants was measured for *rac* complex **3.5b**.

Spectroelectrochemical (SEC) interrogation of the monoruthenium compound **3.4** and the *meso* diruthenium compound **3.5a** was performed to facilitate assignments of the spectral features observed in the TA experiments. The UV-visible-NIR difference spectrum shown in Figure 3.11 was obtained following one-electron reduction of *meso* diruthenium compound **3.5a**. Compound **3.5a** was reduced via controlled potential electrolysis (CPE) at 0.93 V vs Ag/$AgNO_3$ in THF. The spectrum shows features that closely match those observed in the TA experiments of both the *meso* and *rac* compounds, especially in the 350 – 625 nm region. The excellent agreement between the difference spectra obtained in the TA and SEC experiments allows assignment of the transient species as arising from metal-to-ligand charge transfer within the complexes. Likewise, the radical anion of monoruthenium compound **3.4** was generated through CPE at -1.26 V vs. Ag/AgNO$_3$ and the difference spectrum was measured (Figure 3.12). The similar spectral shape observed in the TA and SEC measurements, in particular the 400 nm to 700 nm range, supports the assignment of the transient features as originating from MLCT in the monoruthenium compound **3.4** as well.

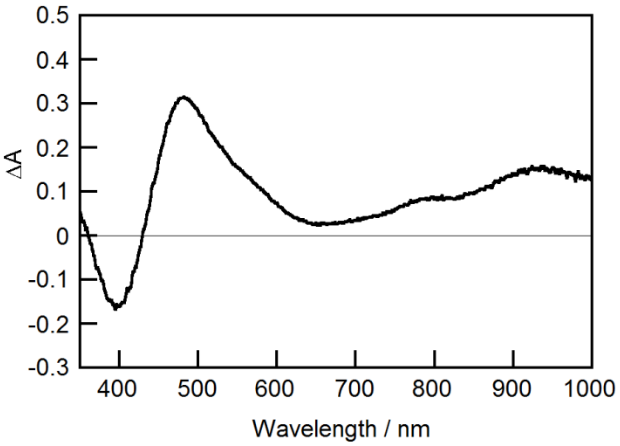

Figure 3.11 UV-visible-NIR spectroelectrochemical data showing the difference spectrum of the radical anion generated by reduction of the *meso* diruthenium complex **3.5a** at 0.93 V vs. Ag/AgNO$_3$ in measured in THF solution.

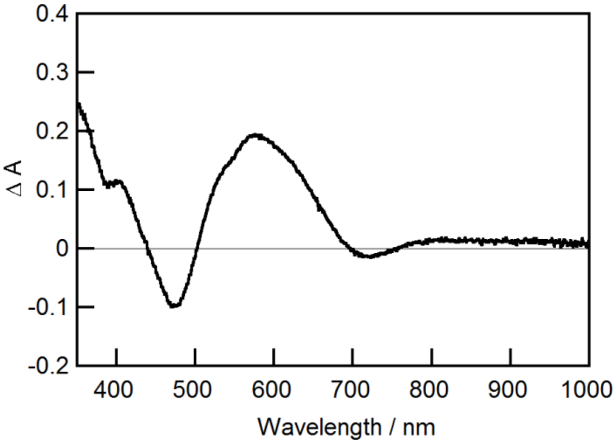

Figure 3.12 UV-visible-NIR spectroelectrochemical data showing the difference spectrum generated from the reduction of the monoruthenium complex **3.4** at -1.26 V vs. $Ag/AgNO_3$ measured in THF solution.

The diastereomeric differences in the excited state decay dynamics and lifetimes for **3.5a** and **3.5b** are exceedingly rare among metal complexes.[137] Keene and co-workers described variations in the luminescence lifetimes of the diastereomers of $[\{Ru(bpy)_2\}_2(\mu\text{-HAT})]^{4+}$ and $[\{Ru(phen)_2\}_2(\mu\text{-HAT})]^{4+}$. However, challenges with sample decomposition and NIR detection limits precluded a full investigation into these phenomena. The observed differences in the lifetimes were suggested to occur because of the disparate symmetries of the diastereomers, giving rise to the contribution of different vibrational modes to non-radiative decay. While this is possible in our system, examination of the photophysical literature of organic compounds provides an interpretation that is more consistent with our observations.

Select organic compounds containing phenone or benzophenone moieties have been reported to display diastereomeric transient lifetime discrimination in the literature.[138-144] In these cases, the difference was attributed to the ability of one diastereomer to adopt a conformation that led to either an additional quenching pathway or a lower energy transition state for the quenching mechanism. Our data suggests that the diastereomeric lifetime differentiation observed in the diruthenium complexes **3.5a,b** may be caused by a similar phenomenon. The variable temperature NMR and TA spectroscopy both indicate diastereomeric differences in conformational behaviour. The *rac* diastereomer exhibits clear exchange between two conformers that exist in a 1:1 ratio. The *meso* diastereomer does not. While the room temperature NMR data of the *meso* diastereomer is consistent with facile conformational exchange, the lack of any evidence of conformational exchange even at 166 K makes a low population or zero population of a second conformation seem more probable. Likewise, the x-ray crystal structures indicate inherent differences in the geometric arrangement of the molecules in the chair-like conformation. These observations point towards a diastereomeric conformational basis for an additional quenching mechanism. However, definitive assignment of such a mechanism is beyond the scope of this study.

3.4 Future Work

Exploration of the origin of the differences in excited state behavior of the two diastereomers should be prioritized, since understanding the basis for the excited state differences is crucial for enabling use of this phenomenon in areas such as chiral sensing or photodynamic therapy. Computational studies of **3.5a** and **3.5b** could shed light on the accessible excited state conformations and transition states for each diastereomer. Preparation of more diastereomeric diimine-diruthenium complexes may also elucidate the structural features of the complexes that enable the diasteroemeric discrimination.

Examination of the bis(rutheniumdihexafluoroacetylacetonate) complex of di-*tert*-butyl diimine **2.3a** could identify whether the noted variations in the number of pi-interactions between the hfac and phenyl rings in the diastereomers' crystal structures influence the observed differences in conformational exchange through stabilization effects. Should the differences in conformational exchange disappear but the disparity in excited state lifetimes remain, it may point to involvement of the ancillary hfac ligands in the diastereoselective quenching processes.

Synthesis of $[\{Ru(bpy)_2\}_2(\mu\text{-diphenylthioindigodiimine})]^{4+}$ complexes would be interesting for two reasons. First, the replacement of the hfac ligands with bipyridyl ligands may help answer questions about the nature of the excited state variances, specifically the role of the ancillary ligand. Second, the bipyridyl ligands could allow distribution of the charge from the MLCT transition throughout the complex. The cyclic voltammetry and spectroelectrochemistry data on complexes **3.4**, and **3.5a,b** indicate that the MLCT is mostly thioindigodiimine centered, and this localization of charge may partially account for the picosecond lifetimes observed for the molecules. The opportunity for charge distribution in the bipyridyl complexes may result in a lengthening of the lifetime of the excited state compared to the hfac complexes, therefore increasing the likelihood of luminescence and enabling experimental investigation that would allow assignment of the excited states.

3.5 Conclusions

The first examples of metal complexes featuring thioindigo diimine ligands have been prepared. Ruthenium dihexafluoroacetylacetonate complexes of diphenyl thioindigo diimine have been isolated and comprehensively characterized. An unusual aspect of these compounds revealed by the photophysical characterization is the diastereomeric distinction between compounds **3.5a** and **3.5b** in the ultrafast transient spectroscopy. The diastereomeric distinctions observed in the transient absorption spectra are linked to the conformational exchange differences evident in the NMR spectroscopy of the *meso* and *rac* compounds. Likewise, the concomitant differences in the excited state decay dynamics and lifetimes for **3.5a** and **3.5b** are believed to arise from inherent differences in the geometric arrangement of the diastereomers which allows one diastereomer to access a transition state or quenching pathway that is not available to the other. Further investigation of similar compounds may allow a deeper understanding of the factors that contribute to diastereomeric variation in the excited state behaviour of metal complexes.

3.6 Experimental Methods

3.6.1 General Synthetic Methods

The reagents used were commercially available with the exception of ruthenium dihexafluoroacetlyacetonate bis acetonitrile, and which was prepared by a modified literature procedure,[145] thioindigo-*N*,*N*'-diphenyldiimine, and zinc dihexafluoroacetylacetonate dihydrate which were prepared by literature procedures.[129, 146] Commercially available reagents were used as received.

^{1}H NMR and ^{13}C NMR were recorded at ambient temperature at a frequency of 500, 360 or 300, and 125, 90 or 75 MHz, respectively, unless otherwise noted. ^{19}F NMR spectra were recorded at ambient temperature at a frequency of 282 MHz unless otherwise noted. The data are reported as follows: proton multiplicities (s = singlet, d = doublet, t = triplet, q = quartet, m =

multiplet, br = broad, app = apparent), coupling constants, and integration. Microanalyses were performed by Canadian Microanalytical Services Ltd., Vancouver, BC. Mass spectrometry was performed by the UBC Mass Spectrometry Center. Melting points are reported uncorrected. Flash chromatography was performed using the indicated solvent system on Caledon Laboratories silica gel (SiO_2) 60 (70–230 mesh). Infrared spectra were recorded using a Perkin-Elmer Spectrum One instrument. Cyclic voltammetry experiments were performed with a Bioanalytical Systems CV50 voltammetric analyzer. CV experiments were performed using a three-electrode setup consisting of a glassy carbon working electrode, platinum electrode, and silver quasi-reference electrode. Ferrocene was used as an internal reference. Electrolyte (tetrabutylammonium tetrafluoroborate) was obtained from a commercial supplier, then purified and dried prior to use.

3.6.2 Variable Temperature NMR and Line Shape Analysis

Temperature calibration of the NMR instruments was performed as described by Braun, Kalinowski and Berger[147] using methanol (for temperatures less than 300 K) and 1,2-ethanediol (for temperatures greater than or equal to 300 K). ^{1}H NMR spectra of **3.5b** at varied temperatures were collected in *d8*-THF at 500 MHz. Line shape analysis of these spectra was performed using winDNMR Pro 7.1. A standard Eyring plot of ln(k/T) versus 1/T was used to determine activation parameters for the conformational exchange. The slope of the graph was used to calculate the enthalpy of activation using equation 3.1 where R is the gas constant 1.9872 calories mol^{-1}.

$$\Delta H^{\ddagger} = -slope \times R \qquad \text{Eq. 3.1}$$

The entropy of activation was calculated with equation 3.2 using the intercept of the plot, where k_b is the Boltzmann constant, h is Planck's constant, and R is the gas constant 1.9872 calories mol^{-1}.

$$\Delta S^{\ddagger} = (Intercept - \ln(k_b/h)) \times R \qquad \text{Eq. 3.2}$$

The Gibbs free energy of activation at 298 K was calculated from the enthalpy and entropy of activation using equation 3.3.

$$\Delta G^{\ddagger} = \Delta H^{\ddagger} - T\Delta S^{\ddagger} \qquad \text{Eq. 3.3}$$

The rate constant k at 298 K was obtained using the line fit from the Eyring plot, rearranged in equation 3.4.

$$k = e^{((-5804.6/T) + 22.85 + \ln T)} \qquad \text{Eq. 3.4}$$

3.6.3 General Photophysical Methods

Ground state absorption spectra were obtained using a Cary 100 UV-visible spectrophotometer or an Agilent 8453 UV-visible spectrophotometer. Luminescence measurements were made using a PTI QM-40 fluorescence spectrophotometer with an InGaAs NIR detector. Room temperature spectra were obtained using a 10 mm × 10 mm quartz fluorescence cell. Low temperature spectra were obtained using a special low-temperature fluorescence cell. The solution of compound in 2-methyl tetrahydrofuran was prepared in a glovebox and placed in a 2 mm diameter quartz sample tube. The sealed tube was removed from the glovebox and frozen by immersion in a liquid nitrogen filled quartz dewar cell. The sample was inspected for homogeneity and luminescence measurements were taken. Control measurements (2-methyl tetrahydrofuran alone, and sample at room temperature) were obtained using the same apparatus. The excitation and emission monochromator slits were set to 5 nm bandwidth. Spectrophotometric grade or higher purity solvents were used for all photophysical experiments. Tetrahydrofuran was checked for peroxides prior to use, and levels of ≤ 2 mg/L were maintained. Oxygen-free ambient temperature solutions were obtained by bubbling nitrogen gas through the solution in the sample cell for at least 20 minutes.

3.6.4 Ultrafast Transient Absorption Spectroscopy

Time-resolved transient absorption (TA) measurements were performed at the NCSU Imaging and Kinetic Spectroscopy Laboratory (IMAKS LAB) in the Department of Chemistry. Sub-picosecond transient absorption measurements were made using a Ti:sapphire laser system described previously.[148] Briefly, a portion of the output from a 1 kHz Ti:Sapphire Coherent Libra regenerative amplifier (4 mJ, 100 fs fwhm at 800 nm) was split into the pump and probe beams. The pump beam was directed into an optical parametric amplifier (OPerA Solo, Coherent) to generate tunable excitation (800 nm and 700 nm where indicated) while the probe beam was delayed using a 6 ns optical delay stage. TA measurements were independently made in the UV-visible and near-IR spectral ranges by focusing the probe pulse onto distinct white light continuum producing crystals. Finally, the pump and probe beams were focused and overlapped into a spot on the sample, with the relative polarizations of the two beams set at the magic angle. Samples were contained in 2 mm pathlength quartz cuvettes and each solution was stirred continuously throughout the course of the experiment to ensure that each laser pulse comes in contact with fresh sample. Spectrophotometric grade tetrahydrofuran was used as the solvent and the ground state absorption spectra were taken before and after each experiment using an Agilent 8453 UV-visible spectrophotometer to ensure there was no sample decomposition. The transient spectra and kinetics were obtained using a commercially available transient absorption spectrometer (Helios, Ultrafast Systems), averaging at least four scans and using 2-3 s of averaging at every given delay. Time constants were obtained by fitting the transient decay traces using the multiexponential functions found in OriginPro 2016.

3.6.5 Spectroelectrochemistry

Visible and near-IR spectroelectrochemical experiments were performed in an inert atmosphere glovebox (MBraun). A 0.1 M solution of $TBAPF_6$ in spectrophotometric grade THF was used as the supporting electrolyte. The $Ag/AgNO_3$ redox couple was used as an internal reference for all measurements, and potentials used are reported relative to Ag/Ag^+. Experiments were performed using a Honeycomb Spectroelectrochemical Cell Kit (Pine Research Instrumentation) in a dual-path length cell with a 1 cm x 1 cm space on the top of the cell and a 1.7 mm x 1 cm path length space on the bottom. The top of the spectroelectrochemical cell housed the $Ag/AgNO_3$ reference electrode and Pt wire counter electrode while the bottom held the Pt honeycomb working electrode. Electronic absorption spectra was taken prior to bulk electrolysis with overpotentials of ~100 mV. The Ocean Optics UV-VIS-NIR Lightsource deuterium and halogen lamps (DT-MINI-2-GS) were used to probe in the visible and near IR spectral regions, respectively. Spectra were collected every 500 milliseconds for 10 minutes and recorded with Ocean Optics HR2000+ spectrometer.

3.6.6 Molar Absorptivity Measurements

To obtain molar absorptivities for each of the compounds, a stock solution and three serial dilutions were made. For each of the four concentrations prepared, the corresponding absorbances of each major absorption band were recorded. The experiment was repeated at least three times on separate days. The absorbance value of the band maximum was plotted against the concentration of the sample (Beer-Lambert law); the molar absorptivity was determined from the slope of the graph.

3.6.7 Synthesis

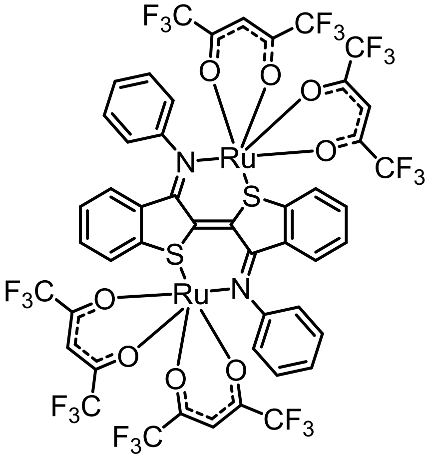

ΔΛ-μ-(Thioindigo-*N*,*N′*-diphenyldiimine) bis(ruthenium dihexafluoroacetylacetonate) (3.5a) Thioindigo-*N*,*N*'-diphenyldiimine (**2.3b**) (100 mg, 0.22 mmol), $Ru(hfac)_2(CH_3CN)_2$ (334 mg, 0.56 mmol) and toluene (26 mL) were added to a round bottom flask. The reaction was heated to reflux. After approximately 18 hours, the reaction was cooled to room temperature and aged for several hours, at which time a precipitate was observed. The reaction was filtered, and the filter cake was washed with toluene, yielding a dark green solid (140 mg). The green solid was dissolved in THF and column chromatography was performed (silica gel, ~2″ x 8″, 100% dichloromethane eluent). A black-green solid was collected (100 mg, 31%)

Crystals suitable for x-ray analysis were grown by slow evaporation of a dichloromethane/hexanes mixture. mp >325 °C; ^{1}H NMR (360 MHz, THF–*d8*) δ 7.48 (t, *J* = 7.5 Hz, 4 H), 7.38 – 7.35 (m, 4H), 7.31 (d, *J* = 8.0 Hz, 2H), 7.10 (t, *J* = 7.5 Hz, 2H), 6.67 (app. d, *J* = 7.6 Hz, 4H), 5.96 (d, *J* = 8.0 Hz, 2H), 5.78 (s, 2H), 5.54 (s, 2H); ^{19}F NMR (282 MHz, THF–*d8*) δ -76.8, -77.0, -77.42, -77.46; ^{13}C NMR (125 MHz, THF–*d8*) δ 176.7 (q, *J* = 34 Hz), 174.5 (q, *J* = 35 Hz), 173.9 (q, *J* = 34 Hz), 172.8 (q, *J* = 34 Hz), 171.1, 149.0, 139.3, 137.8, 135.4, 132.2, 131.0, 130.8, 130.0, 128.7, 128.50, 128.48, 122.7, 121.6, 117.6 (q, *J* = 283 Hz), 117.4 (q, *J* = 283 Hz), 117.3 (q, *J* = 283 Hz), 117.0 (q, *J* = 283 Hz), 91.6, 90.8; IR (KBr) 1750 (br), 1584 (w), 1465, 1264 (s), 1204 (s), 1152 (s) cm^{-1}; Anal. Calcd for $C_{48}H_{22}F_{24}N_{2}O_{8}Ru_{2}S_{2}$: C, 39.04; H, 1.50; N, 1.90. Found: C, 39.71; H, 1.84; N, 1.87. Because of the large number of isotopes and low intensity of the smallest individual masses observed for this compound, HRMS could not be obtained; however, low resolution MS provided good isotope matching with the predicted isotope pattern (see Appendix Figure A20).

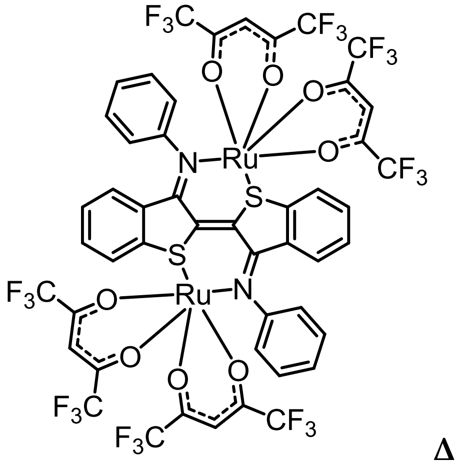

ΔΔ/ΛΛ-μ-(Thioindigo-*N*,*N′*-diphenyldiimine) bis(ruthenium dihexafluoroacetylacetonate) (3.5b) Thioindigo-*N*,*N*'-diphenyldiimine (**2.3b**) (100 mg, 0.22 mmol), $Ru(hfac)_{2}(CH_{3}CN)_{2}$ (334 mg, 0.56 mmol) and toluene (26 mL) were added to a round bottom flask. The reaction was heated to reflux. After approximately 18 hours, the reaction was cooled to room temperature and aged for several hours, at which time a precipitate was observed. The reaction was filtered, and the filter cake was washed with toluene. The filtrate was concentrated and the residue was dissolved in dichloromethane and pre-absorbed onto silica gel. Column chromatography was performed (silica gel, ~2″ x 6″, 3.5:1 hexanes/dichloromethane) which provided some clean fractions. The impure fractions were combined and concentrated and column chromatography was performed again using the same conditions. A black-green solid was collected (60 mg, 19%). Crystals suitable for x-ray analysis were grown by slow evaporation of a dichloromethane/hexanes mixture. mp >325 °C; ^{1}H NMR (300 MHz, THF–*d8*) δ 7.48 – 7.35 (m, 8H), 7.22 (d, *J* = 7.9 Hz, 2H), 7.11 (t, *J* = 7.9 Hz and overlapping br s, 4H), 6.60 (s, br, 2H), 6.06 (d, *J* = 8.2 Hz, 2H), 5.94 (s, and overlapping br s, 4H); ^{19}F NMR (338 MHz, THF–*d8*) δ -77.1 (br), -77.2, -77.4, -77.6; ^{13}C NMR (125 MHz, THF–*d8,* 333K) δ 176.5 (q, *J* = 35 Hz), 173.4 (q, *J* = 35 Hz), 169.8, 150.5, 139.1, 138.6, 134.7, 132.9, 130.6, 130.5, 129.7, 129.0, 128.7, 128.0, 122.6, 121.8, 117.7 (q, *J* = 283 Hz), 117.5 (q, *J* = 283 Hz), 117.3 (q, *J* = 283 Hz), 117.1 (q, *J* = 283 Hz), 91.7; IR (thin film, NaCl) 1582 (w), 1466 (w), 1264 (s), 1209 (s), 1154 (s) cm^{-1}; Anal. Calcd for $C_{48}H_{22}F_{24}N_2O_8Ru_2S_2$: C, 39.04; H, 1.50; N, 1.90. Found: C, 39.32; H, 1.62; N, 1.84. Because of the large number of isotopes and low intensity of the smallest individual masses observed for this compound, high resolution MS could not be obtained; however, low resolution MS provided good isotope matching with the predicted isotope pattern (see Appendix Figure A21).

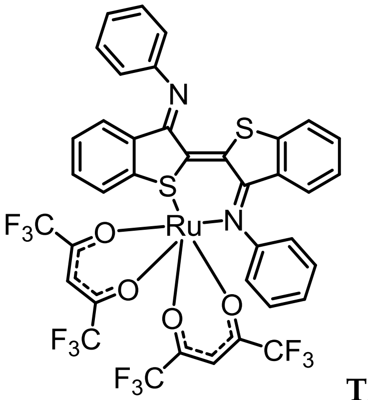

Thioindigo-*N,N′*-diphenyldiimine ruthenium dihexafluoroacetylacetonate (3.4) Thioindigo-*N,N*'-diphenyldiimine (**2.3b**) (160 mg, 0.36 mmol), Ru(hfac)$_2$(CH$_3$CN)$_2$ (180 mg, 0.30 mmol) and toluene (26 mL) were added to a round bottom flask. The reaction was heated to reflux. After approximately 18 hours, the reaction was cooled to room temperature and aged for several hours, generating a precipitate. The reaction was filtered, and the filter cake was washed with toluene. The filtrates were concentrated. The solid residue was stirred in acetonitrile (~60 mL). The remaining reddish solid was filtered off and the filtrate was concentrated. The resulting black solid was dissolved in dichloromethane, and pre-absorbed on silica gel. Column chromatography was preformed (silica gel, ~2″ x 10″, 3.5:1 hexanes/dichloromethane as the eluent). This provided some clean product. The impure fractions were concentrated and pre-absorbed on silica gel. Column chromatography was performed (silica gel, ~2″ x 8″, 9.5:0.5 hexanes/ethyl acetate) and clean fractions were concentrated. A dark green-black solid was obtained (combined yield 75 mg, 26%). Crystals suitable for x-ray analysis were grown by slow evaporation of d8-tetrahydrofuran. mp 219–221°C; ^{1}H NMR (300 MHz, THF–*d8*) δ 7.50 – 7.44 (m, 4H), 7.38 – 7.18 (m, 7H), 6.98 (app dd, *J* = 8.2, 0.9 Hz, 3H), 6.75 – 6.65 (m, 3H), 5.86 (d, *J* = 8.2, Hz, 1H), 5.76 (s, 1H), 5.52 (s, 1H); ^{19}F NMR (282 MHz, THF–*d8*) δ -75.0, -75.2, -75.56, -75.63; ^{13}C NMR (90 MHz, THF–*d8*) 176.2 (q, *J* = 34 Hz), 175.4, 173.7 (q, *J* = 38 Hz), 173.3 (q, *J* = 35 Hz), 171.9 (q, *J* =

34 Hz), 159.7, 150.7, 150.6, 147.0, 140.4, 138.7, 134.2, 133.6, 132.1, 130.5, 130.2, 129.6, 129.4, 129.2, 128.3, 128.0, 127.7, 125.8, 125.4, 124.7, 122.9, 122.2, 118.9, 118.6, 117.7 (q, *J* = 283 Hz), 117.50 (q, *J* = 283 Hz), 117.45 (q, *J* = 283 Hz), 116.9 (q, *J* = 283 Hz), 91.5, 90.7; (IR (thin film, NaCl) 1583 (w), 1543 (w), 1265 (s), 1207 (s), 1155 (s) cm^{-1}; Anal. Calcd for $C_{38}H_{20}F_{12}N_2O_4RuS_2$: C, 47.46; H, 2.10; N, 2.91. Found: C, 46.65; H, 2.09; N, 2.77. Because of the large number of isotopes and low intensity of the smallest individual masses observed for this compound, HRMS could not be obtained; however, low resolution MS provided good isotope matching with the predicted isotope pattern (see supplementary information Figure A22).

Chapter 4

Towards a Synthesis of AzaDIMEs and AzaDicarbazolyls

4.1 Introduction

The development of thioindigo diimines and their coordination chemistry, described in chapters 2 and 3, is an example of using a known dye (thioindigo) as a building block for accessing new compounds with unique photophysical properties through functional group modifications and metal coordination. An alternative approach forgoes the use of known dye molecules as ligand precursors and relies on the design of new chromophores that are capable of metal complexation. This chapter details the investigation into two such chromophores: the azaDIMEs and azaDicarbazolyls.

4.2 AzaDIMEs (Aza Diindolyl Methenes)

The target chromophores, Aza diindolyl methenes (azaDIMEs), (Figure 4.1) consist of two indolyl fragments connected by an azamethene moiety. One indolyl fragment is an indole, while the other fragment is oxidized, creating conjugation throughout the molecule. Neutral azaDIMEs are predicted to take on a generally planar structure in order to maximize conjugation. The extended conjugation within the molecule should lead to and to absorption in the visible region of the EM spectrum, with low energy absorption maxima between approximately 550 nm and 750 nm.

The two halves of the molecules can be connected by the azamethene unit at any of the six available carbon atoms in each indolyl fragment, providing a diverse set of molecules within this class of compound. Representative symmetrically connected azaDIMEs are shown in Figure 4.1.

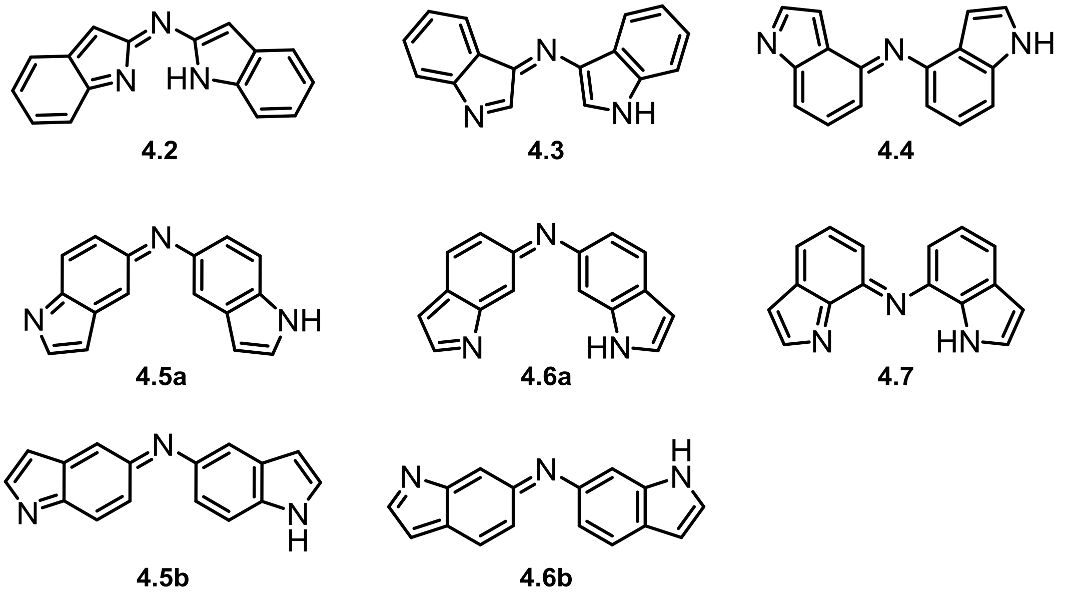

Figure 4.1 Representative azaDIME isomers.

Formation of E/Z imine isomers are possible for all of these compounds, (for example **4.5a,b** and **4.6a,b**) although in some cases the ability to form an intramolecular hydrogen bond may lead to preferential formation of one isomer over another (for example **4.2** and **4.7**). The structural variety introduced by the position of azamethene connectivity means that different azaDIMEs are likely to adopt diverse binding modes for metal complexation. Some of the azaDIMEs are likely to be bridging ligands (**4.3**– **4.5**), some are likely to be bidentate ligands (**4.2**), some could be either (**4.6**), and in the case of 7,7′-azaDIME **4.7**, the compound is likely to behave as a tridentate pincer ligand (Figure 4.2). Because each indolyl fragment would coordinate to metals though either a neutral (the oxidized fragment) or anionic (the indole fragment) nitrogen, multimetallic coordination complexes using azaDIMEs as bridging ligands can be imagined.

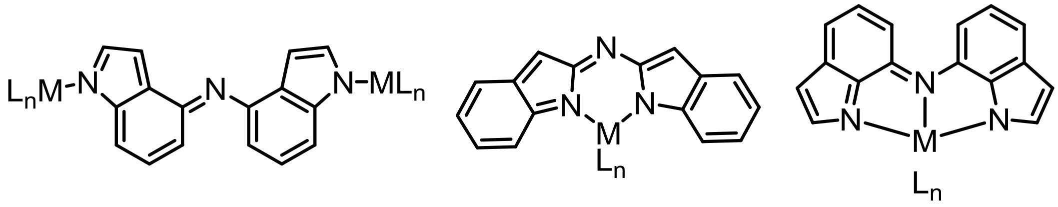

Bridging
4.8

Bidentate
Chelating
4.9

Tridentate Pincer
Chelating
4.10

Figure 4.2 Binding modes of azaDIME ligands in coordination complexes.

No azaDIMEs have been reported in the literature, yet there are noteworthy structural similiarities between azaDIMEs and the dipyrrins (**1.7**) discussed in chapter 1, and more specifically, azadipyrrins **4.1** (Figure 4.3). All three are conjugated ligand systems with two nitrogen-containing heterocyclic units, one oxidized and one unoxidized. In fact, the 2,2′ azaDIME **4.2** could be classed as an azadipyrrin. Azadipyrrins have similar properties to the dipyrrins, but tend to absorb and emit at longerwavelengths.[149] Compared to both the dipyrrins and azadipyrins, the azaDIMEs have a more extended pi system, possibly enabling absorption and emission farther into the NIR. The versatile connectivity of the azaDIMEs gives a structural diversity to the azaDIMEs that is greater than the dipyrrins and azadipyrrins. This allows access to a broader variety of metal complexes than is possible for dipyrrins or azadipyrrins, which are generally restricted to bidentate coordination modes. The most notable examples of dipyrrin and azadipyrrin coordination complexes are with main group elements, usually boron (for example BODIPYs **1.#**).[47, 150-153] However, in recent years, an increasing number of transition metal coordination complexes of azadipyrrins have been reported. Bidentate azadipyrrin complexes with metals including Zn, Co, Cu, Ni, Ru, Rh, Pd, Pt, Ag, Au, and Re are also known.[154-157]

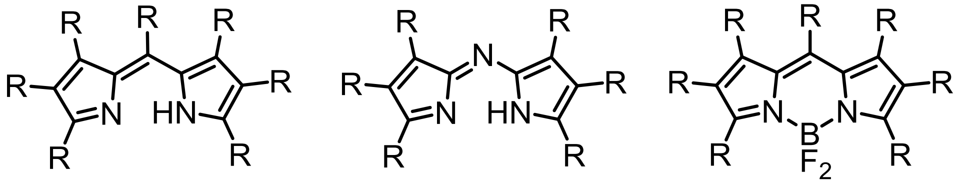

2,2'-Dipyrrin
1.7

AzaDipyrrin
4.1

BODIPY
1.#

Figure 4.3 Dipyrrin ligand systems and boron coordination complexes.

4.2.1 Synthetic Plan

Retrosynthetic analysis of the azaDIMEs leads to a disconnect between the two indolyl fragments, and the synthesis of unsubstituted azaDIMEs **4.11** was originally conceived as a two-step reaction sequence (Scheme 4.1). The azaDIME ligands would be obtained by two-electron, two-proton oxidation of amino-diindole compounds **4.12**. The amino-diindole compounds would be prepared by a Buchwald-Hartwig amination of a bromoindole **4.13** and an aminoindole

4.14. The position of the halide and amine on the indole partners would therefore dictate the connectivity of the indole halves in the amino-diindole compounds, and a wide variety of azaDIMEs could potentially be accessed by this methodology using commercially available bromo and amino indoles.

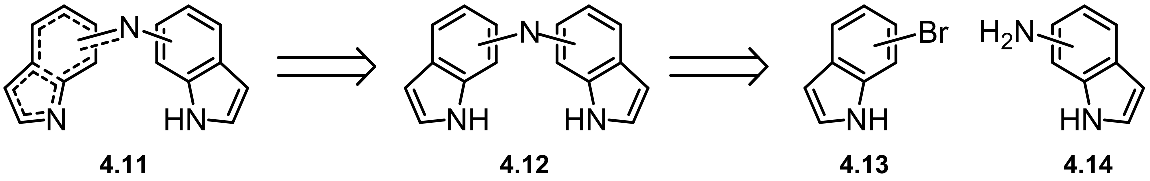

Scheme 4.1 General retrosynthetic plan for the synthesis of AzaDIME ligands.

In the case of substituted azaDIMEs, the appropriately substituted indole precursors, if not commercially available, would require additional synthetic steps to prepare. Modification of the Buchwald-Hartwig amination reaction conditions might also be necessary if the electronic or steric characteristics of the indoles are significantly altered by the introduction of the substituents.

4.2.2 Consideration of the Buchwald-Hartwig Amination

Buchwald-Hartwig amination (BHA) can be a difficult reaction to employ because the nature of the coupling partners, the pre-catalyst, ligand, solvent, and base can all vastly affect the outcome of the reaction. For this reason, a wide variety of catalysts, ligands, and reaction conditions have been developed for this transformation.[158-162] This has been greatly beneficial in terms of broadening the scope of the reaction,[163, 164] but it also introduces a significant challenge in the selection of reagents and conditions for previously unreported coupling partners.

Furthermore, the use of indoles in BHA reactions is complicated by other factors. Indoles contain two reactive sites, the indole N-H and the C-3 position (Figure 4.4), which can compete with the intended reaction between the aniline moiety and the aryl bromide.[165, 166] This presents a potential selectivity problem during the coupling reaction. Literature reports of unwanted C-C coupling at the C-3 exist, but it tends to occur under specific combinations of catalyst and ligand, and appears to be most problematic with highly hindered (*o*-substituted) anilines.[167] C-N coupling between the aryl bromide and the indole N-H is of greater concern, since many examples of this type of reaction are found in the literature.[161]

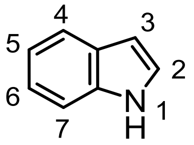

Figure 4.4 Indole numbering conventions.

Another possible issue arises from the structure of the amino-diindole products **4.12**. The amino-diindole compounds are prospective ligands themselves, and under basic conditions in the presence of a metal, i.e. the BHA reaction environment, the amino-diindoles may form coordination complexes with the metal, effectively poisoning the BHA catalyst and stalling the reaction. Judicious choice of metal catalyst and ligands could be effective in controlling the selectivity of the reaction, but protection of the indole nitrogen on one or both coupling partners might be necessary both for selectivity and to avoid coordination of the amino-diindole product with the catalyst.

Therefore a two-prong approach to the synthesis was undertaken: work was begun simultaneously on BHA of the unprotected indoles and on protecting the indole amines. Because of the ready commercial availability and reasonable cost of the starting bromo and aminoindoles, the 6,6′ and 7,7′ azaDIME systems (compounds **4.6a,b** and **4.7**, respectively) were chosen as the target molecules for this exploratory chemistry.

4.2.3 Protecting the Indole Nitrogen

The decision was made to protect the bromoindoles **4.13** in preference to the aminoindole **4.14** because of potential difficulties in selectively protecting the indole nitrogen in the presence of an aniline nitrogen. Formation of a *tert*-butyl carbamate or a silyl ether were prioritized because of they are stable to base and moderate heat.

Treatment of 6-bromoindole **4.15a** with NaH followed by *tert*-butyldimethylsilyl chloride (TBDMSCl) gave the desired compound **4.15b** in 55% yield after fifteen minutes at room temperature (Scheme 4.2). Longer reaction times and addition of extra NaH to try to drive the reaction to completion actually resulted in lower yields. Monitoring of the reaction by TLC demonstrated that the product was formed and then decomposed back to the starting material, implying that unreacted H^- deprotected the silyl ether in a manner similar to F^- (which, in the form of tetrabutylammonium fluoride, is frequently used to remove silyl ether protecting groups).[168] Formation of the TBDMS protected 7-bromoindole was also successful, however the reaction required an overnight reflux, and still resulted in an incomplete reaction. The sluggish reaction was attributed to the added steric hindrance imparted by the 7-position substituent.

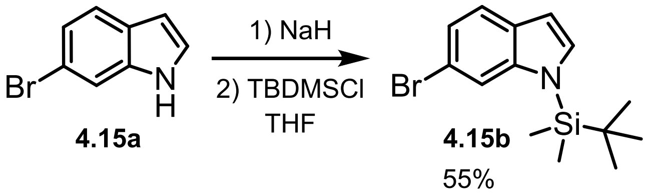

Scheme 4.2 Conditions for the TBDMS protection of 6-bromoindole **4.15a**.

The procedure for installing a *tert*-butyl carbamate (BOC) protecting group on the indole nitrogen was tested using 6-bromoindole. Reaction of the indole with di-*tert*-butyl dicarbonate and potassium carbonate at room temperature in acetonitrile afforded the BOC-protected indole **4.15c** in 80% yield (Scheme 4.3). As with the TBDMS protection, the 7-bromoindole required heating to promote formation of the *tert*-butyl carbamate product.

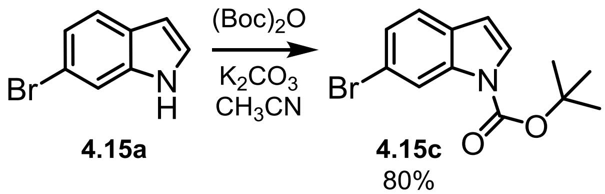

Scheme 4.3 Conditions for the BOC protection of 6-bromoindole **4.15a**.

4.2.4 Development of the Buchwald-Hartwig Amination Reaction

Development of the BHA reaction conditions was initiated using the unprotected 7-substituted indoles. Two promising sets of conditions were identified on the basis of literature precedence. The first combination was based on the lone reported example of BHA coupling using unprotected 7-aminoindole.[169] The conditions include a Josiphos-type (Pd(dppf)Cl_2) ligand/catalyst system (Figure 4.5), NaOtBu, and dioxane. Importantly, this ligand/Pd combination is rarely reported for indolyl N-H coupling, and when a Josiphos-type ligand is reported for indolyl N-H coupling the base is a weak inorganic base such as Cs_2CO_3 or K_2CO_3.[170] The second set of conditions was based on the publications of Buchwald et al. The metal would be palladium and the ligand could be X-Phos (**4.19)** or, better yet, BrettPhos (**4.20**), which is known to be useful for BHA with primary anilines.[171] Buchwald et al. have developed other catalysts to perform arylation of indole N-H.[172] This suggests that the proposed ligand/catalyst system may be selective for the desired aniline coupling.

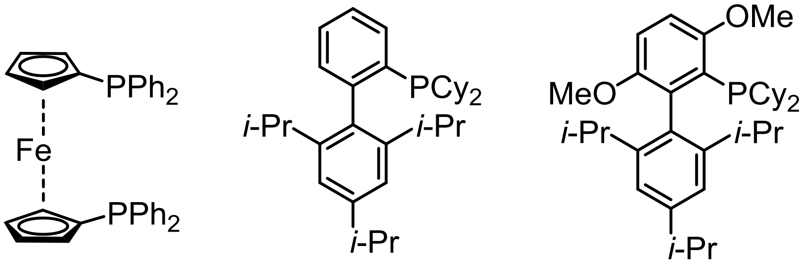

dppf
4.18

XPhos
4.19

BrettPhos
4.20

Figure 4.5 Ligands selected for exploration of the Buchwald-Hartwig Amination reaction.

Table 4.1 summarizes the initial exploration of BHA reaction conditions. Despite the literature precedence for the BHA of 7-aminoindole using $Pd(dppf)Cl_2$, these BHA conditions resulted in no observed reaction (Entry 1). Likewise, reactions using either $Pd(OAc)_2$ or $Pd(dba)_2$ as the metal source, Xphos as the ligand, and Cs_2CO_3 or NaO*t*Bu also resulted in recovery of starting materials (Entries 2 and 3). However, upon changing the base to K_2CO_3, a slow, incomplete reaction was observed (Entry 4). Using the same conditions with 6-aminoindole **4.22** and TBDMS protected 6-bromoindole **4.15b** resulted in formation of the desired product along with deprotection of the bromide (Entry 5). The amount of deprotected bromide compared to coupled product varied with the number of equivalents of ligand used. Higher ligand loadings resulted in a larger ratio of coupled product to deprotected bromide. However, since ligand loadings of 0.3 equiv. still produced mixtures of products, an alternative was necessary. Different bases were explored, but did not yield better outcomes (Entries 6 and 7).

Eventually, 6-aminoindole and 6-bromo-1-TBDMS indole **4.15b** were submitted to a reaction with $Pd(OAc)_2$, Brett-Phos, and K_2CO_3 in refluxing tBuOH. Upon workup, the products of the reaction were found to be deprotected bromide **4.15a** and the unprotected 6,6′-aminodiindole **4.20a** (Entry 8). When these reaction conditions were used on the unprotected 7-amino and 7-bromoindoles, consumption of starting material was observed and the major product of the reaction (by TLC) was the desired 7,7′-aminodiindole **4.21a** (Entry 9).

Table 4.1 Identification of reaction conditions for formation of aminodiindoles using Buchwald-Hartwig Amination.

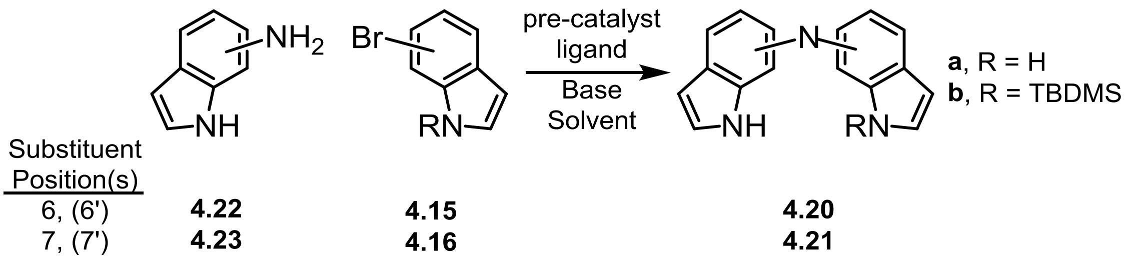

Entry	Reaction Conditions						Products[a]
	Indole Substituent Position		Catalyst		Base	Solvent	
	NH_2	Br	Pre-catalyst	Ligand			
1	7	7**a**	Pd(dppf)Cl_2	4.17	NaO*t*Bu	1,4-Dioxane	N.R.
2	7	7**a**	$Pd(OAc)_2$	4.18	Cs_2CO_3	*t*-BuOH	N.R.
3	7	7**a**	$Pd_2(dba)_2$	4.18	NaO*t*Bu	*t*-BuOH	N.R.
4	7	7**a**	$Pd(OAc)_2$	4.18	K_2CO_3	*t*-BuOH	4.21a (incomplete conversion)
5	6	6**b**	$Pd(OAc)_2$	4.18	K_2CO_3	*t*-BuOH	4.20b 4.15a
6	6	6**b**	$Pd(OAc)_2$	4.18	KO*t*Bu	*t*-BuOH	4.15a major 4.20b trace
7	6	6**b**	$Pd(OAc)_2$	4.18	K_2CO_3/ Et_3N	*t*-BuOH	4.20a trace & unknown
8	6	6**b**	$Pd(OAc)_2$	4.19	K_2CO_3	*t*-BuOH	4.20a 4.15a
9	6	6**a**	$Pd(OAc)_2$	4.19	K_2CO_3	*t*-BuOH	4.20a major

[a] N.R. = no reaction

Identification of the aminodiindole products during reaction optimization was done primarily with ^{1}H NMR because the product were isolated in small amounts – a consequence of the small scale of the reactions and the low yields obtained as a result of incomplete reactions and the formation of mixtures of products. As the reactions were scaled up, however, it became increasingly clear that the low yields and difficulties in product isolation were not a result of the reaction alone, but were also an effect of the instability of the aminodiindoles themselves. During workup and purification (mostly by column chromatography), disappearance of the desired product was noted by TLC and appearance of a dark precipitate was observed. This resulted in the isolation of small amounts of the desired product, which could also be observed changing over minutes to days (depending on the substitution pattern of the diindole system, and whether the indole was protected) from a soluble, colorless compound to a dark, insoluble compound. The instability was greatest in solution, which prevented full characterization of these compounds.

We hypothesized that oxidation to the azaDIME compounds might be occurring in the presence of air, and because of their extended conjugation, the azaDIMEs could adopt a planar structure which caused them to be insoluble. Therefore attempts were made to perform the reaction under rigorously air-free conditions (Schlenk-line reaction, glove-box characterization). This allowed NMR characterization of the crude reaction mixture, but the need for column chromatography to purify the diindole meant that isolation of clean material for characterization was not possible. It is worth noting that even under these conditions formation of a dark precipitate was observed.

4.2.5 Synthesis of 7-Bromo-3-*tert*-butylindole (4.25)

The insoluble nature of the bluish black precipitate formed following the palladium catalyzed cross-coupling of 7-bromoindole and 7-aminoindole prompted consideration of solubilizing substituents that could be directly installed on the indole starting materials. *Tert*-butyl groups are desirable because they provide steric bulk and can be introduced to the ring by electrophilic aromatic substitution. Substitution at the 3-position of the indole ring is favored electronically,[173] but competing substitution at the 2-position and 1-position can be problematic.[174] Many protocols for Friedel-Crafts alkylation of indoles suffer from poor yields caused by the formation of mixtures of products and consequently difficult chromatographic separations.[ref] With this in mind, a somewhat unconventional approach to the alkylation was undertaken, following a report of selective 3-position *tert*-butylation of indoles using K-10 montmorillonite clay and *tert*-butanol under solvent-free microwave conditions.[175]

While these conditions had been reported to give isolated yields of 47-73% for a variety of indoles, in the case of 7-bromoindole **4.16**, the desired 3-*tert*-butyl product was isolated as a very minor product. The major product of the reaction was a relatively insoluble white powder with a ^{1}H NMR spectrum that was incompatible with the structure of the desired compound. The spectrum displayed two distinct indole N-H signals, indicating the presence of chemically inequivalent indole rings. The spectrum also exhibited a total of seven aromatic signals and no *tert*-butyl signals. Taken together, this presented the possibility that a dimerization or oligomerization reaction was occurring.

Further corroborating evidence was obtained from ^{13}C NMR which showed a total of sixteen signals, all aromatic, and from COSY and TOCSY NMR which elucidated two sets of coupled protons and revealed that one indole ring contained a hydrogen at the C2-position while the other indole ring did not. This pointed to a more complex structure than a simple dimer, but the exact nature of the compound was unknown until single crystal X-ray analysis eventually revealed the compound to be the indole tetramer **4.24** (Figure 4.6).

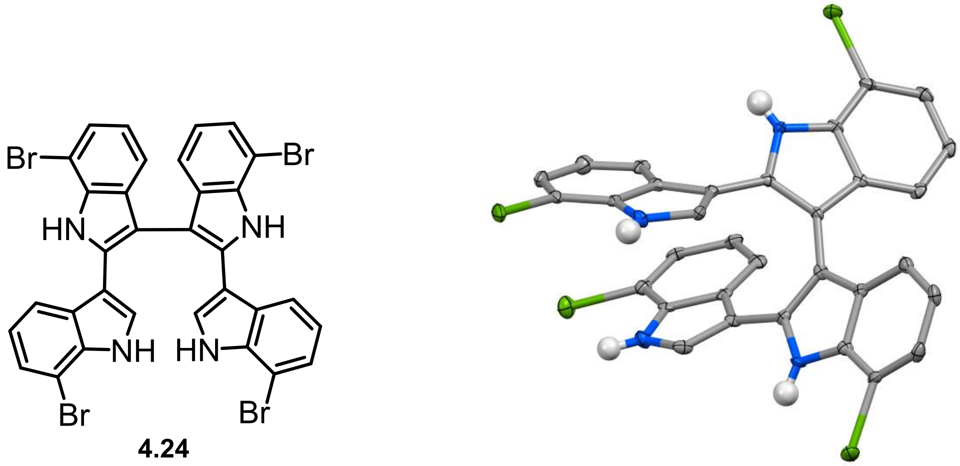

4.24

Figure 4.6 Chemical structure (left) and X-ray crystal structure (right) of 7-bromoindole tetramer **4.24**. Ellipsoids are represented at 50% probability. Hydrogens (except for N-H hydrogens) have been removed for clarity.

While similar compounds to **4.24** have occasionally been reported,[176, 177] in one case as the product of a traditional Freidel-Crafts alkylation,[178] the literature did not provide insight into the cause of the tetramer formation under our conditions. Since the only byproducts described in the original *tert*-butylation paper were those resulting from N-alkylation of the indole, the experimental conditions were scrutinized for any potential differences between the reported and the preparative conditions. One possible discrepancy was the introduction of water to the reaction during the weighing and addition of *tert*-butanol. The *tert*-butanol was highly deliquescent when handled in our ambient conditions, but no mention of hygroscopic behavior was made in the article. Two reactions were performed to test this hypothesis. In the first, *tert*-butanol was replaced with 2-chloro-2-methylpropane (a non-hygroscopic alkyl source). In the second, no alkylating reagent was used, and extra water was added to the reaction. The outcomes of both reactions indicated that water was involved in the oligomerization reaction. In the reaction using 2-chloro-2-methylpropane, no tetramer was observed and the desired 3-substituted indole **4.25** was the major product. Likewise, in the reaction with added water and no alkylating agent, the only product observed was the tetramer, which was isolated in 30 % yield. In a reaction with *tert*-butanol (1.5 equiv) and added water (21.7 equiv.), only tetramer was formed.

The microwave reaction conditions to alkylate 7-bromoindole were then further modified to minimize the production of di- and tri-alkylated compounds that were also observed when 2-chloro-2-methylpropane was used. The dialkylated compound was tentatively assigned to 3,5-di-*tert*-butylindole on the basis of ^{1}H and COSY NMR spectra. The structure of the tri-alkylated compound was not identified. Formation of these compounds was likely a consequence of a number of coinciding factors: the high temperatures and higher than stoichiometric equivalents of alkylating agent, and the increased electrophilicity of the indole upon introduction of the first *tert*-butyl substituent. Lowering the reaction temperature by 20 °C and decreasing the reaction time eliminated the formation of the trialkylated product and reduced the amount of dialkylated product created. Surprisingly, lowering the amount of 2-chloro-2-methylpropane appeared to have an effect opposite of the desired, as the amount of dialkylated product increased from 7% to 15% (by NMR) when the number of equivalents was lowered from 1.5 to 1.0. Under the optimized conditions, the desired 3-*tert*-butyl-7-bromoindole was isolated in 36% yield following column chromatography (Scheme 4.4).

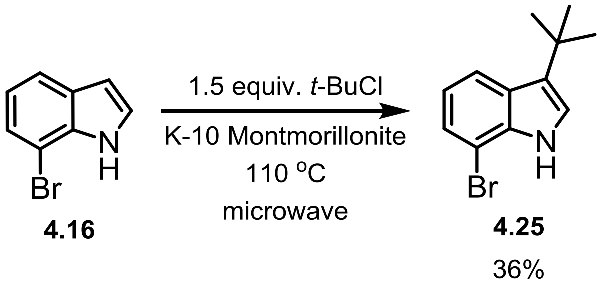

Scheme 4.4 Optimized conditions for the formation of 7-bromo-3-*tert*-butylindole **4.25**.

4.2.6 Synthesis of 7,7′-Amino-3-*tert*-butyldiindole 4.26 and Attempted Formation of AzaDIME 4.27

The previously established palladium catalyzed cross-coupling conditions for the 6,6′-aminodiindole and unsubstituted 7,7′-aminodiindole systems were applied to the reaction of 7-aminoindole with 7-bromo-3-*tert*-butylindole (Scheme 4.5). This provided one major product that was isolated by column chromatography as slightly grayish oil that solidified upon exposure to deuterated chloroform. The ^1H NMR spectrum of the material was consistent with the desired compound **4.26**, but the ^{13}C spectrum appeared to be missing one aromatic quaternary carbon signal. DEPT135, HSQC, and HMBC NMR experiments were performed and analyzed in order to verify the structure. These experiments revealed overlapping ^{13}C carbon signals for the 7 and 7′ carbon atoms and confirmed the assignment of the product as the 7,7′-amino-3-tert-butyldiindole **4.26**.

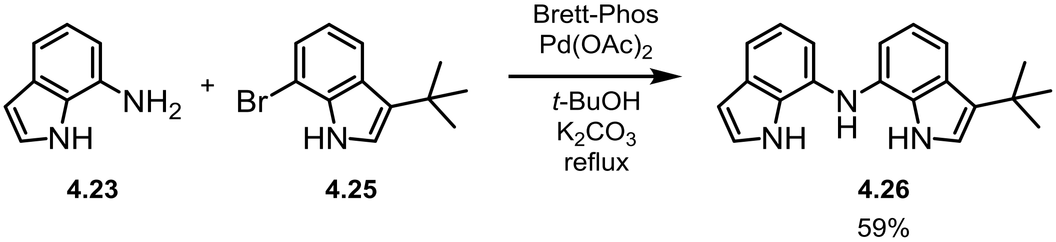

Scheme 4.5 Palladium catalyzed cross coupling reaction of **4.23** and **4.25** to form 7,7′-amino-3-*tert*-butyl-diindole **4.26**.

Unlike the unsubstituted diindole compounds **4.20** and **4.21**, the *tert*-butyl substituted compound **4.26** exhibited moderate stability in air. In the solid phase, the compound was stable for several months at room temperature or below. However, as an oil, or in solution, the compound completely decomposed in days to weeks, even when stored at subzero Celsius temperatures. The instability of the compound in solution prevented the acquisition of a single crystal X-ray structure of diindole **4.26**, as attempts to grow crystals invariably led to decomposition.

With the diindole **4.26** in hand, the two electron, two proton oxidation to form the AzaDIME **4.27** was explored. Oxidation using DDQ at room temperature afforded a dark precipitate immediately following the addition of DDQ to a solution of diindole **4.26**, and TLC indicated complete consumption of starting material within ten minutes. The precipitate was isolated as a black solid which dissolved in *d6*-acetone to give a dark blue solution. The ^{1}H NMR spectrum was inconclusive, displaying very broad peaks, which could have been caused by a number of phenomena. The broadened peaks were consistent with either aggregation, slow tautomerization of azaDIME **4.27** on the NMR timescale (Figure 4.7), or formation of oligomers during the oxidation reaction.

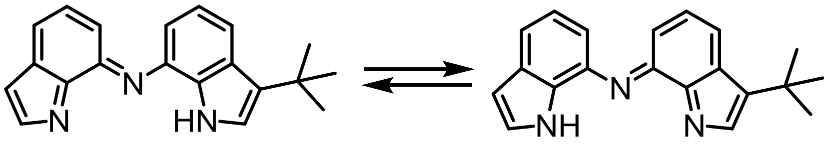
4.27 **4.28**

Figure 4.7 Possible tautomerization of asymmetric *tert*-butyl azaDIME **4.27**.

Attempts to purify the precipitate were hindered by general insolubility in less polar solvents than acetone, which rendered column chromatography ineffectual. Mass spectroscopy was also inconclusive, providing no [M+H] peak, but a possible [2M+H] peak. In order to elucidate whether tautomerization was occurring, several attempts were made to either N-alkylate or metalate the azaDIME **4.27** on the supposition that even if mixtures of products were obtained, they might be separable, and would, at least, be visible and identifiable by NMR since they would not be able to tautomerize. However, treatment with sodium hydride and iodomethane or with triethylamine and either $PtCl_2(PhCN)_2$ or $PtCl_2(COD)_2$ resulted in mixtures of unidentifiable products despite initially promising color changes from blue to green during the reaction.

Oxidation of **4.26** using Ag_2O in dichloromethane resulted in a much slower reaction (consumption of starting material in five days) which yielded a qualitatively more soluble black product. The ^1H NMR spectrum of the product was again very broad, and UV-Visible-NIR absorption spectra of the products of the two oxidation reactions (DDQ and Ag_2O) were obtained for comparative identification (Figure 4.8).

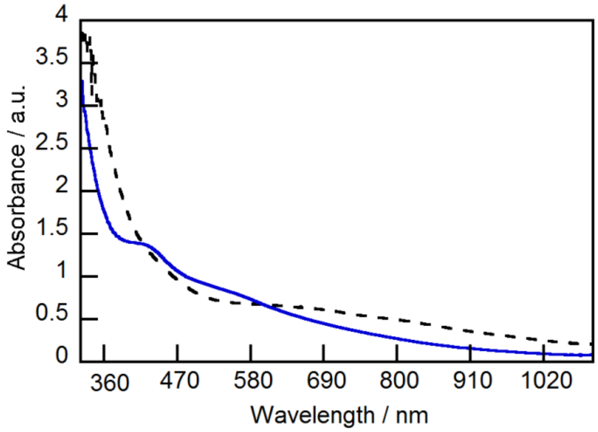

Figure 4.8 UV-Visible-NIR Absorption spectra of the products of oxidation of **4.26** with DDQ (dashed black line) and Ag_2O (solid blue line).

The absorption spectra of the two products are demonstrably different, although they share similar features. Both absorb most strongly in the UV, and have a broad, relatively shapeless absorption band across the rest of the spectral region examined. These features, along with the trailing absorption past 1100 nm, suggests the idea that oligomerization is the outcome of oxidation of **4.26**. The differences in the absorption spectra could be the result of the two oxidation reactions generating mixtures of oligomers that have different product distributions.

Cyclic voltammetry experiments on 7,7′-amino-3-*tert*-butyl-diindole **4.26** provided further evidence that oligomerization was occurring during oxidation. The diindole **4.26** has an irreversible one-electron oxidation at 0.165 V vs. Fc/Fc^+, and a multi-electron irreversible oxidation at 0.99–1.29 V vs. Fc/Fc^+ (Figure 4.9). Isolation of the first oxidation wave did not change the irreversible nature of the oxidation, which presumably happens with loss of a proton, and repeated cycling showed no change in the shape, indicating that oligomerization is not an issue in the first oxidation (Figure 4.10). The second oxidation does show evidence of oligomerization, with the shape of the wave changing dramatically with repeat cycling (Appendix Figure A.27), and concurrent deposition of a dark, glossy material on the carbon working electrode. These observations are consistent with oxidative oligomerization in the *tert*-butyldiindole compound **4.26**, and suggests that the dark insoluble precipitates formed during preparation and isolation of the unsubstituted diindoles **4.20** and **4.21** were not the desired azaDIMEs, but were in fact mixtures of oligomers formed through air oxidation.

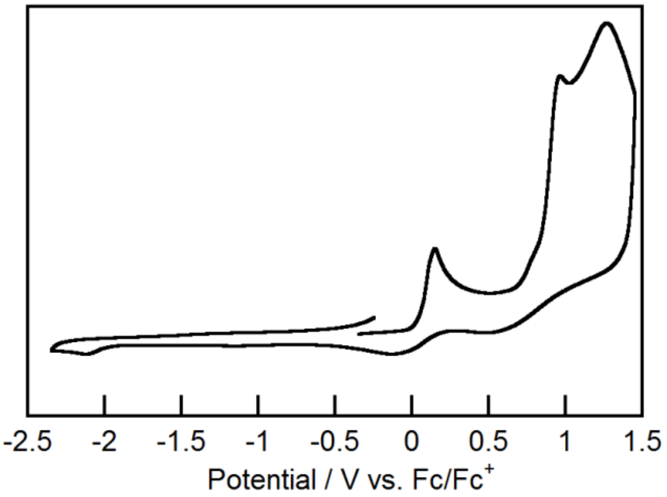

Figure 4.9 Cyclic voltammogram of 7,7′-amino-3-*tert*-butyl-diindole **4.26**. The concentration of analyte in dichloromethane is ~1 mM. The standard is Fc/Fc$^+$, the electrolyte is 0.1 M Bu_4NPF_6 and the scan rate is 100 mV s^{-1}.

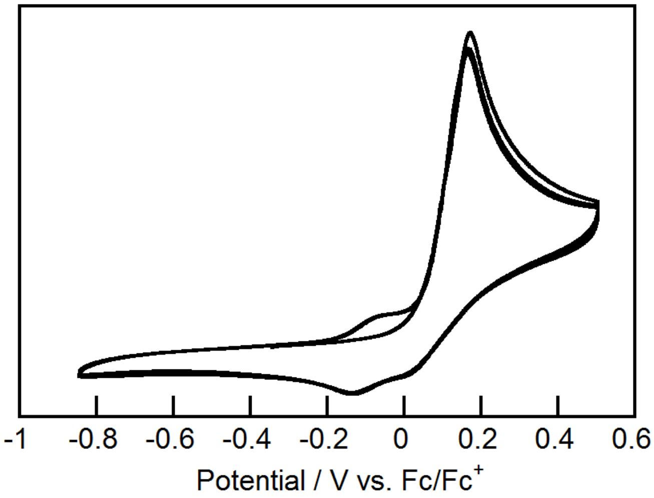

Figure 4.10 Cyclic voltammogram of 7,7′-amino-3-*tert*-butyl-diindole **4.26**, cycled six times. The concentration of analyte in dichloromethane is ~1 mM. The standard is Fc/Fc$^+$, the electrolyte is 0.1 M Bu_4NPF_6 and the scan rate is 250 mV s^{-1}.

4.2.7 One-Pot Complexation/Oxidation Attempts

In light of the absorption and electrochemical data supporting oligomerization of **4.26** during oxidation, the focus shifted from isolating the azaDIME ligands themselves to identifying alternative methods of obtaining the azaDIME-metal coordination complexes. Two related approaches that eliminated the need for isolation of the azaDIME ligand were selected. One method employed low temperature oxidation and in-situ complexation of the oxidized ligand, while the other method reversed the reaction sequence, forming diindole-metal complexes first, followed by oxidation of the metal complex (either by air during the complexation or as a separate reaction) (Scheme 4.6).

Low temperature ligand oxidation followed by in-situ complexation is a technique that has been employed in the synthesis of some BoDIPY complexes. The unsubstituted dipyrrin ligand is unstable and has never been isolated, yet unsubstituted dipyrrin-boron complexes have been synthesized. A recent report synthesizing unsubstituted BoDIPYs[179] detailed improved conditions for low temperature (-40 to -78 °C) oxidation of the dipyrromethane and in-situ trapping of the resulting dipyrrin in a boron complex. Although the pincer-type chelation envisioned for 7,7′-azaDIMEs is not ideal for complexation with boron, which adopts a tetrahedral geometry rather than square planar, the similarities between the dipyrromethane/dipyrrin and the diindole/azaDIME scaffolds suggest that low temperature oxidation might yield the desired azaDIME. Assuming a successful oxidation, in-situ trapping with an appropriate metal would produce the azaDIME-metal complex if the reaction with the metal precursor proved to be faster than the oligomerization of the azaDIME.

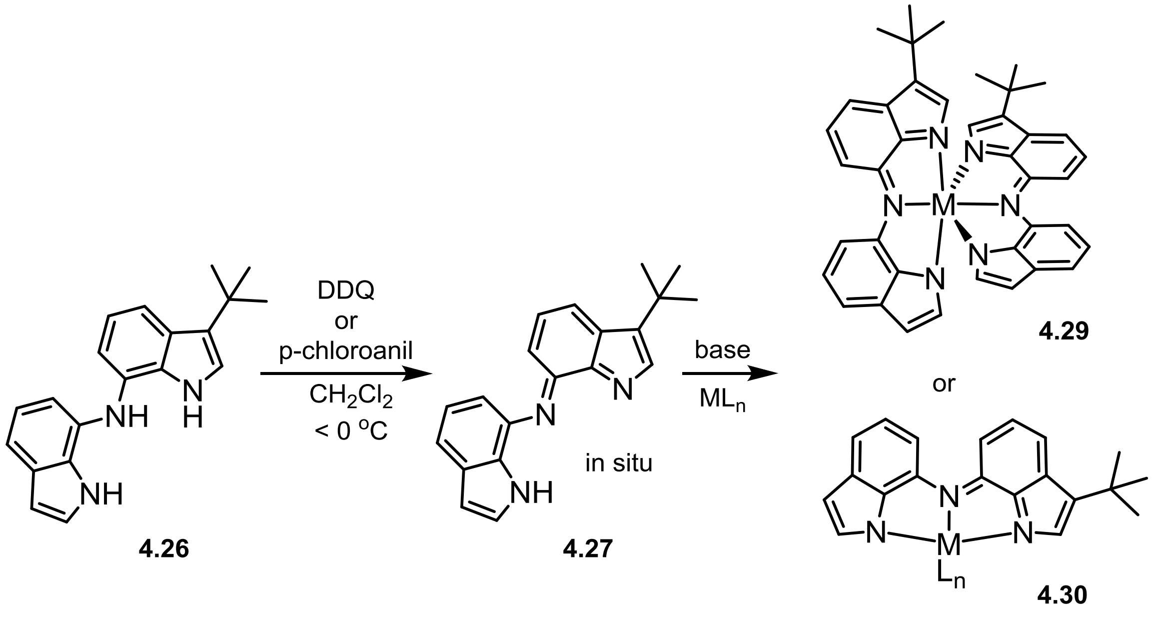

Scheme 4.6 Attempted one-pot oxidation and in-situ metal complexation of aminodiindole **4.26**.

Attempts were made using either DDQ or 2,3,5,6-tetrachloro-1,4-benzoquinone (*p*-chloranil) as the oxidant. The trapping metal reagent was either $ZnBr_2$ or $Zn(OAc)_2$, and *N,N*-diisopropylethylamine was used as the base during the complexation step. Following addition of a solution of the diindole **4.26** to the oxidant at -40 °C in dichloromethane, the solution became dark blue over a matter of minutes (DDQ) to hours (*p*-chloranil). Analysis of the oxidations by TLC indicated the formation of what appeared to be one major product in the case of DDQ (although the TLC was not conclusive as the product spot streaked on the plate), and three products in the case of *p*-chloranil. In the case of p-chloranil, more than one equivalent of oxidizing agent was needed to achieve complete consumption of starting diindole **4.26**. The variation in the two oxidation reactions is almost certainly a result of the difference in the reagent's oxidizing potentials. Indeed, cyclic voltammograms of *p*-chloranil in dichloromethane (Appendix Figure A.28) revealed that based on reduction potential alone (-0.429 and -1.173 V vs Fc/Fc^+), the oxidation should not occur, but it is presumably enabled by intermolecular interactions within the reaction mixture.[ref?]

After approximately three hours at -40 °C, the base and zinc complex were added to the oxidation reactions, and after aging several hours, the reactions were allowed to warm to room temperature without the removal of the cold bath. Unfortunately, the reactions showed no sign of metal complexation, and ^1H NMR spectra of the isolated product spots were generally broad and reminiscent of the oligomerization products. Efforts at precipitating and isolating the products of the oxidation steps were likewise unsuccessful.

Preliminary investigation into the metal complexation of the diindole moieties followed by oxidation was carried out on the unsubstituted 7,7′-diindole **4.21a**. Because the air oxidation of the unsubstituted indole was much more rapid than the *tert*-butyl derivative **4.26**, the chances of the complexed ligand oxidizing in air seemed more favorable. Additionally, characterization of the unsubstituted diindole **4.21a** had been limited by its reactivity, and isolation of a metal complex, even without oxidation to the azaDIME, would provide useful corroborating characterization data. However, the facile oxidation of **4.21a** necessitated metal complexation of the crude compound, preferably as a one-pot sequence with the Buchwald-Hartwig amination forming the ligand. Therefore, 0.5 equivalents of $Zn(CH_3OO)_2$ were added to a completed amination reaction, refluxed for several hours, and then exposed to air. The resulting solution yielded black precipitate, but no products that could be assigned to metal complexation. In a second iteration, the solution phase of the amination reaction was cannula transferred to a clean flask and solvent-switched to acetonitrile. The solution was treated with sodium hydride and then $Ni(Pyr)_4BF_4$. After heating for 30 minutes, analysis by TLC showed consumption of the diindole **4.21a**, but despite collection of a dark precipitate, no metal complexes could be identified.

4.2.8 Path Forward

Future work on the azaDIMEs should take two directions: 1) continued examination of combined oxidation/complexation methodologies, and 2) further substitution of the indole framework to block sites that may be active in oligomerization.

Low temperature oxidation and complexation appears promising from an oxidation perspective – the TLC data combined with the absence of a precipitate at low temperature seems to indicate that oligomerization may not occur at these temperatures. Identifying the right combination of metal and ancillary ligand to afford the desired metal complexes is the main challenge. One metal-ligand combination with potential is $PtCl_2(COD)$, which did show multiple products by TLC when it was reacted with what was later assigned as oligomer (Section 4.1.5). A useful proof of concept could be obtained through formation of the BF_2 complexes (Figure 4.11). It is probable that the *tert*-butyl diindole **4.26** will act as a bidentate ligand in such a complex, which is acceptable for the purposes of verifying the feasibility of this route. Alternative candidates for boron complexation using this method are the 6,6′- or 2,2′-diindole systems. The unsubstituted 6,6′-diindole **4.20a** was more easily isolated and appears less susceptible to air oxidation than the 7,7′-diindole **4.21a**, and both of these systems would be amenable to the tetrahedral geometry preferred by boron complexes.

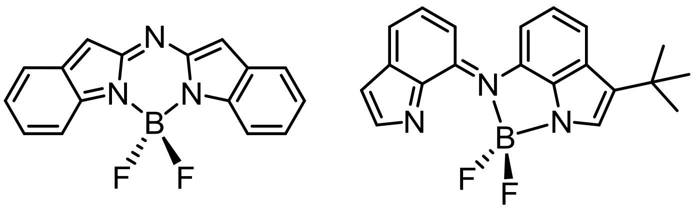

4.31 **4.32**

Figure 4.11 Proposed Boron complexes of azaDIMEs.

Formation of a diindole metal complex followed by oxidation is also worth pursuing, but poses greater obstacles to success. Work in this area should focus on the *tert*-butyl diindole **4.26**, as it can reliably be isolated and purified, providing a clean starting material for complexation reactions. Again, the combination of metal and ancillary ligand will be important with weakly bound ligands such as NO_3 increasing the chance of success. Selecting the oxidation state of the metal and the reaction stoichiometry to produce diamagnetic metal complexes will also be a significant benefit in evaluating the success of these reactions.

Stabilization of the diindole compounds towards oxidative oligomerization will require further substitution of the indole precursors at activated positions, namely the 3 and 5 positions. Tert-butyl groups are the preferred substituents for this purpose since alkylation of 7-bromoindole produced the desired 3-tert-butyl compound and the tert-butyl diindole showed improved stability to air oxidation and oligomerization. Because one of the byproducts of the alkylation of 7-bromoindole with 2-chloro-2-methylpropane was a dialkylated product tentatively assigned to alkylation at the 3 and 5 positions, it may possible, by increasing the reaction temperature and molar ratio of alkylating agent, to optimize the alkylation for formation of the 7-bromo-3,5-di-*tert*-butylindole. Alkylation of the 7-aminoindole at the 3-position will probably be possible using the conditions developed for the 7-bromoindole, but alkylation at the 5-position is less likely because aniline is strongly deactivating under Friedel-Crafts conditions. In order to produce the desired dialkylated substitution pattern, it may be necessary to install the desired substitution on the aryl ring prior to forming the indole.

4.3 AzaDicarbazolyls: Analogues of AzaDIMEs

The difficulties encountered in the synthesis of the azaDIME scaffold, namely the susceptibility of the amino-diindolyl compounds to oxidative oligomerization, necessitated a reexamination of the ligand design. As discussed above, one potential modification kept the indole moieties intact and added blocking substituents at the most reactive sites on the rings. A second strategy was to exchange the indoles for less reactive heterocycles. Carbazoles were identified as a viable replacement.

In addition to being relatively stable heterocycles, carbazoles were selected because oxidation of the coupled carbazole compound would lead to a delocalized π system analogous to the azaDIME ligand. The specific proposed dicarbazolyl ligand was anticipated to be a tridentate pincer ligand with a bite angle similar to the 7,7′-azaDIME **4.7**. Additionally, literature precedence for *tert*-butylated carbazoles was well-developed,[ref] which was advantageous since we desired to introduce solubilizing groups on an otherwise planar ligand.

4.3.1 Synthetic Plan

The synthesis of aza-dicarbazolyl ligand **4.39** was envisioned as a convergent synthesis, outlined in Scheme 4.7. In this synthesis, ligand **4.39** was imagined as resulting from a two electron, two proton oxidation of amino-dicarbazole compound **4.38**. The amino-dicarbazole would be accessed by a copper or palladium-catalyzed cross-coupling reaction between a 1-bromocarbazole (**4.35**) and a 1-aminocarbazole (**4.37**). 1-aminocarbazole **4.35** would be be made by reduction of 1-nitrocarbazole **4.36**. The 1-bromocarbazole **4.35** and 1-nitrocarbazole **4.36** would, respectively, be prepared by bromination and nitration of a common intermediate, 3,6-di-*tert*-butylcarbazole **4.34**. This intermediate would, in turn, be formed by Friedel-Crafts alkylation of a commercially available carbazole (**4.33**).

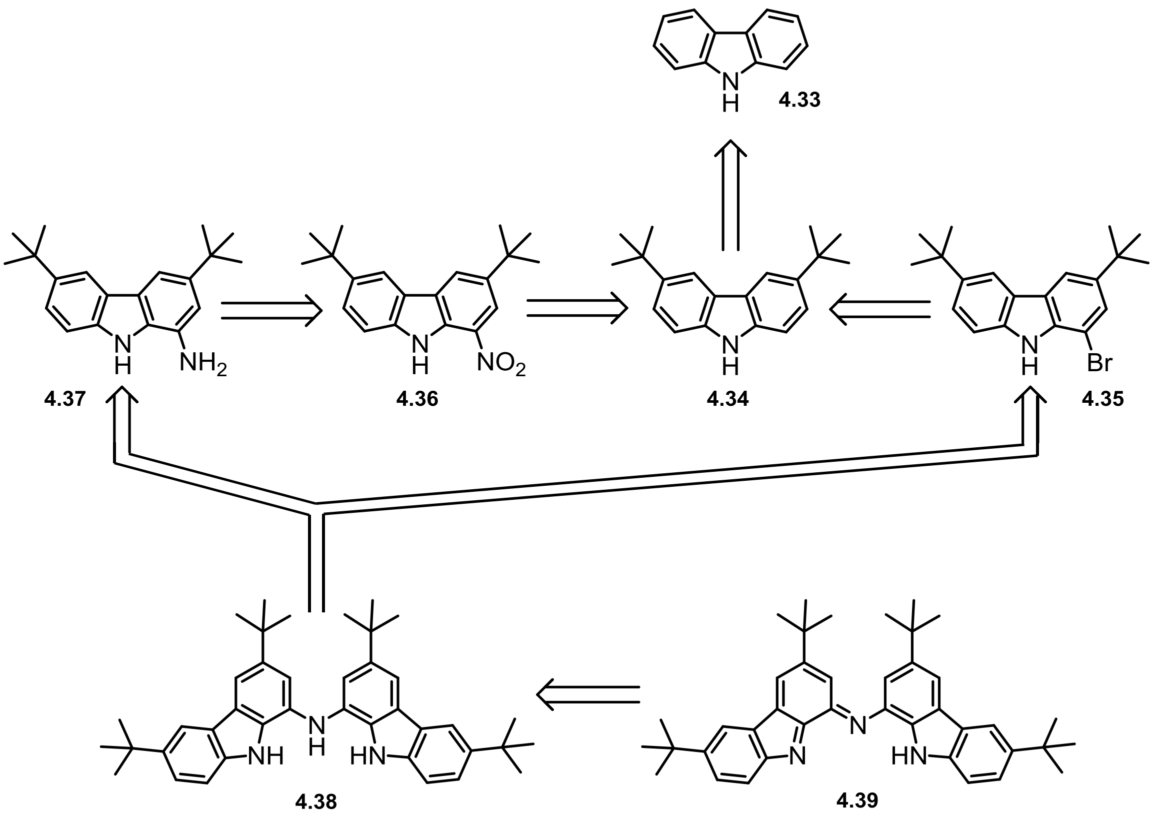

Scheme 4.7 Retrosynthetic plan for the synthesis of aza-dicarbazolyl ligand **4.39**.

4.3.2 Preparation of 3,6-Di-*tert*-butylcarbazole (4.34) and 1-Bromo-3,6-di-*tert*-butylcarbazole (4.35)

The di-*tert*-butyl carbazole **4.34** was prepared using a modified literature procedure.[180] Treatment of carbazole **4.33** with aluminum trichloride followed by dropwise addition of 2-chloro-2-methylpropane at 0 °C and an overnight age at room temperature afforded the Friedel-Crafts alkylation product **4.34**. Aqueous workup of the reaction and purification of the product by slurrying in refluxing hexanes provided the desired product as white solid in 42% yield (Scheme 4.8).

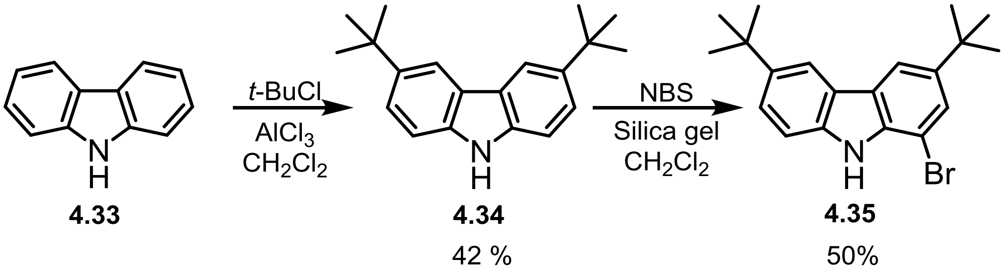

Scheme 4.8 Synthetic conditions and isolated yields for the Friedel-Crafts alkylation of carbazole **4.33** and the mono-bromination of di-*tert*-butyl carbazole **4.34**.

Mono-bromination of carbazole **4.34** was effected with N-bromosuccinimide using a modified literature procedure.[181] Reaction of NBS and carbazole **4.34** in the presence of silica gel and the absence of light produced the monobrominated carbazole **4.35** as a colorless foam in 50% yield after purification by column chromatography. The compound was relatively stable in air at room temperature, but after several months, an impurity was observed by TLC. The unidentified impurity was easily removed by column chromatography using silica gel and 100% hexanes followed by a 3:7 ratio of ethyl acetate/hexanes as the eluent.

4.3.3 Synthesis of 1-Nitro-3,6-di-*tert*-butylcarbazole (4.36)

The 1-nitrocarbazole **4.36** was initially prepared using 0.50 equivalents of cupric nitrate trihydrate at 60 °C in an acetic acid/acetic anhydride mixture, conditions influenced by nitration reactions of related carbazoles.[182] This provided the desired product in moderate yield (58%) after a challenging chromatographic purification (Scheme 4.9). The purification was complicated by the presence of several reaction by-products, two of which were present in reasonably high quantities. One of the major by-products was identified as the

1,8-dinitro-3,6-di-*tert*-butylcarbazole **4.41** after comparison of NMR data to literature values.[183] Identification of the second major byproduct (>25% by NMR) was more difficult and required a combination of ^{1}H, ^{13}C, and COSY NMR, HRMS, and x-ray crystallography (Figure 4.12) to confirm the assignment of the compound as the 3-nitro-6-t*ert*-butylcarbazole (**4.40**).

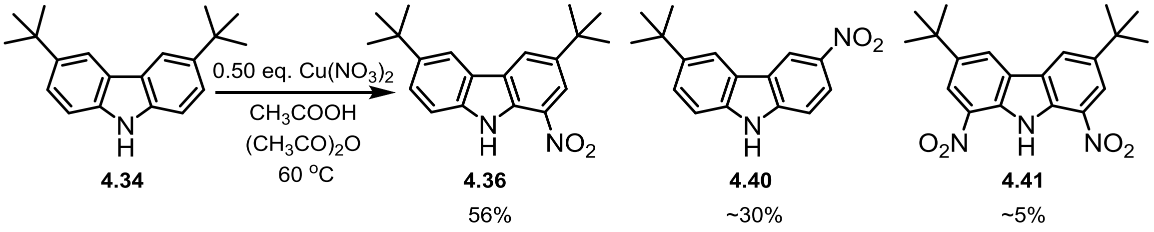

Scheme 4.9 Initial reaction conditions and major products obtained for the nitration of of 3,6-di-*tert*-butylcarbazole **4.34**.

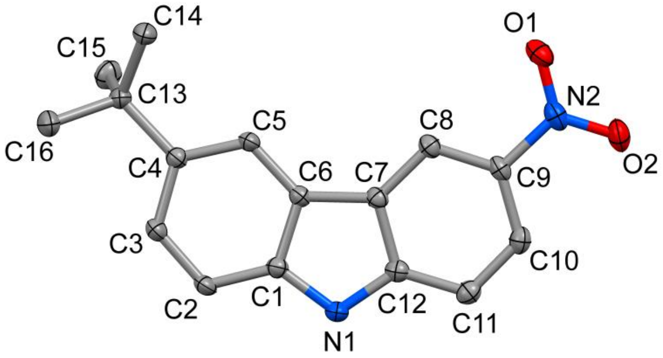

Figure 4.12 X-ray crystal structure of 3-nitro-6-*tert*-butylcarbazole **4.40**. Ellipsoids are represented at 50% probability. Hydrogens have been removed for clarity.

For the reaction to be feasible on larger scale, modification of both the reaction conditions and purification methods was necessary. Table 4.2 summarizes the reaction optimization. Lowering the temperature of the reaction from 60 °C to 25 °C resulted in formation of large amounts of dinitrocarbazole **4.41** when an excess of cupric nitrate was present (entry 2). The dinitrocarbazole was still evident at 25 °C even after decreasing the excess of cupric nitrate to 0.04 equivalents (entry 3). Further reducing the temperature of the reaction to 10–15 °C eliminated formation of the dinitrocarbazole. The temperature dependence of the dinitration was corroborated by resubmission of the 1-nitrocarbazole to the reaction conditions, which showed no formation of the dinitrocarbazole.

Table 4.2 Optimization of the reaction conditions for the formation of 1-nitro-3,6-di-*tert*-butylcarbazole **4.36**.

Entry	Reaction Conditions		Approximate %yield determined by NMR		
	Equiv. $Cu(NO_3)_2{\cdot}3H_2O$	Temp (°C)	**4.36** (% desired)	**4.40** (% 3-nitro)	**4.41** (% dinitro)
1	0.50	60	(56)[a]	30	5
2	1.0	25	35	7	52
3	0.52	25	60	35	3
4	0.52	12–20	68	30	0[b]
5	0.55	10–15	70 (58)[a]	28 (18)[a]	0 (0)[a]

[a] Isolated yield. [b] Trace dinitro compound observed by TLC

Surprisingly, the 3-nitrocarbazole **4.40** was present in considerable amounts in all of the conditions surveyed. Formation of this by-product may occur by one of two possible pathways. In one scenario, dealkylation occurs first, involving one of the *tert*-butyl groups on the 3,6-di-*tert*-butylcarbazole, which is then followed by nitration at the newly vacated reactive site. Alternatively, *ipso* nitration could occur, with subsequent rearomatization of the carbazole via loss of the *tert*-butyl group. However, the dealkylation pathway does not have literature precedence under the mild conditions used in the nitration. De-*tert*-butylation of aromatic rings typically requires either reflux of the substrates with superacids such as Nafion-H in high boiling point solvents[184] or reaction with lewis acid catalysts in refluxing benzene or toluene.[185, 186] In both cases the reaction is generally part of a transalkylation sequence in which a second aromatic molecule is alkylated with the removed *tert*-butyl group. *Ipso* nitration, on the other hand, has been shown to occur at low temperatures in acetic acid or acetic anhydride,[187, 188] often with fuming nitric acid as the nitrate source.[189, 190] *Ipso* nitration has been used to replace aromatic tert-butyl groups in calixarene synthesis,[191-193] but in systems to analogous to carbazole (particularly anisoles and phenols), the structure of the isolated product is often complicated by rearrangement of cyclohexadienone adduct, and therefore is not the direct alkyl substitution product.[194]

Identification of reaction conditions that avoid the formation of 3-nitrocarbazole **4.40** may be possible. UV-active intermediates are visible during TLC monitoring of the reaction's progress, suggesting that the intermediates could potentially be isolated and characterized, leading to confirmation of the synthetic pathway involved. In the case of *ipso* nitration, a change in solvent system away from acetic acid/acetic anhydride may be beneficial, while a move to even milder conditions may be necessary in the case of de-*tert*-butylation.

Nevertheless, compared to the original conditions, the currently optimized conditions allow for a much easier and more scalable purification by column chromatography, since the dinitrocarbazole and several small, unidentified impurities are no longer present in the crude reaction mixture. The optimized reaction affords isolated yields of 58% for the desired 1-nitrocarbazole **4.36** and 18% for the 3-nitro carbazole **4.40** (entry 5 and Scheme 4.10).

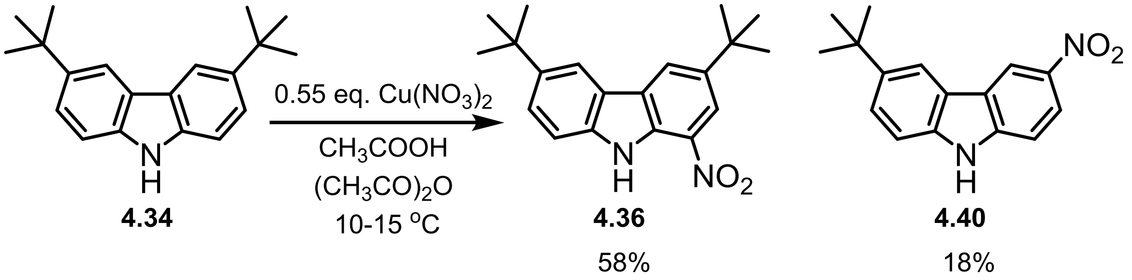

Scheme 4.10 Optimized conditions and isolated yields of products obtained in the nitration of 3,6-di-*tert*-butylcarbazole **4.34**.

4.3.4 Synthesis of 1-Amino-3,6-di-*tert*-butylcarbazole (4.37)

Although reduction of aryl nitro groups to aryl amines is a well-known transformation, the initial attempts using a literature procedure[195] for a related compound were not promising (Scheme 4.11). The reaction generated a multitude of compounds, but none in sufficient amounts to deem them major products. Exhaustive column chromatography eventually provided the desired product in 1% yield. With proof of principle in hand, efforts to improve the reaction began.

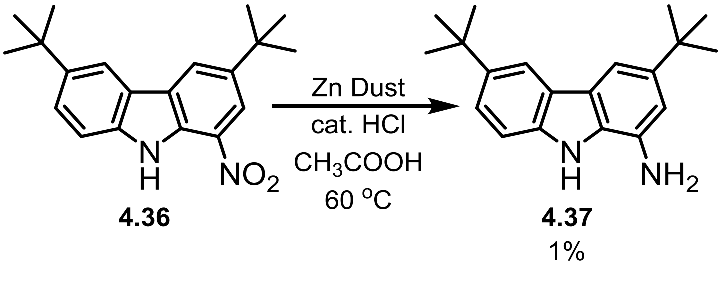

Scheme 4.11 Initial reaction conditions for reduction of 1-nitro-3,6-di-*tert*-butylcarbazole **4.36**.

The solvent was changed from acetic acid to methanol and the amount of concentrated hydrochloric acid was accordingly increased from catalytic to stoichiometric (4.5 molar equivalents). Initially, the temperature was kept at 60 °C. Reaction progress was examined by TLC, which revealed fast initial formation of the desired amine **4.37** followed within twenty minutes by complete stalling of the reaction. Two extra aliquots of hydrochloric acid (2.5 equivalents each) were charged to the reaction, each time resulting in reaction progress followed by a stalling or slowing (after the last addition) of the reaction. Addition of all 9.5 equivalents of hydrochloric acid at the beginning of the reaction resulted in complete formation of the amine within twenty minutes.

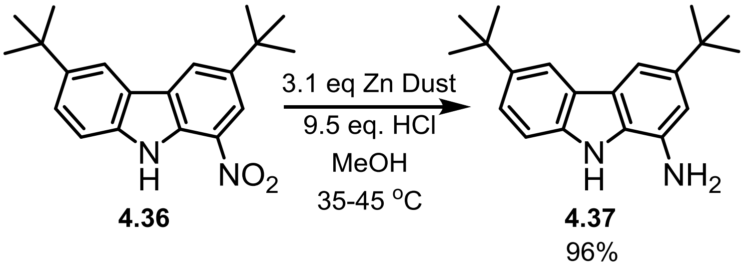

Scheme 4.12 Optimized conditions for the reduction of 1-nitro-3,6-di-*tert*-butylcarbazole **4.36**.

Evaluation of the internal temperature of the reaction showed that the initial exotherm upon hydrochloric acid addition heats the solution to 35 °C and even with application of a 60 °C sandbath, the reaction proceeds to completion before the internal temperature reaches 45 °C. Therefore a higher temperature is unnecessary. By-product formation was not observed under the optimized conditions (3.1 equiv. activated zinc dust and 9.5 equiv. concentrated HCl at 35–45 °C in MeOH). The desired 1-aminocabazole **4.37** was obtained in 96% yield upon aqueous workup of the optimized reaction (Scheme 4.12).

4.3.5 Attempted Synthesis of Amino-dicarbazole (4.38) and Possible Formation of Aza-dicarbazolyl (4.39)

Coupling of the 1-aminocarbazole **4.37** and the 1-bromocarbazole **4.5** was attempted using the Buchwald-Hartwig amination conditions developed for the preparation of the azaDIME precursors, amino-diindole compounds **4.21a** and **4.26**. However, despite consumption of the starting 1-bromocarbazole, the coupled product was not formed. The major product isolated from this reaction was instead the 3,6-di-tertbutylcarbazole **4.34** (Scheme 4.13), most likely the outcome of hydrodehalogenation during the catalytic cycle.

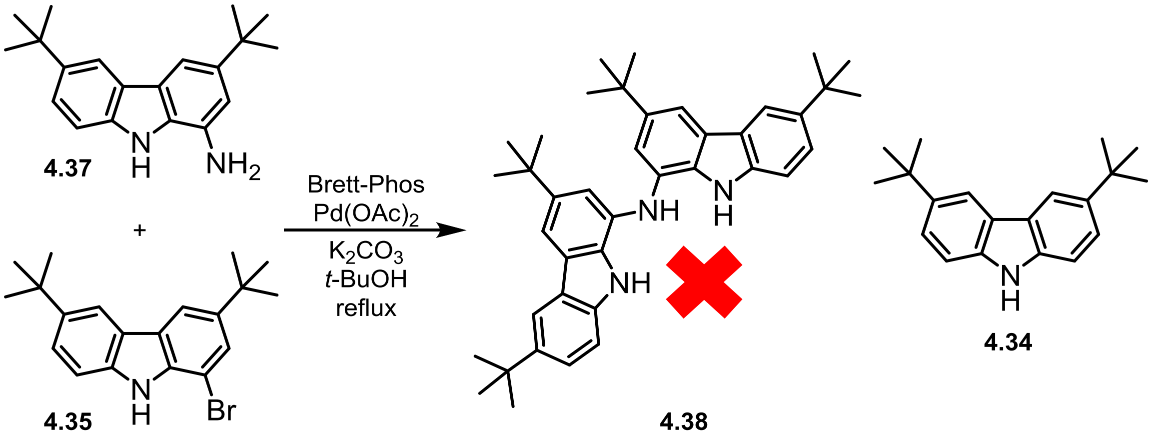

Scheme 4.13 Reaction of carbazoles **4.35** and **4.37** under the Buchwald-Hartwig amination conditions developed for the azaDIMEs leads to hydrodehalogenation product **4.34**.

The presence of 3,6-di-*tert*-butyl carbazole **4.34** instead of amino-dicarbazole **4.38** indicated that hydrodehalogenation was occurring preferentially over the reductive elimination of the coupled product. Two explanations for this are possible. Either deprotonation of the amine to form the palladium-amido complex was slow or nonexistent, or the reductive elimination of the coupled product was slow compared to hydrodehalogenation. If the reductive elimination itself was the limiting step, switching from BrettPhos to an even more sterically hindered ligand would theoretically increase the rate of amino-dicarbazole formation. However, changing the ligand could also lead to unforeseen consequences in selectivity and other reaction outcomes. Fortunately, deprotonation was rate-limiting in this case: changing from potassium carbonate to the more basic cesium carbonate completely eliminated formation of 3,6-di-*tert*-butyl carbazole in the reaction.

Instead, a new product was detected by TLC. The R_f of the product compared to that of the amino and bromocarbazole starting materials was similar to the ratios observed in the formations of the amino-diindole compounds **4.20a**, **4.21a** and **4.26**. An analysis of the crude reaction mixture gave a ^{1}H NMR spectrum that, while not definitive, was consistent with the formation of desired product. (Five major aromatic peaks were present in the aromatic region integrating to approximately 10 protons – three singlets, a doublet of doublets and one multiplet. The position of NH protons was less certain, with only one observed at approximately 8.7 ppm integrating to one hydrogen. However, exchangeable protons such as NH are not reliably visualized by ^{1}H NMR. The tert butyl region was messy and contained residual tert-butanol, so identification of the expected two singlets was not possible.) Nevertheless, the desired amino-dicarbazole was not recovered following attempted purification by column chromatography. A time-dependent change in the color of the TLC spot of the purported amino-dicarbazole compound was also noticed. After the TLC plate was removed from eluent and allowed to dry, the product spot underwent a gradual change from colorless (UV-active) to reddish-purple. This is analogous to the TLC behavior of the amino-diindole compounds, and together with the loss of product during chromatography, implies that air oxidation of the amino-dicarbazole compounds was occurring (Scheme 4.14).

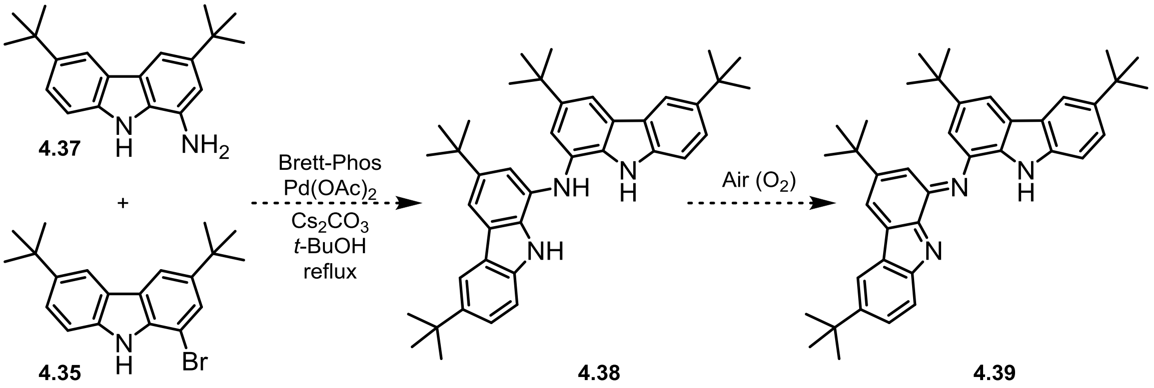

Scheme 4.14 Provisional reaction conditions and tentative assignment of the products observed in the Buchwald-Hartwig amination reaction of 1-bromocarbazole **4.35** and 1-aminocarbazole **4.37**.

Further scrutiny of the coupling reaction indicated that the reaction does not go to completion, and introduction of a second aliquot of base or other reactants yields inconsistent results, sometimes leading to disappearance of the presumed amino-dicarbazole, possibly because of an introduction of air to the reaction vessel during the addition. One possible cause for the incomplete reaction is inactivation of the catalyst through coordination of the coupled product (either oxidized or unoxidized) with palladium. While this was a concern that ultimately did not materialize in the azaDIMEs system, even subtle changes in the binding pocket upon moving to the carbazole scaffold could enable formation of a stable palladium-carbazole complex.

To date, the most promising outcomes have been achieved by concentrating down the incomplete reaction (obtained without addition of extra reagents) and submitting the resulting blackish solid to column chromatography using neutral aluminum oxide and 3:1 dichloromethane/hexanes followed by 3:1: 0.1 dichloromethane/hexanes/acetone. This afforded two products: a colorless oil that appeared to be the amino-dicarbazole **4.38** by ^{1}H NMR spectroscopy, but decomposed upon further purification, and a viscous purple oil that, although contaminated with a plasticizer from the tygon tubing used on the Schlenck manifold, had a ^{1}H NMR spectrum that was reasonable for the oxidized product, azadicarbazolyl **4.39**.

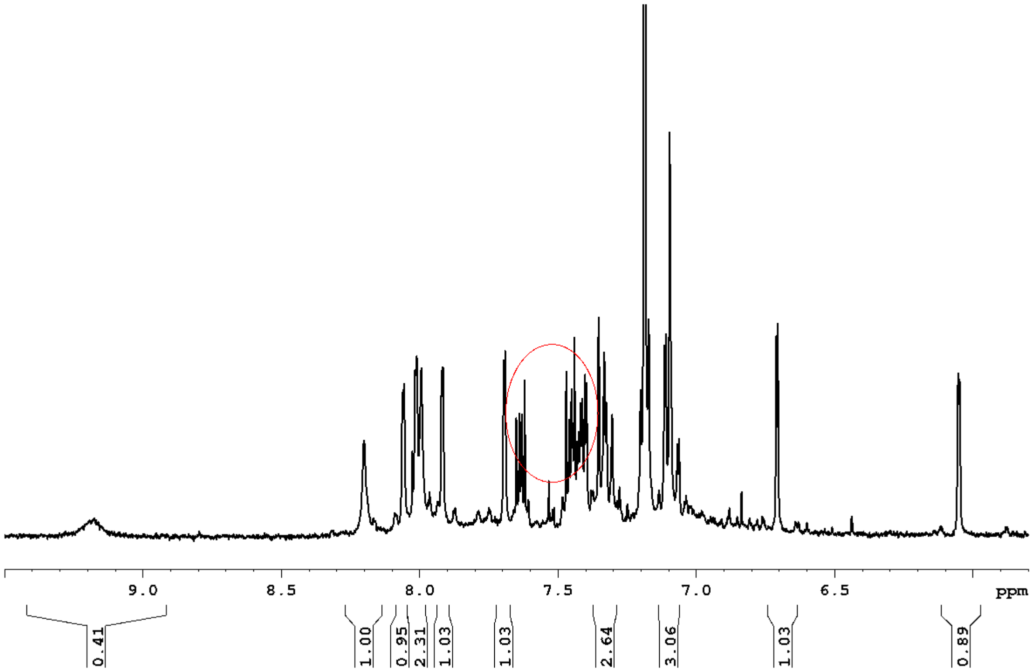

Figure 4.13 Aromatic region of the ^{1}H NMR spectrum (300 MHz, CDCl3) of purported azadicarbazolyl **4.39**. The peaks circled in red are plasticizer from tygon tubing.

Upon acid-base extraction (an unsuccessful attempt to separate the plasticizer), a reversible color change from purple to blue and back to purple was observed, confirming the existence basic sites in the compound. The purple color signifies shorter wavelength absorptions than expected for the conjugated, planar azaDIME and aza-dicarbazolyl scaffolds, but it is still consistent with the *tert*-butyl aza-dicarbazolyl structure. Molecular models of the compound demonstrate steric interactions between the central *tert*-butyl groups, which could cause distortions in the planarity of the compound and lead to the noted higher energy absorptions.

4.3.6 Path Forward.

Future work on this project should focus on better synthetic methods for the preparation and isolation of amino-dicarbazole **4.38** and aza-dicarbazolyl **4.39**. Increasing the yield of either compound will be contingent on reproducible reactions that go to completion. Adding an amine protecting group to the bromocarbazole prior to Buchwald-Hartwig amination is an appealing prospect in this respect. In the azaDIMEs system, the coupling reaction with protected bromides yielded the aminodiindole products, and with a protecting group in place, irreversible complexation of the dicarbazole to the metal is less likely since the tridentate binding mode is disrupted. Air oxidation of the protected amino-dicarbazole may also be less likely as the overall scaffold would be less electron rich, which could in turn provide an easier isolation.

4.4 Conclusions

Buchwald-Hartwig amination conditions have been identified for coupling of bromo indoles and amino indoles. The conditions are selective for reaction of the aryl bromide and anilino groups in the presence of the unprotected indole N–H moiety and appear to be amenable to coupling reactions using N–protected indoles as well. The facile and problematic oxidation of the aminodiindole products has been investigated, and the resulting insoluble precipitates have been attributed to oxidation induced oligomerization based on evidence from ^{1}H NMR spectroscopy, UV-visible absorption spectroscopy, and cyclic voltammetry. Introduction of a tert-butyl group at the C3 position of the bromoindole was proven to be synthetically viable, allowing isolation and characterization of the less easily oligomerized 7, 7′-Amino-3-*tert*-butyl diindole **4.26**. Investigations into one-pot oxidation and complexation reactions using **4.26** revealed that further substitution of the indole rings may be necessary to avoid oligomerization under these reaction conditions and afford the desired azaDIME ligands and their metal complexes.

The synthesis of azaDicarbazolyl analogs of azaDIMEs has been initiated. A scalable synthesis of the aminocarbazole **4.37** has been developed, and bromocarbazole **4.36** has been prepared. The BHA reaction has been optimized for the carbazole scaffold to eliminate formation of the hydrodehalogenation product. The reaction appears to produce the desired amino-dicarbazole compound **4.38**, which undergoes rapid decomposition (possibly oxidation to the azadicarbazolyl **4.39**) under atmospheric conditions. However, further examination is necessary for unequivocal identification of the desired amino-dicarbazole and azadicarbazolyl compounds.

4.5 Experimental Details

4.5.1 General Synthetic Methods

The reagents used were commercially available. Commercially available reagents were used as received with the exception of *tert*-butanol which was dried and stored over 4Å molecular sieves, and zinc dust which was activated by treatment with 1M HCl prior to use.[196] Reactions under inert atmosphere were performed using a Schlenck manifold, equipment, and techniques unless otherwise indicated. Concentration of liquids was accomplished by rotary evaporation unless stated otherwise.

^{1}H NMR and ^{13}C NMR were recorded at ambient temperature at a frequency of 500, 360 or 300, and 125, 90 or 75 MHz, respectively, unless otherwise noted. The data are reported as follows: proton multiplicities (s = singlet, d = doublet, t = triplet, q = quartet, m = multiplet, br = broad, app = apparent), coupling constants, and integration. Microanalyses were performed by Canadian Microanalytical Services Ltd., Vancouver, BC. Mass spectrometry was performed by the UBC Mass Spectrometry Center. Melting points are reported uncorrected. Flash chromatography was performed using the indicated solvent system on Caledon Laboratories silica gel (SiO_2) 60 (70–230 mesh) or Alfa Aesar neutral activated aluminium oxide (Al_2O_3), Brockman Grade 1, 58Å (60 mesh). Infrared spectra were recorded using a Perkin-Elmer Spectrum One instrument. Cyclic voltammetry experiments were performed with a Bioanalytical Systems CV50 voltammetric analyzer. CV experiments were performed using a three-electrode setup consisting of a glassy carbon working electrode, platinum electrode, and silver quasi-reference electrode. Ferrocene was used as an internal reference. Electrolyte (tetrabutylammonium hexafluorophosphate) was obtained from a commercial supplier and used as received. Ground state absorption spectra were obtained using an Agilent 8453 UV-visible spectrophotometer.

4.5.2 Synthesis

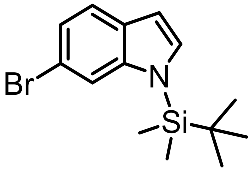

6-Bromo-1-*tert*-butyldimethylsilyl indole (**4.15b**) Tetrahydrofuran (6 mL) and 6-bromoindole (250 mg, 1.3 mmol) were added to a round bottom flask under ambient conditions. NaH (60% in mineral oil, 60 mg, 1.5 mmol) was added in portions, resulting in a clear, reddish-orange mixture which was aged for ten minutes. *Tert*-butyldimethylsilyl chloride (211 mg, 1.4 mmol) was added and the reaction immediately became cloudy and yellow. After fifteen minutes, the reaction was quenched with water followed by ethyl acetate. The mixture was transferred to a separatory funnel and the organic layer was washed twice with water. The organic layer was dried over anhydrous sodium sulfate, decanted, and concentrated to a faintly brown oil. Column chromatography using silica gel (0.5 in. × 8 in.) and 1:4 ethyl acetate/hexanes afforded the desired compound as a white solid (220 mg, 55%). ^{1}H NMR (300 MHz, $CDCl_3$) δ 7.63 (s, 1H), 7.47 (d, *J* = 8.3 Hz, 1H), 7.21 (dd, *J* = 8.4, 1.7 Hz, 1H), 7.15 (d, *J* = 3.2 Hz, 1H), 6.58 (dd, *J* = 3.2, 0.8 Hz, 1H), 0.93 (s, 9H), 0.60 (s, 6H); ^{13}C NMR (90 MHz, $CDCl_3$) δ 141.9, 131.6, 130.2, 123.0, 121.7, 116.6, 115.0, 104.8, 26.2, 19.4; -4.0; IR (solid-ATR) 2927, 2855, 1147, 803, 789 cm-1; HRMS (ESI-TOF) *m*/*z*: $[M+H]^+$ calcd for $C_{14}H_{21}BrNSi$ 310.0627;

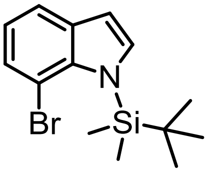

7-Bromo-1-*tert*-butyldimethylsilyl indole (**4.16b**) Tetrahydrofuran (5 mL) and 7-bromoindole (250 mg, 1.3 mmol) were added to a round bottom flask under N_2. The homogeneous solution was cooled to 0 C in an ice/water bath and NaH (60% in mineral oil, 62 mg, 1.6 mmol) was added in portions. The reaction was aged for ten minutes and then *tert*-butyldimethylsilyl chloride (211 mg, 1.4 mmol) was added and the ice bath was removed. After four hours only trace product was observed by TLC. The raction was heated to reflux and aged overnight. The reaction was cooled to room temperature before water was added, followed by dichloromethane. The organic layer was washed twice with water, dried over anhydrous sodium sulfate, decanted, and concentrated to a reddish oil. Column chromatography using silica gel (0.5 in. × 8 in.) and 1:4 ethyl acetate/hexanes gave the desired compound as a pale yellow oil. ^{1}H NMR (300 MHz, $CDCl_3$) δ 7.55 (dd, *J* = 7.8, 1.2 Hz, 1H), 7.39–7.37 (m, 2H), 6.95 (t, *J* = 7.7 Hz, 1H), 6.63 (d, *J* = 3.4 Hz, 1H), 0.98 (s, 9H), 0.72 (s, 6H).

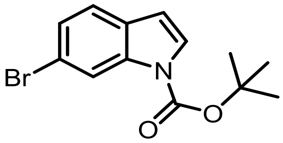

6-Bromo-1-*tert*-butyloxy indole (**4.15c**) Acetonitrile (10 mL) and 6-bromoindole (250 mg, 1.28 mmol) were added to a round bottom flask and stirred until a homogeneous solution was obtained. Boc anhydride (306 mg, 1.40 mmol) and potassium carbonate (360 mg, 2.61 mmol) were added and the reaction was aged for 24 hours. The reaction was diluted with ethyl acetate and water. The organic layer was collected, extracted with water, dried over anhydrous sodium sulfate, filtered, and concentrated to an oil. A pale pink viscous oil (308 mg, 80%) was isolated following column chromatography using silica gel and 1:4 ethyl acetate/hexanes. The oil solidifies upon standing. ^{1}H NMR (300 MHz, $CDCl_3$) δ 8.36 (s, 1H), 7.55 (d, *J* = 3.7 Hz, 1H), 7.41 (d, *J* = 8.5 Hz, 1H), 7.34 (dd, *J* = 8.3, 1.8 Hz, 1H), 6.53 (dd, *J* = 3.7, 0.7 Hz, 1H), 1.68 (s, 9H); ^{13}C NMR (90 MHz, $CDCl_3$) δ 149.3, 135.9, 129.3, 126.3, 125.9, 121.9, 118.4, 117.9, 107.0, 84.2, 28.1; IR (solid-ATR) 3003, 2975, 1748, 1728, 1346, 1158, 804 cm^{-1}; HRMS (ESI-TOF) *m/z*: $[M+H]^+$ calcd for $C_{13}H_{15}BrNO_2$ 296.0286; found 296.0293.

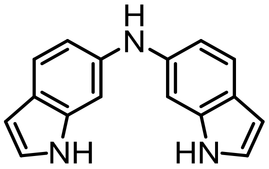

Di(1*H*-indol-6-yl)amine (**4.20a**) Brett-Phos (8 mg, 0.015 mmol), $Pd(OAc)_2$ (1.5 mg, 0.007 mmol) and *tert*-butanol (≈ 1.5 mL)were added to a Schlenk flask. The flask was sealed with a rubber septum and evacuated and back-filled with N_2 four times. The flask was placed in an approximately 110 °C sand bath for three minutes until the reaction became dark brown and homogeneous. The flask was removed from the sand bath and 6-bromoindole (13 mg, 0.065 mmol), 6-aminoindole (10 mg, 0.075 mmol), and potassium carbonate (20 mg, 0.145 mmol) were added under a steady N_2 stream. The flask was carefully evacuated and back-filled with N_2 three times. The side-arm tap was closed and the septum and tap were parafilmed in place. The reaction was placed in the 110 sand bath °C and aged overnight. The reaction was removed from the sand bath, diluted with ethyl acetate, filtered, and concentrated using rotary evaporation. Column chromatography using silica gel (0.25 in. × 7 in.) and 1:4 ethyl acetate/hexanes followed by 100% ethyl acetate afforded the desired compound as a viscous grey oil. Because the isolated compound decomposed rapidly, the compound was not fully characterized. ^{1}H NMR (300 MHz, $CDCl_3$) δ

7.93 (s, br, 2H), 7.52 (d, *J* = 8.4 Hz, 2 H), 7.13 (d, *J* = 0.8 Hz, 2H), 7.09 (dd, *J* = 2.8, 2.4 Hz, 2H), 6.90 (dd, *J* = 8.4, 1.9 Hz, 2H), 6.48 (m, 2H), 5.68 (s, br, 1H).

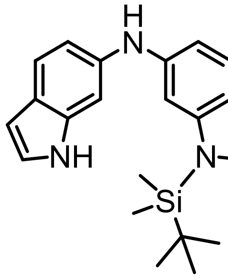

1*H*-indol-*N*-(1*H*-indol-6-yl)-6-amine (**4.20b**) X-Phos (12 mg, 0.03 mmol), Pd(OAc)$_2$ (2.0 mg, 0.01 mmol) and *tert*-butanol (≈ 3 mL)were added to a Schlenk flask. The flask was sealed with a rubber septum, evacuated and back-filled with N$_2$ four times. The flask was placed in an approximately 110 °C sand bath for three minutes until the reaction became yellow and homogeneous. The flask was removed from the sand bath and 6-bromo-1-*tert*-butyldimethylsilyl indole **4.15b** (40 mg, 0.13 mmol), 6-aminoindole (20 mg, 0.15 mmol), and potassium carbonate (40 mg, 0.29 mmol) were added under a steady N$_2$ stream. The flask was carefully evacuated and back-filled with N$_2$ three times. The side-arm tap was closed and the septum and tap were parafilmed in place. The reaction was placed in the 110 sand bath °C and aged for 60 hours. The reaction was removed from the sand bath, diluted with ethyl acetate and water. The layers were separated and the organic layer was concentrated using rotary evaporation. Column chromatography using silica gel (1 in. × 4 in.) and 1:4 ethyl acetate/hexanes gave the desired compound as a vanishingly small amount of oil. Because the isolated compound decomposed rapidly, the compound was not fully characterized. ^{1}H NMR (300 MHz, CDCl$_3$) δ 7.89 (s, br, 1H), 7.51 (d, *J* = 8.3 Hz, 1 H), 7.50 (d, *J* = 8.4 Hz, 1 H), 7.30 (d, *J* = 1.0 Hz, 1H), 7.08–7.05 (m, 3H), 6.89 (app dt, *J* = 8.3, 2.0 Hz, 2H), 6.55 (dd, *J* = 3.2, 0.8 Hz, 1H), 6.49–6.46 (m, 1H), 5.68 (s, br, 1H), 0.92 (s, 9H), 0.53 (s, 6H).

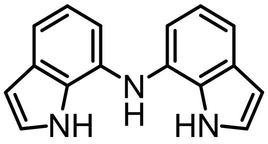

Di(1*H*-indol-7-yl)amine (**4.21a**) Brett-Phos (8 mg, 0.015 mmol), Pd(OAc)$_2$ (1.5 mg, 0.007 mmol) and *tert*-butanol (≈ 1.5 mL)were added to a Schlenk flask. The flask was sealed with a rubber septum and evacuated and back-filled with N$_2$ four times. The flask was placed in an approximately 110 °C sand bath for three minutes until the reaction became reddish-brown and homogeneous. The flask was removed from the sand bath and 7-bromoindole (13 mg, 0.065 mmol), 7-aminoindole (10 mg, 0.075 mmol), and potassium carbonate (20 mg, 0.145 mmol) were added under a steady N$_2$ stream. The flask was carefully evacuated and back-filled with N$_2$ three times. The side-arm tap was closed and the septum and tap were parafilmed in place. The reaction was placed in the 110 sand bath °C and aged overnight. The reaction was removed from the sand bath, diluted with ethyl acetate, filtered, and concentrated using rotary evaporation. Column chromatography using silica gel and 1:4:1 ethyl acetate/hexanes/acetone afforded the desired compound as a viscous oil. Because the isolated compound decomposed rapidly, the compound was not fully characterized. ^{1}H NMR (300 MHz, CDCl$_3$) δ 8.06 (s, br, 2H), 7.37 (d, *J* = 7.9 Hz, 2H), 7.08 (app t, *J* = 2.8 Hz, 2H), 7.03 (t, *J* = 7.7 Hz, 2H), 6.74 (dd, *J* = 7.5, 0.6 Hz, 2H), 6.54 (dd, *J* = 3.1, 2.1 Hz, 2H), 5.80 (s, br, 1H).

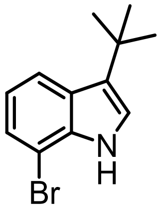

7-Bromo-3-*tert*-butylindole (**4.25**) Dichloromethane (10 mL) and 7-bromoindole (1.00 g, 5.1 mmol) were added to a round bottom flask. The solution was mixed until homogeneous. K-10 montmorillonite clay (2.0 g) was added, the solution was thoroughly mixed and then concentrated to dryness.

The resulting tan solid was transferred to a microwave vial. 2-chloro-2-methylpropane (0.83 mL, 7.7 mmol) was added, and the mixture was thoroughly combined. The reaction was heated in a microwave at 110 °C for 5 minutes, and allowed to cool to room temperature. Dichloromethane was added, the heterogeneous mixture was stirred, filtered, and the filtrate was concentrated to an oil. After purification by column chromatography using silica gel and hexanes, the title compound was obtained as a colorless oil (0.463 g, 36%). ^{1}H NMR (300 MHz, CDCl$_3$) δ 8.06 (br s, 1H), 7.77 (d, *J* = 8.0 Hz, 1H), 7.34 (dd, *J* = 7.6, 0.6 Hz, 1H), 7.02–6.97 (m, 2H), 1.46 (s, 9H); ^{13}C NMR (90 MHz, CDCl$_3$) δ 135.9, 128.2, 127.3, 123.9, 120.6, 120.04, 119.96, 105.1, 31.9, 30.8; IR (liquid-ATR) 3427, 2962, 1691, 778, 737 cm^{-1}; HRMS (ESI-TOF) *m*/*z*: [M - H]$^-$ calcd for C$_{12}$H$_{14}$NBr 250.0231; found 250.0231.

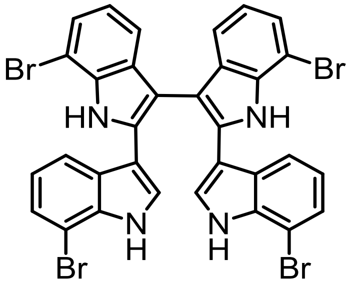

7,7′,7′′,7′′′-Tetrabromo-1H,1′H,1′′H,1′′′H-3,2′:3′,3′′:2′′,3′′′tetraindole (**4.24**) Dichloromethane (3 mL) and 7-bromoindole (100 mg, 0.51 mmol) were added to a round bottom flask. The solution was mixed until homogeneous. K-10 montmorillonite clay (254 mg), and water (0.1 mL) was added, the solution was thoroughly mixed and then concentrated until no dichloromethane remained. The reaction was microwaved on high power for ten min, another 0.1 mL of water was added, and the reaction was microwaved for another five minutes. The reaction was allowed to cool to room temperature. Dichloromethane was added, the heterogeneous mixture was stirred and filtered, and the filtrate was concentrated to dryness. Treatment of the crude product with a mixture of dichloromethane and hexanes removed a colored oil, leaving behind the desired compound as a white solid, (30 mg, 30%). ^{1}H NMR (500 MHz, acetone–*d6*) δ 10.35 (s, 2H), 10.29 (br s, 2H), 7.35 (d, *J* = 7.9 Hz, 2H), 7.32 (d, *J* = 7.6 Hz, 2H), 7.21 (d, *J* = 7.5 Hz, 2H), 7.12–7.11 (m, 4H), 6.92 (t, *J* = 7.8 Hz, 2H), (6.69 (t, *J* = 7.8 Hz, 2H); ^{13}C NMR (125 MHz, acetone–*d6*) δ 136.1, 135.5, 133.7, 132.3, 128.4, 126.4, 124.9, 124.6, 121.43, 121.36, 120.1, 119.6, 110.5, 108.7, 104.9, 104.8; IR (KBr) 3414, 3369, 2921, 1718(br), 1433, 1314, 1205, 777, 742 cm^{-1}; HRMS (ESI-TOF) *m*/*z*: [M - H]$^-$ calcd for $C_{32}H_{17}Br_4N_4$ 772.8187; found 772.8201.

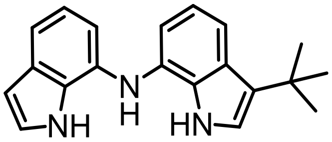

3-(*Tert*-butyl)-*N*-(1*H*-indol-7-yl)-1*H*-indol-7-amine (4.26) Brett-Phos (78 mg, 0.15 mmol), Pd(OAc)$_2$ (16 mg, 0.070 mmol) and *tert*-butanol (≈ 8 mL)were added to a Schlenk flask. The flask was sealed with a rubber septum and evacuated and back-filled with N$_2$ three times. The flask was placed in an approximately 100 °C sand bath for several minutes until the reaction became dark reddish-brown and homogeneous. The flask was removed from the sandbath and 7-bromo-3-*tert*-butylindole **4.25** (160 mg, 0.64 mmol dissolved in approximately 6 mL *tert*-butanol), 7-aminoindole (84 mg, 0.64 mmol), and potassium carbonate (193 mg, 1.4 mmol) were added under a steady N$_2$ stream. The flask was carefully evacuated and back-filled with N$_2$ three times. The side-arm tap was closed and the septum and tap were parafilmed in place. The reaction was placed in the sandbath and the reaction was aged overnight. The reaction was transferred from the Schlenk flask to a round bottom flask using dichloromethane and the reaction was concentrated to a dark oily solid. The mixture was pre-absorbed onto silica gel and purified by column chromatography using 4:1 dichloromethane/hexanes as the eluent. This afforded the desired compound as foam which became a pale gray solid upon treatment with $CDCl_3$ (115 mg, 59%). ^{1}H NMR (360 MHz, $CDCl_3$) δ 9.09 (br s, 1H), 8.80 (br s, 1H), 7.46 (d, *J* = 8.0 Hz, 1H), 7.26 (d, *J* = 7.9 Hz, 1H), 7.22 (app t, *J* = 2.8 Hz, 1H), 6.97–6.90 (m, 3H), 6.66 (d, *J* = 7.2 Hz, 1H), 6.65 (d, *J* = 7.4Hz, 1H), 6.50 (dd, *J* = 2.0, 3.1 Hz, 1H), 6.37 (br s, 1H), 1.45 (s, 9H); ^{13}C NMR (125 MHz, CD_3CN) δ131.1, 130.4, 130.1, 129.7, 128.2, 127.4, 125.3, 121.0, 120.4, 120.0, 115.9, 115.0, 111.3, 111.1, 103.2, 32.2, 31.1; IR (solid-ATR) 3407, 3385, 2959, 1572, 1415, 1340, 722 cm^{-1}; HRMS (ESI-TOF) *m/z*: $[M + H]^+$ calcd for $C_{20}H_{22}N_3$ 304.1814; found 304.1811.

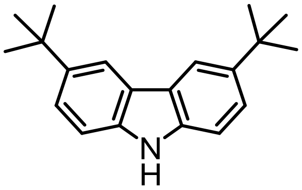

3,6-Di-*tert*-butylcarbazole (**4.34**) was prepared by a modified literature procedure.[180] Carbazole 4.# (30.0 g, 179.4 mmol) was added to dichloromethane (150 mL) in 1L round bottom flask. To the resulting light brown slurry was added aluminum trichloride (23.94 g, 179.4 mmol) and the mixture was then cooled to 0 (± 3) °C. 2-Chloro-2-methylpropane (50.0 mL, 466.8 mmol) was added dropwise to the reaction via addition funnel. The light brown mixture became more homogeneous as the 2-chloro-2-methylpropane addition proceeded. When the addition was completed, the reaction was allowed to warm to room temperature and was aged overnight. The reaction was then diluted with dichloromethane (750 mL) and transferred to a 2L beaker. Hydrochloric acid (1M, 450 mL) was added slowly, with vigorous stirring. After quenching, the green aqueous layer was removed and the red organic layer was washed twice with 1M HCl, three times with brine, and once with water. The resulting yellow organic solution was dried with anhydrous magnesium sulfate and concentrated to a sticky yellow powder. The powder was boiled in refluxing hexanes until the powder appeared white. Upon filtration this yielded a white solid (20.93 g, 42%). The characterization data was consistent with reported literature values.

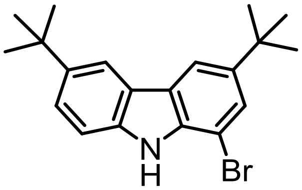

1-Bromo-3,6-di-*tert*-butylcarbazole (**4.35**) was prepared by a modified literature procedure.[181] 3,6-Di-tert-butylcarbazole (4.#) (9.00 g, 32.21 mmol) was added to dichloromethane (360 mL) and silica gel (90 g) in a 3-neck round bottom flask equipped with an mechanical overhead stirrer. A solution of N-bromosuccinimide (5.73 g, 32.21 mmol) in dichloromethane (486 mL) was added dropwise to the foggy, off-white solution. The resulting gray-green reaction was stirred for 21 hours, at which time the now beige reaction was filtered. The filtrate was collected and the filter plug was washed with 3 × 180 mL of dichloromethane. The filtrates were combined, washed with 540 mL of water, dried over anhydrous magnesium sulfate, and concentrated to a viscous beige oil. The oil was purified column chromatography: the oil was preabsorbed on silica gel, and the column was eluted with 10:1 hexanes/ether, affording a clear, faintly tan, viscous oil (5.71 g, 50%). The characterization data was consistent with reported literature values.

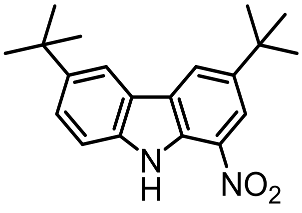

1-Nitro-3,6-di-*tert*-butylcarbazole (**4.36**) 3,6-Di-*tert*-butylcarbazole (4.#) (4.00 g, 14.3 mmol) was added to 240 mL of acetic acid in a round bottom flask. Separately, cupric nitrate trihydrate (1.90 g, 7.9 mmol) was dissolved in a mixture of acetic acid (42 mL) and acetic anhydride (76 mL). The almost clear, colorless carbazole solution was cooled to 15 °C using an ice/water bath. A precipitate forms upon cooling, resulting in a thick slurry. The cupric nitrate solution was added over 20 minutes, keeping the temperature at 10–15 °C. A homogeneous solution was formed and maintained during the addition and the color became dark green. After aging at 10–15 °C for three hours, the reaction was allowed to warm to room temperature and aged overnight. The reaction was then poured into distilled water (600 mL), stirred vigorously for 20 minutes, the filtered, washing with distilled water (4 × 100 mL). The orange solid was dried overnight under vacuum, then added to dichloromethane (130 mL). Most of the solid dissolved, leaving a yellow solid which was removed by filtration. Neutral aluminum oxide was then added to the filtrate and the filtrate was concentrated to dryness. The pre-absorbed compound on aluminum oxide was loaded onto a neutral alumina column. Column chromatography was performed using a gradient system starting with 5:1 hexanes/dichloromethane and ending with 100% dichloromethane. This afforded 2.67 g (58%) of an orange solid. mp 132–134 °C; ^{1}H NMR (300 MHz, $CDCl_3$) δ 9.81 (br s, 1 H), 8.42 (d, *J* = 1.4 Hz, 1H), 8.36 (d, *J* = 1.7 Hz, 1H), 8.10 (d, *J* = 1.8 Hz, 1H), 7.60 (dd, *J* = 8.6, 1.9 Hz, 1H), 7.49 (dd, *J* = 8.3, 0.4 Hz, 1H), 1.49 (s, 9H), 1.46 (s, 9H); ^{13}C NMR (75 MHz, CD_2Cl_2) δ 144.6, 142.9, 138.7, 132.8, 131.9, 127.9, 122.5, 125.9, 125.1, 119.1, 117.1, 111.4, 35.2, 34.1, 32.0, 31.9; IR (solid-ATR) 3440, 2956, 1516, 1279, 623 cm^{-1}; Anal. Calcd for $C_{20}H_{24}N_2O_2$: C, 74.05; H, 7.46; N, 8.63. Found: C, 74.09; H, 7.25; N, 8.69; HRMS (ESI-TOF) *m*/*z*: $[M + H]^+$ calcd for $C_{20}H_{25}N_2O_2$ 325.1916; found 325.1925.

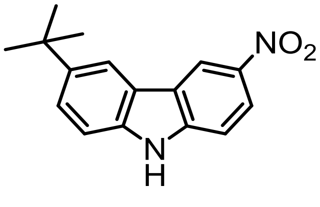

3-Nitro-6-*tert*-butylcarbazole (**4.40**) 3,6-Di-*tert*-butylcarbazole (4.#) (4.00 g, 14.3 mmol) was added to 240 mL of acetic acid in a round bottom flask. Separately, cupric nitrate trihydrate (1.90 g, 7.9 mmol) was dissolved in a mixture of acetic acid (42 mL) and acetic anhydride (76 mL). The almost clear, colorless carbazole solution was cooled to 15 °C using an ice/water bath. A precipitate forms upon cooling, resulting in a thick slurry. The cupric nitrate solution was added over 20 minutes, keeping the temperature at 10–15 °C. A homogeneous solution was formed and maintained during the addition and the color became dark green. After aging at 10–15 °C for three hours, the reaction was allowed to warm to room temperature and aged overnight. The reaction was then poured into distilled water (600 mL), stirred vigorously for 20 minutes, the filtered, washing with distilled water (4 × 100 mL). The orange solid was dried under vacuum overnight, then added to dichloromethane (130 mL). Most of the solid dissolved, leaving a yellow solid which was removed by filtration. Neutral aluminum oxide was then added to the filtrate and the filtrate was concentrated to dryness. The pre-absorbed compound on aluminum oxide was loaded onto a neutral alumina column. Column chromatography was performed using first a gradient system starting with 5:1 hexanes/dichloromethane and ending with 100% dichloromethane, followed by 100% ethyl acetate. This afforded 0.71 g (18%) of a yellow solid. Crystals suitable for X-ray analysis were grown by slow evaporation of dichloromethane. mp 238–241 °C; ^{1}H NMR (360 MHz, $CDCl_3$) δ 9.03 (d, *J* = 2.1 Hz, 1H), 8.41 (br s, 1H), 8.33 (dd, *J* = 8.9, 2.2 Hz, 1H), 8.15 (d, *J* = 1.5 Hz, 1H), 7.60 (dd, *J* = 8.6, 1.8 Hz, 1H), 7.45 (d, *J* = 1.5 Hz, 1H), 7.43 (d, *J* = 1.9 Hz, 1H), 1.46 (s, 9H); ^{13}C NMR (90 MHz, $CDCl_3$) δ 144.6, 143.2, 141.2, 138.7, 125.8, 123.6, 123.1, 121.7, 117.3, 117.2, 111.0, 110.3, 35.0, 32.0; IR (solid-ATR) 3348, 2959, 1486, 1312, 1286, 817, 733, 638 cm-1; Anal. Calcd for $C_{16}H_{16}N_2O_2$: C, 71.62; H, 6.01; N, 10.44. Found: C, 70.43; H, 6.13; N, 10.49 the slightly low carbon value is probably caused by a trace amount of CH_2Cl_2; HRMS (ESI-Orbitrap) *m*/*z*: $[M + H]^+$ calcd for $C_{16}H_{16}N_2O_2H$ 269.1290; found 269.1281.

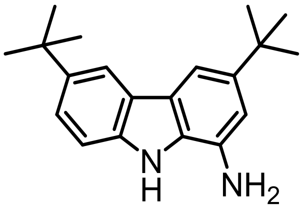

1-amino-3,6-di-*tert*-butylcarbazole (**4.37**) 1-Nitro-3,6-di-*tert*-butylcarbazole (4.#) (1.00 g, 3.1 mmol) was dissolved in methanol (100 mL) in a round bottom flask. Activated zinc dust (2.00 g, 30.6 mmol) was added to the clear yellow solution. Concentrated HCl (0.8 mL, 9.5 mmol) was added dropwise to the mixture. The reaction turned reddish-black in color and the internal temperature of the reaction rose to 35 °C. The reaction was place in a 60 °C sand bath. The reaction was complete (monitored by TLC) after 16 minutes, and the sand bath was removed. (The internal temperature of the reaction reached 45 °C.) The reaction was allowed to cool to room temperature and was then poured into a pH = 12 solution of aqueous sodium carbonate. A white precipitate formed. Dichloromethane (50 mL) was added and the mixture was transferred to a separatory funnel. The aqueous layer was extracted with dichloromethane (2 × 75 mL). The organic layers were combined, dried over anhydrous sodium sulfate, filtered, and concentrated to a tan solid (0.87g, 96%). The compound was characterized without further purification. However, over the course of several months, the solid becomes a purplish color. If desired, column chromatography using silica gel and eluting with 10:1 hexanes/acetone, then 5:1 hexanes/acetone, can remove the purple impurity and provide the desired compound as an off-white solid. mp 248–250 °C; ^1H NMR (360 MHz, $CDCl_3$) δ 8.03 (d, *J* = 1.7 Hz, 1 H), 7.61 (d, *J* = 1.5 Hz, and overlapping br s, 2H), 7.45 (dd, *J* = 8.5, 1.9 Hz, 1H), 7.35 (d, *J* = 8.5 Hz, 1H), 6.89 (d, *J* = 1.6 Hz, 1H), 3.63 (br s, 2H), 1.45 (s, 9H), 1.43 (s, 9H); ^{13}C NMR (90 MHz, $CDCl_3$) δ 143.8, 142.6, 138.4, 130.1, 129.0, 124.6, 124.4, 123.6, 116.6, 111.2, 110.6, 108.2, 34.8, 32.2; IR (solid-ATR) 3369, 3197, 2955, 1595, 1495, 1238, 851 cm-1; Anal. Calcd for $C_{20}H_{26}N_2H$: C, 81.58; H, 8.90; N, 9.51. Found: C, 81.56; H, 9.16; N, 9.68; HRMS (ESI-Orbitrap) *m*/*z*: $[M + H]^+$ calcd for $C_{20}H_{26}N_2H$ 295.2174; found 295.2166.

Bibliography

1. Barbieri, A.; Bandini, E.; Monti, F.; Praveen, V. K.; Armaroli, N. The Rise of Near-Infrared Emitters: Organic Dyes, Porphyrinoids, and Transition Metal Complexes. *Topics in Current Chemistry* **2016,** 374 (4), 47 DOI: 10.1007/s41061-016-0048-9.
2. Kasha, M. Characterization of electronic transitions in complex molecules. *Discussions of the Faraday Society* **1950,** 9 (0), 14-19 DOI: 10.1039/DF9500900014.
3. Klemp, D.; Nickel, B. Relative quantum yield of the S2 → S1 fluorescence from azulene. *Chemical Physics Letters* **1986,** 130 (6), 493-497 DOI: 10.1016/0009-2614(86)80245-7.
4. Ceroni, P. Design of Phosphorescent Organic Molecules: Old Concepts under a New Light. *Chem* **2016,** 1 (4), 524-526 DOI: 10.1016/j.chempr.2016.09.011.
5. Barbieri, A.; Accorsi, G.; Armaroli, N. Luminescent complexes beyond the platinum group: the d10 avenue. *Chemical Communications* **2008,** (19), 2185-2193 DOI: 10.1039/B716650H.
6. Chia, Y. Y.; Tay, M. G. An insight into fluorescent transition metal complexes. *Dalton Transactions* **2014,** 43 (35), 13159-13168 DOI: 10.1039/C4DT01098A.
7. Balzani, V.; Bergamini, G.; Campagna, S.; Puntoriero, F. In *Photochemistry and Photophysics of Coordination Compounds I*; Balzani, V., Campagna, S., Ed.; Springer Berlin Heidelberg: Berlin, Heidelberg, 2007; pp 1-36.
8. Turro, N. J.; Ramamurthy, V.; Scaiano, J. C. *Modern Molecular Photochemistry of Organic Molecules*. 2010; p 290.
9. Chiang, L.; R. Jones, M.; L. Ferreira, S.; Storr, T. T. Multifunctional Ligands in Medicinal Inorganic Chemistry- Current Trends and Future Directions. *Current Topics in Medicinal Chemistry* **2012,** 12 (3), 122-144 DOI: 10.2174/156802612799078973.
10. Takanabe, K. Photocatalytic Water Splitting: Quantitative Approaches toward Photocatalyst by Design. *ACS Catalysis* **2017,** 7 (11), 8006-8022 DOI: 10.1021/acscatal.7b02662.
11. Hagfeldt, A.; Boschloo, G.; Sun, L.; Kloo, L.; Pettersson, H. Dye-Sensitized Solar Cells. *Chemical Reviews* **2010,** 110 (11), 6595-6663 DOI: 10.1021/cr900356p.
12. Knoll, J. D.; Turro, C. Control and utilization of ruthenium and rhodium metal complex excited states for photoactivated cancer therapy. *Coordination Chemistry Reviews* **2015,** 282, 110-126 DOI: 10.1016/j.ccr.2014.05.018.

13. Stacey, O. J.; Pope, S. J. A. New avenues in the design and potential application of metal complexes for photodynamic therapy. *RSC Advances* **2013,** 3 (48), 25550-25564 DOI: 10.1039/C3RA45219K.

14. Xu, H.; Chen, R.; Sun, Q.; Lai, W.; Su, Q.; Huang, W.; Liu, X. Recent progress in metal-organic complexes for optoelectronic applications. *Chemical Society Reviews* **2014,** 43 (10), 3259-3302 DOI: 10.1039/C3CS60449G.

15. Henry, M. S.; Hoffman, M. Z. Photophysics and photochemistry of aromatic nitrogen heterocycles. Fluorescence from 2,2'-bipyridine and 1,10-phenanthroline. *The Journal of Physical Chemistry* **1979,** 83 (5), 618-625 DOI: 10.1021/j100468a012.

16. Burstall, F. H. 34. Optical activity dependent on co-ordinated bivalent ruthenium. *Journal of the Chemical Society (Resumed)* **1936,** (0), 173-175 DOI: 10.1039/JR9360000173.

17. Paris, J. P.; Brandt, W. W. CHARGE TRANSFER LUMINESCENCE OF A RUTHENIUM(II) CHELATE. *Journal of the American Chemical Society* **1959,** 81 (18), 5001-5002 DOI: 10.1021/ja01527a064.

18. Lytle, F. E.; Hercules, D. M. Luminescence of tris(2,2'-bipyridine)ruthenium(II) dichloride. *Journal of the American Chemical Society* **1969,** 91 (2), 253-257 DOI: 10.1021/ja01030a006.

19. Hercules, D. M.; Lytle, F. E. Chemiluminescence from Reduction Reactions. *Journal of the American Chemical Society* **1966,** 88 (20), 4745-4746 DOI: 10.1021/ja00972a052.

20. Bock, C. R.; Meyer, T. J.; Whitten, D. G. Electron transfer quenching of the luminescent excited state of tris(2,2'-bipyridine)ruthenium(II). Flash photolysis relaxation technique for measuring the rates of very rapid electron transfer reactions. *Journal of the American Chemical Society* **1974,** 96 (14), 4710-4712 DOI: 10.1021/ja00821a078.

21. Young, R. C.; Meyer, T. J.; Whitten, D. G. Kinetic relaxation measurement of rapid electron transfer reactions by flash photolysis. Conversion of light energy into chemical energy using the tris(2,2'-bipyridine)ruthenium(3+)-tris(2,2'-bipyridine)ruthenium(2+*) couple. *Journal of the American Chemical Society* **1975,** 97 (16), 4781-4782 DOI: 10.1021/ja00849a064.

22. Thompson, D. W.; Ito, A.; Meyer, T. J. [Ru(bpy)3]2+* and other remarkable metal-to-ligand charge transfer (MLCT) excited states. *Pure and Applied Chemistry* **2013,** Vol. 85 (7), 1257-1305 DOI: 10.1351/PAC-CON-13-03-04.

23. Huynh, M. H. V.; Dattelbaum, D. M.; Meyer, T. J. Exited state electron and energy transfer in molecular assemblies. *Coordination Chemistry Reviews* **2005,** 249 (3), 457-483 DOI: 10.1016/j.ccr.2004.07.005.

24. Zeitler, K. Photoredox Catalysis with Visible Light. *Angewandte Chemie International Edition* **2009,** 48 (52), 9785-9789 DOI: 10.1002/anie.200904056.

25. Koike, T.; Akita, M. In *Ruthenium in Catalysis*; Dixneuf, P. H., Bruneau, C., Ed.; Springer International Publishing: Cham, 2014; pp 371-395.

26. Dongare, P.; Myron, B. D. B.; Wang, L.; Thompson, D. W.; Meyer, T. J. [Ru(bpy)3]2+∗ revisited. Is it localized or delocalized? How does it decay? *Coordination Chemistry Reviews* **2017,** 345 (Supplement C), 86-107 DOI: 10.1016/j.ccr.2017.03.009.

27. Nazeeruddin, M. K.; Baranoff, E.; Grätzel, M. Dye-sensitized solar cells: A brief overview. *Solar Energy* **2011,** 85 (6), 1172-1178 DOI: 10.1016/j.solener.2011.01.018.

28. Nazeeruddin, M. K.; Péchy, P.; Renouard, T.; Zakeeruddin, S. M.; Humphry-Baker, R.; Comte, P.; Liska, P.; Cevey, L.; Costa, E.; Shklover, V.; Spiccia, L.; Deacon, G. B.; Bignozzi, C. A.; Grätzel, M. Engineering of Efficient Panchromatic Sensitizers for Nanocrystalline TiO2-Based Solar Cells. *Journal of the American Chemical Society* **2001,** 123 (8), 1613-1624 DOI: 10.1021/ja003299u.

29. Giovannetti, R. In *Macro To Nano Spectroscopy*; Uddin, D. J., Ed.; 2012. DOI: 10.5772/38797.

30. Moore, M. R. A Historical Introduction to Porphyrin and Chlorophyll Synthesis. In *Tetrapyrroles: Birth, Life, and Death*; Warren, M. J., Smith, A. G., Ed.; Landes Bioscience and Springer Science, New York: 2009; pp 1–28.

31. Moan, J.; Peng, Q. An Outline of the History of PDT. In *Photodynamic Therapy*; Patrice, T., Ed.; Royal Society of Chemistry: Cambridge, UK: 2003; pp 3–17.

32. Hoppe-Seyler, F. Das hamatin. *Tubinger Med Chem Untersuchungen* **1871,** 4, 523-533.

33. Kuster, W. Betrage zur Kenntnis des Bilirubins und Hamins. *Hoppe-Seyler's Zeitschrift Fur Physiologische Chemie* **1912,** (82), 463-483.

34. Wood, T. E.; Uddin, M. I.; Thompson, A. In *Handbook of Porphyrin Science*; World Scientific Publishing Company: 2012; pp 235-291.

35. H. Fischer; Orth, H. *Die Chemie des Pyrrols*. Akademische Verlagsgesellschaft: Leipzig, 1937.

36. Fischer, H.; Schubert, M. Synthetische Versuche mit Blutfarbstoff-Spaltprodukten und Komplexsalz-Bildung bei Dipyrryl-methenen (II.). *Berichte der deutschen chemischen Gesellschaft (A and B Series)* **1924,** 57 (3), 610-617 DOI: 10.1002/cber.19240570342.

37. Fergusson, J. E.; Ramsay, C. A. 971. Dipyrromethene complexes of transition metals. Part I. Tetrahedral complexes of cobalt(II), nickel(II), copper(II),

and zinc(II). *Journal of the Chemical Society (Resumed)* **1965,** (0), 5222-5225 DOI: 10.1039/JR9650005222.

38. Ferguson, J.; West, B. O. The properties of transition-metal complexes of dipyrromethenes. Part I. The spectra and magnetic moments of some nickel(II) complexes. *Journal of the Chemical Society A: Inorganic, Physical, Theoretical* **1966**, 1565-1568 DOI: 10.1039/J19660001565.

39. Ferguson, J.; West, B. O. The properties of transition-metal complexes of dipyrromethenes. Part II. Dipyrromethenes as unidentate ligands. *Journal of the Chemical Society A: Inorganic, Physical, Theoretical* **1966,** (0), 1569-1572 DOI: 10.1039/J19660001569.

40. Murakami, Y.; Sakata, K. Transition-metal complexes of pyrrole pigments. I. Electronic and vibrational spectra of cobalt(II), nickel(II) and copper(II) complexes of some dipyrromethenes. *Inorganica Chimica Acta* **1968,** 2, 273-279 DOI: 10.1016/S0020-1693(00)87041-3.

41. Treibs, A.; Kreuzer, F.-H. Difluorboryl-Komplexe von Di- und Tripyrrylmethenen. *Justus Liebigs Annalen der Chemie* **1968,** 718 (1), 208-223 DOI: 10.1002/jlac.19687180119.

42. de Wael, E. V.; Pardoen, J. A.; van Koeveringe, J. A.; Lugtenburg, J. Pyrromethene-BF2 complexes (4,4′-difluoro-4-bora-3a,4a-diaza-s-indacenes). Synthesis and luminescence properties. *Recueil des Travaux Chimiques des Pays-Bas* **1977,** 96 (12), 306-309 DOI: 10.1002/recl.19770961205.

43. Wories, H. J.; Koek, J. H.; Lodder, G.; Lugtenburg, J.; Fokkens, R.; Driessen, O.; Mohn, G. R. A novel water-soluble fluorescent probe: Synthesis, luminescence and biological properties of the sodium salt of the 4-sulfonato-3,3′,5,5′-tetramethyl-2,2′-pyrromethen-1,1′-BF2 complex. *Recueil des Travaux Chimiques des Pays-Bas* **1985,** 104 (11), 288-291 DOI: 10.1002/recl.19851041104.

44. Monsma, F. J.; Barton, A. C.; Chol Kang, H.; Brassard, D. L.; Haugland, R. P.; Sibley, D. R. Characterization of Novel Fluorescent Ligands with High Affinity for D1 and D2 Dopaminergic Receptors. *Journal of Neurochemistry* **1989,** 52 (5), 1641-1644 DOI: 10.1111/j.1471-4159.1989.tb09220.x.

45. Molecular Probes, Inc. Chemically reactive dipyrrometheneboron difluoride dyes. US4774339A, Sep 27, 1988.

46. https://www.atdbio.com/content/41/BODIPY-dyes

47. Loudet, A.; Burgess, K. BODIPY Dyes and Their Derivatives: Syntheses and Spectroscopic Properties. *Chemical Reviews* **2007,** 107 (11), 4891-4932 DOI: 10.1021/cr078381n.

48. Bertrand, B.; Passador, K.; Goze, C.; Denat, F.; Bodio, E.; Salmain, M. Metal-based BODIPY derivatives as multimodal tools for life sciences. *Coordination Chemistry Reviews* **2018,** 358, 108-124 DOI: 10.1016/j.ccr.2017.12.007.

49. Durantini, A. M.; Heredia, D. A.; Durantini, J. E.; Durantini, E. N. BODIPYs to the rescue: Potential applications in photodynamic inactivation. *European Journal of Medicinal Chemistry* **2018,** 144, 651-661 DOI: 10.1016/j.ejmech.2017.12.068.

50. Bessette, A.; Hanan, G. S. Design, synthesis and photophysical studies of dipyrromethene-based materials: insights into their applications in organic photovoltaic devices. *Chemical Society Reviews* **2014,** 43 (10), 3342-3405 DOI: 10.1039/C3CS60411J.

51. Baudron, S. A. Luminescent dipyrrin based metal complexes. *Dalton Transactions* **2013,** 42 (21), 7498-7509 DOI: 10.1039/C3DT50493J.

52. Wood, T. E.; Thompson, A. Advances in the Chemistry of Dipyrrins and Their Complexes. *Chemical Reviews* **2007,** 107 (5), 1831-1861 DOI: 10.1021/cr050052c.

53. Sakamoto, R.; Iwashima, T.; Tsuchiya, M.; Toyoda, R.; Matsuoka, R.; Kogel, J. F.; Kusaka, S.; Hoshiko, K.; Yagi, T.; Nagayama, T.; Nishihara, H. New aspects in bis and tris(dipyrrinato)metal complexes: bright luminescence, self-assembled nanoarchitectures, and materials applications. *Journal of Materials Chemistry A* **2015,** 3 (30), 15357-15371 DOI: 10.1039/C5TA02040A.

54. Marketed as Vat Red 41.

55. Wyman, G. M.; Brode, W. R. The Relation between the Absorption Spectra and the Chemical Constitution of Dyes XXII. cis-trans Isomerism in Thioindigo Dyes1. *Journal of the American Chemical Society* **1951,** 73 (4), 1487–1493 DOI: 10.1021/ja01148a023.

56. Kirsch, A. D.; Wyman, G. M. Evidence for the intermediacy of the triplet state in the direct photoisomerization of thioindigo dyes. *The Journal of Physical Chemistry* **1975,** 79 (5), 543–544 DOI: 10.1021/j100572a023.

57. Rondão, R.; Seixas de Melo, J. S. Thio-Mayan-like Compounds: Excited State Characterization of Indigo Sulfur Derivatives in Solution and Incorporated in Palygorskite and Sepiolite Clays. *The Journal of Physical Chemistry C* **2013,** 117 (1), 603-614 DOI: 10.1021/jp306209y.

58. Yamazaki, S.; Sobolewski, A. L.; Domcke, W. Molecular mechanisms of the photostability of indigo. *Physical Chemistry Chemical Physics* **2011,** 13, 1618-1628 DOI: 10.1039/C0CP01901A.

59. Iwakura, I.; Yabushita, A.; Kobayashi, T. Why is Indigo Photostable over Extremely Long Periods? *Chemistry Letters* **2009,** 38 (11), 1020– 1021 DOI: 10.1246/cl.2009.1020.

60. Elsaesser, T.; Kaiser, W.; Luttke, W. Picosecond spectroscopy of intramolecular hydrogen bonds in 4,4',7,7'-tetramethylindigo. *The Journal of Physical Chemistry* **1986,** 90 (13), 2901–2905 DOI: 10.1021/j100404a024.

61. Seixas de Melo, J.; Moura, A. P.; Melo, M. J. Photophysical and Spectroscopic Studies of Indigo Derivatives in Their Keto and Leuco Forms. *The Journal of Physical Chemistry A* **2004,** 108 (34), 6975–6981 DOI: 10.1021/jp049076y.

62. Rahman, A. N. A.; Mansour, A. F. Trans-thioindigo as a possible dye for solar collectors. *Journal of Physics D: Applied Physics* **1985,** 18 (6), L49 DOI: 10.1088/0022-3727/18/6/005.

63. Burns, D. A.; Pavelka, L. A. Durable fluorescent solar collectors. US5816238 A, 06 October 1998.

64. Dahlberg, S. C.; Reinganum, C. B. The absence of photochromic switching in semiconducting films of thioindigo. *The Journal of Chemical Physics* **1981,** 75 (5), 2429-2431 DOI: 10.1063/1.442307.

65. Fukushima, K.; Nakatsu, K.; Takahashi, R.; Yamamoto, H.; Gohda, K.; Homma, S. Crystal Structures and Photocarrier Generation of Thioindigo Derivatives. *The Journal of Physical Chemistry B* **1998,** 102 (31), 5985–5990 DOI: 10.1021/jp9814552.

66. Brode, W. R.; Pearson, E. G.; Wyman, G. M. The Relation between the Absorption Spectra and the Chemical Constitution of Dyes. XXVII. cis-trans Isomerism and Hydrogen Bonding in Indigo Dyes1. *Journal of the American Chemical Society* **1954,** 76 (4), 1034–1036 DOI: 10.1021/ja01633a033.

67. Maeda, Y.; Okada, T.; Mataga, N. Picosecond spectroscopy of trans-thioindigo and the mechanism of trans cis photoisomerization. *The Journal of Physical Chemistry* **1984,** 88 (6), 1117–1119 DOI: 10.1021/j150650a017.

68. Karstens, T.; Kobs, K.; Memming, R.; Schroeppel, F. Photoisomerization mechanism of thioindigo dyes. Thioindigo in nonpolar solvents. *Chemical Physics Letters* **1977,** 48 (3), 540-544 DOI: 10.1016/0009-2614(77)85088-4.

69. Petersen, J.; Strohmaier, R.; Gompf, B.; Eisenmenger, W. Monolayers of tetrachloro-thioindigo and thioindigo in the STM: orientational disorder and the absence of photochromism. *Surface Science* **1997,** 389, 329-337 DOI: 10.1016/S0039-6028(97)00446-9.

70. Whitten, D. G. Photochemical reactions in organized monolayer assemblies. I. Cis-trans isomerization of thioindigo dyes. *Journal of the American Chemical Society* **1974,** 96 (2), 594–596 DOI: 10.1021/ja00809a052.

71. Collins-Gold, L.; Moebius, D.; Whitten, D. G. Interfacial effects on excited-state potential energy surfaces. Interrelationship between photoreactivity and surface properties. *Langmuir* **1986,** 2 (2), 191–194 DOI: 10.1021/la00068a014.

72. Breuer, H. D.; Jacob, H. Photoisomerization of thioindigo adsorbed on alumina. *Chemical Physics Letters* **1980,** 73 (1), 172-174 DOI: 10.1016/0009-2614(80)85228-6.

73. Vlahakis, J. Z.; Wand, M. D.; Lemieux, R. P. Photoinduced Polarization Inversion in a Ferroelectric Liquid Crystal Using an Ambidextrous Chiral Thioindigo Dopant. *Journal of the American Chemical Society* **2003,** 125 (23), 6862–6863 DOI: 10.1021/ja0353309.

74. Lemieux, R. P. Photoswitching of ferroelectric liquid crystals using chiral thioindigo dopants: The development of a photochemical switch hitter. *The Chemical Record* **2004,** 3 (5), 288–295 DOI: 10.1002/tcr.10067.

75. Irie, M.; Kato, M. Photoresponsive molecular tweezers. Photoregulated ion capture and release using thioindigo derivatives having ethylenedioxy side groups. *Journal of the American Chemical Society* **1985,** 107 (4), 1024–1028 DOI: 10.1021/ja00290a045.

76. Dittmann, M.; Graupner, F. F.; Maerz, B.; Oesterling, S.; de Vivie-Riedle, R.; Zinth, W.; Engelhard, M.; Lüttke, W. Photostability of 4,4′-Dihydroxythioindigo, a Mimetic of Indigo. *Angewandte Chemie International Edition* **2014,** 53 (2), 591-594 DOI: 10.1002/anie.201307016.

77. Jacquemin, D.; Preat, J.; Wathelet, V.; Fontaine, M.; Perpete, E. A. Thioindigo Dyes: Highly Accurate Visible Spectra with TD-DFT. *Journal of the American Chemical Society* **2006,** 128, 2072–2083 DOI: 10.1021/ja056676h.

78. Fyles, T. M.; Zheng, B. Chemical Switching of Vesicle Bilayer Membrane Disruption by Bis(crown ether) Bolaamphiphiles. *The Journal of Organic Chemistry* **1998,** 63 (23), 8337–8345 DOI: 10.1021/jo981195k.

79. Zarnegar, B. M.; Wyman, G. M. Excited state chemistry of indigoid dyes. I. Fluorescence versus cis-trans isomerization. *The Journal of Physical Chemistry* **1973,** 77 (6), 831–837 DOI: 10.1021/j100625a020.

80. Fukushima, K.; Gohda, K. Molecular Surface Structure of 4,4‘,7,7‘-Tetrachlorothioindigo Crystal Observed by Atomic Force Microscopy. *The Journal of Physical Chemistry B* **1999,** 103 (18), 3582–3586 DOI: 10.1021/jp983705k.

81. Voss, G. Analysis of sulphur-containing indigoid dyes as leuco forms by NMR spectroscopy. *Coloration Technology* **2006,** 122 (6), 317–323 DOI: 10.1111/j.1478-4408.2006.00046.x.

82. Wilhelm, S.; Wolfbeis, O. Irreversible sensing of oxygen ingress. *Sensors and Actuators B: Chemical* **2011,** 153 (1), 199–204 DOI: 10.1016/j.snb.2010.10.037.

83. Schroth, W.; Hintzsche, E.; Viola, H.; Winkler, R.; Klose, H.; Boese, R.; Kempe, R.; Sieler, J. Bis(benzo[4,5]thieno)[3,2-c:2′,3′-e][1,2]dithiin, ein Valenzisomer von „Dithioxo-thioindigo". *Chemische Berichte* **1994,** 127 (2), 401–408 DOI: 10.1002/cber.19941270217.

84. Shimkin, A. A.; Mailian, A. K.; Shirinian, V. Z.; Krayushkin, M. M. Fischer Synthesis of 1H- and 3H-[1]Benzothieno[3,2-b]pyrroles. *Synthesis* **2007,** (17), 2706-2710 DOI: 10.1055/s-2007-983821.

85. Fries, K.; Hemmecke, E. Zur Kenntnis des Thionaphtens. *Justus Liebigs Annalen der Chemie* **1929,** 470 (1), 1–19 DOI: 10.1002/jlac.19294700102.

86. Nawn, G.; Waldie, K. M.; Oakley, S. R.; Peters, B. D.; Mandel, D.; Patrick, B. O.; McDonald, R.; Hicks, R. G. Redox-Active Bridging Ligands Based on Indigo Diimine ("Nindigo") Derivatives. *Inorganic Chemistry* **2011,** 50 (20), 9826–9837 DOI: 10.1021/ic200388y.

87. Hall, H. K.; Padias, A. B.; Williams, P. A.; Gosau, J. M.; Boone, H. W.; Park, D. K. Novel Polyaromatic Quinone Imines. *Macromolecules* **1995,** 28 (1), 1–8 DOI: 10.1021/ma00105a001.

88. Oakley, S. R.; Nawn, G.; Waldie, K. M.; MacInnis, T. D.; Patrick, B. O.; Hicks, R. G. “Nindigo”: synthesis, coordination chemistry, and properties of indigo diimines as a new class of functional bridging ligands. *Chemical Commununications* **2010,** 46, 6753-6755 DOI: 10.1039/C0CC01736A.

89. Burfield, D. R.; Lee, K. H.; Smithers, R. H. Desiccant efficiency in solvent drying. A reappraisal by application of a novel method for solvent water assay. *The Journal of Organic Chemistry* **1977,** 42 (18), 3060–3065 DOI: 10.1021/jo00438a024.

90. Williams, D. B. G.; Lawton, M. Drying of Organic Solvents: Quantitative Evaluation of the Efficiency of Several Desiccants. *The Journal of Organic Chemistry* **2010,** 75 (24), 8351–8354 DOI: 10.1021/jo101589h.

91. Harley-Mason, J.; Mann, F. G. 73. The comparative reactivity of the carbonyl groups in the thionaphthenquinones. Part I. The constitution of certain thioindigoid dyes. *Journal of the Chemical Society (Resumed)* **1942,** (0), 404-415 DOI: 10.1039/JR9420000404.

92. Murov, S. L.; Carmichael, I.; Hug, G. L. *Handbook of Photochemistry*. 1993.

93. Grellmann, K. H.; Hentzschel, P. Mechanism of the photochemical cis⇌trans isomerization of thioindigo and 6,6′-diethoxy-thioindigo in solution. *Chemical Physics Letters* **1978,** 53 (3), 545-551 DOI: 10.1016/0009-2614(78)80066-9.

94. Görner, H.; Schulte-Frohlinde, D. Laser flash studies of thioindigo and indigo dyes. Evidence for a trans configuration of the triplet state. *Chemical Physics Letters* **1979,** 66 (2), 363-369 DOI: 10.1016/0009-2614(79)85035-6.

95. Kirsch, A. D.; Wyman, G. M. Excited state chemistry of indigoid dyes. 5. The intermediacy of the triplet state in the direct photoisomerization and the effect of substituents. *The Journal of Physical Chemistry* **1977,** 81 (5), 413–420 DOI: 10.1021/j100520a010.

96. Dahne, S.; Leupold, D. Coupling Principles in Organic Dyes. *Angewandte Chemie International Edition* **1966,** 5 (12), 984–993 DOI: 10.1002/anie.196609841.

97. Blanc, J.; Ross, D. Procedure for determining the absorption spectra of mixed photochromic isomers not requiring their separation. *The Journal of Physical Chemistry* **1968,** 72 (8), 2817–2824 DOI: 10.1021/j100854a022.

98. Rogers, D. A.; Margerum, J. D.; Wyman, G. M. Spectroscopic Studies on Dyes. IV. The Fluorescence Spectra of Thioindigo Dyes1. *Journal of the American Chemical Society* **1957,** 79 (10), 2464–2468 DOI: 10.1021/ja01567a031.

99. Corval, A.; Trommsdorff, H. P. Optical spectra and excited-state dynamics of cis-thioindigo. *The Journal of Physical Chemistry* **1989,** 93 (20), 7081–7087 DOI: DOI: 10.1021/j100357a014.

100. Gahl, C.; Brete, D.; Leyssner, F.; Koch, M.; McNellis, E. R.; Mielke, J.; Carley, R.; Grill, L.; Reuter, K.; Tegeder, P.; Weinelt, M. Coverage- and Temperature-Controlled Isomerization of an Imine Derivative on Au(111). *Journal of the American Chemical Society* **2013,** 135 (11), 4273-4281 DOI: 10.1021/ja309330e.

101. Javed, I.; Ayub, K.; Arshad, M. N.; Wang, Y. Photophysical and electrochemical properties and temperature dependent geometrical isomerism in alkyl quinacridonediimines. *New Journal of Chemistry* **2014,** 38, 752-761 DOI: 10.1039/C3NJ00477E.

102. Bourque, A. N.; Dufresne, S.; Skene, W. G. Thiophene-Phenyl Azomethines with Varying Rotational Barriers - Model Compounds for Examining Imine Fluorescence Deactivation. *The Journal of Physical Chemistry C* **2009,** 113 (45), 19677–19685 DOI: 10.1021/jp907263p.

103. Dufresne, S.; Roche, I. U.; Skalski, T.; Skene, W. G. Insights into the Effect of the Ketylimine Group on the Fluorescence Deactivation of Oligofluorenes. *The Journal of Physical Chemistry C* **2010,** 114 (30), 13106–13112 DOI: 10.1021/jp104026y.

104. Yeh, L. S. H.; Bard, A. J. The electroreduction of cis- and trans-thioindigo in N,N-dimethylformamide solutions. *Journal of Electroanalytical Chemistry* **1976,** 70 (2), 157-169 DOI: 10.1016/S0022-0728(76)80103-9.

105. Brode, W. R.; Wyman, G. M. The Relation Between the Absorption Spectra and the Chemical Constitution of Dyes. XXIV. Absorption Spectra of Some Thioindigo Dyes in Sulfuric Acid. *Journal of the American Chemical Society* **1951,** 73 (9), 4267-4270 DOI: 10.1021/ja01153a070.

106. Nicholls-Allison, E. C.; Nawn, G.; Patrick, B. O.; Hicks, R. G. Protoisomerization of indigo di- and monoimines. *Chemical Communications* **2015,** 51 (62), 12482-12485 DOI: 10.1039/C5CC04492H.

107. Iwakura, I.; Yabushita, A.; Kobayashi, T. Kinetic isotope effect on the proton-transfer in indigo carmine. *Chemical Physics Letters* **2010,** 484 (4), 354-357 DOI: 10.1016/j.cplett.2009.11.029.

108. Wyman, G. M.; Zarnegar, B. M. Excited state chemistry of indigoid dyes. II. Interaction of thio- and selenoindigo dyes with hydroxylic compounds and its implications on the photostability of indigo. *The Journal of Physical Chemistry* **1973,** 77 (10), 1204-1207 DOI: 10.1021/j100629a004.

109. Liao, Y.; Bohne, C. Alcohol Effect on Equilibrium Constants and Dissociation Dynamics of Xanthone–Cyclodextrin Complexes. *The Journal of Physical Chemistry* **1996,** 100 (2), 734–743 DOI: 10.1021/jp951697r.

110. Eaton, D. F. Reference materials for fluorescence measurement. *Pure and Applied Chemistry* **1988,** 60 (7), 1107-1114 DOI: 10.1351/pac198860071107.

111. Eaton, D. F.; Scaiano, J. C. *Handbook of Organic Photochemistry*. 1989; Vol. I.

112. Kalle. & Co., Akt.-Ges. 3-hydroxy-(1)-thionaphthene. DE 188702 Jul 29, 1905.

113. Kalle & Co., Akt.-Ges. Red dyestuff. DE 194237 May 9, 1905

114. Kalle & Co., Aktiengesellschaft. Process of manufacturing a red dyestuff. DE 192260 Nov 14, 1905.

115. Friedlaender, P. Ueber Thionaphtenderivate und Thioindigo. *Justus Liebigs Annalen der Chemie* **1907,** 351 (1-3), 390-420 DOI: 10.1002/jlac.19073510131.

116. Friedländer, P. Über indigoide Farbstoffe. *Berichte der deutschen chemischen Gesellschaft* **1908,** 41 (1), 772-777 DOI: 10.1002/cber.190804101144.

117. Wirther, R. Thioindigo Scarlet R. *Faerber-Zeitung* **1907,** 18, 161-63.

118. Friedlaender, P. Über Oxy- und Methoxy-Derivate des Thioindigos. *Berichte der deutschen chemischen Gesellschaft* **1916,** 49 (1), 955-966 DOI: 10.1002/cber.19160490198.

119. Griffith, R. H.; Hope, E. CXXXV.-Synthesis of 5:5'-dibromo-6:6'-dimethoxy-2:2'-bisoxythionaphthen. *Journal of the Chemical Society, Transactions* **1925,** 127, 990-995 DOI: 10.1039/CT9252700990.

120. Hixson, A. W.; Cauwenberg, W. J. METHYL ISOPROPYL THIOINDIGOID DYES FROM PARACYMENE. II. DYES FROM SODIUM CYMENE SULFONATE1. *Journal of the American Chemical Society* **1930,** 52 (5), 2125-2130 DOI: 10.1021/ja01368a065.

121. Guha, S. K. Indigoid vat dyes of the isatin series. IV. 3-Indole-2'-(7'-methylthianaphthene)indigos. *Journal of the Indian Chemical Society* **1944,** 21, 87-90.

122. Shibata, R.-n.; Sassa, A. The synthesis of thioindigo. III. The condensation products of thioindigo-7,7'-dicarboxylic acid chloride with aromatic amines. *Kogyo Kagaku Zasshi* **1936,** 39 (Suppl. binding), 283-284.

123. Kalb, L.; Berrer, E. Indigo group. V. 5,7,5',7'-Tetraiodoindigo and related compounds. *Berichte der Deutschen Chemischen Gesellschaft [Abteilung] B: Abhandlungen* **1924,** 57B, 2105-2117.

124. Hermann, H.; Lüttke, W. Theoretische und spektroskopische Untersuchungen an Indigofarbstoffen, VII. Die Darstellung des 3.3′-Dioxo-4.4.4′.4′-tetramethyl-2.2′-bithiolanylidens, einer Verbindung mit dem Grundchromophorsystem des Thioindigos. *Chemische Berichte* **1968,** 101 (5), 1708-1714 DOI: 10.1002/cber.19681010523.

125. S. Sun, P. Sun, W. Zhang, M. Han, G. Chen. Application of thioindigo as an organic positive electrode material of lithium ion battery. CN 105206838 A, Dec 30, 2015

126. Hosseinnezhad, M. Cosensitization with Vat-Based Organic Dyes for Enhanced Spectral Response of Dye-Sensitized Solar Cells. *Journal of Electronic Materials* **2017,** 46 (4), 2290-2295 DOI: 10.1007/s11664-016-5261-3.

127. D. A. Burns, L.A. Pavelka. Durable fluorescent solar collectors. US 5816238 A, October 6, 1998.

128. Castellano, F. N. Altering Molecular Photophysics by Merging Organic and Inorganic Chromophores. *Accounts of Chemical Research* **2015,** 48 (3), 828-839 DOI: 10.1021/ar500385e.

129. Boice, G.; Patrick, B. O.; McDonald, R.; Bohne, C.; Hicks, R. Synthesis and Photophysics of Thioindigo Diimines and Related Compounds. *The Journal of Organic Chemistry* **2014,** 79 (19), 9196-9205 DOI: 10.1021/jo501630f.

130. Curcio, M.; Pankhurst, J. R.; Sproules, S.; Mignard, D.; Love, J. B. Triggering Redox Activity in a Thiophene Compound: Radical Stabilization and Coordination Chemistry. *Angewandte Chemie International Edition* **2017,** 56 (27), 7939-7943 DOI: 10.1002/anie.201703576.

131. Kaim, W. Concepts for metal complex chromophores absorbing in the near infrared. *Coordination Chemistry Reviews* **2011,** 255 (21), 2503-2513 DOI: 10.1016/j.ccr.2011.01.014.

132. Kohlmann, S.; Ernst, S.; Kaim, W. Extremely Long-Wavelength Charge-Transfer Absorptions of Binuclear Complexes with Azo-Modified 2,2′-Bipyridyl Ligands. *Angewandte Chemie International Edition in English* **1985,** 24 (8), 684-685 DOI: 10.1002/anie.198506841.

133. Zhou, C.; Liu, Y.; Zhao, X. Effect of substituted sites and coordinated metal atoms on the absorption properties of porphyrin and phthalocyanine derivatives. *Inorganica Chimica Acta* **2015,** 425, 11-16 DOI: 10.1016/j.ica.2014.10.012.

134. Dickson, R. S.; Fallon, G. D.; Zhang, Q.-Q. Dimeric diphenylzinc adducts with cyclic thioethers. *Journal of the Chemical Society, Dalton Transactions* **2000,** (13), 1973-1974 DOI: 10.1039/B003985N.

135. Mondal, P.; Ehret, F.; Bubrin, M.; Das, A.; Mobin, S. M.; Kaim, W.; Lahiri, G. K. A Diruthenium Complex of a “Nindigo” Ligand. *Inorganic Chemistry* **2013,** 52 (15), 8467-8475 DOI: 10.1021/ic400390b.

136. Mondal, P.; Plebst, S.; Ray, R.; Mobin, S. M.; Kaim, W.; Lahiri, G. K. Uncommon cis Configuration of a Metal–Metal Bridging Noninnocent Nindigo Ligand. *Inorganic Chemistry* **2014,** 53 (17), 9348-9356 DOI: 10.1021/ic501460d.

137. Rutherford, T. J.; Van Gijte, O.; Kirsch-De Mesmaeker, A.; Keene, F. R. Stereoisomers of Mono-, Di-, and Triruthenium(II) Complexes Containing the Bridging Ligand 1,4,5,8,9,12-Hexaazatriphenylene and Studies of Their Photophysical Properties. *Inorganic Chemistry* **1997,** 36 (20), 4465-4474 DOI: 10.1021/ic961374p.

138. Moorthy, J. N.; Patterson, W. S.; Bohne, C. Remarkable Discrimination in the Triplet Lifetimes of the Diastereomers of 1,4-Bis(p-methoxyphenyl)- 2,3-diphenylbutan-1,4-dione. *Journal of the American Chemical Society* **1997,** 119 (45), 11094-11095 DOI: 10.1021/ja971296k.

139. Moorthy, J. N.; Monahan, S. L.; Sunoj, R. B.; Chandrasekhar, J.; Bohne, C. Modulation of Lifetimes and Diastereomeric Discrimination in Triplet-Excited Substituted Butane-1,4-diones through Intramolecular Charge-Transfer Quenching. *Journal of the American Chemical Society* **1999,** 121 (13), 3093-3103 DOI: 10.1021/ja9818708.

140. Moorthy, J. N., Koner, A. L., Samanta, S., Singhal, N., Nau, W. M. and Weiss, R. G. . Diastereomeric Discrimination in the Lifetimes of Norrish Type II Triplet 1,4-Biradicals and Stereocontrolled Partitioning of Their Reactivity (Yang Cyclization versus Type II Fragmentation). *Chemistry a European Journal* **2006,** 12 (34), 8744–8749 DOI: 10.1002/chem.200600880.

141. Samanta, S.; Mishra, B. K.; Pace, T. C. S.; Sathyamurthy, N.; Bohne, C.; Moorthy, J. N. β-Phenyl Quenching of Triplet Excited Ketones: How Critical Is the Geometry for Deactivation? *The Journal of Organic Chemistry* **2006,** 71 (12), 4453-4459 DOI: 10.1021/jo060200e.

142. Abad, S.; Boscá, F.; Domingo, L. R.; Gil, S.; Pischel, U.; Miranda, M. A. Triplet Reactivity and Regio-/Stereoselectivity in the Macrocyclization of Diastereomeric Ketoprofen−Quencher Conjugates via Remote Hydrogen Abstractions. *Journal of the American Chemical Society* **2007,** 129 (23), 7407-7420 DOI: 10.1021/ja0712827.

143. Singhal, N.; Koner, A. L.; Mal, P.; Venugopalan, P.; Nau, W. M.; Moorthy, J. N. Diastereomer-Differentiating Photochemistry of β-Arylbutyrophenones: Yang Cyclization versus Type II Elimination. *Journal of the American Chemical Society* **2005,** 127 (41), 14375-14382 DOI: 10.1021/ja0523643.

144. Consuelo Jimenez, M.; Stiriba, S.-E.; Tormos, R.; Perez-Prieto, J.; Miranda, M. A. Stereoselectivity in the triplet decay of chiral benzophenone-naphthalene bichromophoric systems. *Photochemical & Photobiological Sciences* **2004,** 3 (1), 36-38 DOI: 10.1039/B308195H.

145. Baird, I. R.; Rettig, S. J.; James, B. R.; Skov, K. A. Synthesis and X-ray structural characterization of the ruthenium β-diketonato complexes: Ru(hfac)$_3$, cis-Ru(hfac)$_2$(MeCN)$_2$, and cis-Ru(hfac)(acac)(MeCN)$_2$. *Canadian Journal of Chemistry* **1999,** 77 (11), 1821-1833 DOI: 10.1139/v99-175.

146. Olivier, J.; Golhen, S.; Świetlik, R.; Cador, O.; Pointillart, F.; Ouahab, L. X-ray Structures, Spectroscopic and Magnetic Studies of a Coordination Polymer Series Based on a TTF Derivative and Paramagnetic Transition Metals. *European Journal of Inorganic Chemistry* **2009,** 2009 (22), 3282-3290 DOI: 10.1002/ejic.200900365.

147. Braun, S.; Kalinowski, H.-O.; Berger, S. *150 and More Basic NMR Experiments A Practical Course*. Second ed.; Wiley-VCH: Weinheim, 1998.

148. Garakyaraghi, S.; Danilov, E. O.; McCusker, C. E.; Castellano, F. N. Transient Absorption Dynamics of Sterically Congested Cu(I) MLCT Excited States. *The Journal of Physical Chemistry A* **2015,** 119 (13), 3181-3193 DOI: 10.1021/acs.jpca.5b00901.

149. Bessette, A.; Ferreira, J. G.; Giguère, M.; Bélanger, F.; Désilets, D.; Hanan, G. S. Azadipyrromethene Dye Derivatives in Coordination Chemistry: the Structure–Property Relationship in Homoleptic Metal(II) Complexes. *Inorganic Chemistry* **2012,** 51 (22), 12132-12141 DOI: 10.1021/ic300872m.

150. Ge, Y.; O'Shea, D. F. Azadipyrromethenes: from traditional dye chemistry to leading edge applications. *Chemical Society Reviews* **2016,** 45 (14), 3846-3864 DOI: 10.1039/C6CS00200E.

151. Al-Imarah, E. M. A.; Derrick, P. J.; Partridge, A. New wavelength-tunable aza-dipyrromethene dyes with intense near-infrared absorption and emission. *Journal of Photochemistry and Photobiology A: Chemistry* **2017,** 337, 82-90 DOI: 10.1016/j.jphotochem.2017.01.024.

152. Jiang, X.-D.; Zhao, J.; Xi, D.; Yu, H.; Guan, J.; Li, S.; Sun, C.-L.; Xiao, L.-J. A New Water-Soluble Phosphorus-Dipyrromethene and Phosphorus-Azadipyrromethene Dye: PODIPY/aza-PODIPY. *Chemistry – A European Journal* **2015,** 21 (16), 6079-6082 DOI: 10.1002/chem.201406535.

153. Antina, E. V.; Bumagina, N. A. Tetraaryl-substituted aza-BODIPY: synthesis, spectral properties, and possible applications (microreview). *Chemistry of Heterocyclic Compounds* **2017,** 53 (1), 39-41 DOI: 10.1007/s10593-017-2018-8.

154. Deligonul, N.; Browne, A. R.; Golen, J. A.; Rheingold, A. L.; Gray, T. G. Cyclometalated Iridium(III) Complexes of Azadipyrromethene Chromophores. *Organometallics* **2014,** 33 (3), 637-643 DOI: 10.1021/om4007032.

155. Deligonul, N.; Gray, T. G. Azadipyrromethene Complexes of d8 Metal Centers: Rhodium(I), Iridium(I), Palladium(II), and Platinum(II). *Inorganic Chemistry* **2013,** 52 (22), 13048-13057 DOI: 10.1021/ic4017239.

156. Teets, T. S.; Updegraff, J. B.; Esswein, A. J.; Gray, T. G. Three-Coordinate, Phosphine-Ligated Azadipyrromethene Complexes of Univalent Group 11 Metals. *Inorganic Chemistry* **2009,** 48 (17), 8134-8144 DOI: 10.1021/ic900208a.

157. Gao, L.; Deligonul, N.; Gray, T. G. Gold(I) Complexes of Brominated Azadipyrromethene Ligands. *Inorganic Chemistry* **2012,** 51 (14), 7682-7688 DOI: 10.1021/ic300709n.

158. Beletskaya, I. P.; Cheprakov, A. V. The Complementary Competitors: Palladium and Copper in C–N Cross-Coupling Reactions. *Organometallics* **2012,** 31 (22), 7753-7808 DOI: 10.1021/om300683c.

159. Navalón, S.; Álvaro, M.; García, H. Polymer- and Ionic Liquid-Containing Palladium: Recoverable Soluble Cross-Coupling Catalysts. *ChemCatChem* **2013,** 5 (12), 3460-3480 DOI: 10.1002/cctc.201300339.

160. Valente, C.; Çalimsiz, S.; Hoi, K. H.; Mallik, D.; Sayah, M.; Organ, M. G. The Development of Bulky Palladium NHC Complexes for the Most-Challenging Cross-Coupling Reactions. *Angewandte Chemie International Edition* **2012,** 51 (14), 3314-3332 DOI: 10.1002/anie.201106131.

161. Surry, D. S.; Buchwald, S. L. Dialkylbiaryl phosphines in Pd-catalyzed amination: a user's guide. *Chemical Science* **2011,** 2 (1), 27-50 DOI: 10.1039/C0SC00331J.

162. Senra, J. D.; Aguiar, L. C. S.; Simas, A. B. C. Recent Progress in Transition-Metal-Catalyzed C-N Cross-Couplings: Emerging Approaches Towards Sustainability. *Current Organic Synthesis* **2011,** 8 (1), 53 - 78.

163. Ruiz-Castillo, P.; Buchwald, S. L. Applications of Palladium-Catalyzed C–N Cross-Coupling Reactions. *Chemical Reviews* **2016,** 116 (19), 12564-12649 DOI: 10.1021/acs.chemrev.6b00512.

164. Schlummer, B.; Scholz, U. Palladium-Catalyzed C—N and C—O Coupling–A Practical Guide from an Industrial Vantage Point†. *Advanced Synthesis & Catalysis* **2004,** 346 (13-15), 1599-1626 DOI: 10.1002/adsc.200404216.

165. Yamaguchi, M.; Suzuki, K.; Sato, Y.; Manabe, K. Palladium-Catalyzed Direct C3-Selective Arylation of N-Unsubstituted Indoles with Aryl Chlorides and Triflates. *Organic Letters* **2017,** 19 (19), 5388-5391 DOI: 10.1021/acs.orglett.7b02669.

166. Cacchi, S.; Fabrizi, G. Update 1 of: Synthesis and Functionalization of Indoles Through Palladium-Catalyzed Reactions. *Chemical Reviews* **2011,** 111 (5), PR215-PR283 DOI: 10.1021/cr100403z.

167. Hartwig, J. F.; Kawatsura, M.; Hauck, S. I.; Shaughnessy, K. H.; Alcazar-Roman, L. M. Room-Temperature Palladium-Catalyzed Amination of Aryl Bromides and Chlorides and Extended Scope of Aromatic C−N Bond Formation with a Commercial Ligand. *The Journal of Organic Chemistry* **1999,** 64 (15), 5575-5580 DOI: 10.1021/jo990408i.

168. Greene, T. W.; Wutz, P. G. M. *Protective Groups in Organic Synthesis*. Third ed.; John Wiley & Sons: New York, 1999.

169. Kolczewski, S.; Riemer, C.; Steward, L.; Wichmann, J.; Woltering, T., 2-aminoquinolines as 5-ht(5a) receptor antagonists. WO2008068157A1 Jun 12, 2008.

170. Mann, G.; Hartwig, J. F.; Driver, M. S.; Fernández-Rivas, C. Palladium-Catalyzed C−N(sp2) Bond Formation: N-Arylation of Aromatic and Unsaturated Nitrogen and the Reductive Elimination Chemistry of Palladium Azolyl and Methyleneamido Complexes. *Journal of the American Chemical Society* **1998,** 120 (4), 827-828 DOI: 10.1021/ja973524g.

171. Fors, B. P.; Watson, D. A.; Biscoe, M. R.; Buchwald, S. L. A Highly Active Catalyst for Pd-Catalyzed Amination Reactions: Cross-Coupling Reactions Using Aryl Mesylates and the Highly Selective Monoarylation of Primary Amines Using Aryl Chlorides. *Journal of the American Chemical Society* **2008,** 130 (41), 13552-13554 DOI: 10.1021/ja8055358.

172. Old, D. W.; Harris, M. C.; Buchwald, S. L. Efficient Palladium-Catalyzed N-Arylation of Indoles. *Organic Letters* **2000,** 2 (10), 1403-1406 DOI: 10.1021/ol005728z.

173. Sundberg, R. J. In *Heterocyclic Scaffolds II: Reactions and Applications of Indoles*; Gribble, G. W., Ed.; Springer Berlin Heidelberg: Berlin, Heidelberg, 2010; pp 47-115.

174. Bandini, M.; Eichholzer, A. Catalytic Functionalization of Indoles in a New Dimension. *Angewandte Chemie International Edition* **2009,** 48 (51), 9608-9644 DOI: 10.1002/anie.200901843.

175. Kulkarni, A.; Quang, P.; Török, B. Microwave-Assisted Solid-Acid-Catalyzed Friedel-Crafts Alkylation and Electrophilic Annulation of Indoles Using Alcohols as Alkylating Agents. *Synthesis* **2009,** 2009 (23), 4010-4014 DOI: 10.1055/s-0029-1217052.

176. Arcadi, A.; Chiarini, M.; D'Anniballe, G.; Marinelli, F.; Pietropaolo, E. Brønsted Acid Catalyzed Cascade Reactions of 2-[(2-Aminophenyl)ethynyl]phenylamine Derivatives with Aldehydes: A New

Approach to the Synthesis of 2,2′-Disubstituted 1H,1′H-3,3′-Biindoles. *Organic Letters* **2014,** 16 (6), 1736-1739 DOI: 10.1021/ol500401p.

177. Berlin, A.; Canavesi, A.; Schiavon, G.; Zecchin, S.; Zotti, G. Electrooxidation products of methylindoles: Mechanisms and structures. *Tetrahedron* **1996,** 52 (23), 7947-7960 DOI: 10.1016/0040-4020(96)00366-3.

178. Mahato, S. B.; Garai, S.; Weber, M.; Luger, P. Synthesis of novel 1-methylindole trimer and tetramer under Friedel-Crafts reaction conditions and determination of their structures by X-ray crystallography. *Journal of the Chemical Society, Perkin Transactions 1* **2000,** (16), 2767-2769 DOI: 10.1039/B002074P.

179. Groves, B. R.; Crawford, S. M.; Lundrigan, T.; Matta, C. F.; Sowlati-Hashjin, S.; Thompson, A. Synthesis and characterisation of the unsubstituted dipyrrin and 4,4-dichloro-4-bora-3a,4a-diaza-s-indacene: improved synthesis and functionalisation of the simplest BODIPY framework. *Chemical Communications* **2013,** 49 (8), 816-818 DOI: 10.1039/C2CC37480C.

180. Gibson, V. C.; Spitzmesser, S. K.; White, A. J. P.; Williams, D. J. Synthesis and reactivity of 1,8-bis(imino)carbazolide complexes of iron, cobalt and manganese. *Dalton Transactions* **2003,** (13), 2718-2727 DOI: 10.1039/B301902K.

181. Araneda, J. F.; Piers, W. E.; Heyne, B.; Parvez, M.; McDonald, R. High Stokes Shift Anilido-Pyridine Boron Difluoride Dyes. *Angewandte Chemie International Edition* **2011,** 50 (51), 12214-12217 DOI: 10.1002/anie.201105228.

182. Huo, Z.; Li, Z.; Wang, T.; Zeng, H. Carbazole N-substituent effect upon DTMA: stabilizing and photochromic modulating. *Tetrahedron* **2013,** 69 (42), 8964-8973 DOI: 10.1016/j.tet.2013.07.040.

183. Sanchez, G.; Espinosa, A.; Curiel, D.; Tarraga, A.; Molina, P. Bis(carbazolyl)ureas as Selective Receptors for the Recognition of Hydrogenpyrophosphate in Aqueous Media. *The Journal of Organic Chemistry* **2013,** 78 (19), 9725-9737 DOI: 10.1021/jo401430d.

184. Olah, G. A.; Prakash, G. K. S.; Iyer, P. S.; Tashiro, M.; Yamato, T. Catalysis by solid superacids. 21. Nafion-H catalyzed de-tert-butylation of aromatic compounds. *The Journal of Organic Chemistry* **1987,** 52 (9), 1881-1884 DOI: 10.1021/jo00385a048.

185. Pandit, P.; Nakamura, T.; Higashibayashi, S. Synthesis and Acid-responsive Electron-transfer Disproportionation of Non- and Tetramesityl-substituted 1,1′,9,9′-Bicarbazole. *Chemistry Letters* **2015,** 44 (10), 1336-1338 DOI: 10.1246/cl.150557.

186. Tashiro, M.; Fukata, G. Studies on Friedel-Crafts chemistry. 2. The aluminum trichloride-nitromethane catalyzed novel transbenzylation of 4,4'-dihydroxydiphenylmethanes in toluene. *The Journal of Organic Chemistry* **1977,** 42 (7), 1208-1213 DOI: 10.1021/jo00427a023.

187. Fischer, A.; Henderson, G.; Thompson, R. Ipso nitration. XIX. Formation of cyclohexadiene adducts from nitration of 4-ethyltoluene and 1,4-diethylbenzene in nitric acid and acetic anhydride. *Australian Journal of Chemistry* **1978,** 31 (6), 1241-1247 DOI: 10.1071/CH9781241.

188. Fischer, A.; Henderson, G. N. IPSO nitration: nitration of 2-alkylphenols in acetic anhydride. Formation of 6-alkyl-6-nitrocyclohexa-2,4-dienones. *Tetrahedron Letters* **1980,** 21 (49), 4661-4662 DOI: 10.1016/0040-4039(80)88087-7.

189. Hudecek, O.; Budka, J.; Eigner, V.; Lhoták, P. Regioselective ipso-nitration of calix[4]arenes. *Tetrahedron* **2012,** 68 (22), 4187-4193 DOI: 10.1016/j.tet.2012.03.102.

190. Sawada, T.; Hongo, T.; Matsuo, N.; Konishi, M.; Kawaguchi, T.; Ihara, H. Hemisphere-shaped calixarenes and their analogs: synthesis, structure, and chiral recognition ability. *Tetrahedron* **2011,** 67 (25), 4716-4722 DOI: 10.1016/j.tet.2011.04.025.

191. Lejeune, M.; Picron, J.-F.; Mattiuzzi, A.; Lascaux, A.; De Cesco, S.; Brugnara, A.; Thiabaud, G.; Darbost, U.; Coquière, D.; Colasson, B.; Reinaud, O.; Jabin, I. Ipso-Nitration of Calix[6]azacryptands: Intriguing Effect of the Small Rim Capping Pattern on the Large Rim Substitution Selectivity. *The Journal of Organic Chemistry* **2012,** 77 (8), 3838-3845 DOI: 10.1021/jo300179h.

192. Redon, S.; Li, Y.; Reinaud, O. Unprecedented Selective ipso-Nitration of Calixarenes Monitored by the O-Substituents. *The Journal of Organic Chemistry* **2003,** 68 (18), 7004-7008 DOI: 10.1021/jo034557j.

193. Coquière, D.; Marrot, J.; Reinaud, O. Innovative Methodologies for the N-Protection of N-Alkylimidazole Groups: Application to the First Synthesis of a Water-Soluble Calix[6]arene Presenting Three Ammonium Substituents at the Large Rim and Three Neutral N-Donors at the Small Rim. *Organic Letters* **2007,** 9 (17), 3271-3274 DOI: 10.1021/ol071208t.

194. Moodie, R. B.; Schofield, K. Ipso attack in aromatic nitration. *Accounts of Chemical Research* **1976,** 9 (8), 287-292 DOI: 10.1021/ar50104a002.

195. Bonesi, S. M.; Ponce, M. A.; Erra-Balsells, R. A study of substituent effect on 1H and 13C nmr spectra of N- and C-substituted carbazoles. *Journal of Heterocyclic Chemistry* **2004,** 41 (2), 161-171 DOI: 10.1002/jhet.5570410205.

196. Yamamura, S.; Toda, M.; Hirata, Y. Modified Clemmensen Reduction: Cholestane. *Organic Syntheses* **1973,** 53, 86 DOI: 10.15227/orgsyn.053.0086.

Appendices

Appendix A. Supplementary Information for Chapters 2–4

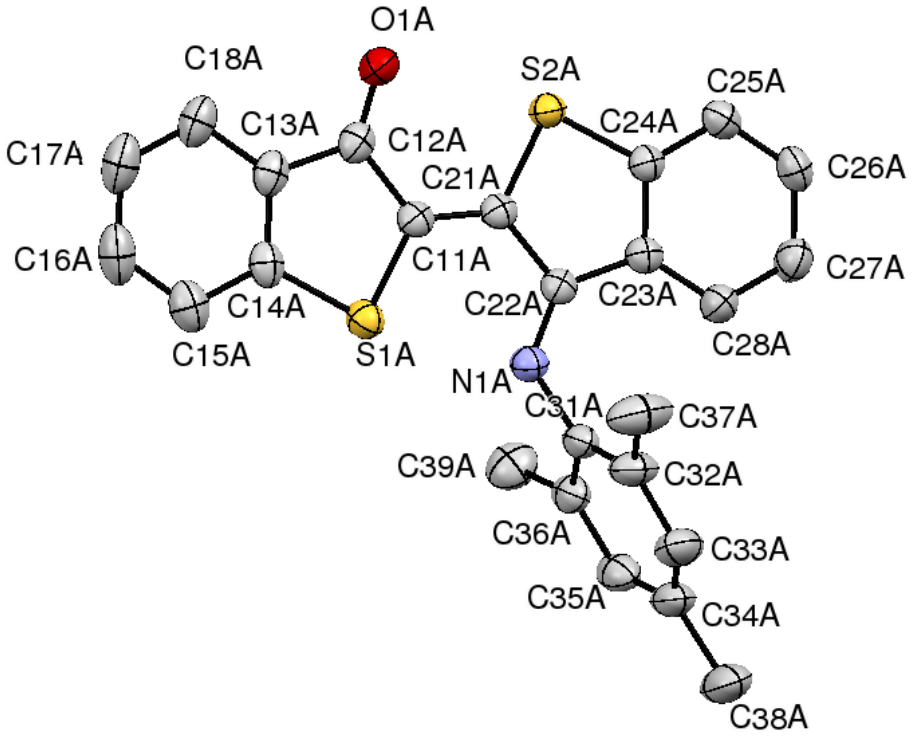

Figure A1. X-ray crystal structure of monoamine **2.5c**. Hydrogen atoms are omitted for clarity. Thermal ellipsoids are represented at 50% probability.

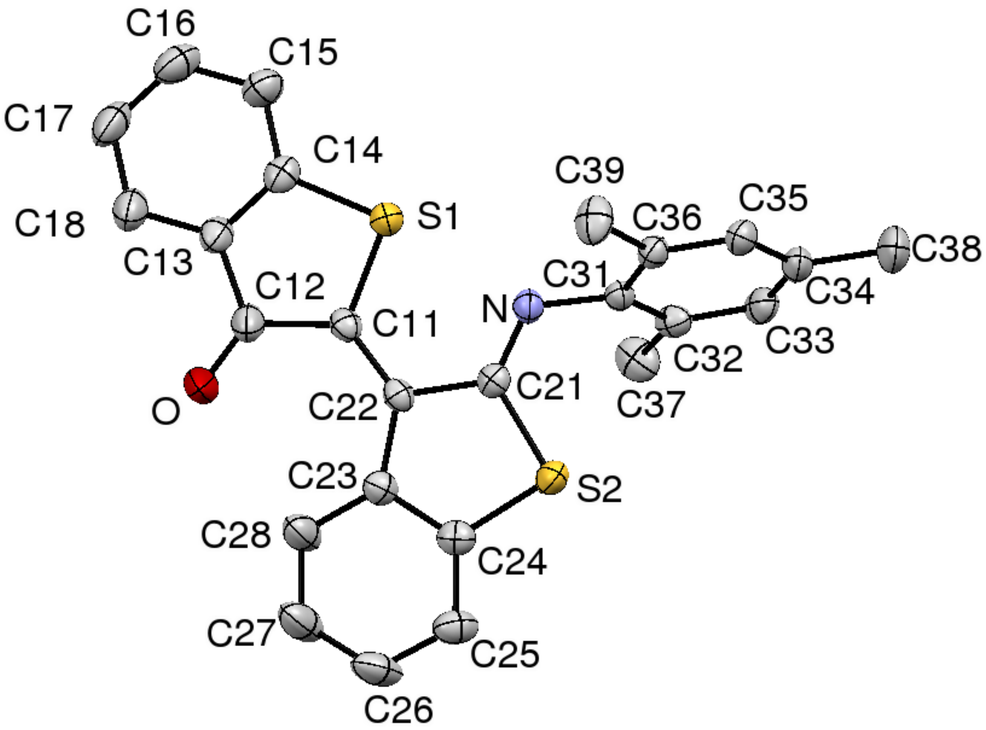

Figure A2. X-ray crystal structure of thioindirubin derivative **2.6c**. Hydrogen atoms are omitted for clarity. Thermal ellipsoids are represented at 50% probability.

Table A1. Fluorescence (singlet excited state) lifetimes of **2.2a** in varied solvents.

Solvent	**τ (ns)[a]** **N_2 Purged**	χ^2	**τ (ns)[a]** **Aerated**	χ^2
Cyclohexane	1.23± 0.01	0.947	1.15± 0.01	0.959
Methanol	1.81± 0.06	0.978	1.59 ± 0.03	1.090
Methanol (490 nm)[b]	NA	NA	1.56 ± 0.01	1.165
Ethanol	1.88± 0.01	1.027	1.66± 0.04	0.911
Acetone	2.12± 0.02	1.056	1.78± 0.04	1.052
Acetonitrile	1.96± 0.06	1.100	1.68± 0.05	0.904
Toluene	1.88± 0.01	0.981	1.69± 0.04	0.909

[a] Lifetime values are the average of two measurements obtained on different days. The errors in the lifetimes correspond to the average errors for two independent experiments. All samples were found to have single exponential decays. [b] The decay of **2.2a** in aerated methanol solution was checked at emission wavelengths of 450 nm and 490 nm and the lifetimes were found to be the same, confirming a single species.

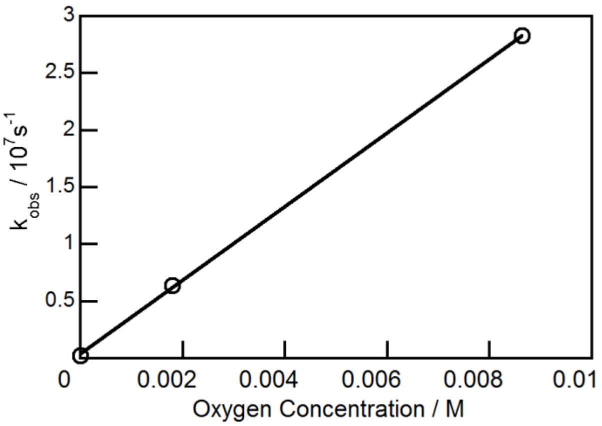

Figure A3. Quenching plot of the triplet state of **2.2a** by oxygen at 20 °C.

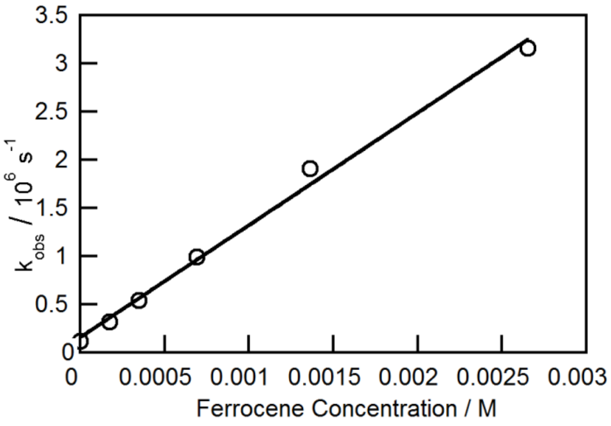

Figure A4. Quenching of the triplet state of **2.2a** by ferrocene.

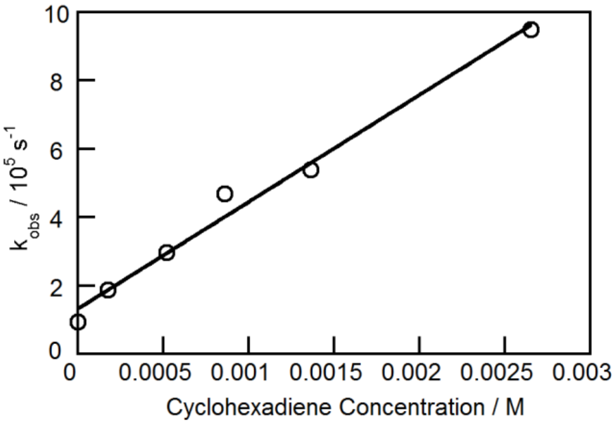

Figure A5. Quenching of the triplet state of **2.2a** by 1,3-cyclohexadiene.

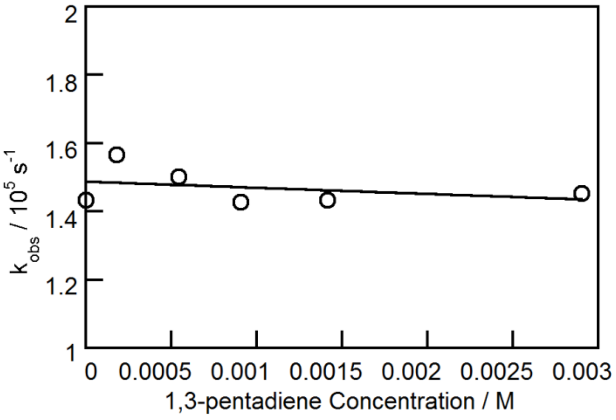

Figure A6. Quenching of the triplet state of **2.2a** by 1,3-pentadiene.

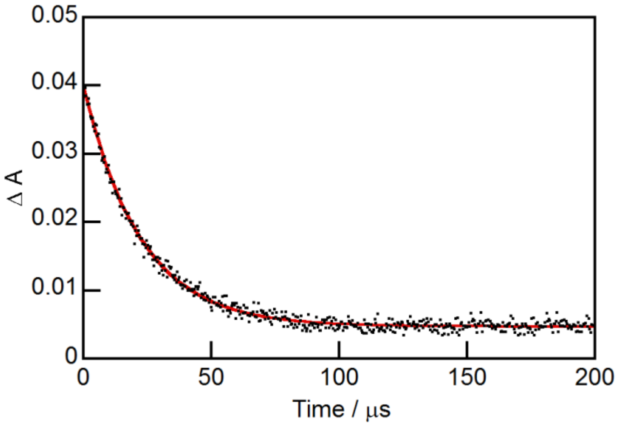

Figure A7. The transient decay kinetics of **2.2b** in toluene (4.5×10^{-5} M) observed by laser flash photolysis using a pulsed laser excitation wavelength of 355 nm and a monitoring wavelength of 440 nm. Fitted to a single exponential decay using Kaleidagraph.

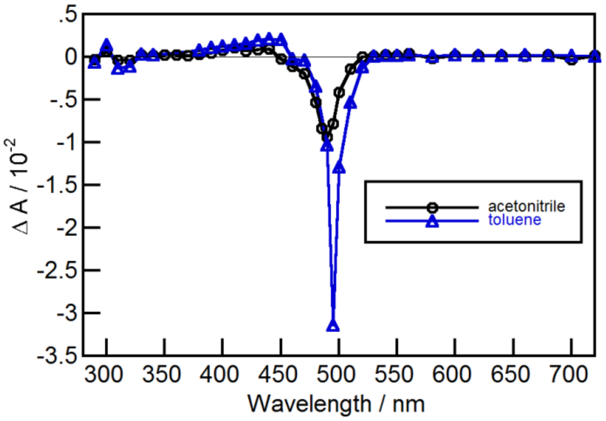

Figure A8. Transient absorbance spectra of **2.3a** in (blue triangles) toluene (5.7 × 10^{-5} M), with pulsed laser excitation at 355 nm, integrated between 132 and 391 ns after the laser pulse; and in (black circles) acetonitrile, (~1.5 × 10^{-5} M), with pulsed laser excitation at 266 nm, integrated between 167 and 611 ns after the laser pulse (black). The observed intensity difference is caused by the decreased solubility of **2.3a** in acetonitrile as compared to toluene.

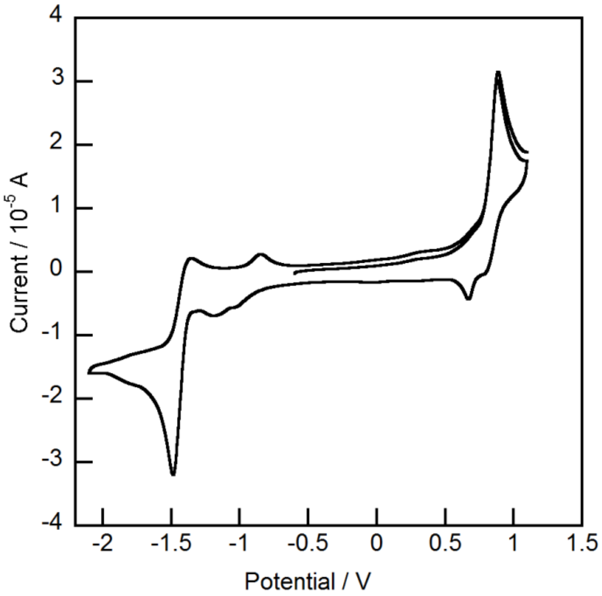

Figure A9. Cyclic voltammogram of diimine **2.3b** in dichloromethane, ~1 mM analyte. The standard is Fc^+/Fc, the electrolyte is 0.1 M Bu_4NBF_4 and the scan rate is 100 mV/s.

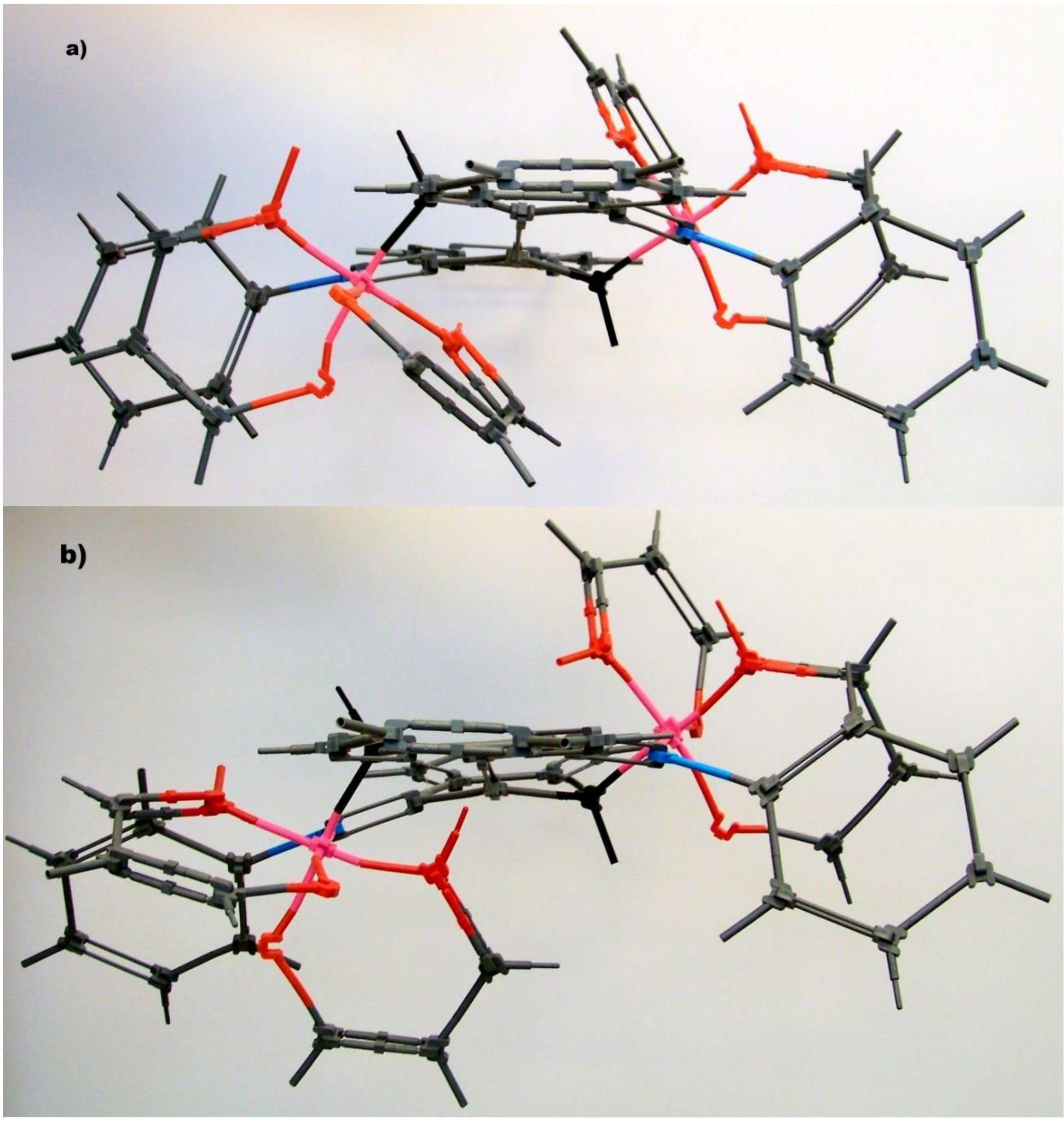

Figure A10. Physical molecular models of a) *meso* diruthenium complex **3.5a** and b) the ΔΔ enantiomer of *rac* diruthenium complex **3.5b**. The trifluoromethyl groups of the β-diketonate ligands have been removed for clarity.

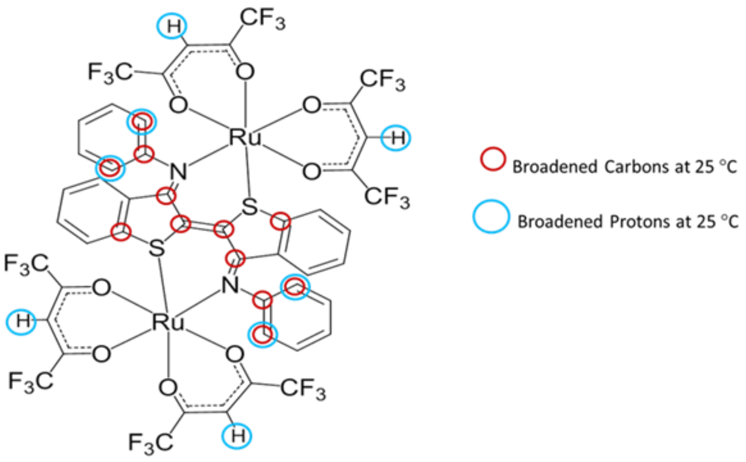

Figure A11. *Rac* diruthenium complex **3.5b**. Carbon atoms with broadened NMR signals at 25 °C are circled in red. Hydrogen atoms (or the carbon to which they are bonded) with broadened NMR signals at 25 °C are circled in blue.

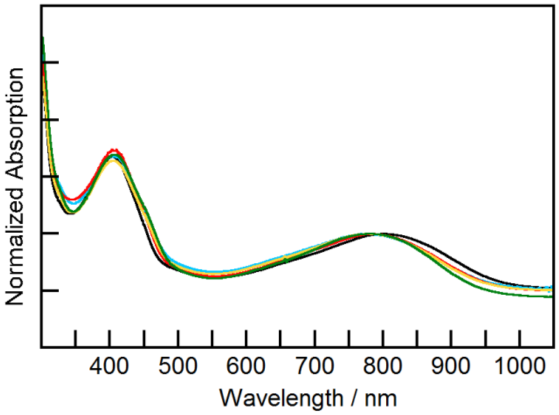

Figure A12. Normalized absorption spectrum of *rac* diruthenium complex **3.5b** in solvents, from right to left: hexanes (black), toluene (red), tetrahydrofuran (blue), methanol (yellow), acetonitrile (green).

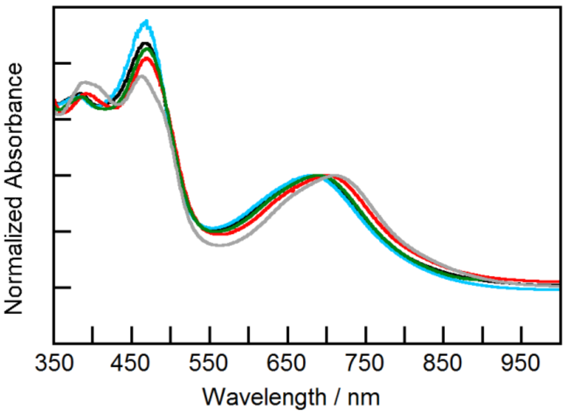

Figure A13. Normalized absorption spectrum of monoruthenium complex **3.4** in solvents, from right to left: hexanes (grey), toluene (red), tetrahydrofuran (green), methanol (black), acetonitrile (blue).

Table A2. Absorbance maxima of compounds **3.5b** and **3.4** in solvents of varying polarity.

Solvent	**Monoruthenium 3.4**				***Rac* diruthenium 3.5b**			
	λ_{max1}^{abs}		λ_{max2}^{abs}		λ_{max1}^{abs}		λ_{max2}^{abs}	
	/ nm	**/ cm^{-1}**	**/ nm**	**/ cm^{-1}**	**/ nm**	**/ cm^{-1}**	**/ nm**	**/ cm^{-1}**
Acetonitrile	679	14728	468	21368	775	12903	405	24691
Methanol	683	14641	465	21505	774	12920	405	24691
Tetrahydrofuran	689	14514	469	21322	773	12937	406	24630
Toluene	698	14327	469	21322	785	12739	403	24814
Hexane	710	14085	463	21598	801	12484	404	24753

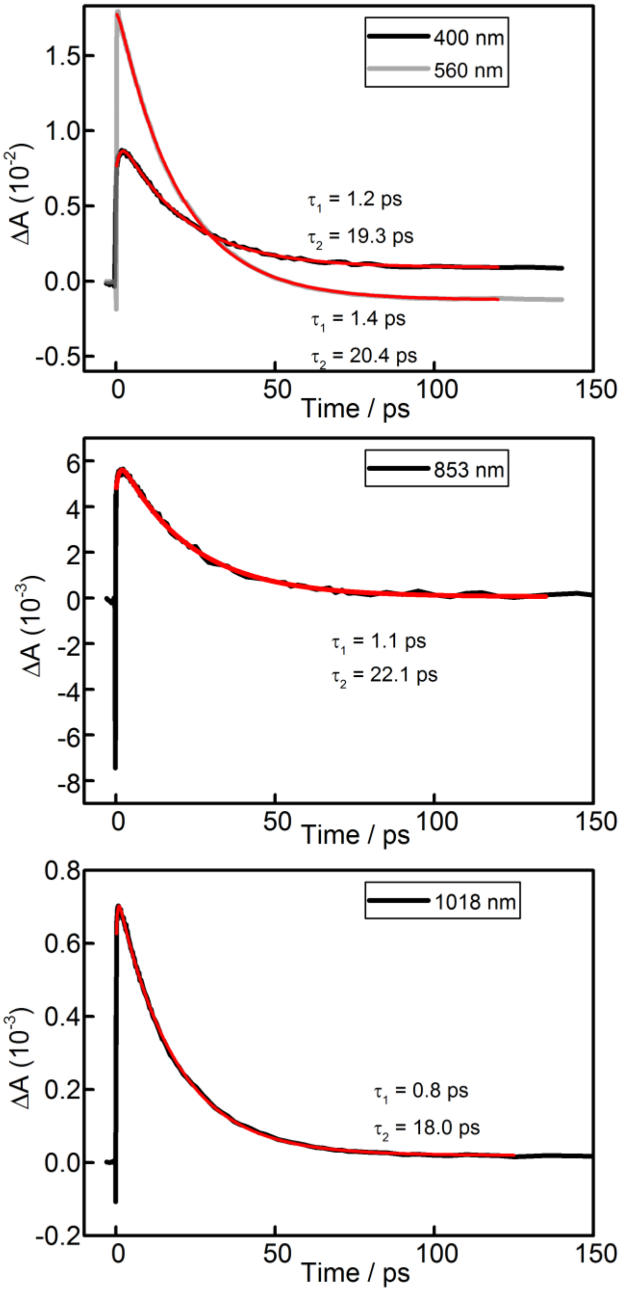

Figure A14. Transient decay traces (black) and kinetics of monoruthenium complex **3.4**. The pulsed laser excitation wavelength is 700 nm. The pulse power is 0.5 μJ. The monitoring wavelengths and extracted rate constants are indicated in the graphs. The decays were fit to a sum of two exponentials (red trace) using Origin 2016.

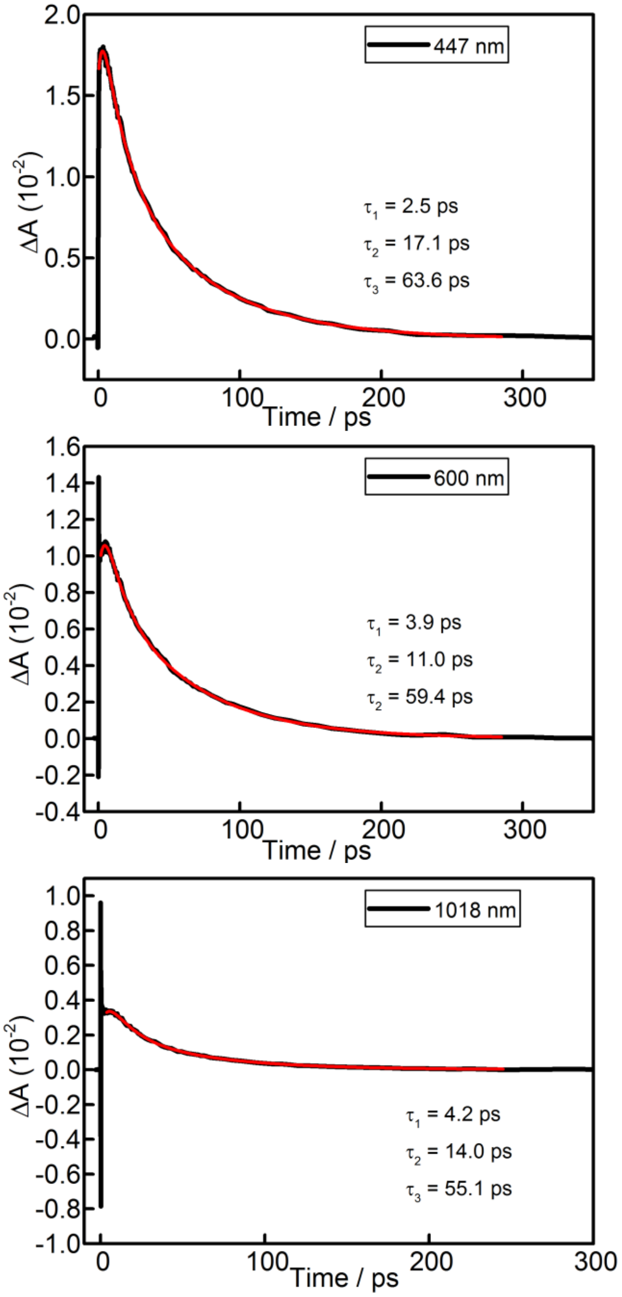

Figure A15. Transient decay traces (black) and kinetics of *meso* diruthenium complex **3.5a**. The pulsed laser excitation wavelength is 800 nm and the pulse power is 1.0 μJ. The monitoring wavelengths and extracted rate constants are indicated in the graphs. The decays were fit to a sum of three exponentials (red trace) using Origin 2016.

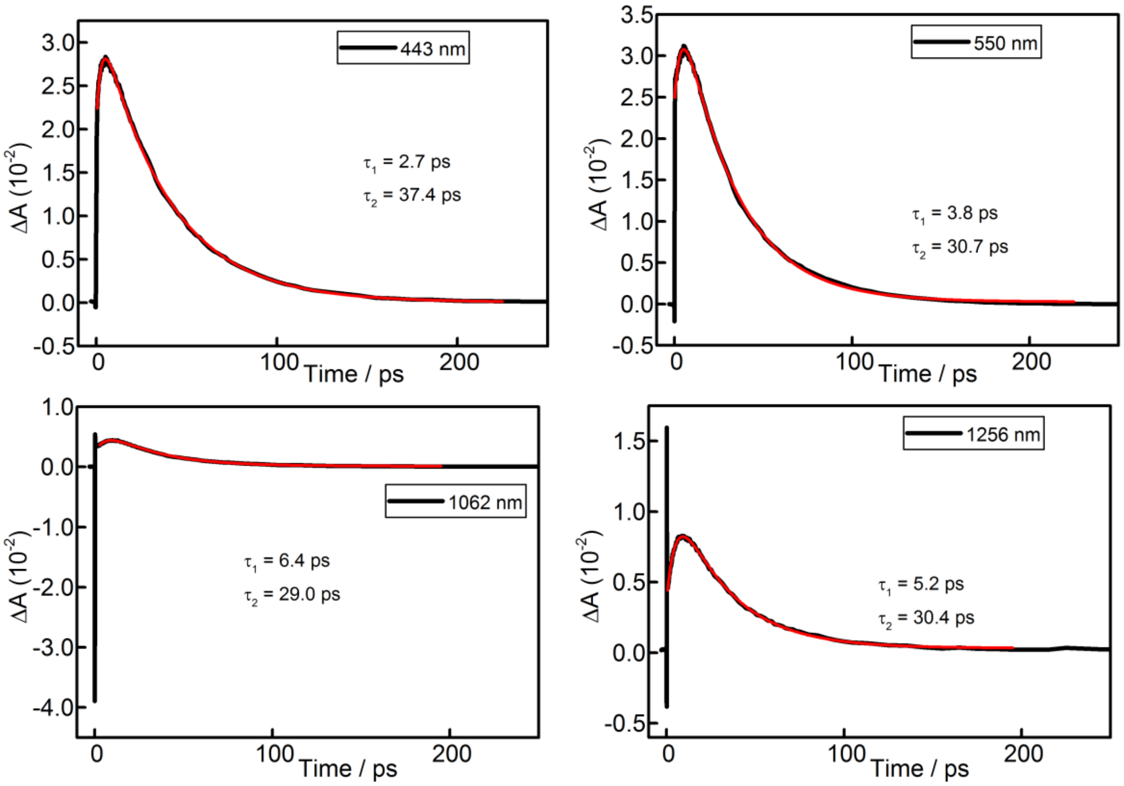

Figure A16. Transient decay traces (black) and kinetics of *rac* diruthenium complex **3.5b**. The pulsed laser excitation wavelength is 800 nm. The pulse power is 1.5 μJ in the 443 and 550 nm traces; it is 1.0 μJ in the 1062 and 1256 traces. The monitoring wavelengths and extracted rate constants are indicated in the graphs. The decays were fit to a sum of two exponentials (red trace) using Origin 2016.

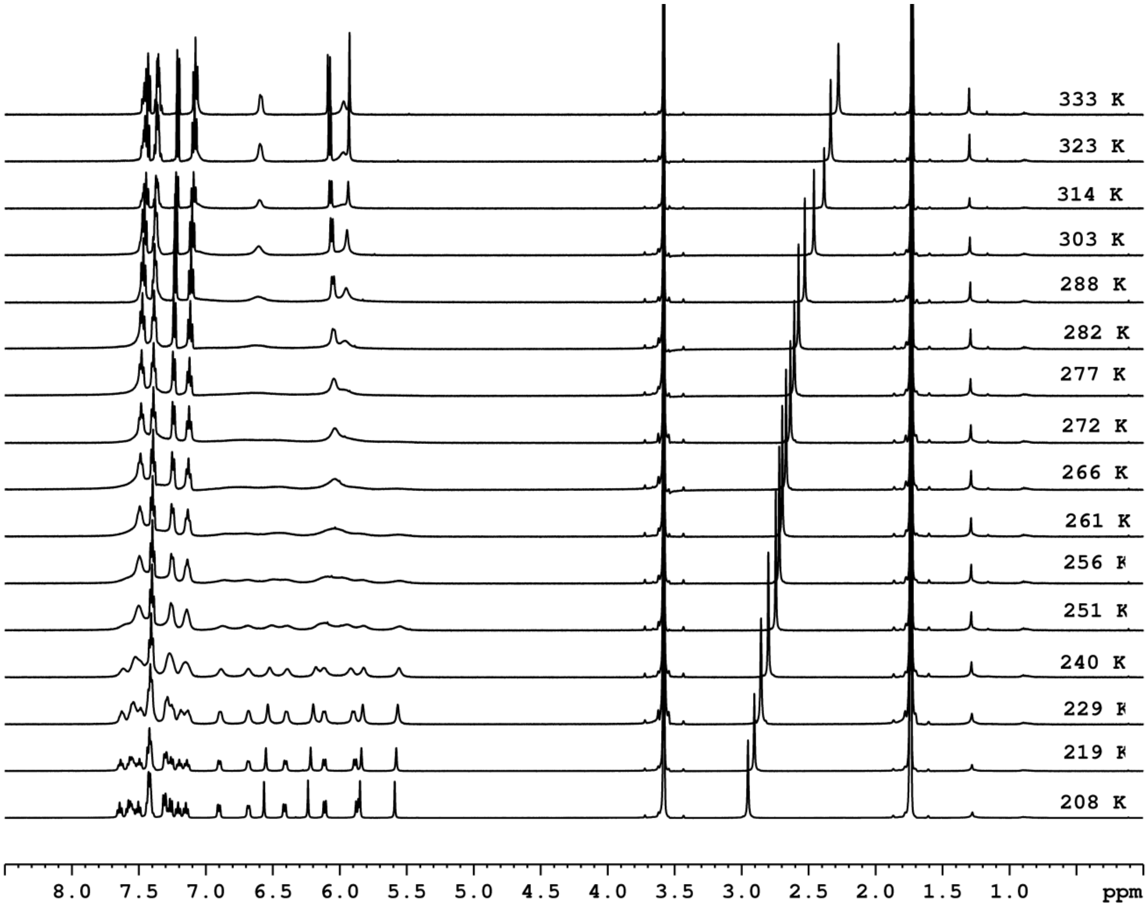

Figure A17. Variable temperature ^{1}H NMR spectra (THF-*d8*, 500 MHz) for *rac* diruthenium complex **3.5b**. The temperature at which each spectrum was collected is indicated in the figure.

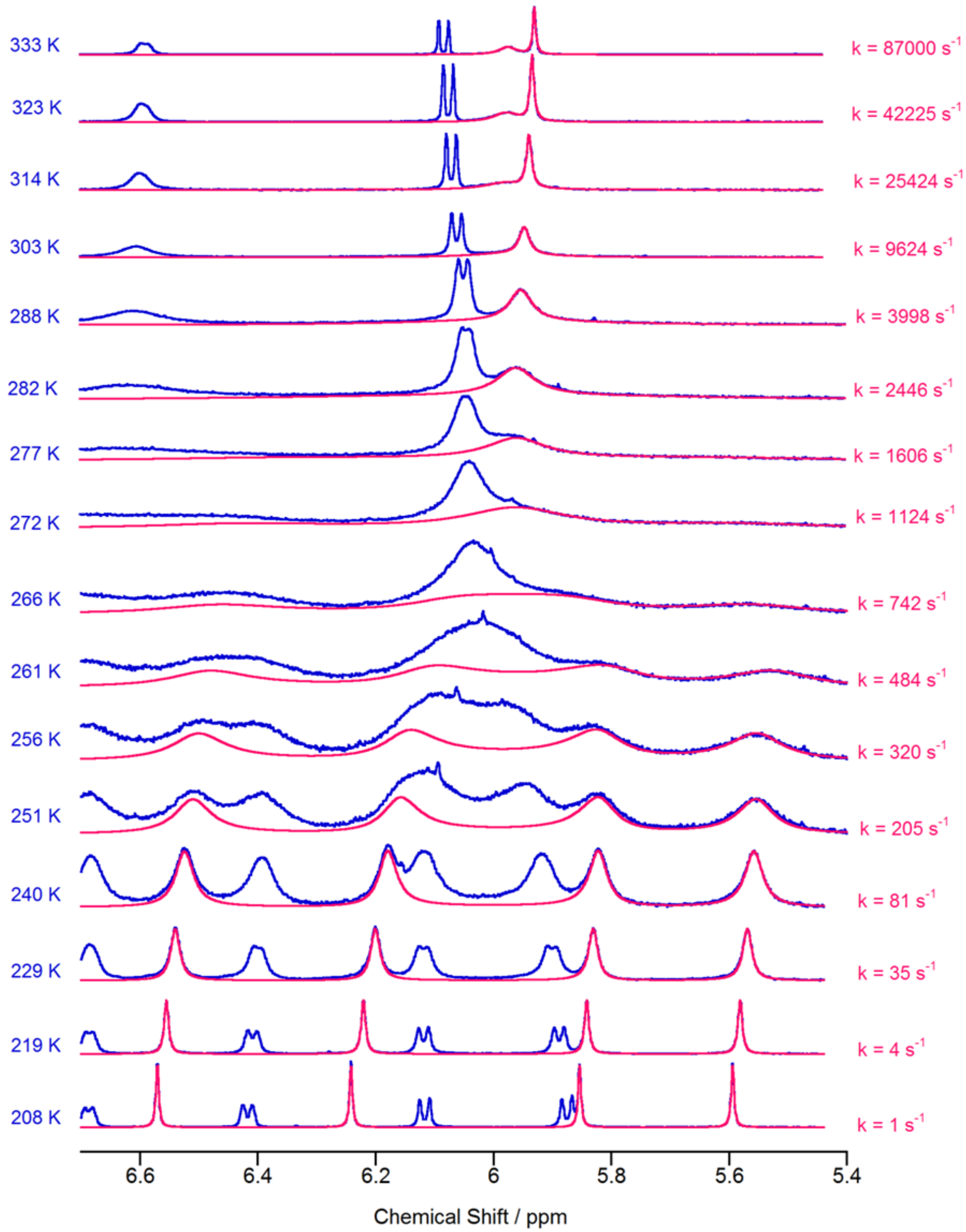

Figure A18. Variable temperature ^{1}H NMR spectra (blue) and winDNMR simulations (red) for *rac* diruthenium complex **3.5b**. The temperatures of the spectra and the rate constants obtained for the corresponding simulations are indicated in the figure.

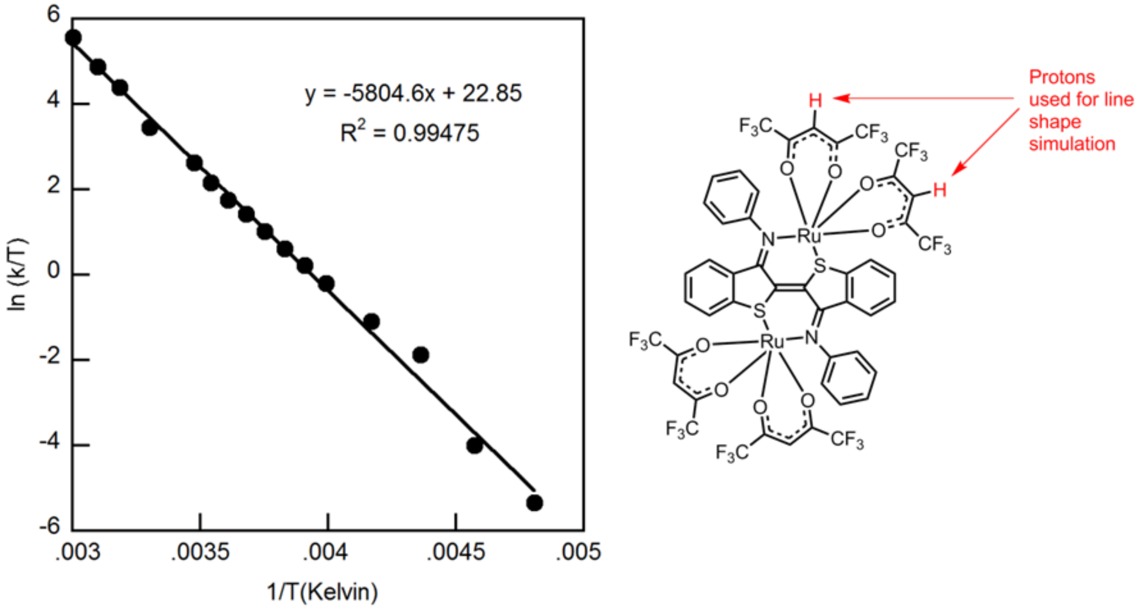

$\Delta H^‡ = 11.5$ kcal mol^{-1}
$\Delta S^‡ = -1.8$ cal mol^{-1} K^{-1}
$\Delta G^‡_{298} = 12.0$ kcal mol^{-1}

Figure A19. Eyring plot (left) using data from the variable temperature spectra and simulations of **3.5b** shown in figure A18 above. The structure of **3.5b** (right) showing the protons used for the line shape analysis.

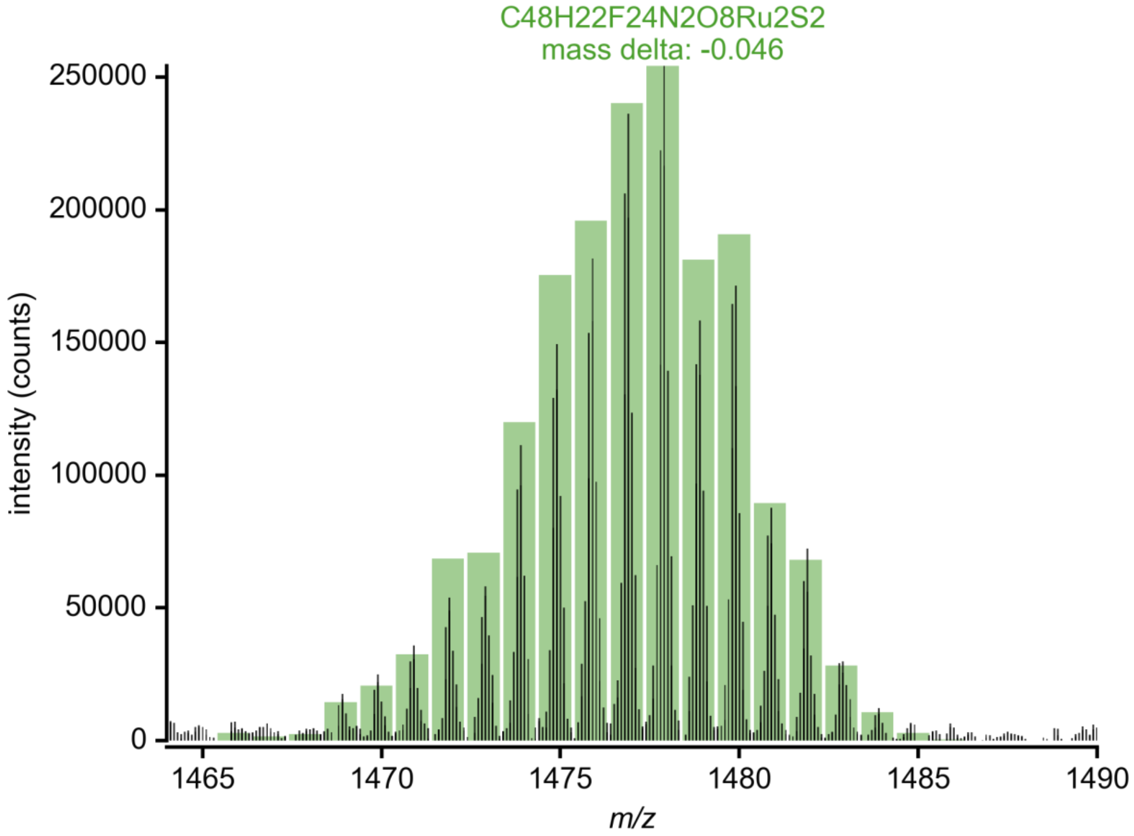

Figure A20. Low resolution mass spectrum of *meso* diruthenium complex **3.5a** with overlay of predicted isotope pattern for M+.

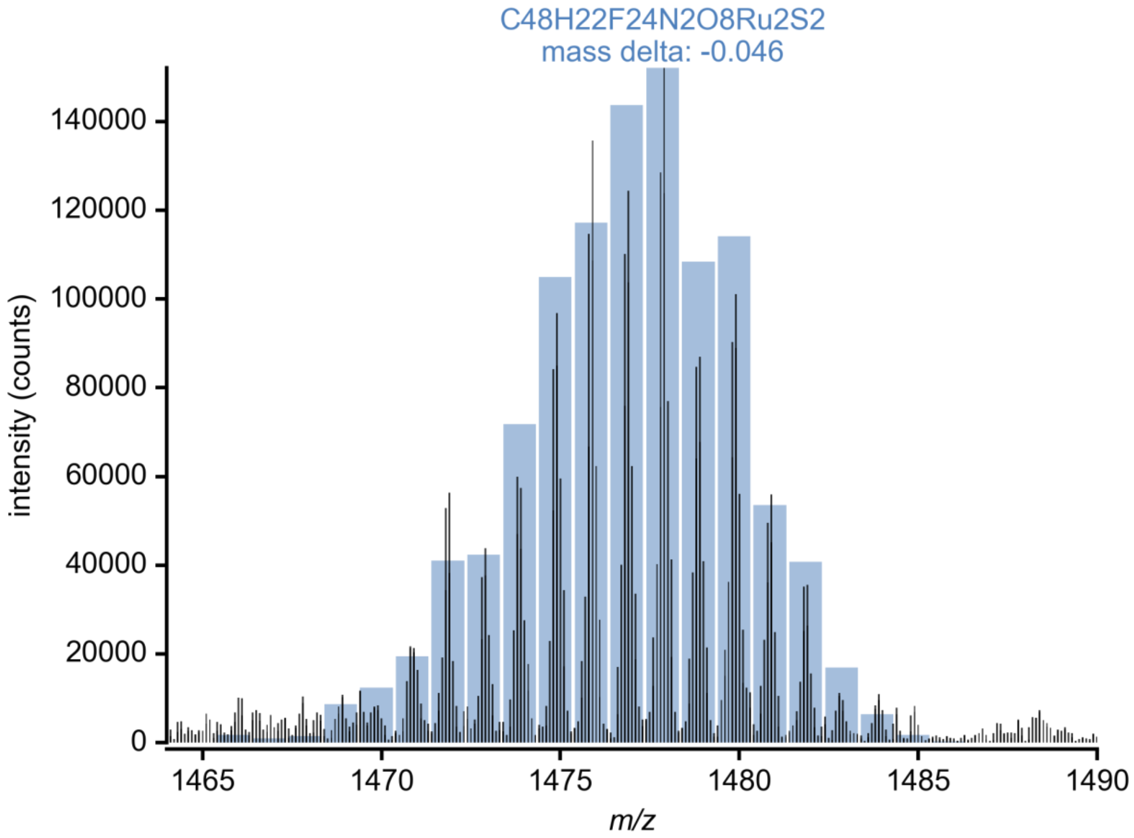

Figure A21. Low resolution mass spectrum of *rac* diruthenium complex **3.5b** with overlay of predicted isotope pattern for M+.

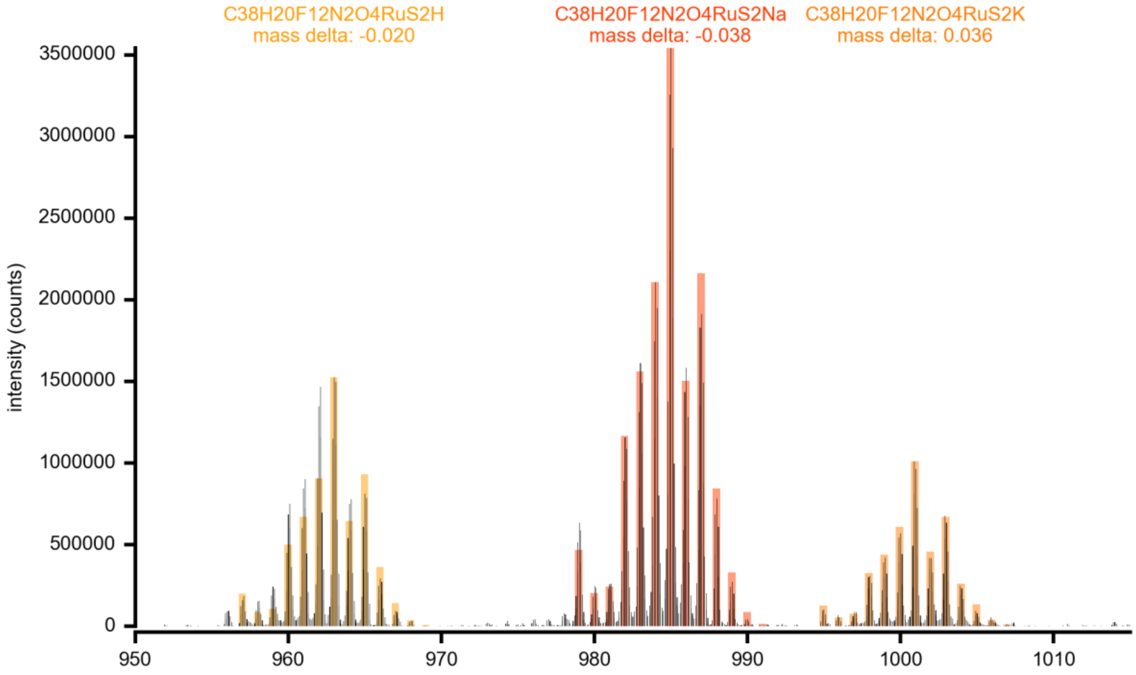

Figure A22. Low resolution mass spectrum of monoruthenium complex **3.4** with overlay of predicted isotope pattern for M+H (left), M+Na (middle), and M+K (right).

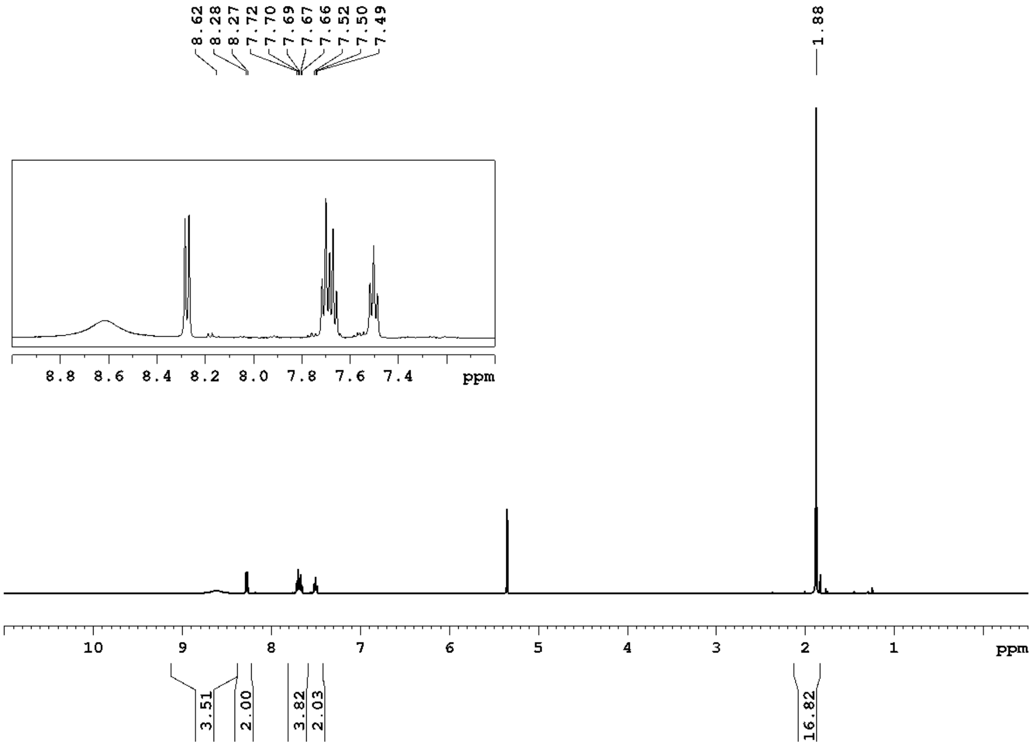

Figure A23. ^{1}H NMR spectrum (360MHz, CD_2Cl_2, 293 K) of **2.3a** with 1 equiv. of TFAA.

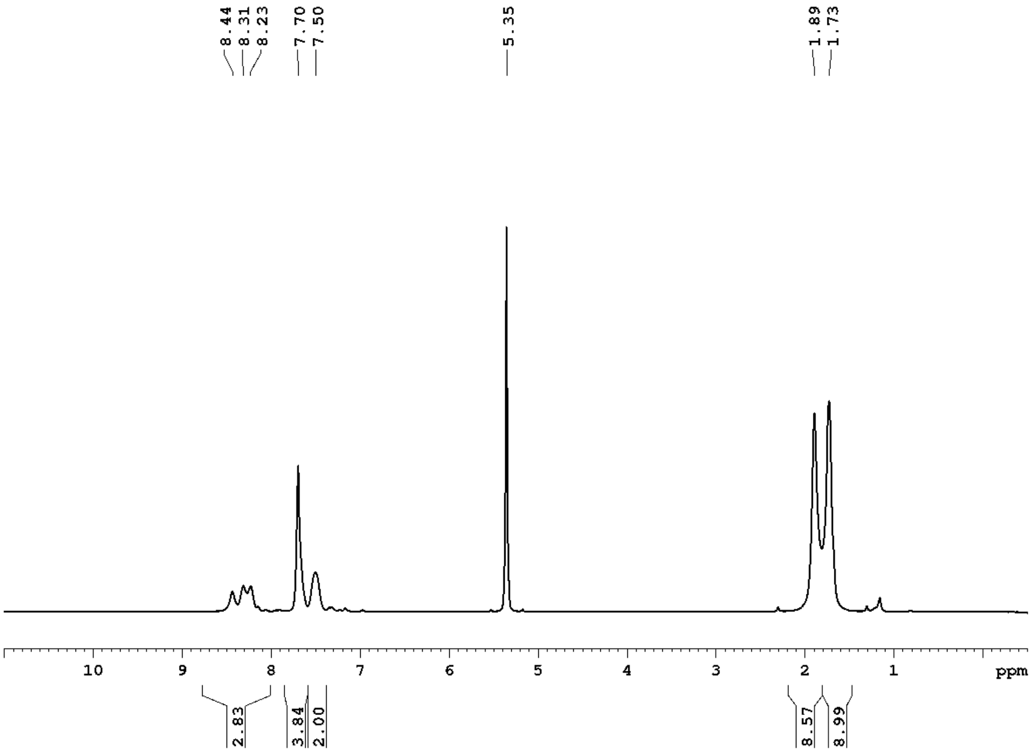

Figure A24. ^{1}H NMR spectrum (360MHz, CD_2Cl_2, 183 K) of **2.3a** with 1 equiv. of TFAA.

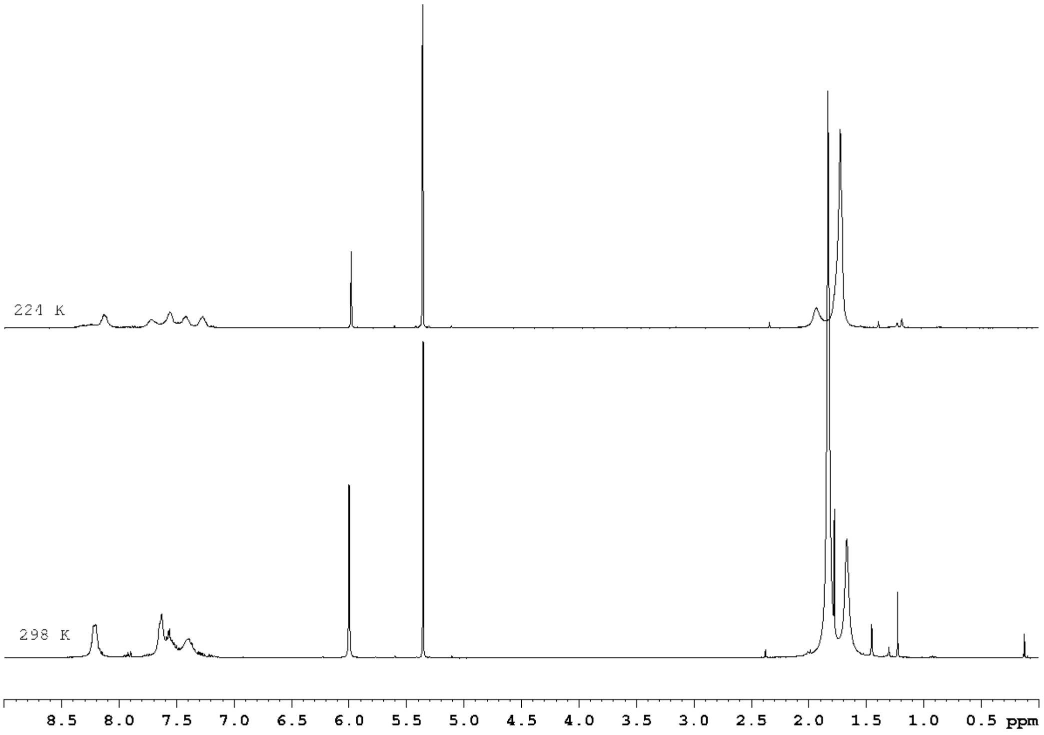

Figure A25. ^{1}H NMR spectra (360 MHz, CD_2Cl_2) of the reaction of **2.3a** with $Zn(Hfac)_2 \cdot 2H_2O$. The upper spectrum was obtained at a temperature of 224 K and the lower spectrum was obtained at a temperature of 293 K.

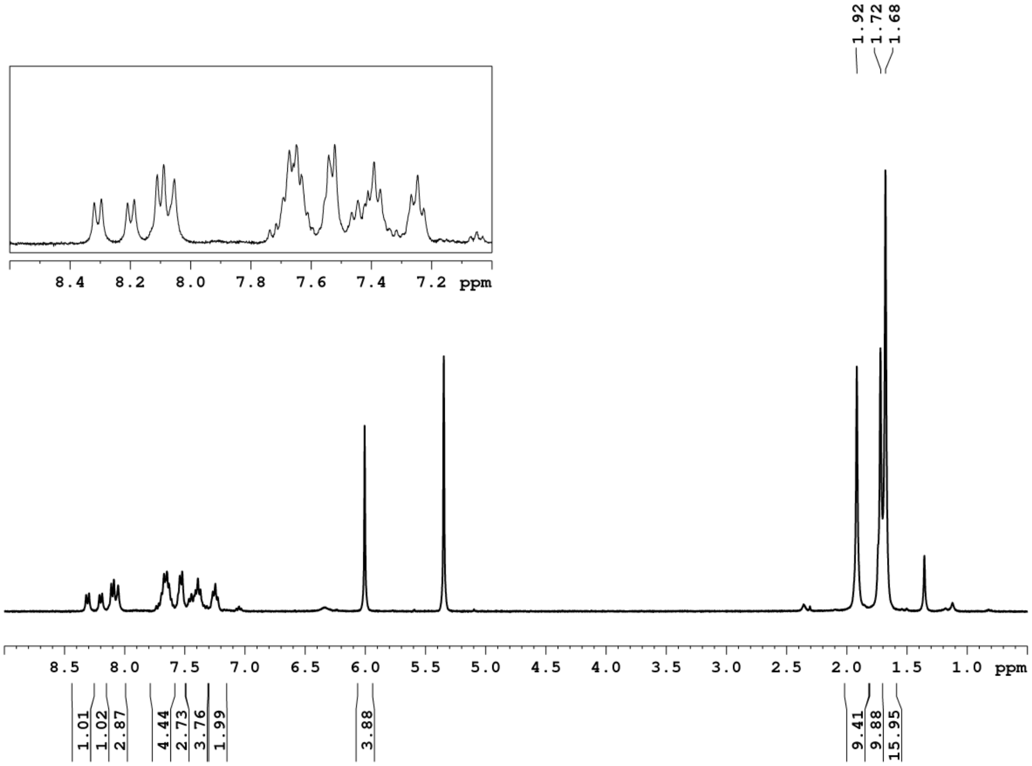

Figure A26. ^{1}H NMR spectrum (360 MHz, CD_2Cl_2) of the reaction of **2.3a** with $Zn(Hfac)_2 \cdot 2H_2O$ after heating. The spectrum was obtained at a temperature of 191 K.

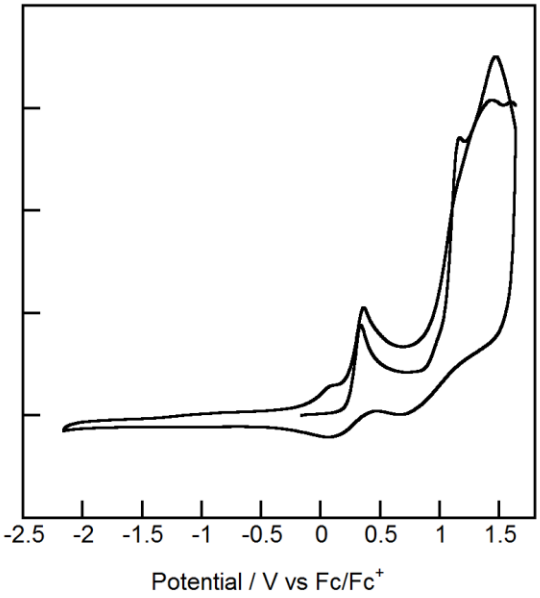

Figure A27. Cyclic voltammogram of 7,7′-amino-3-*tert*-butyl-diindole **4.26,** cycled twice in the region from -0.2 to 1.6 V. The concentration of analyte in dichloromethane is ~1 mM. The standard is Fc/Fc$^+$, the electrolyte is 0.1 M Bu_4NPF_6 and the scan rate is 100 mV s^{-1}.

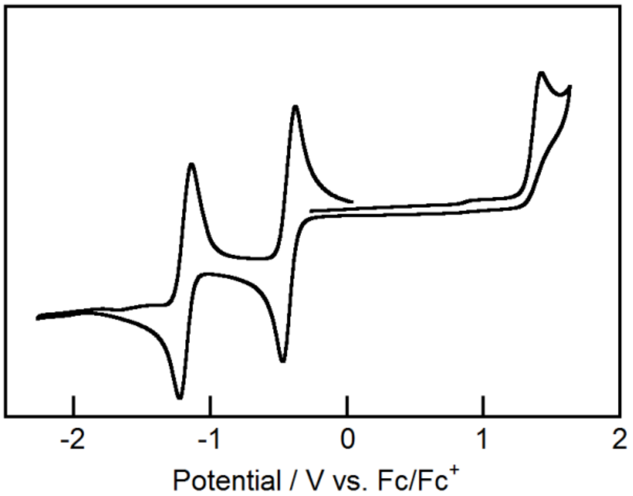

Figure A28. Cyclic voltammogram of p-chloranil in dichloromethane. The concentration of analyte in dichloromethane is ~1 mM. The standard is Fc/Fc$^+$, the electrolyte is 0.1 M Bu_4NPF_6 and the scan rate is 100 mV s^{-1}.

Appendix B. NMR Spectra of Characterized Compounds

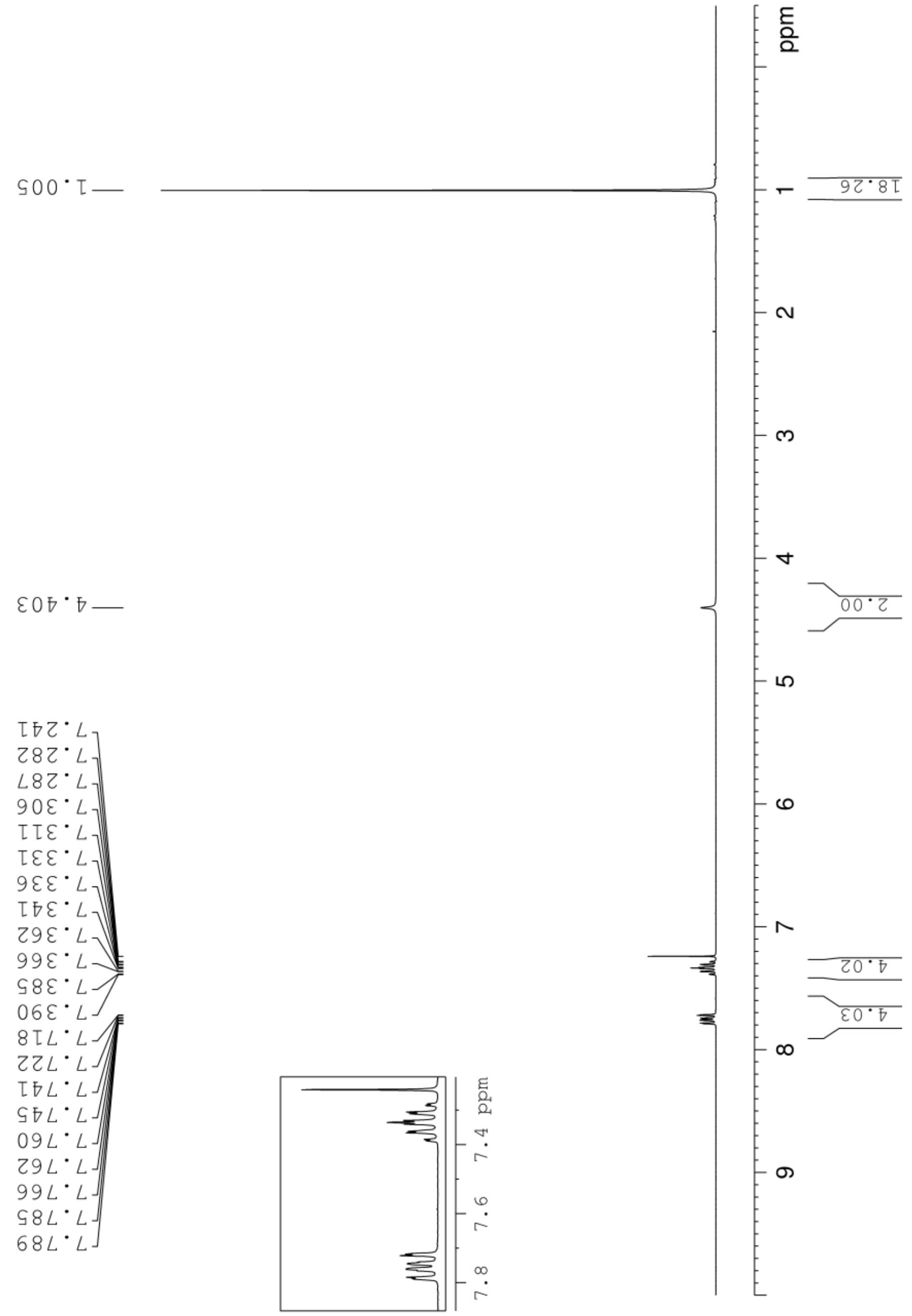

Figure A29. ^{1}H NMR (300 MHz, $CDCl_3$) spectrum of compound **2.2a**.

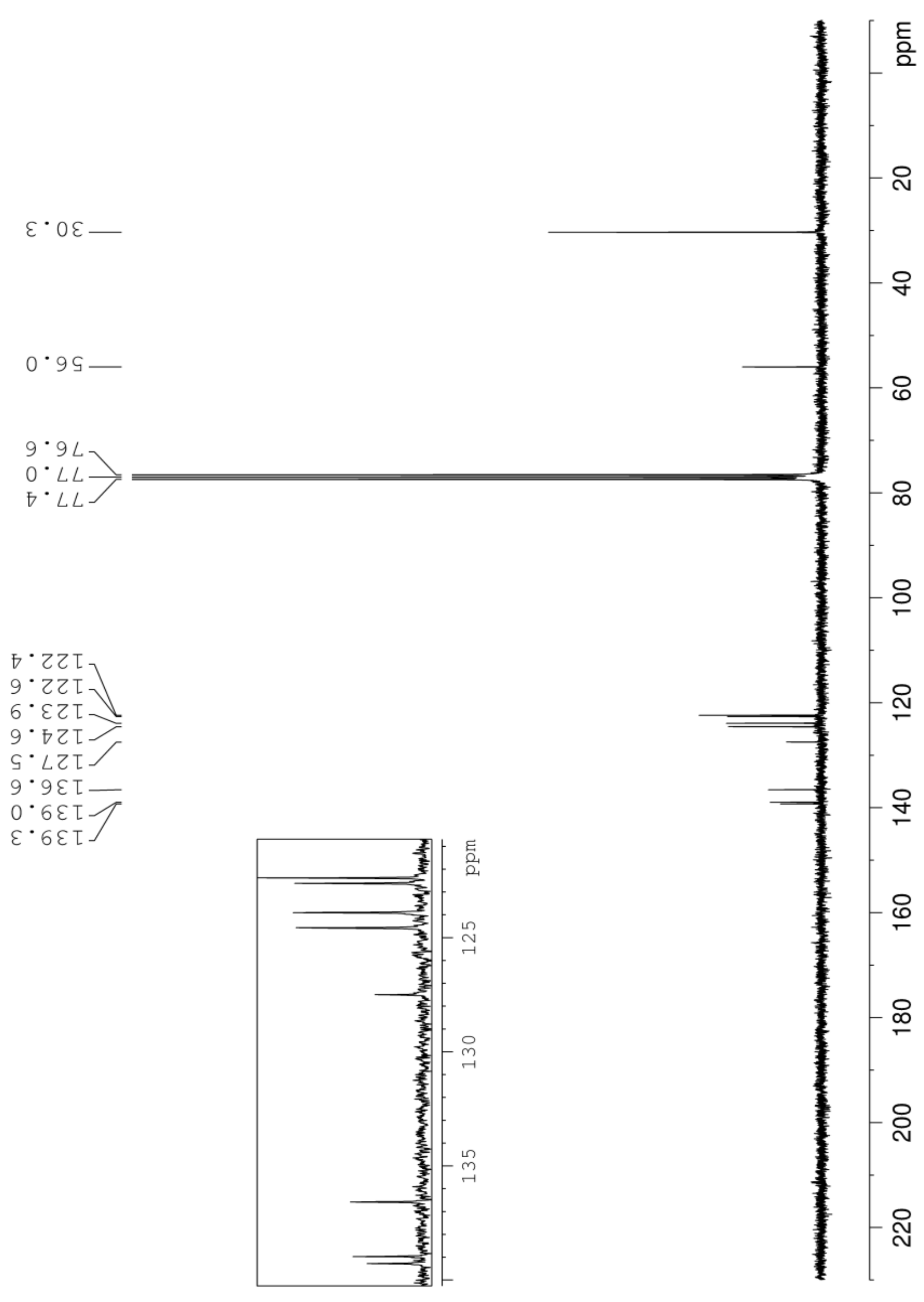

Figure A30. ^{13}C NMR (75 MHz, CDCl$_3$) spectrum of compound **2.2a**.

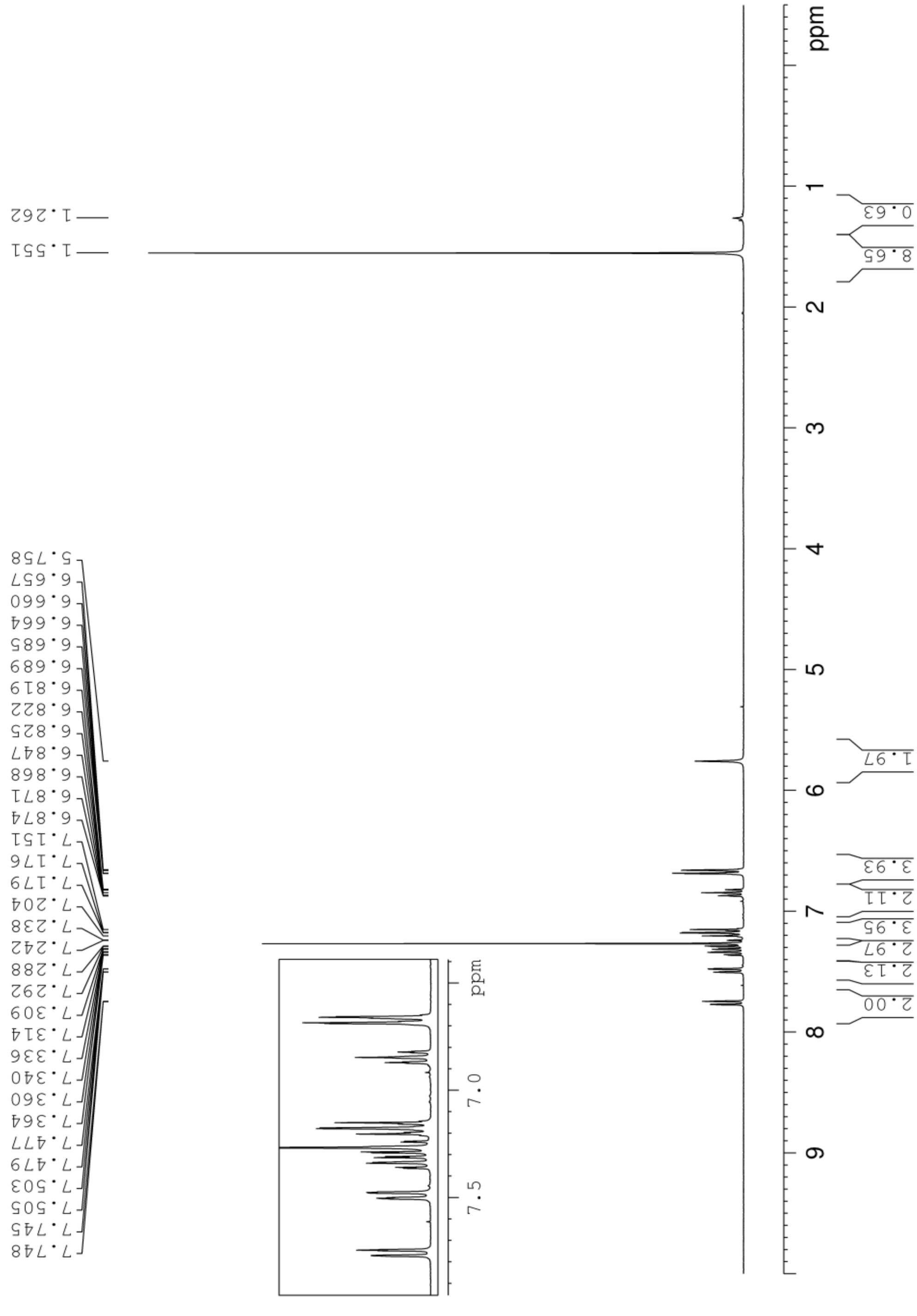

Figure A31. ^{1}H NMR (300 MHz, $CDCl_3$) spectrum of compound **2.2b**.

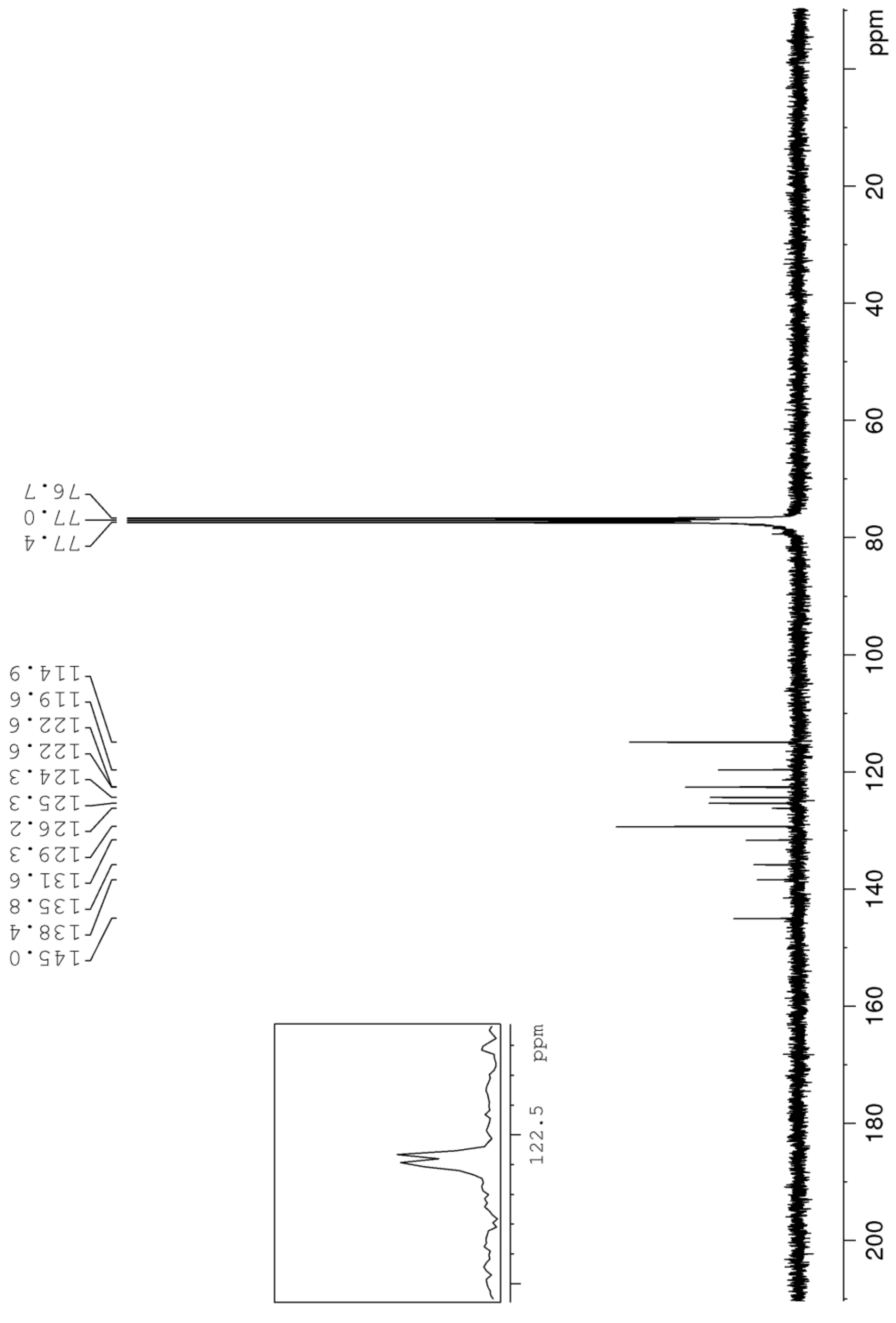

Figure A32. ^{13}C NMR (90 MHz, $CDCl_3$) spectrum of compound **2.2b**.

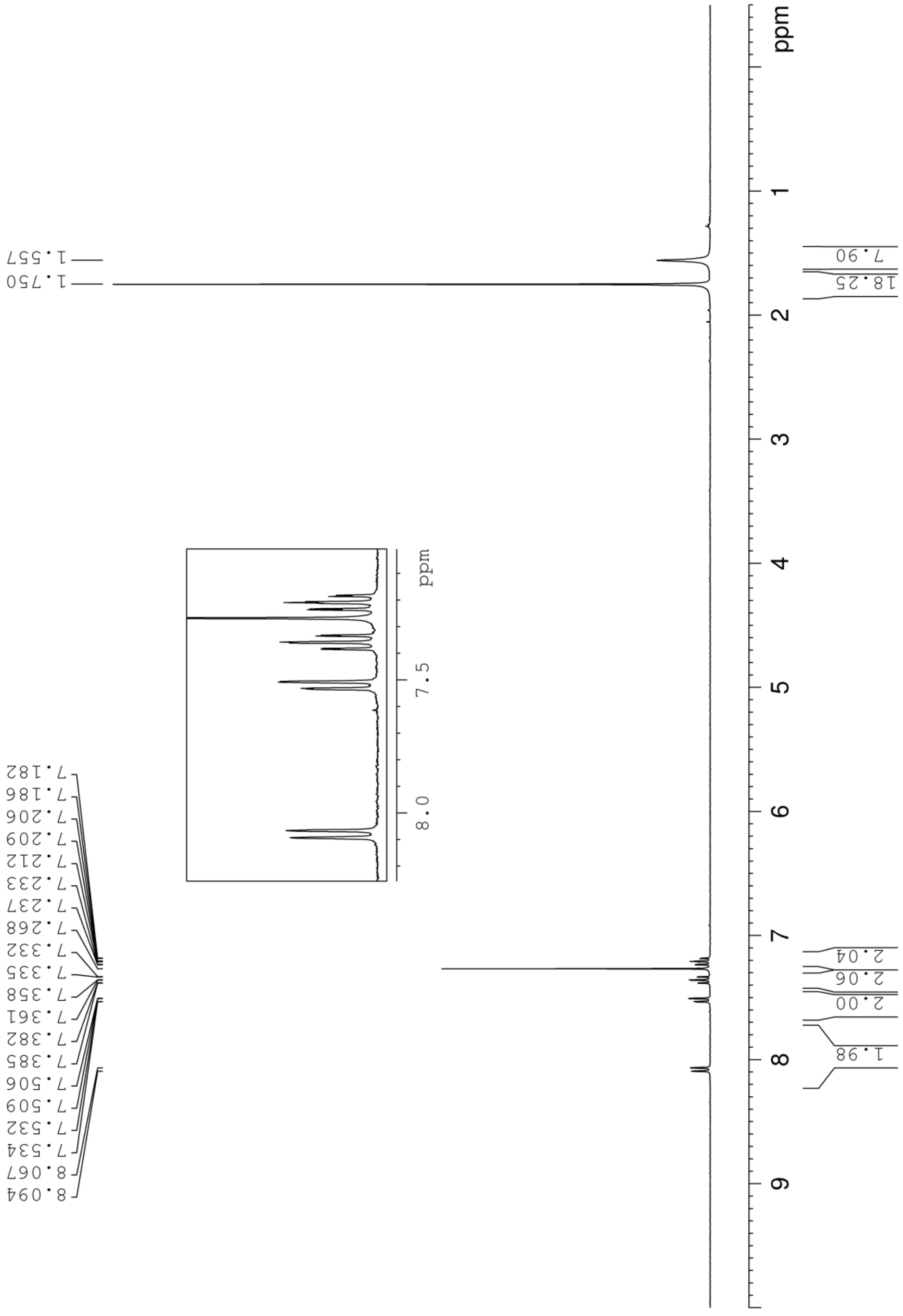

Figure A33. ¹H NMR (300 MHz, $CDCl_3$) spectrum of compound **2.3a**.

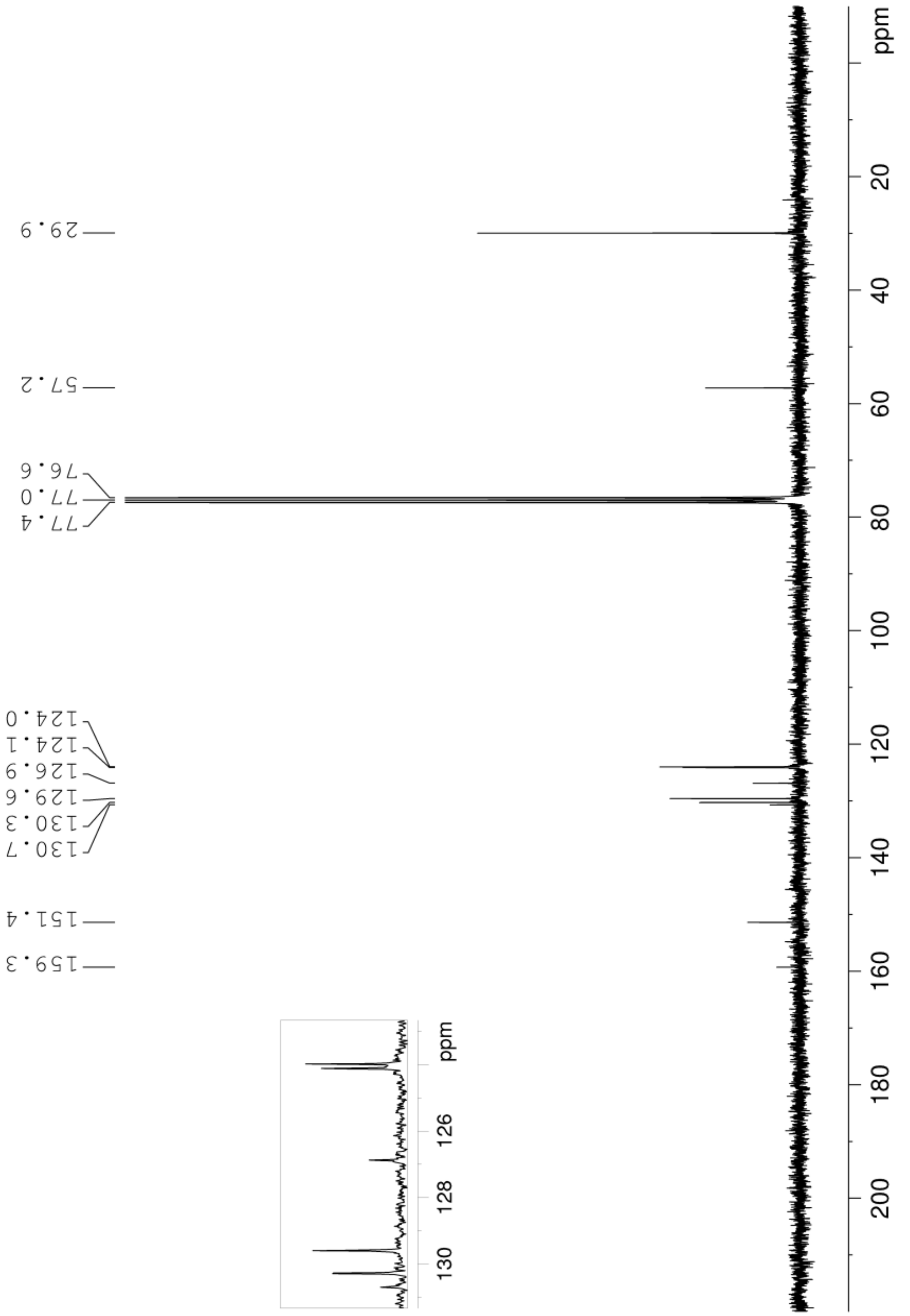

Figure A34. ^{13}C NMR (75 MHz, $CDCl_3$) spectrum of compound **2.3a**.

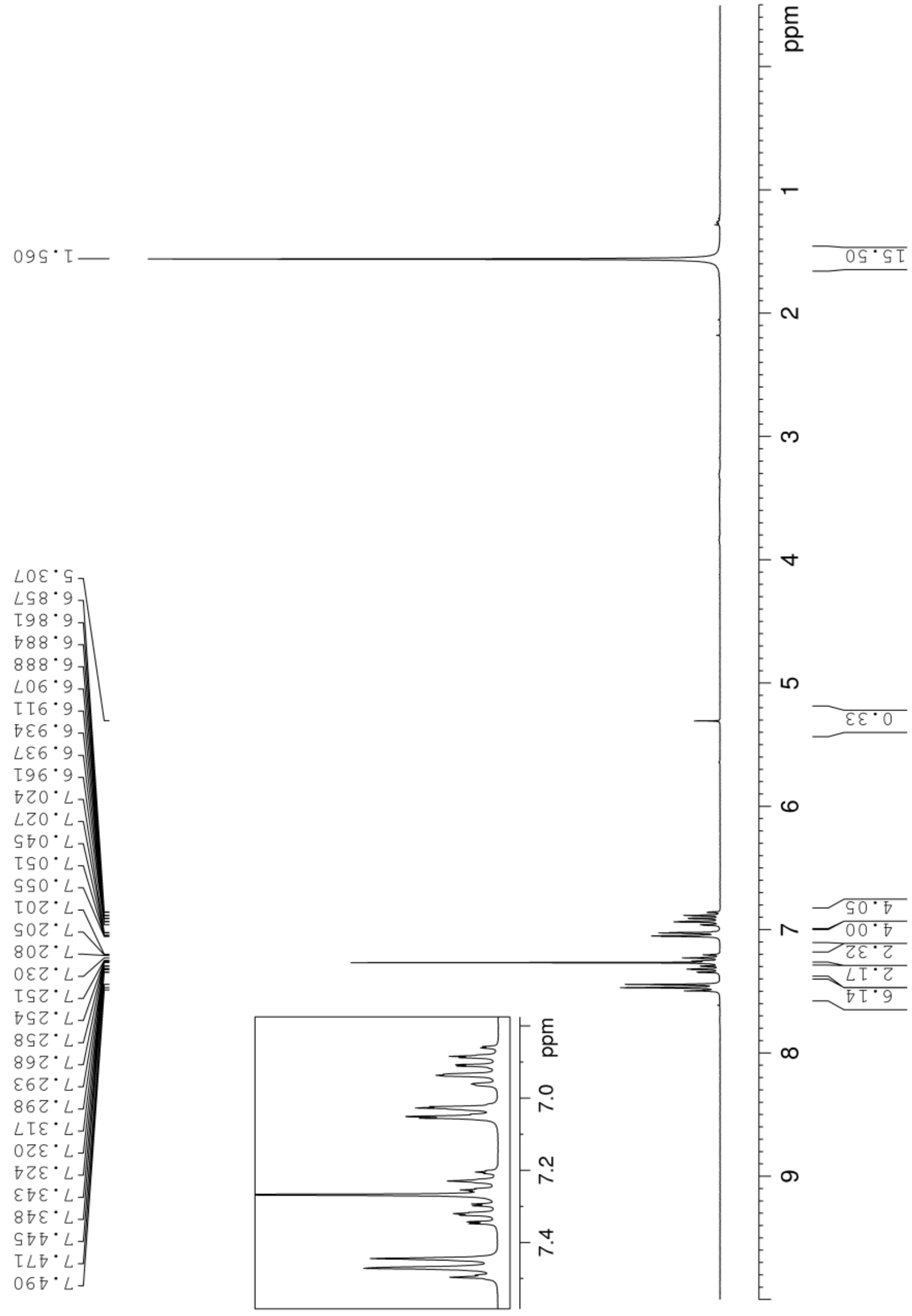

Figure A35. ¹H NMR (300 MHz, CDCl₃) spectrum of compound **2.3b**.

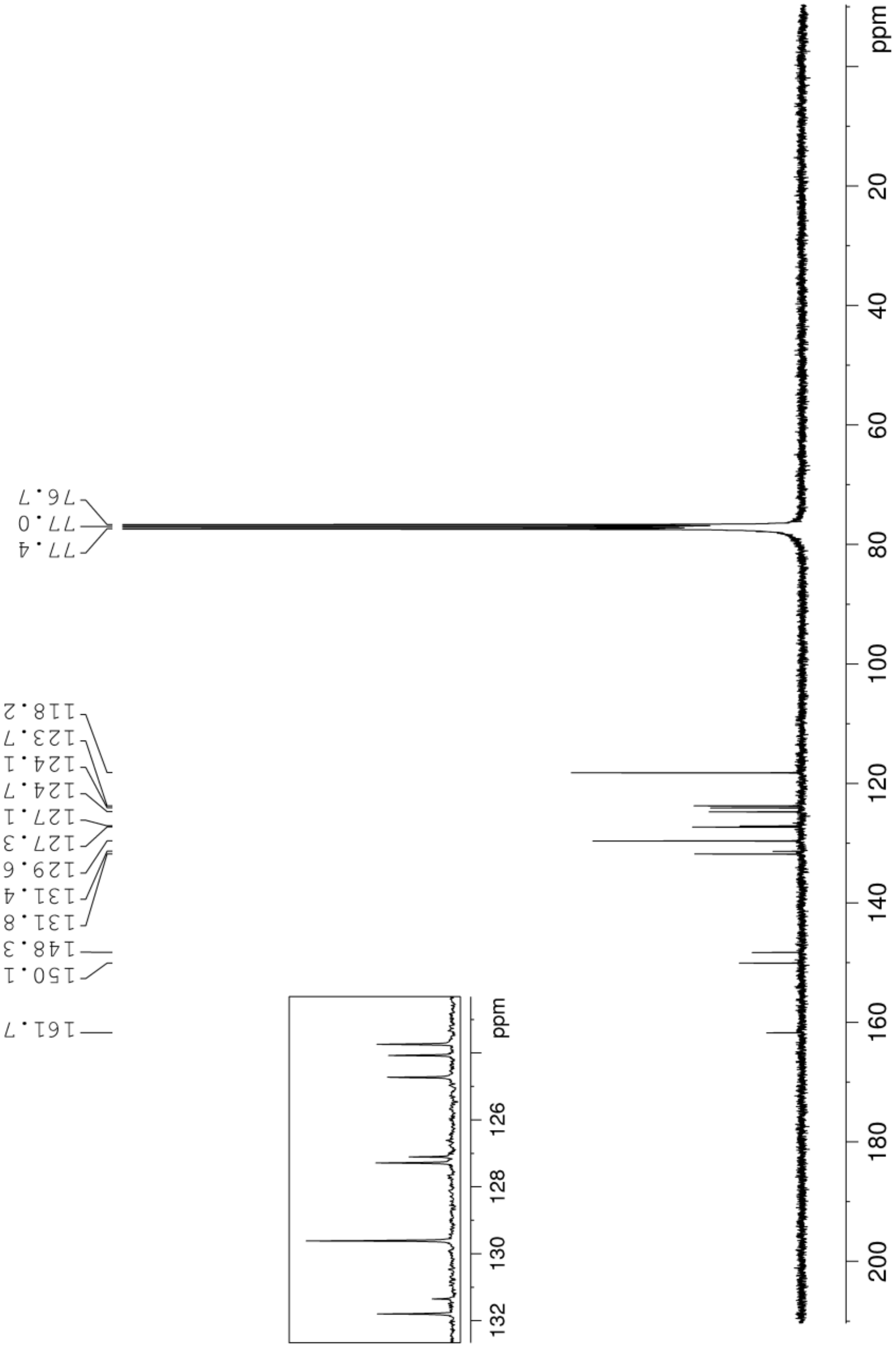

Figure A36. ^{13}C NMR (90 MHz, $CDCl_3$) spectrum of compound **2.3b**.

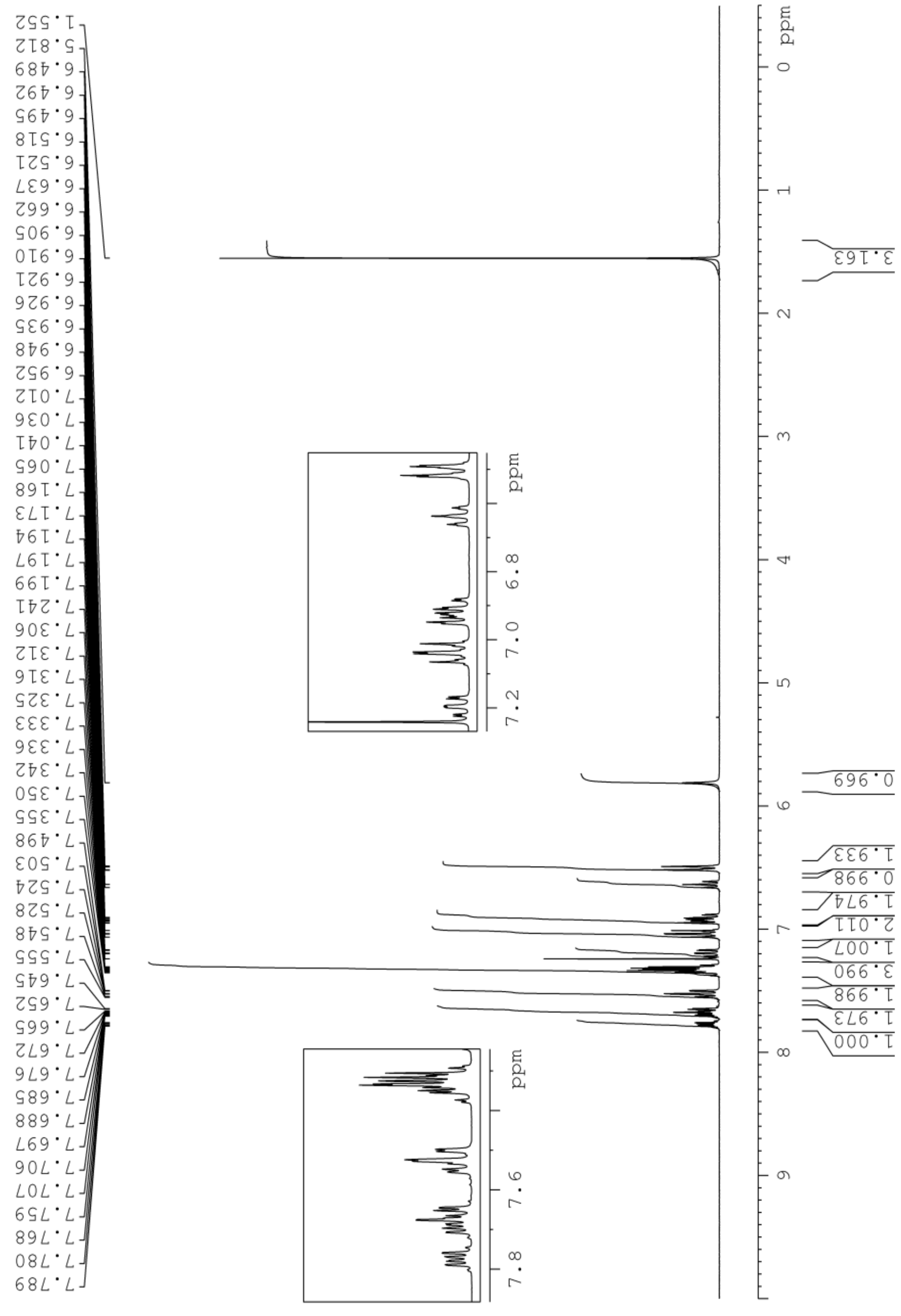

Figure A37. ^{1}H NMR (360 MHz, $CDCl_3$) spectrum of compound **2.4b**.

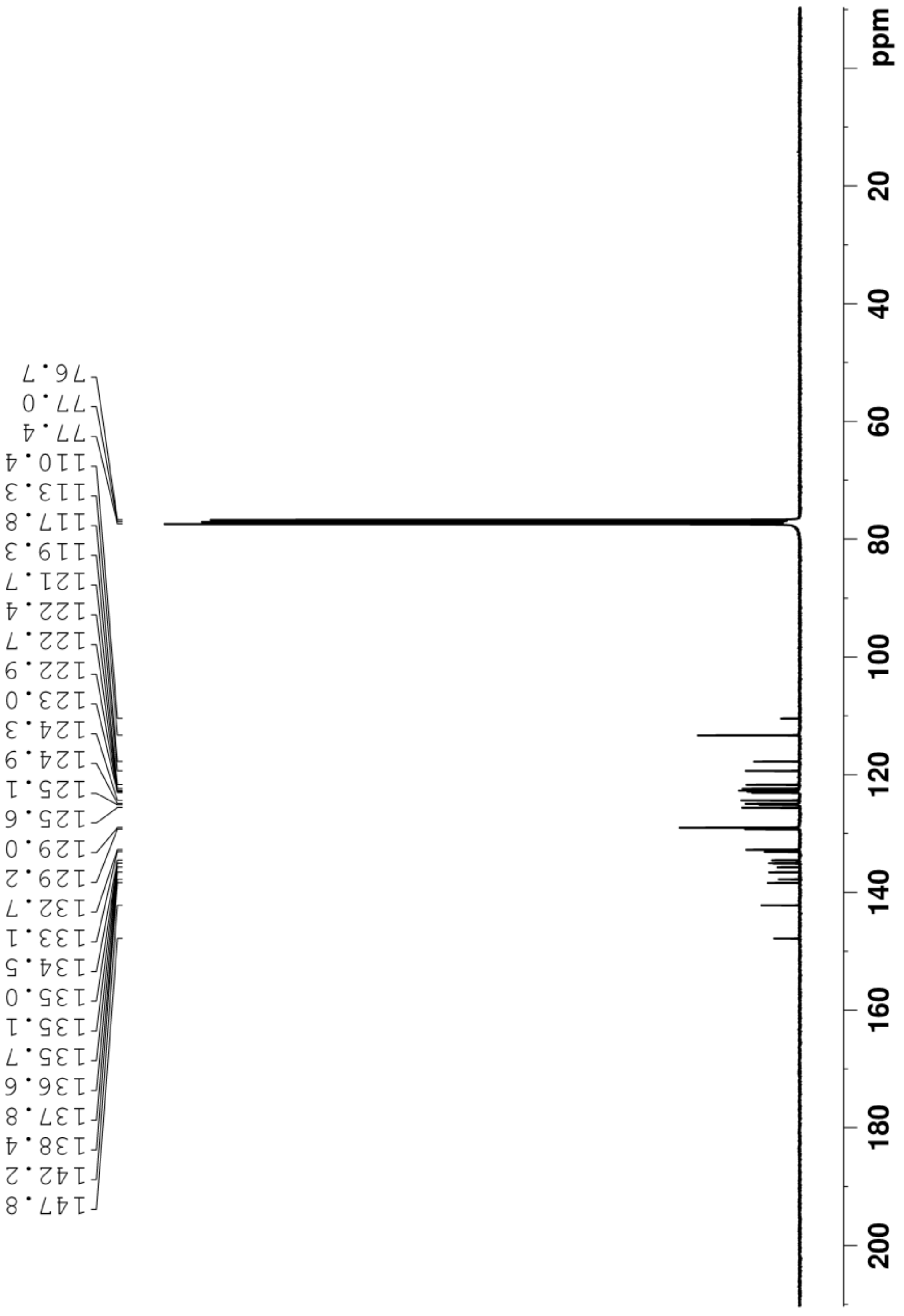

Figure A38. ^{13}C NMR (90 MHz, $CDCl_3$) spectrum of compound **2.4b**.

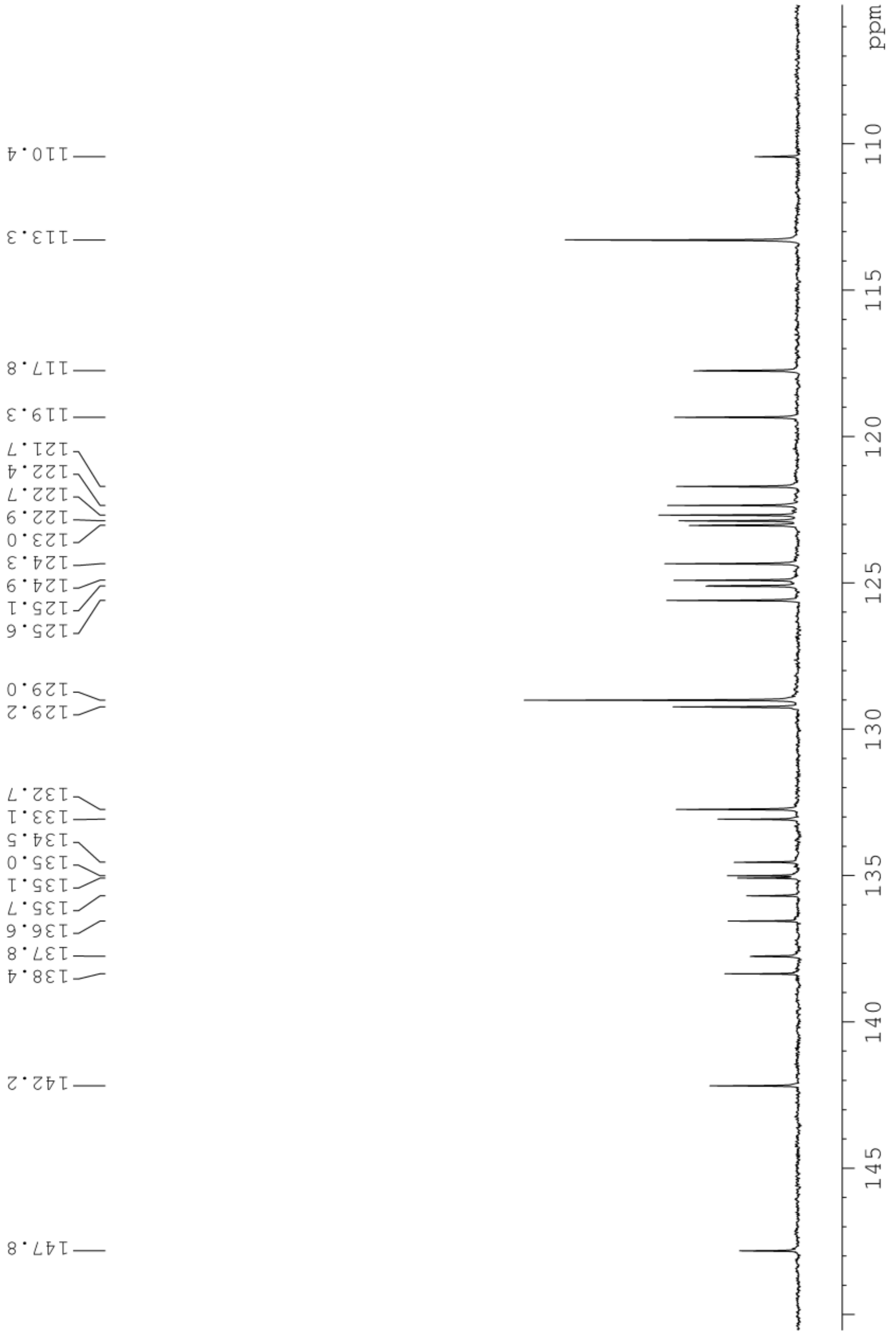

Figure A39. ^{13}C NMR (90 MHz, $CDCl_3$) expanded spectrum of compound **2.4b**.

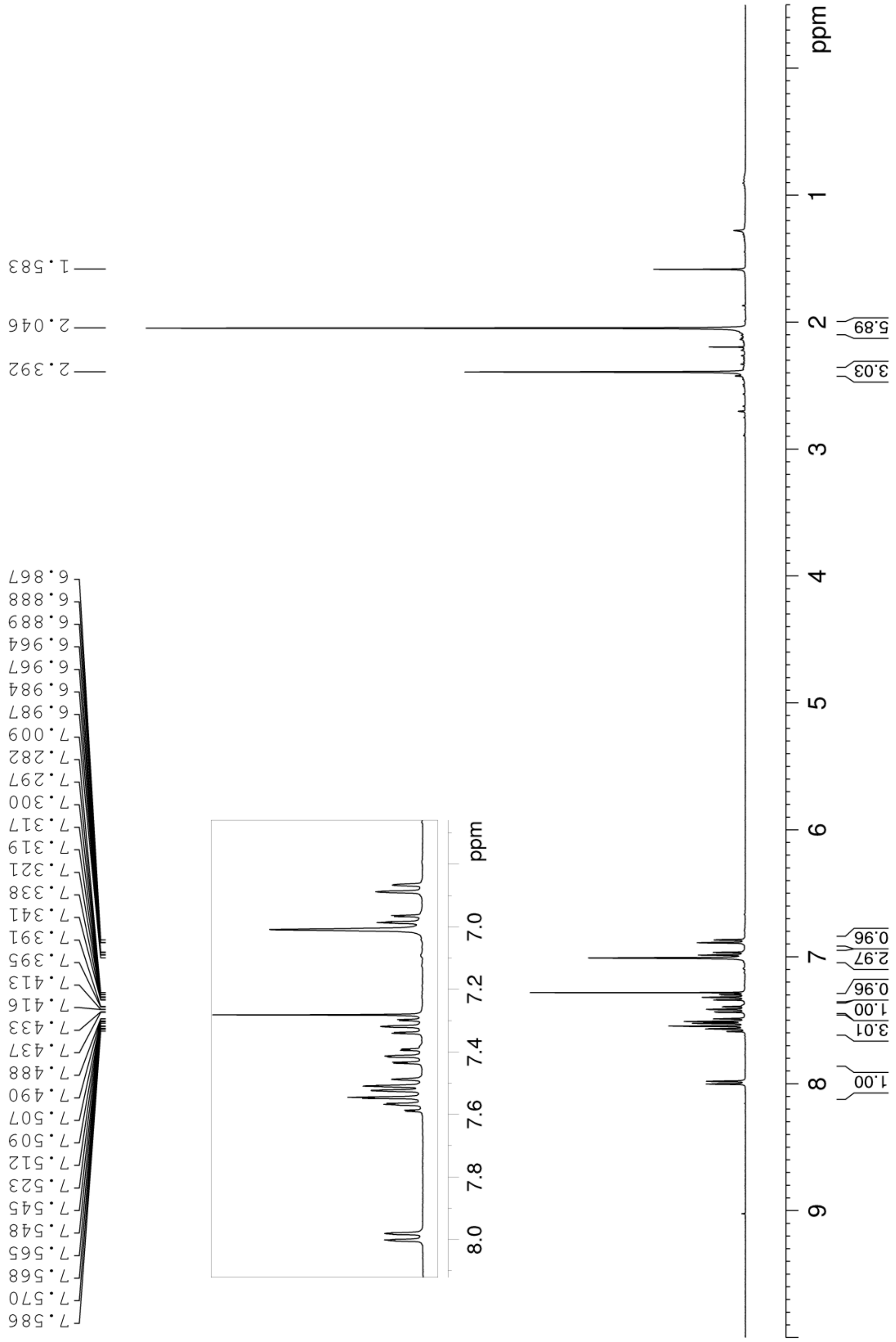

Figure A40. ^{1}H NMR (360 MHz, $CDCl_3$) spectrum of compound **2.5c**.

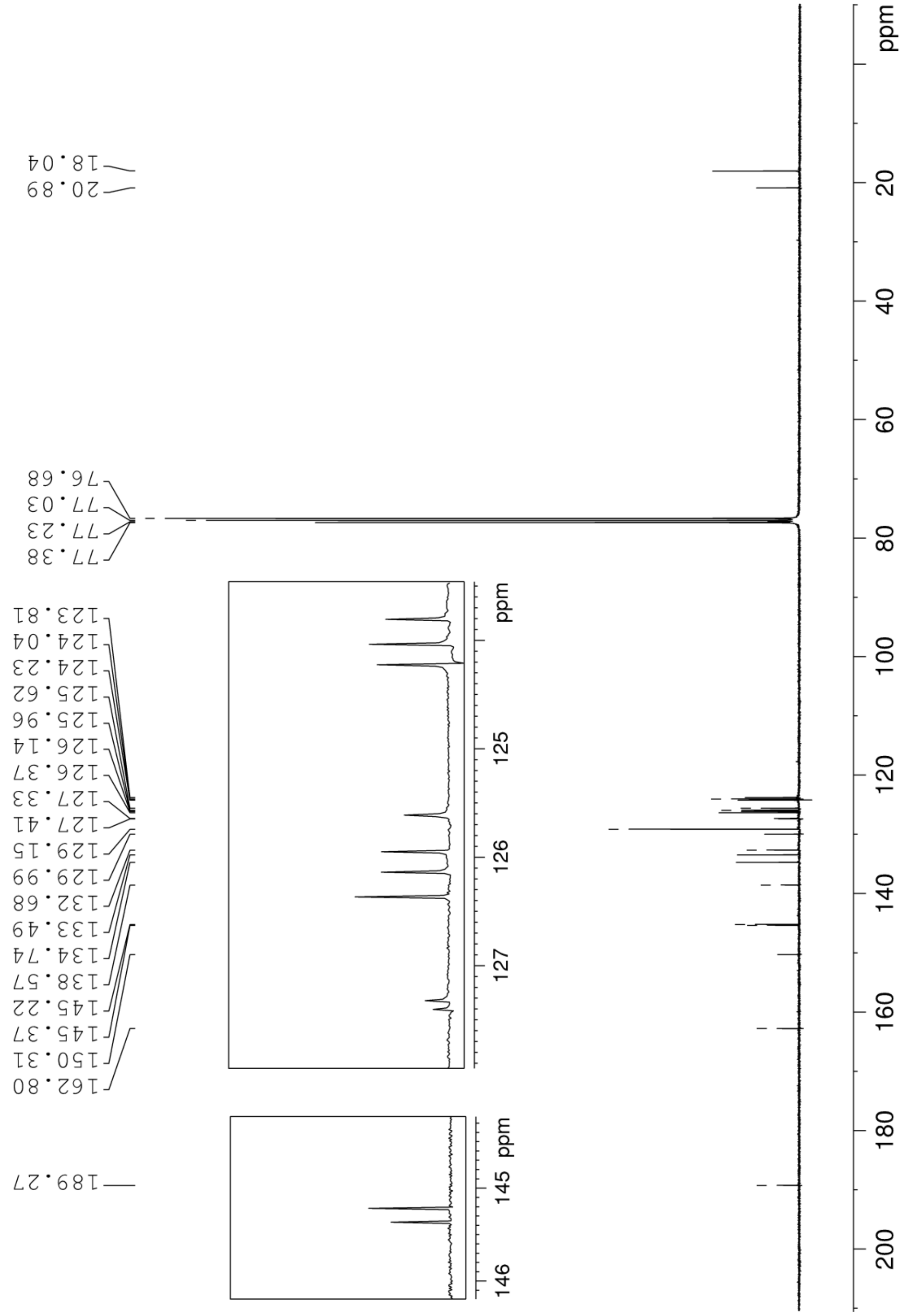

Figure A41. ^{13}C NMR (360 MHz, CDCl$_3$) spectrum of compound **2.5c**.

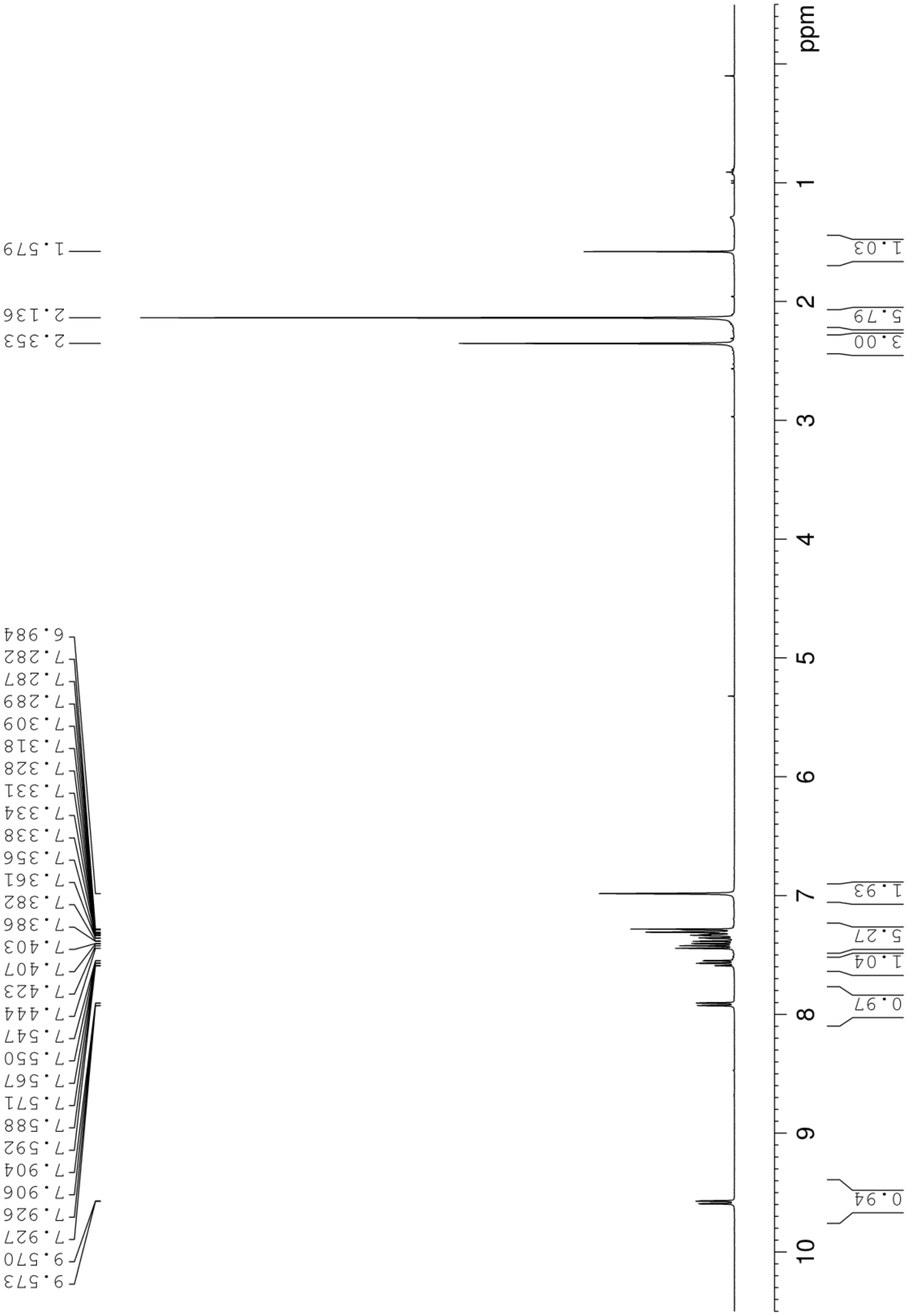

Figure A42. ^{1}H NMR (360 MHz, $CDCl_3$) spectrum of compound **2.6c**.

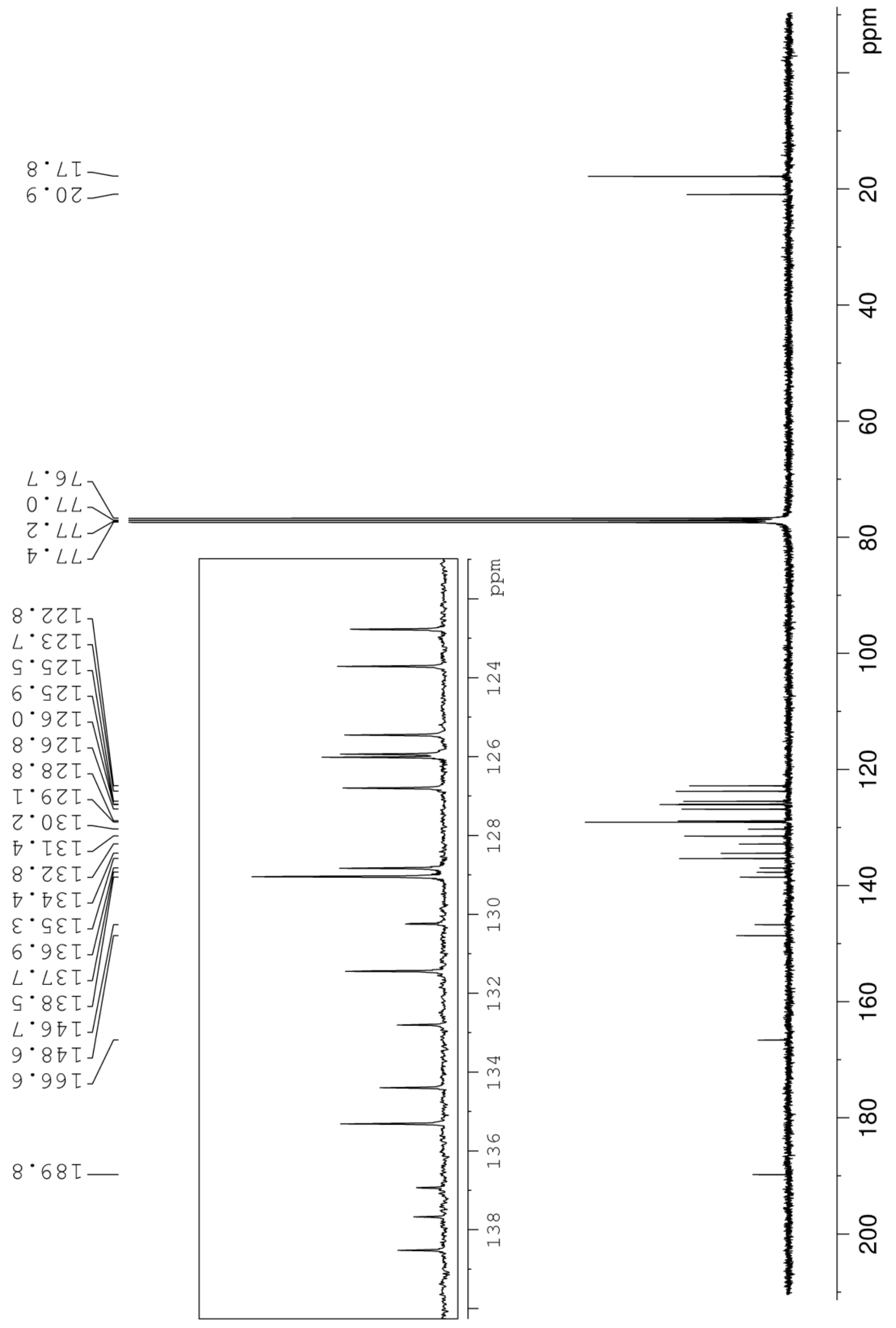

Figure A43. ^{13}C NMR (90 MHz, $CDCl_3$) spectrum of compound **2.6c**.

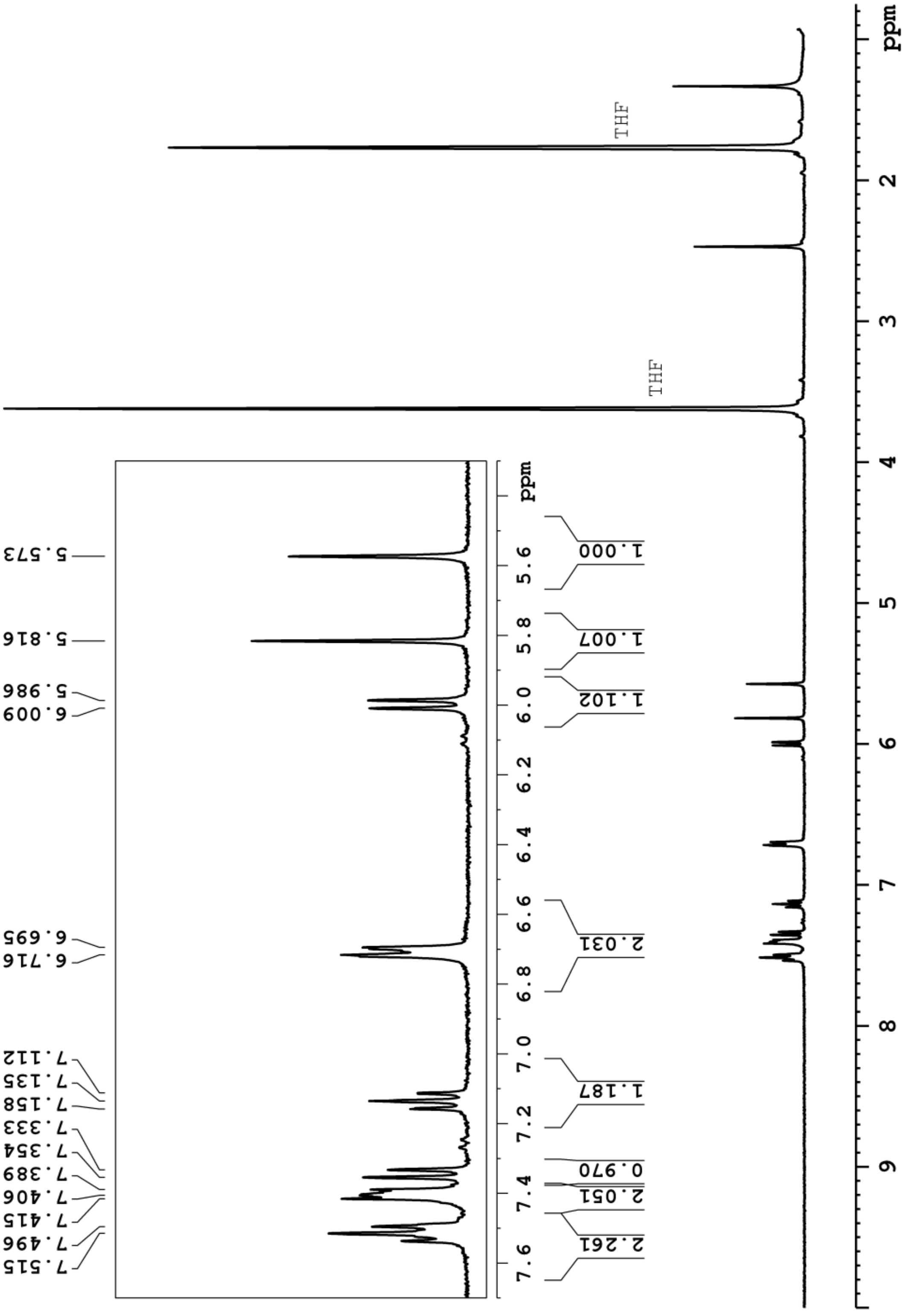

Figure A44. ^{1}H NMR (360 MHz, *d8*-THF, 298 K) spectrum of *meso* diruthenium complex **3.5a**.

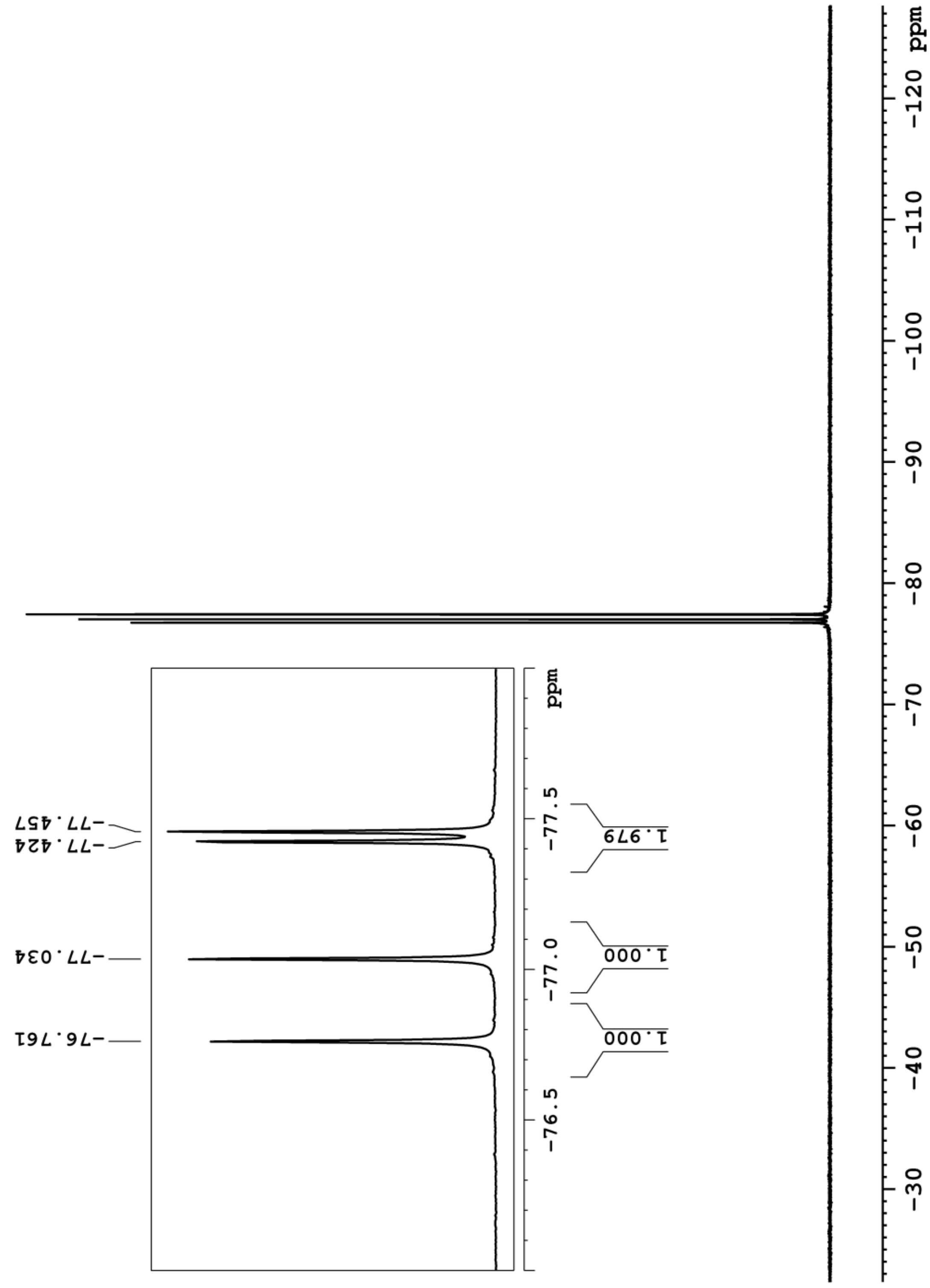

Figure A45. ^{19}F NMR (282 MHz, *d8*-THF, 298 K) spectrum of *meso* diruthenium complex **3.5a**.

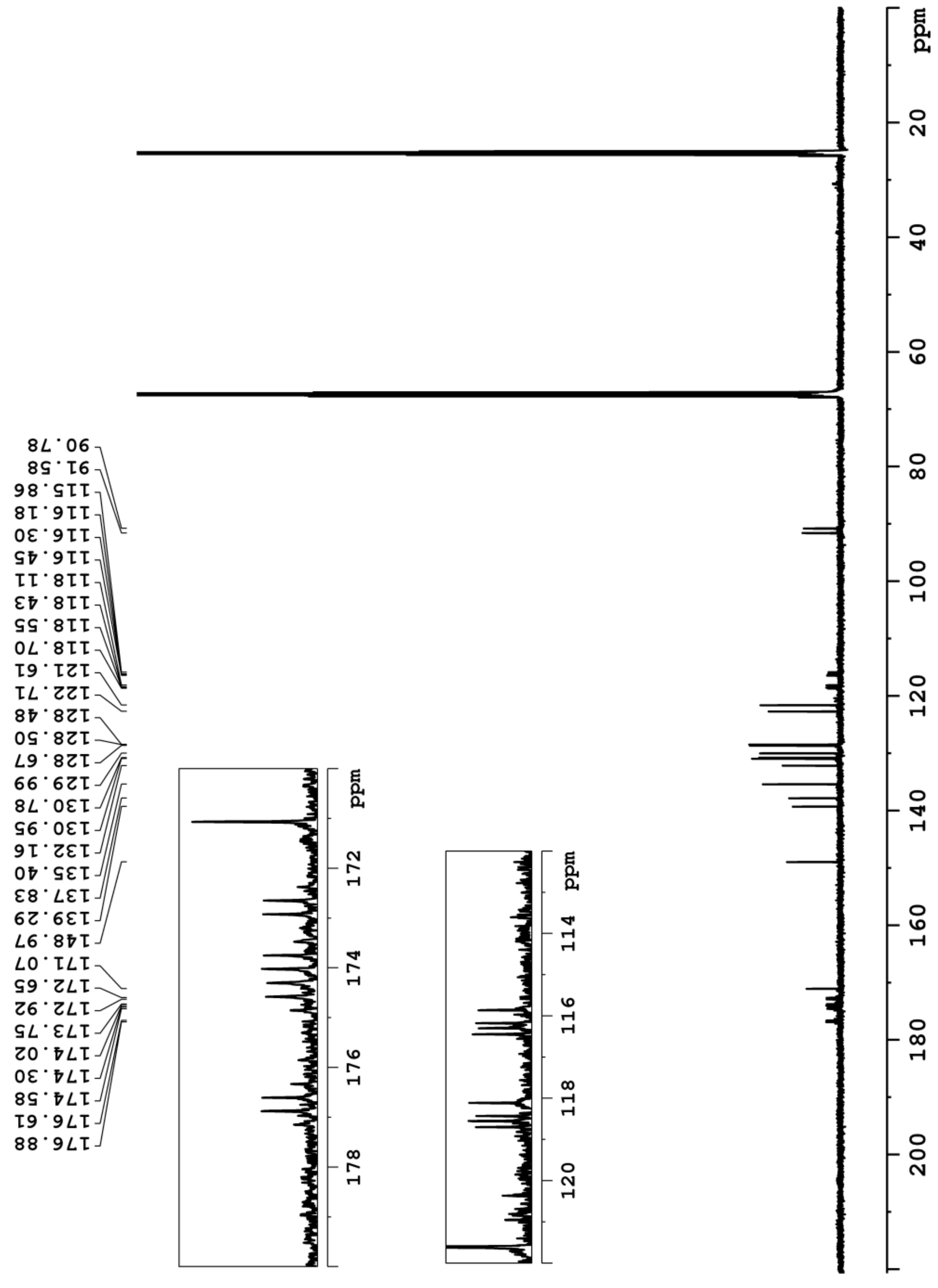

Figure A46. ^{13}C NMR (125 MHz, *d8*-THF, 298 K) spectrum of *meso* diruthenium complex **3.5a**.

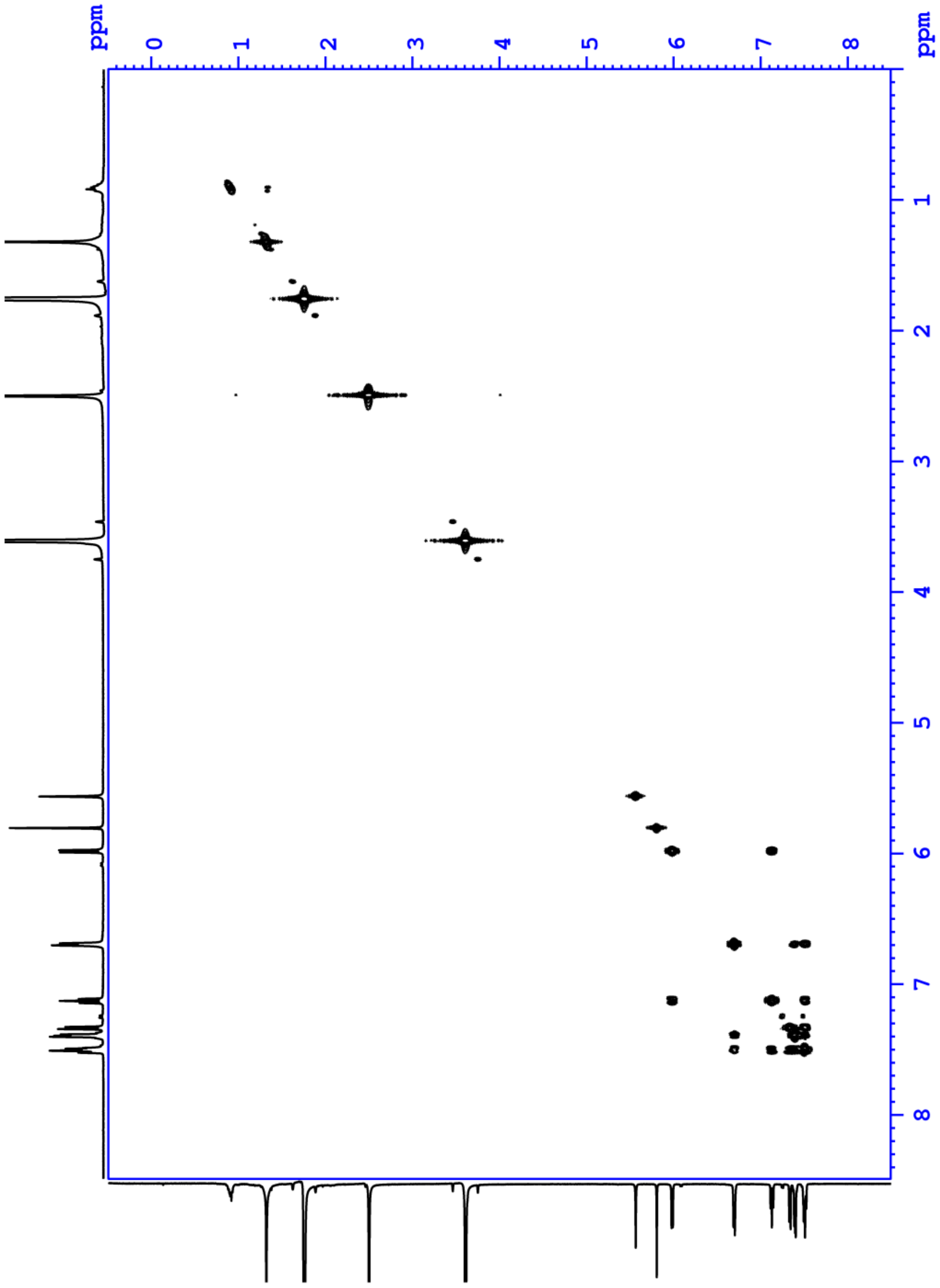

Figure A47. COSY NMR (500 MHz, *d8*-THF, 298 K) spectrum of *meso* diruthenium complex **3.5a**.

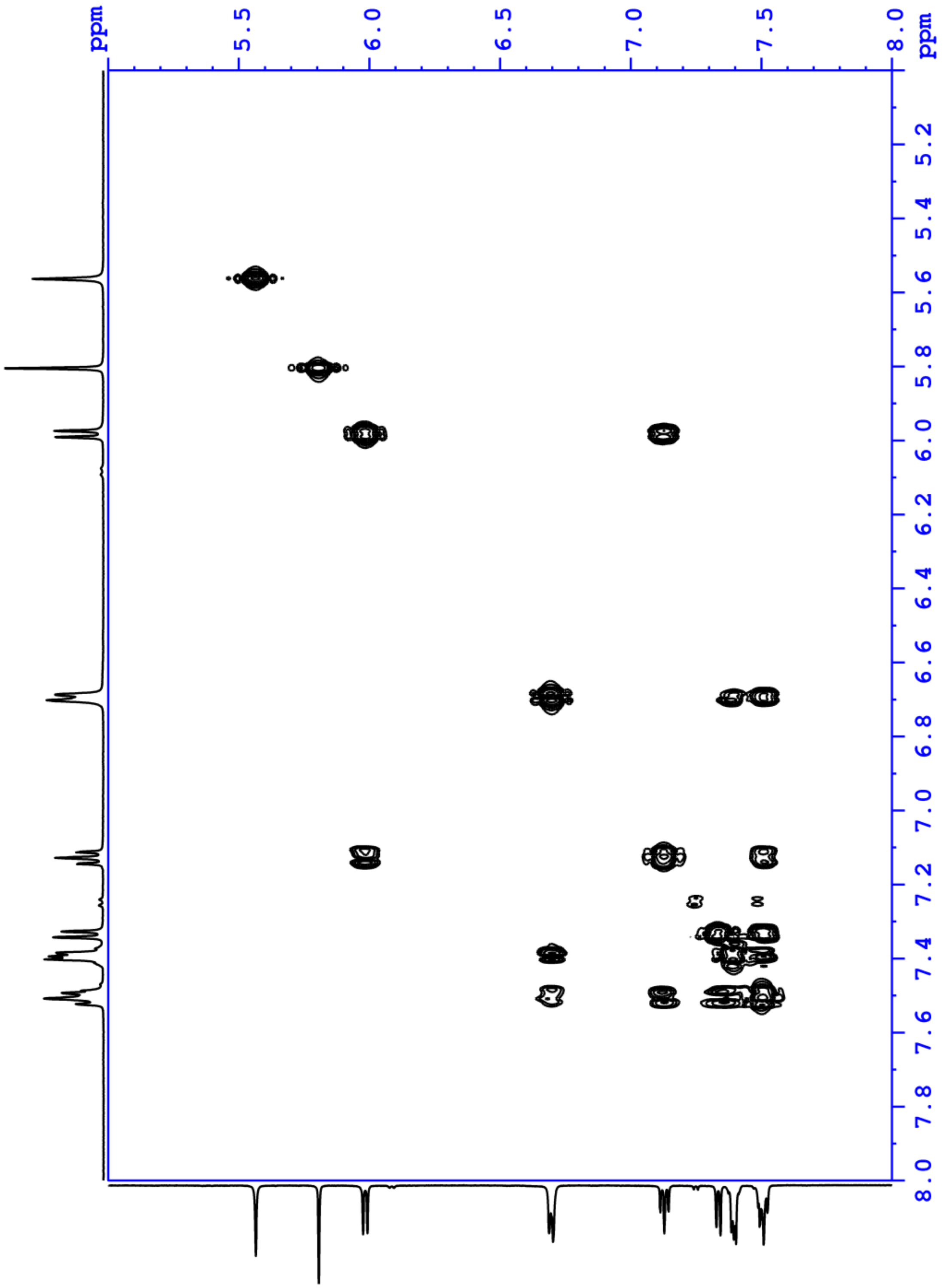

Figure A48. COSY NMR (500 MHz, *d8*-THF, 298 K) expanded spectrum of *meso* diruthenium complex **3.5a** showing the region 8–5ppm.

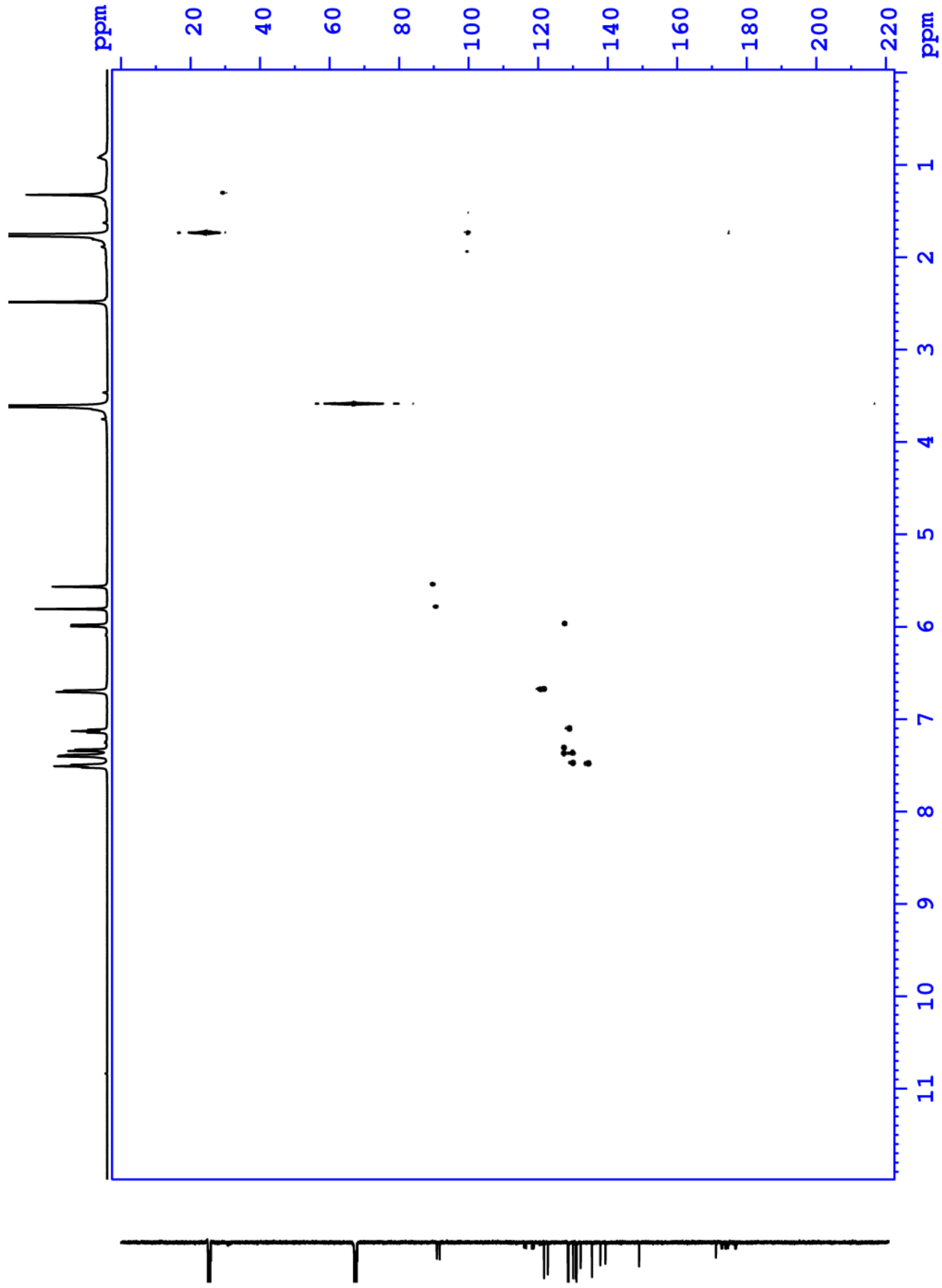

Figure A49. HSQC NMR (500 MHz, *d8*-THF, 298 K) spectrum of *meso* diruthenium complex **3.5a**.

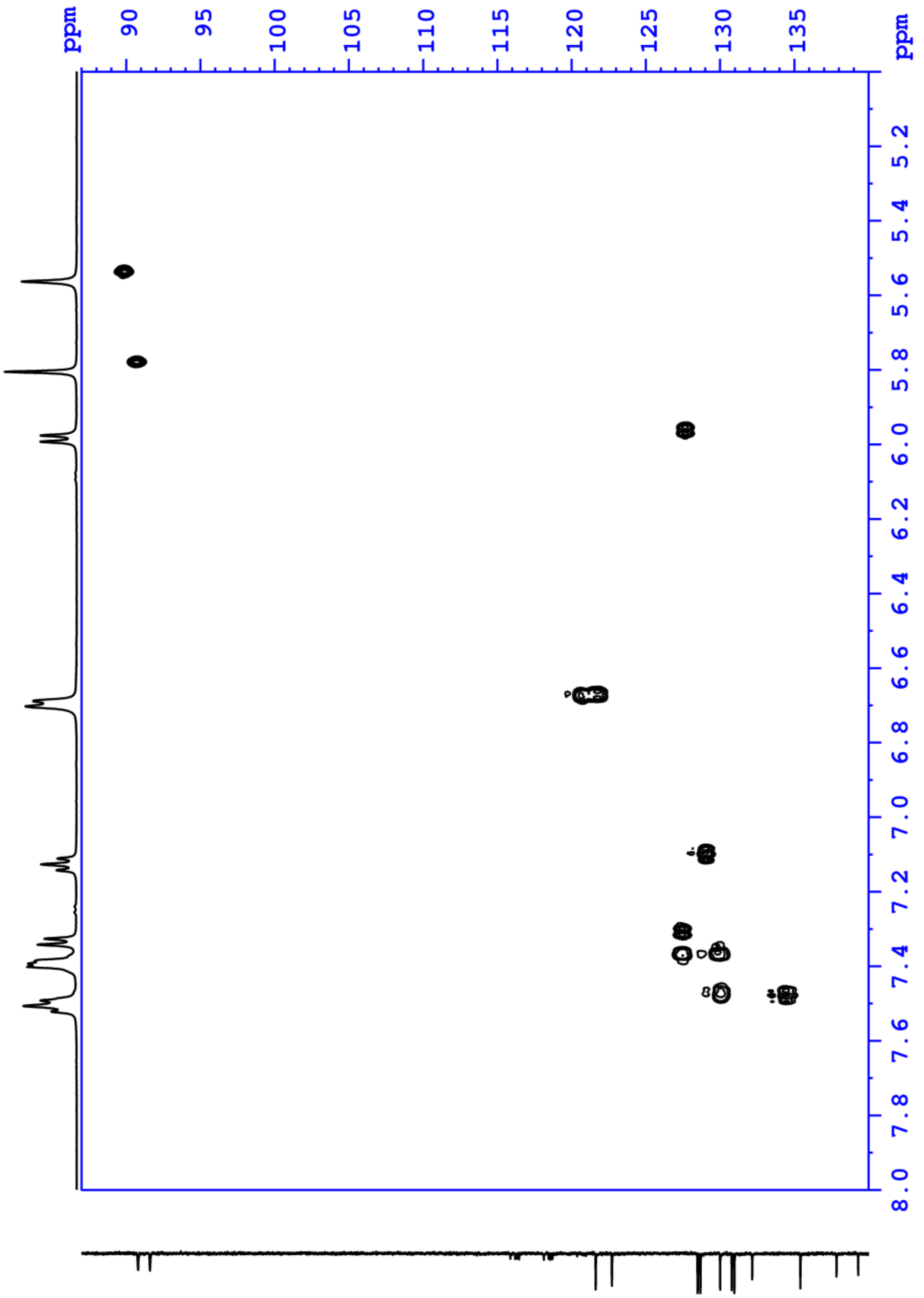

Figure A50. HSQC NMR (500 MHz, *d8*-THF, 298 K) expanded spectrum of *meso* diruthenium complex **3.5a** showing the region 8–5ppm and 140–87 ppm.

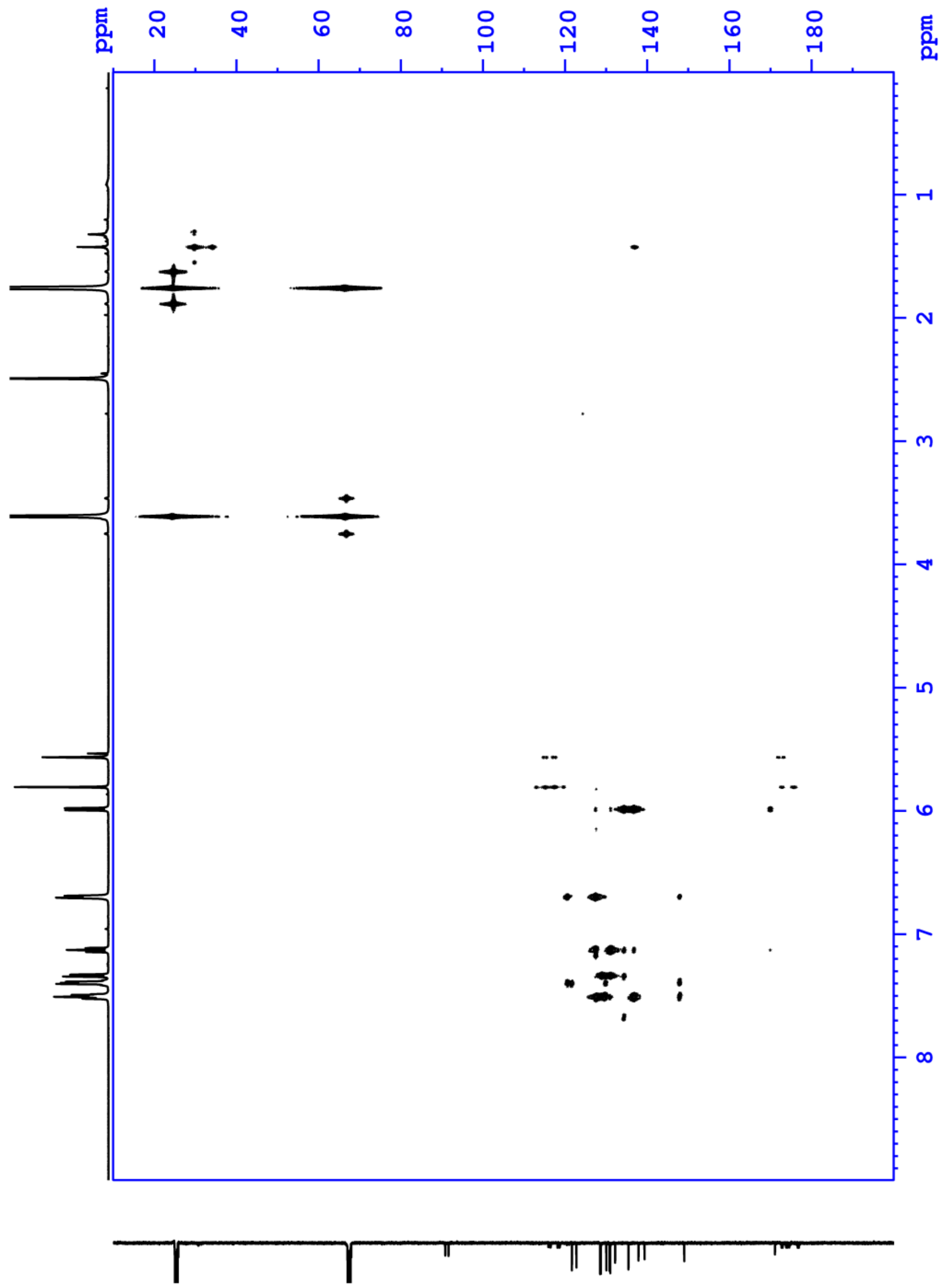

Figure A51. HMBC NMR (500 MHz, *d8*-THF, 298 K) spectrum of *meso* diruthenium complex **3.5a**.

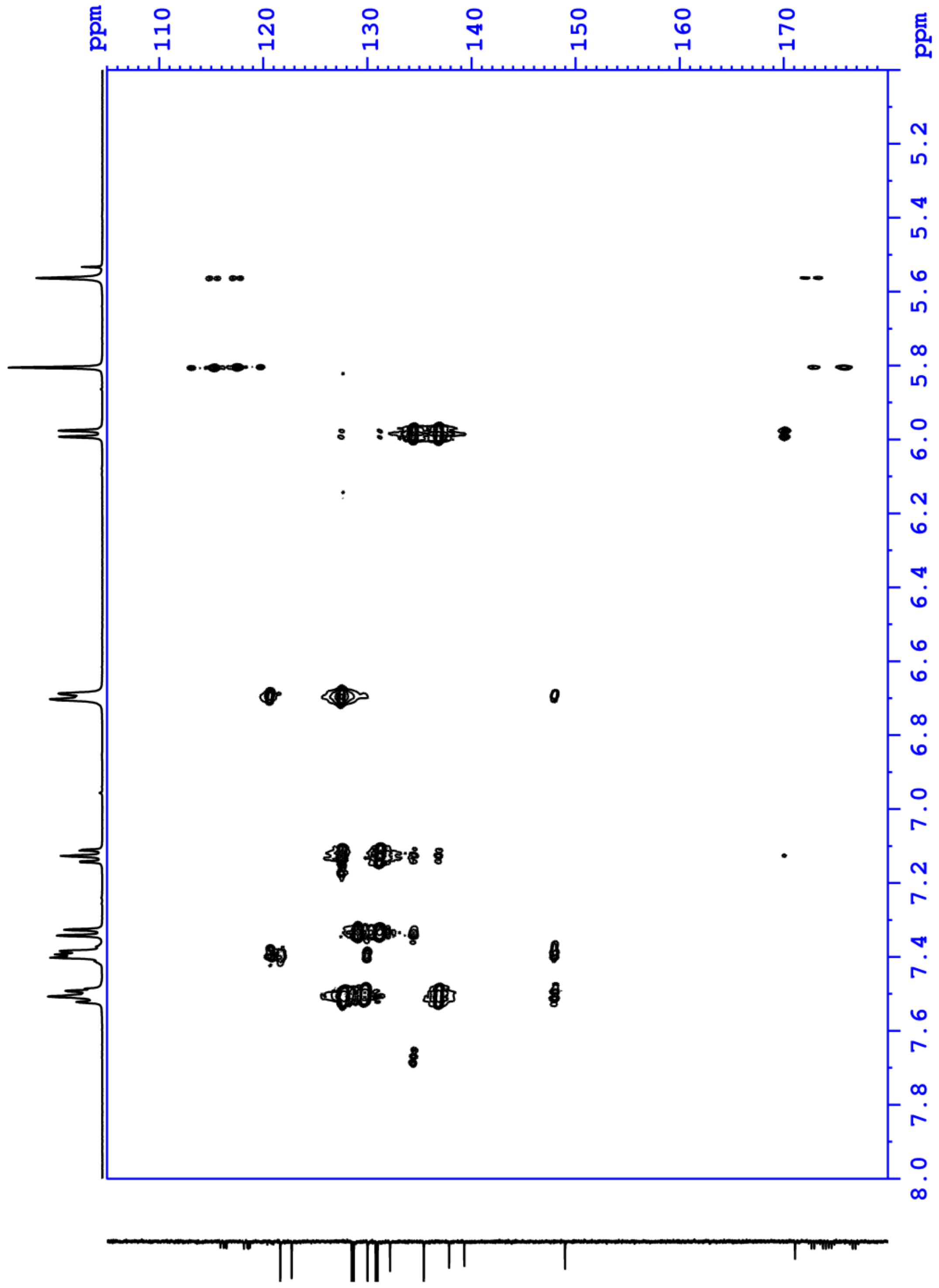

Figure A52. HMBC NMR (500 MHz, *d8*-THF, 298 K) expanded spectrum of *meso* diruthenium complex **3.5a** showing the region 8–5ppm and 180–105 ppm.

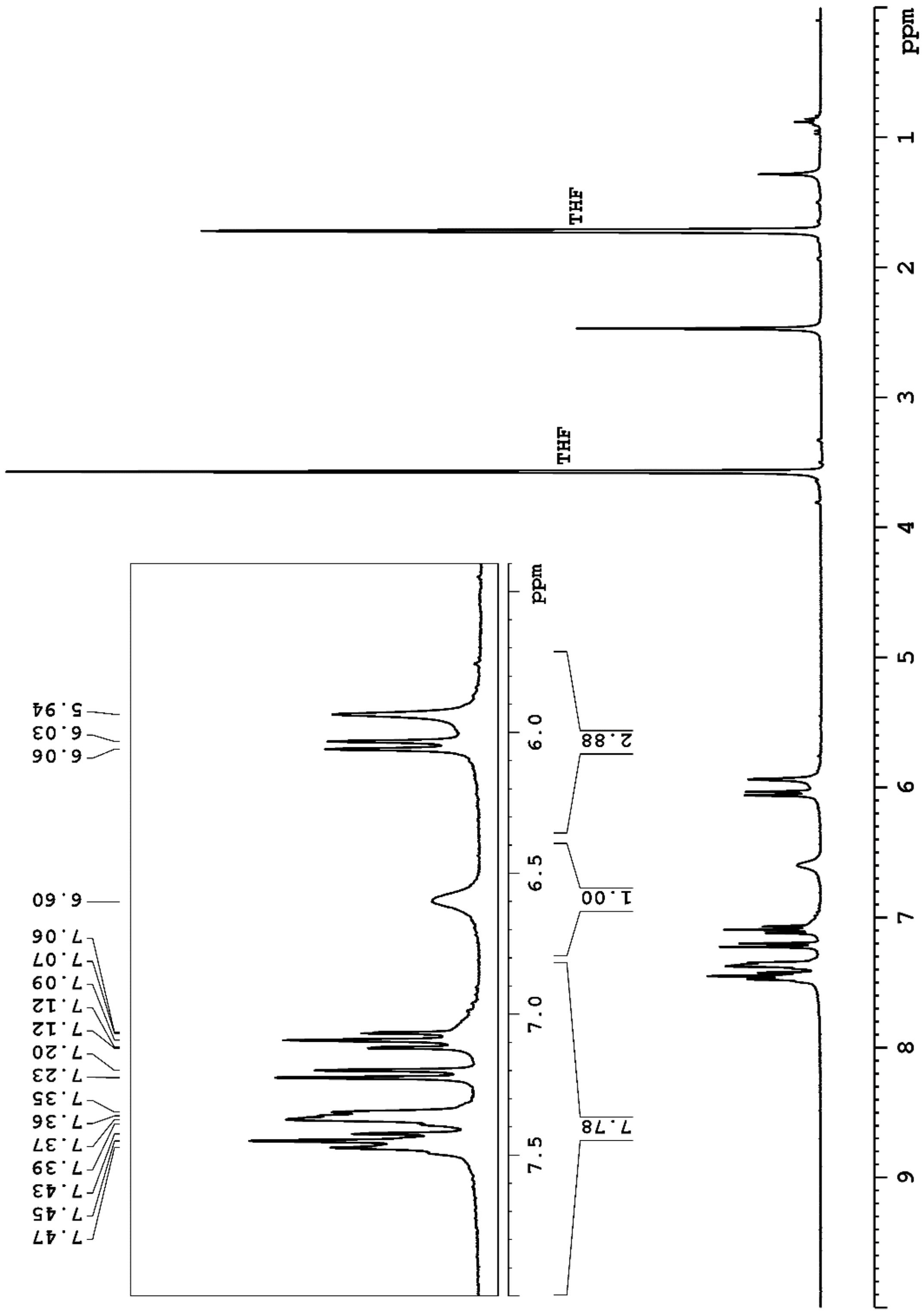

Figure A53. ^{1}H NMR (300 MHz, *d8*-THF, 298 K) spectrum of *rac* diruthenium complex **3.5b**.

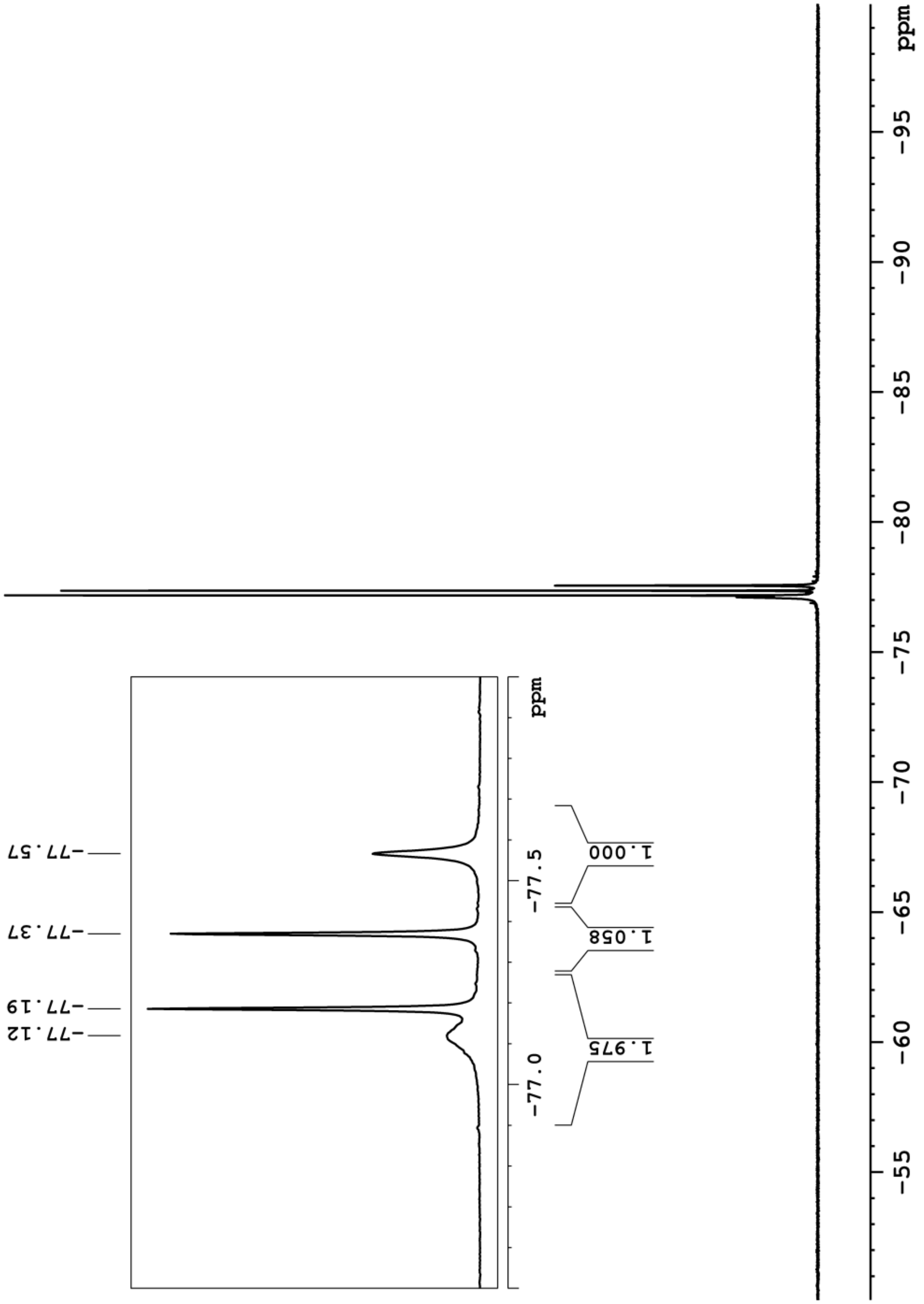

Figure A54. ^{19}F NMR (338 MHz, *d8*-THF, 298 K) spectrum of *rac* diruthenium complex **3.5b**.

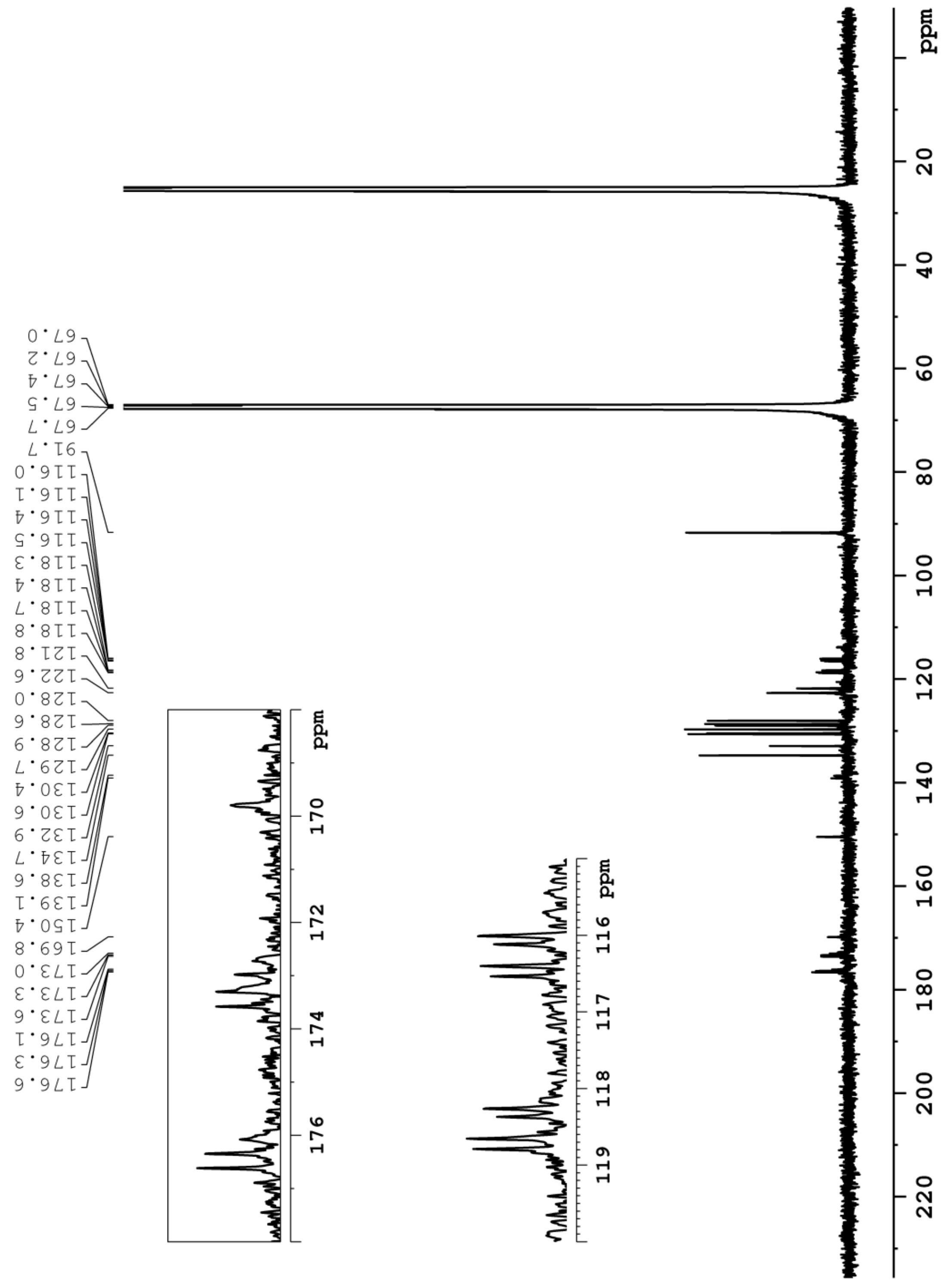

Figure A55. ^{13}C NMR (125 MHz, *d8*-THF, 333 K) spectrum of *rac* diruthenium complex **3.5b**.

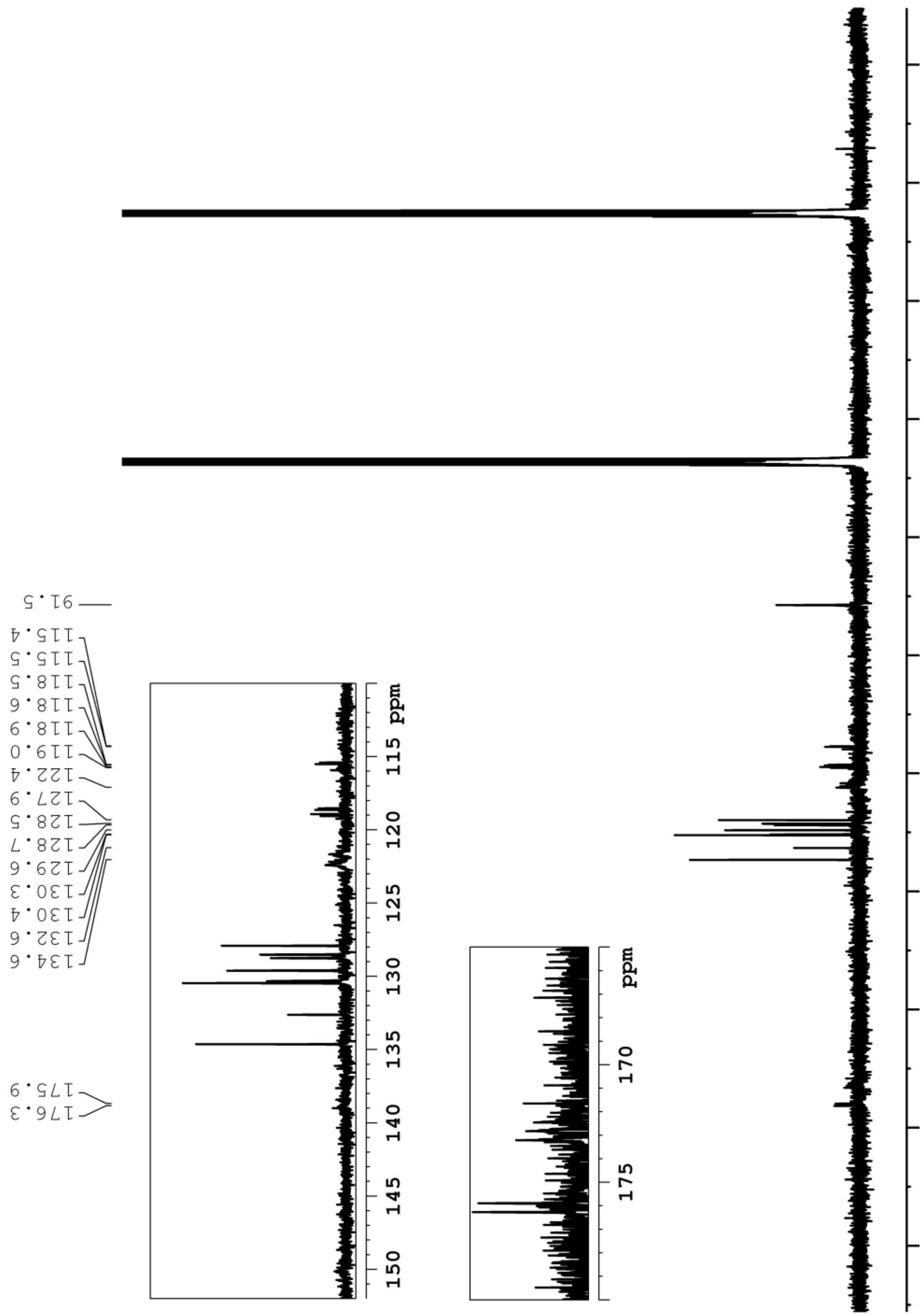

Figure A56. ^{13}C NMR (90 MHz, *d8*-THF, 298 K) spectrum of *rac* diruthenium complex **3.5b**.

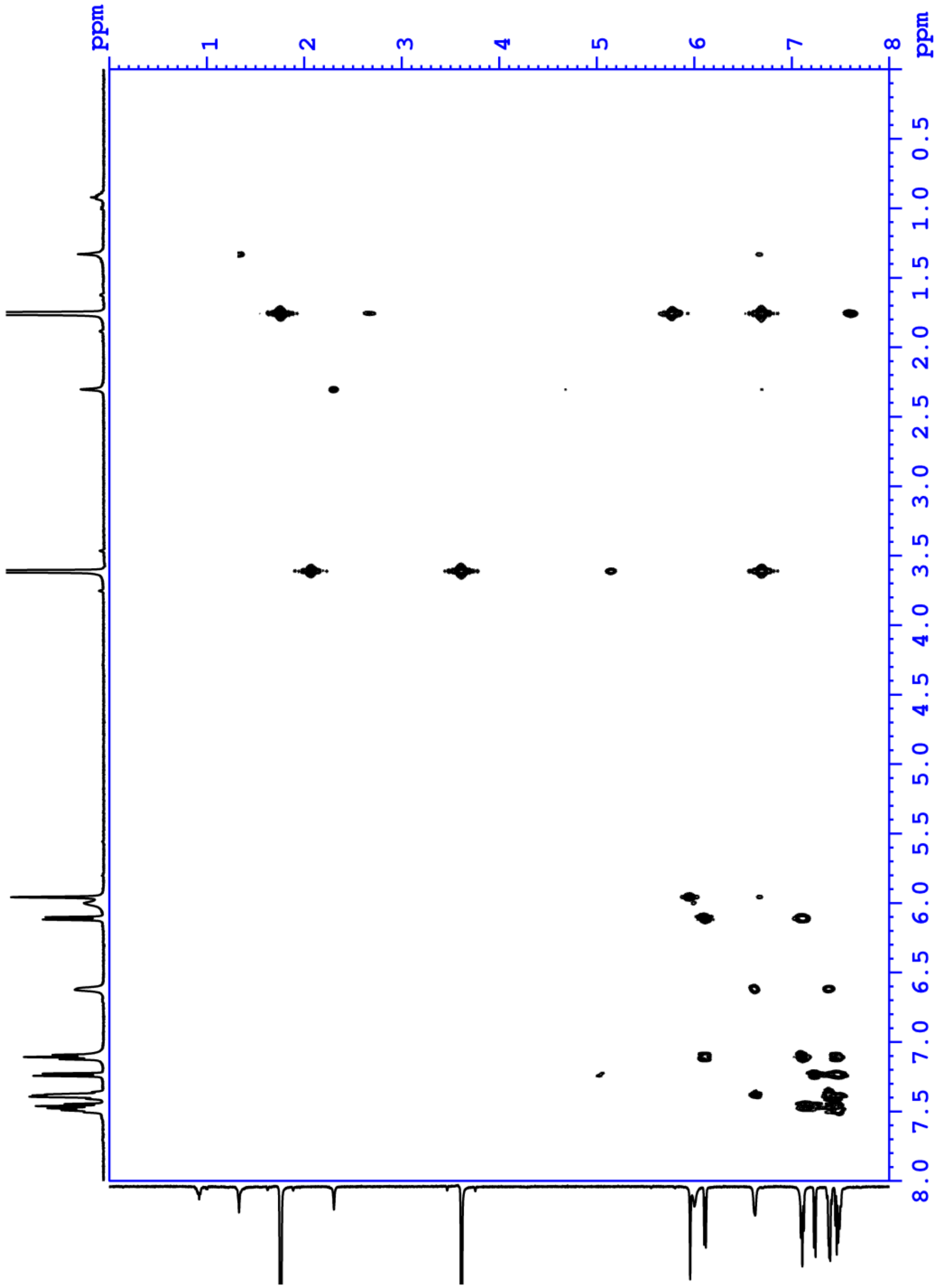

Figure A57. COSY NMR (500 MHz, *d8*-THF, 333 K) spectrum of *rac* diruthenium complex **3.5b**.

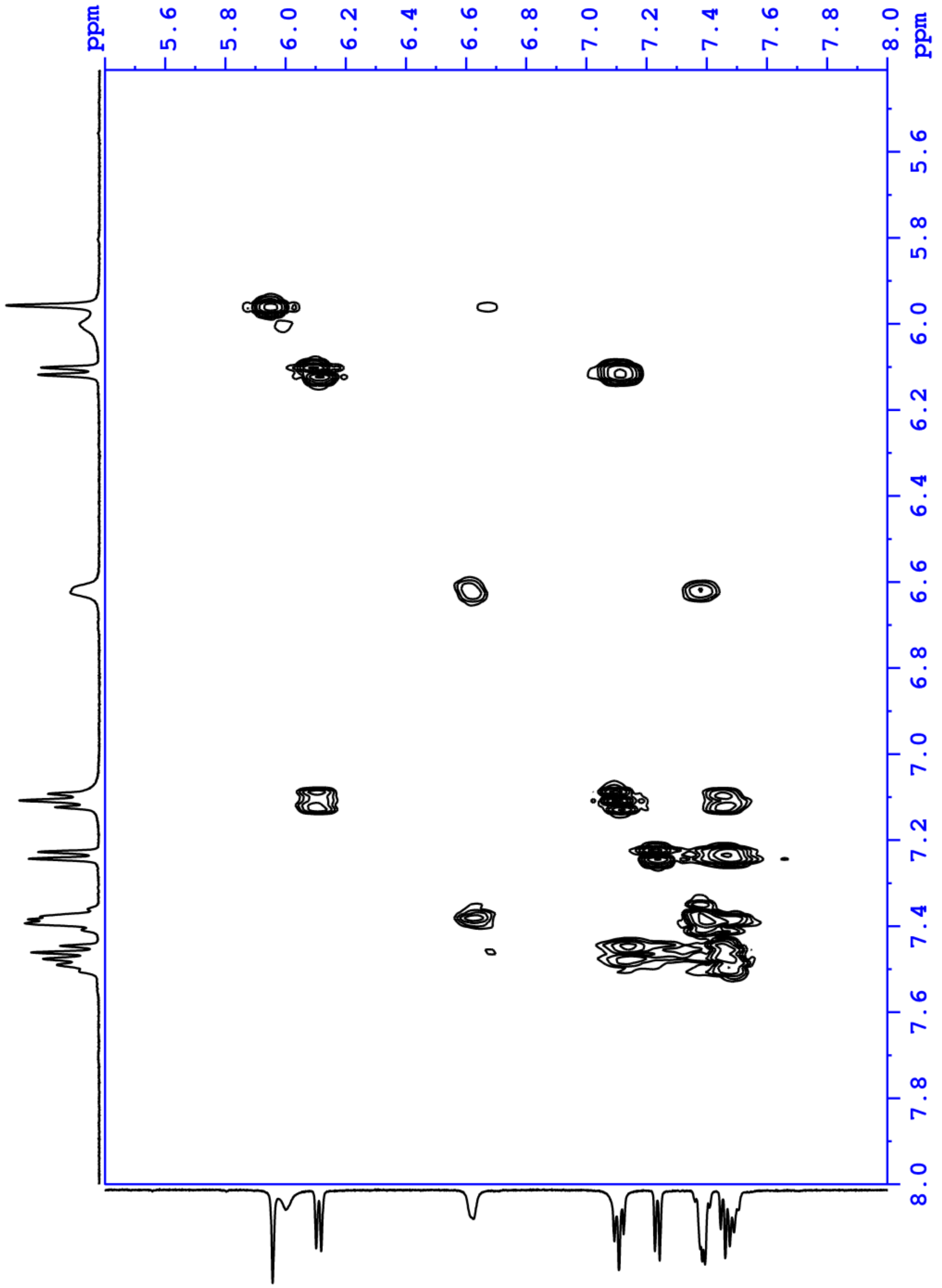

Figure A58. COSY NMR (500 MHz, *d8*-THF, 333 K) expanded spectrum of *rac* diruthenium complex **3.5b** showing the region 8–5.4ppm.

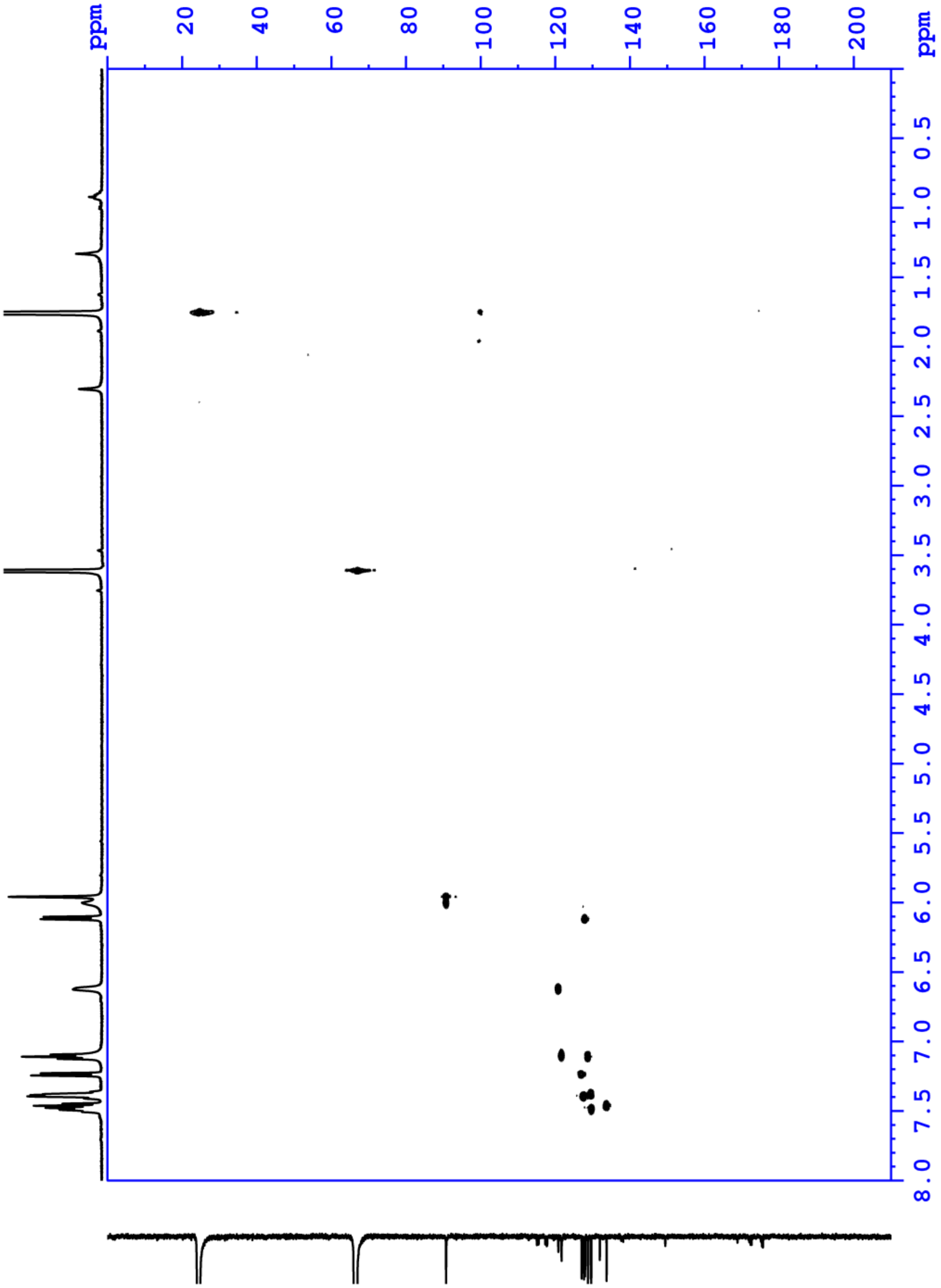

Figure A59. HSQC NMR (500 MHz, *d8*-THF, 333 K) spectrum of *rac* diruthenium complex **3.5b**.

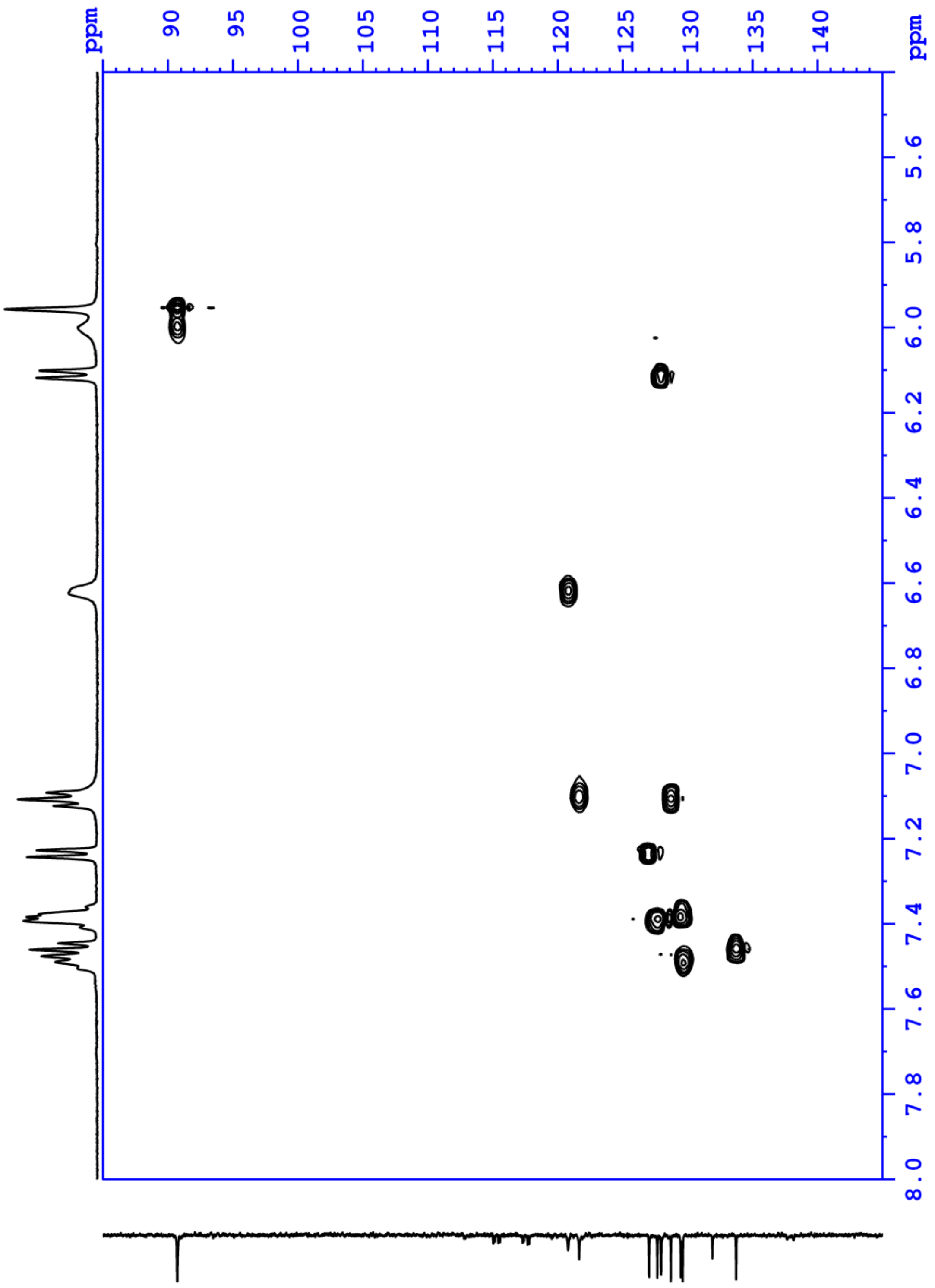

Figure A60. HSQC NMR (500 MHz, *d8*-THF, 333 K) expanded spectrum of *rac* diruthenium complex **3.5b** showing the region 8–5.5 ppm and 145–85 ppm.

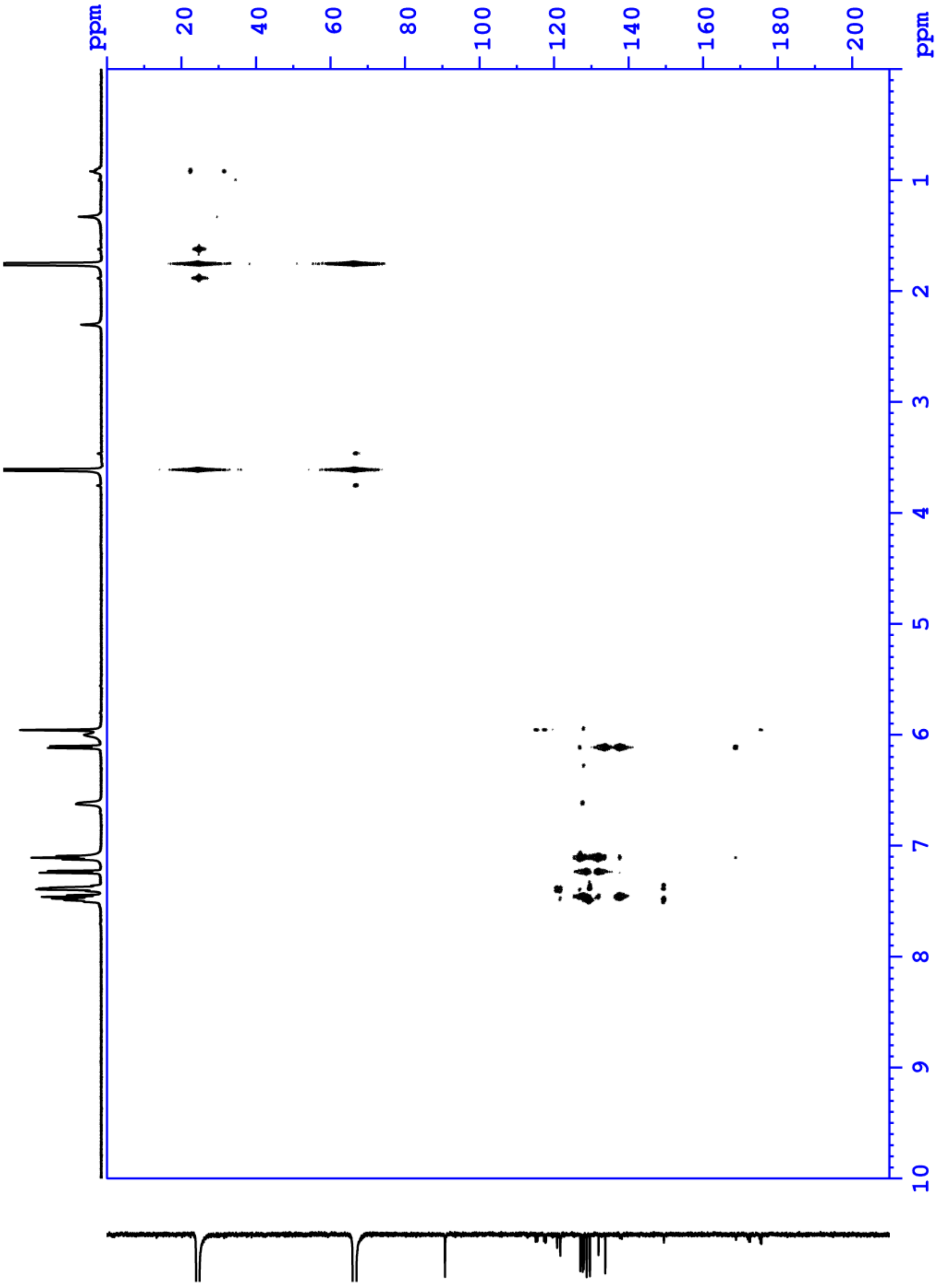

Figure A61. HMBC NMR (500 MHz, *d8*-THF, 333 K) spectrum of *rac* diruthenium complex **3.5b**.

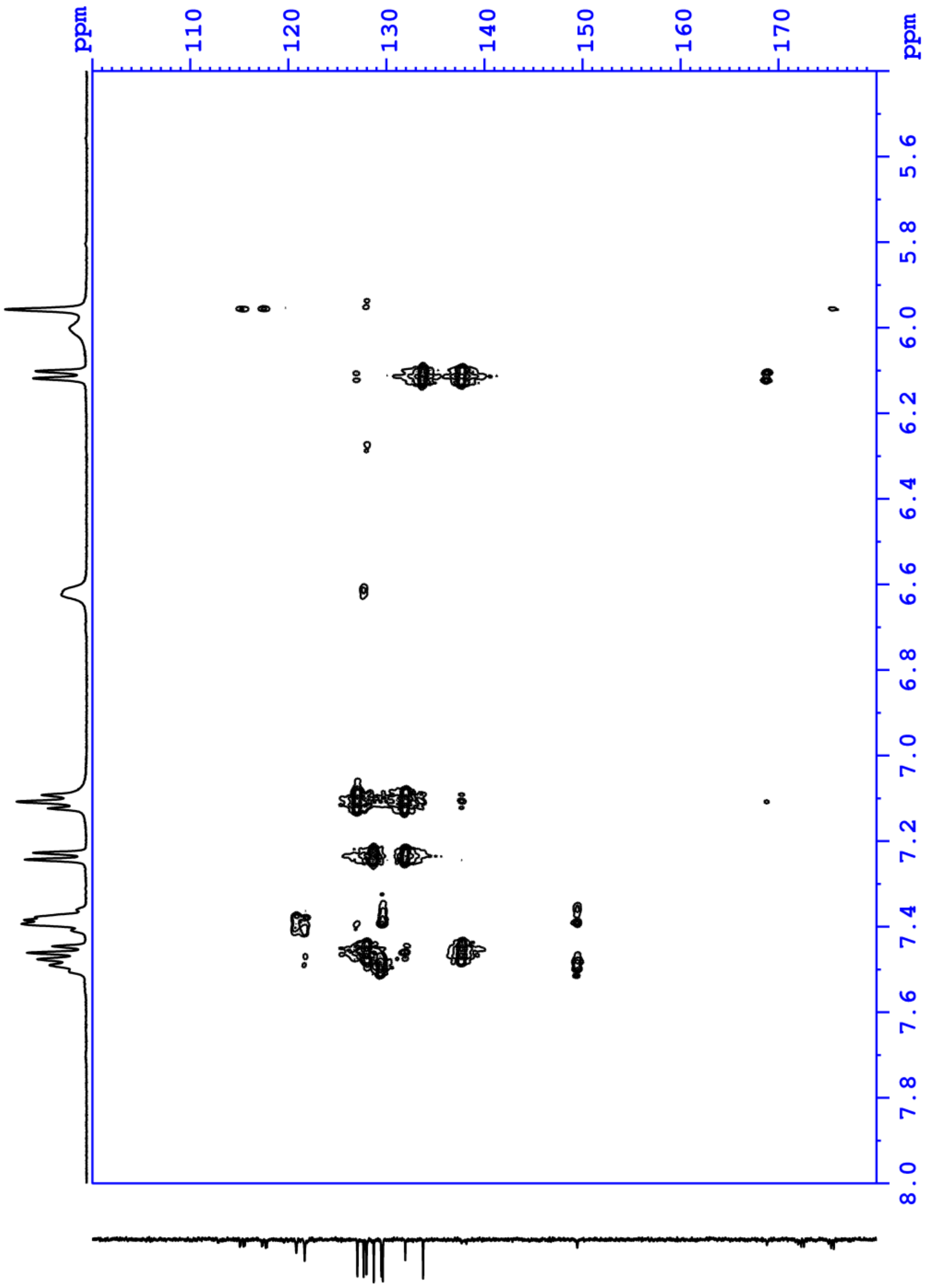

Figure A62. HMBC NMR (500 MHz, *d8*-THF, 333 K) expanded spectrum of *rac* diruthenium complex **3.5b** showing the region 8–5.5 ppm and 180–100 ppm

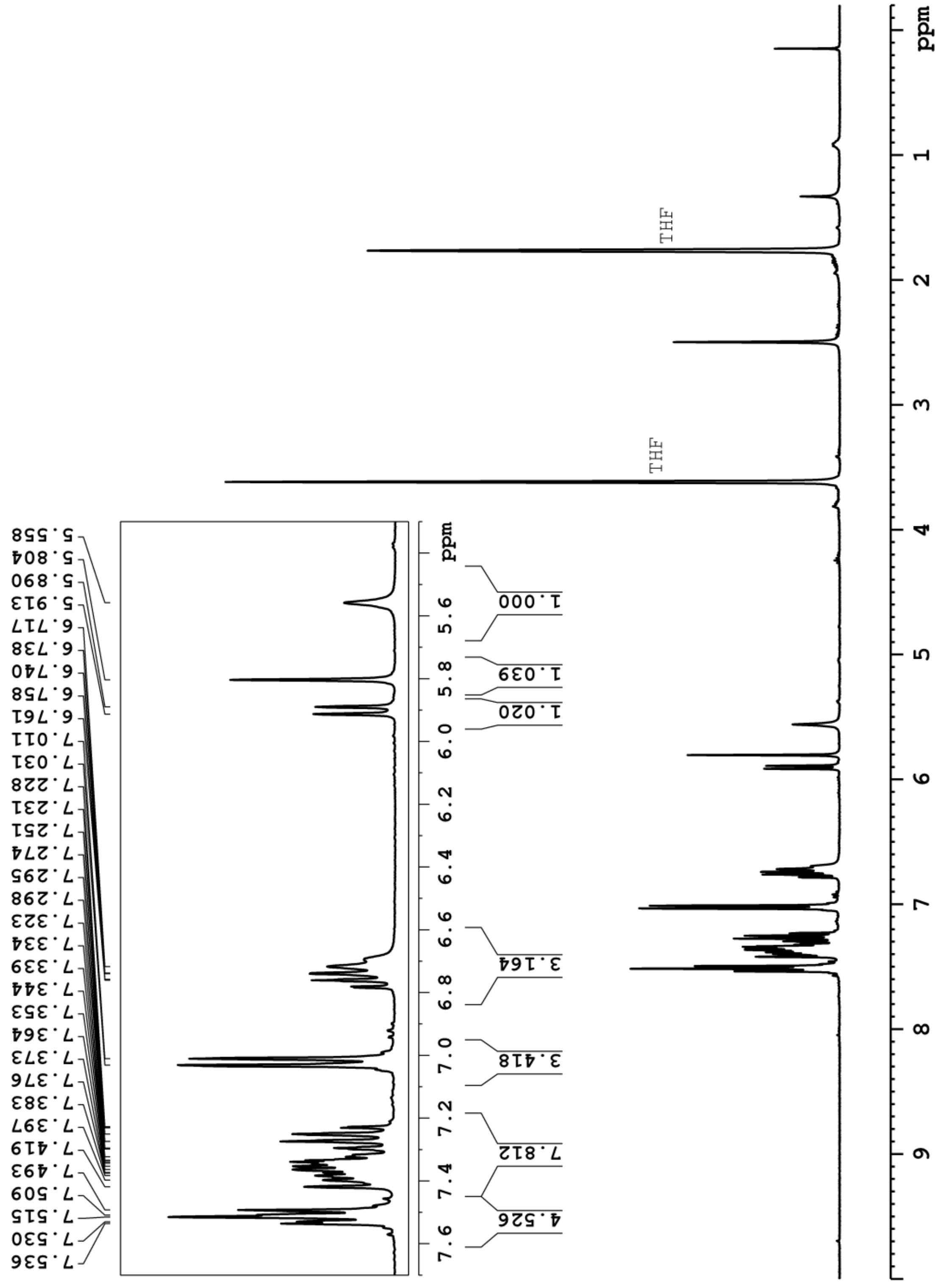

Figure A63. ^{1}H NMR (360 MHz, *d8*-THF, 298 K) spectrum of monoruthenium complex **3.4**.

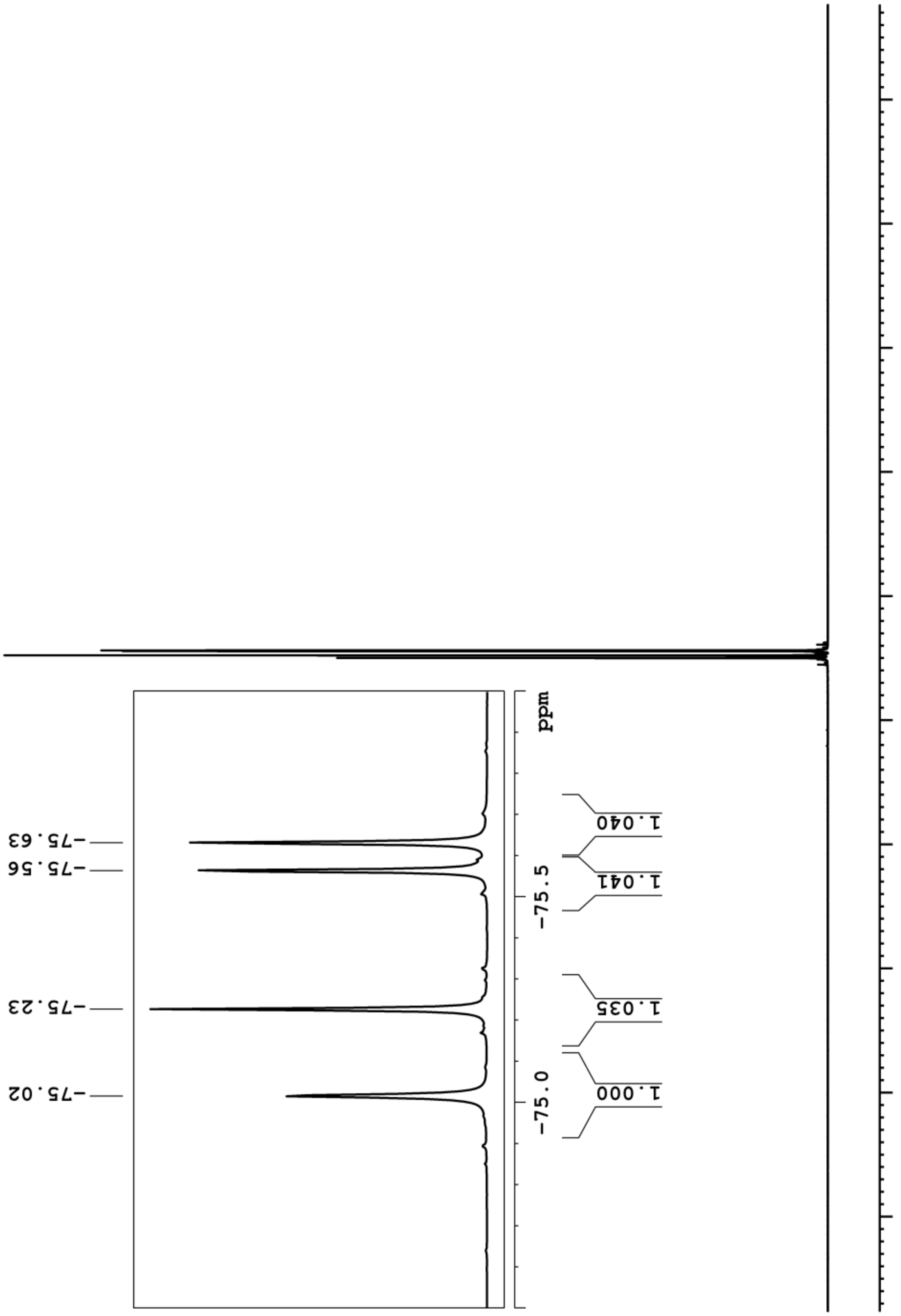

Figure A64. ^{19}F NMR (282 MHz, *d8*-THF, 298 K) spectrum of monoruthenium complex **3.4**.

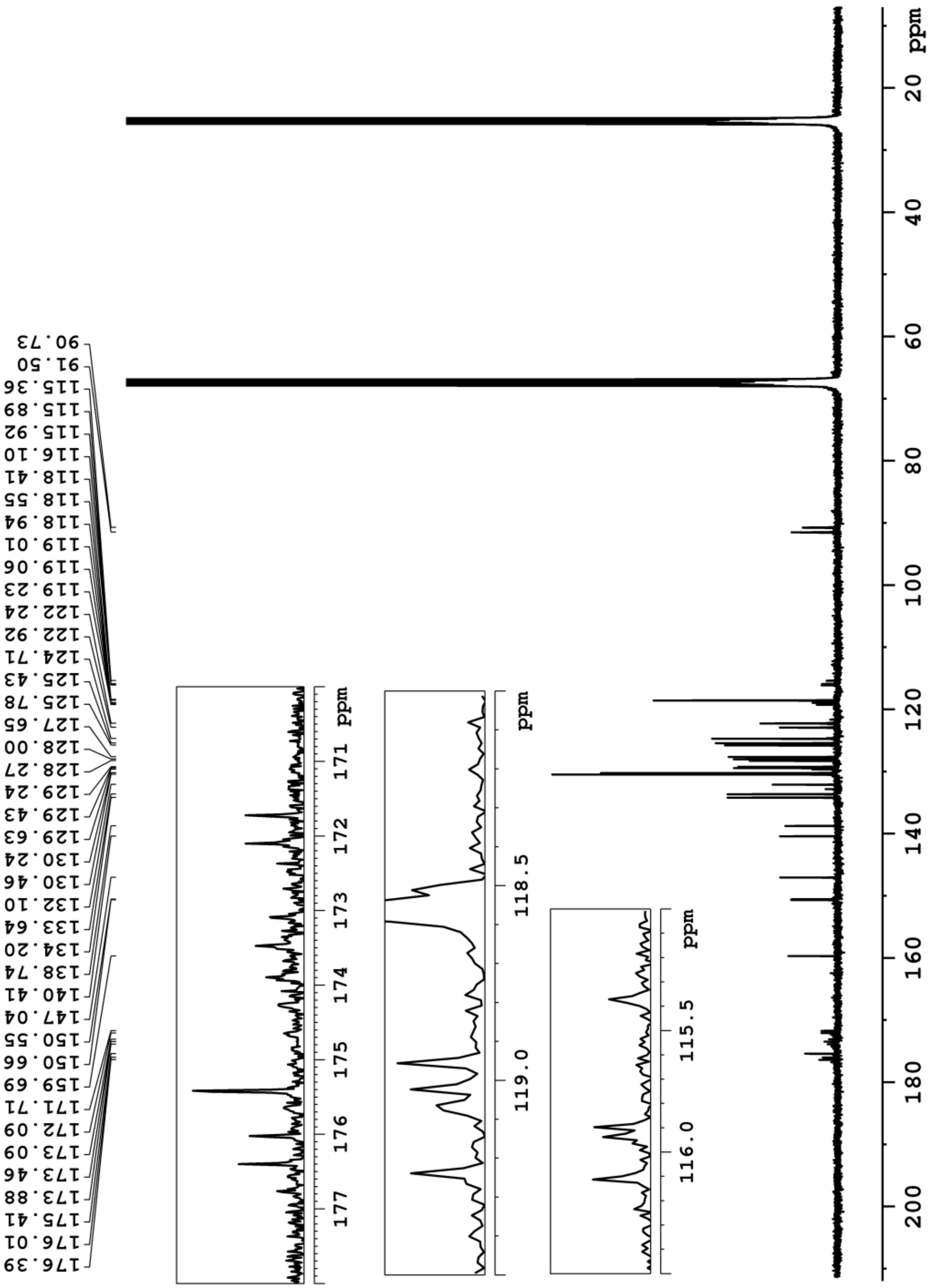

Figure A65. ^{13}C NMR (90 MHz, *d8*-THF, 298 K) spectrum of monoruthenium complex **3.4**.

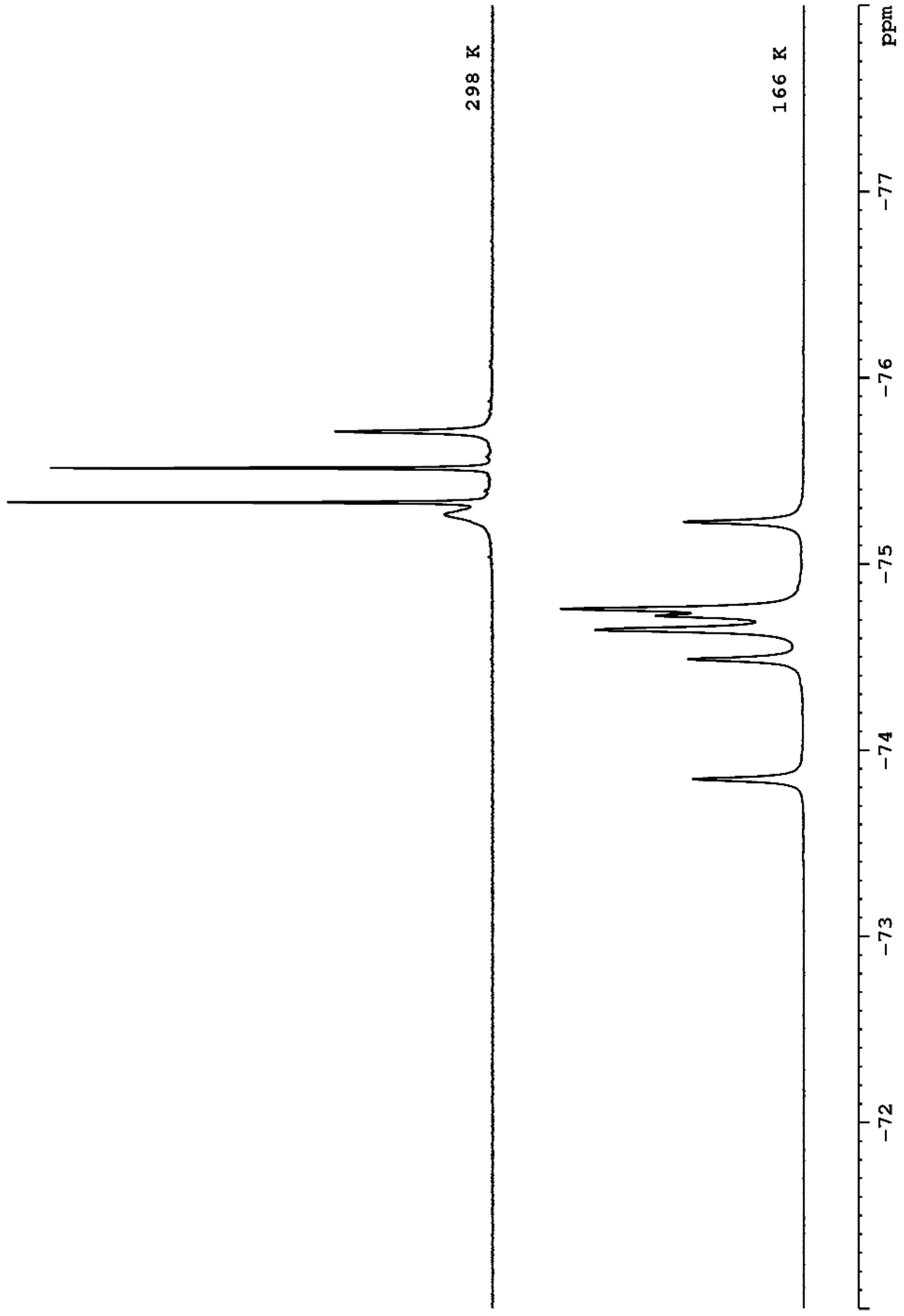

Figure A66. Variable temperature ^{19}F NMR spectra of *rac* diruthenium **3.5b** (338 MHz, THF-*d8*) showing the effects of temperature-dependent rates of conformational exchange at 298 K and 166 K. The resolved peaks of the two conformers are seen at 166 K. Broadening and coalescence of these peaks is evident at 298 K.

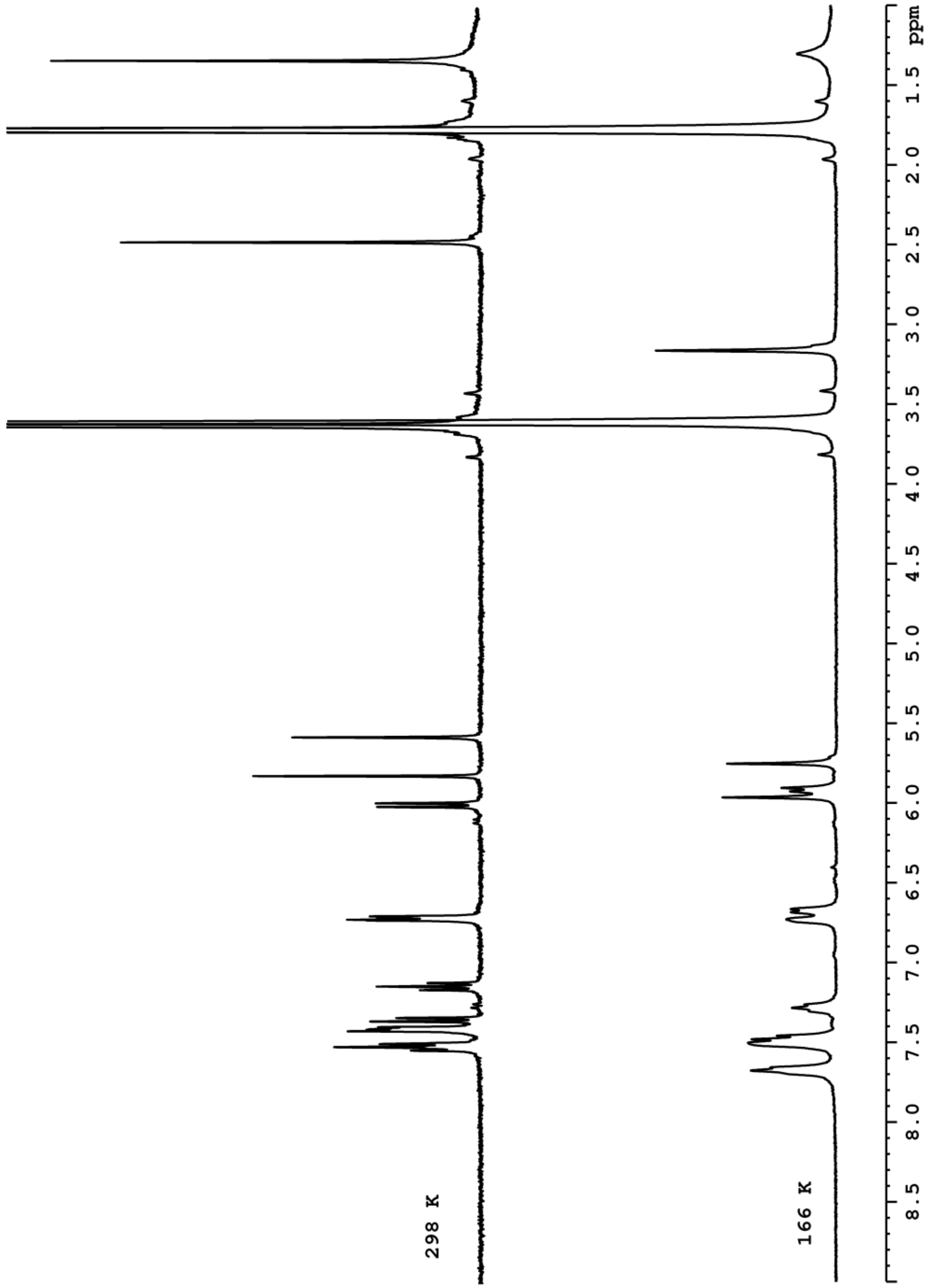

Figure A67. Variable temperature ^{1}H NMR spectra of *meso* diruthenium **3.5a** (360 MHz, THF-*d8*, 298 K and 166 K). The spectrum obtained at 166 K is uniformly broadened but does not show any evidence of dynamic exchange.

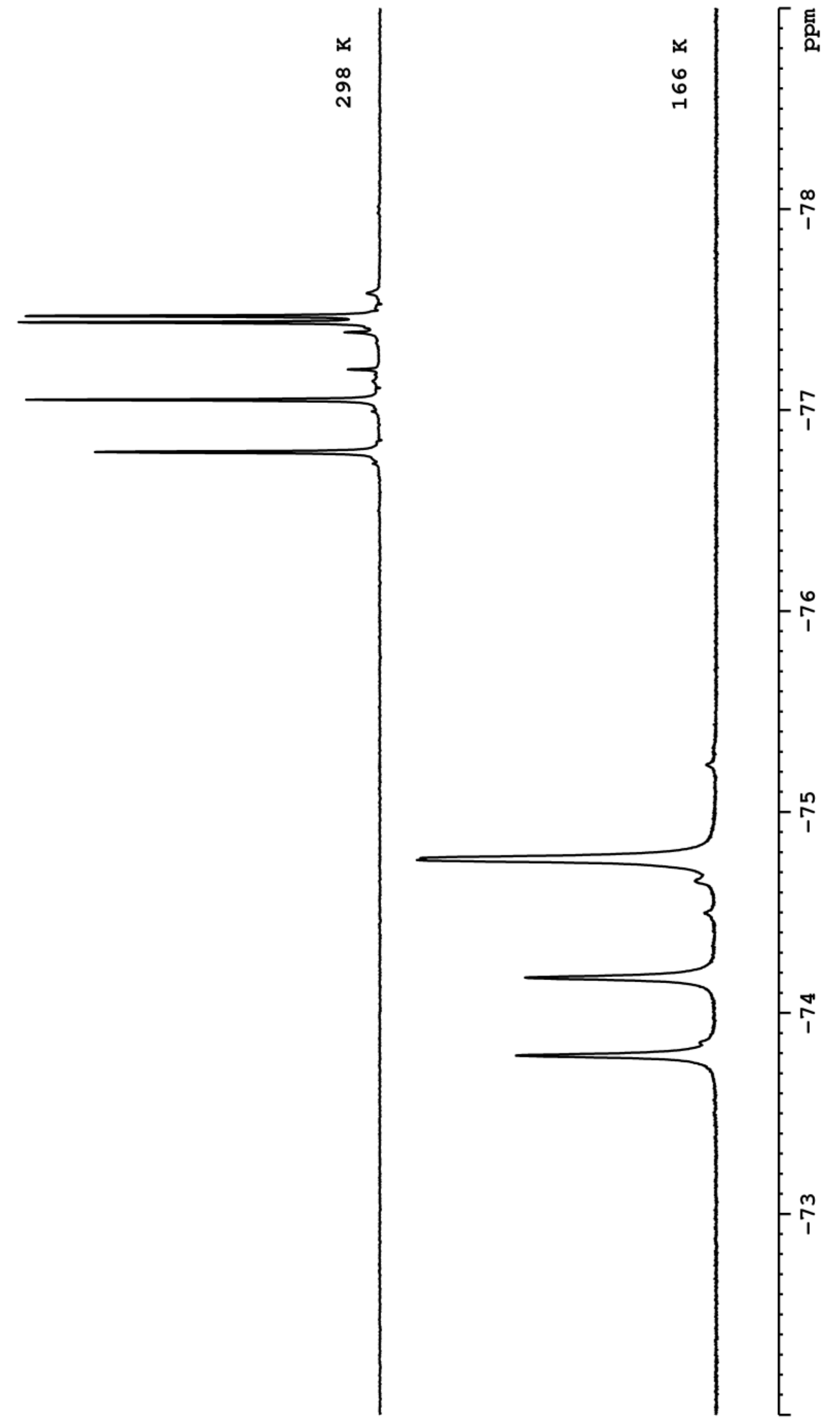

Figure A68. Variable temperature ^{19}F NMR spectra of *meso* diruthenium **3.5a** (338 MHz, THF-*d8*, 298 K and 166 K). The spectra do not show any evidence of dynamic exchange at 298 or 166 K.

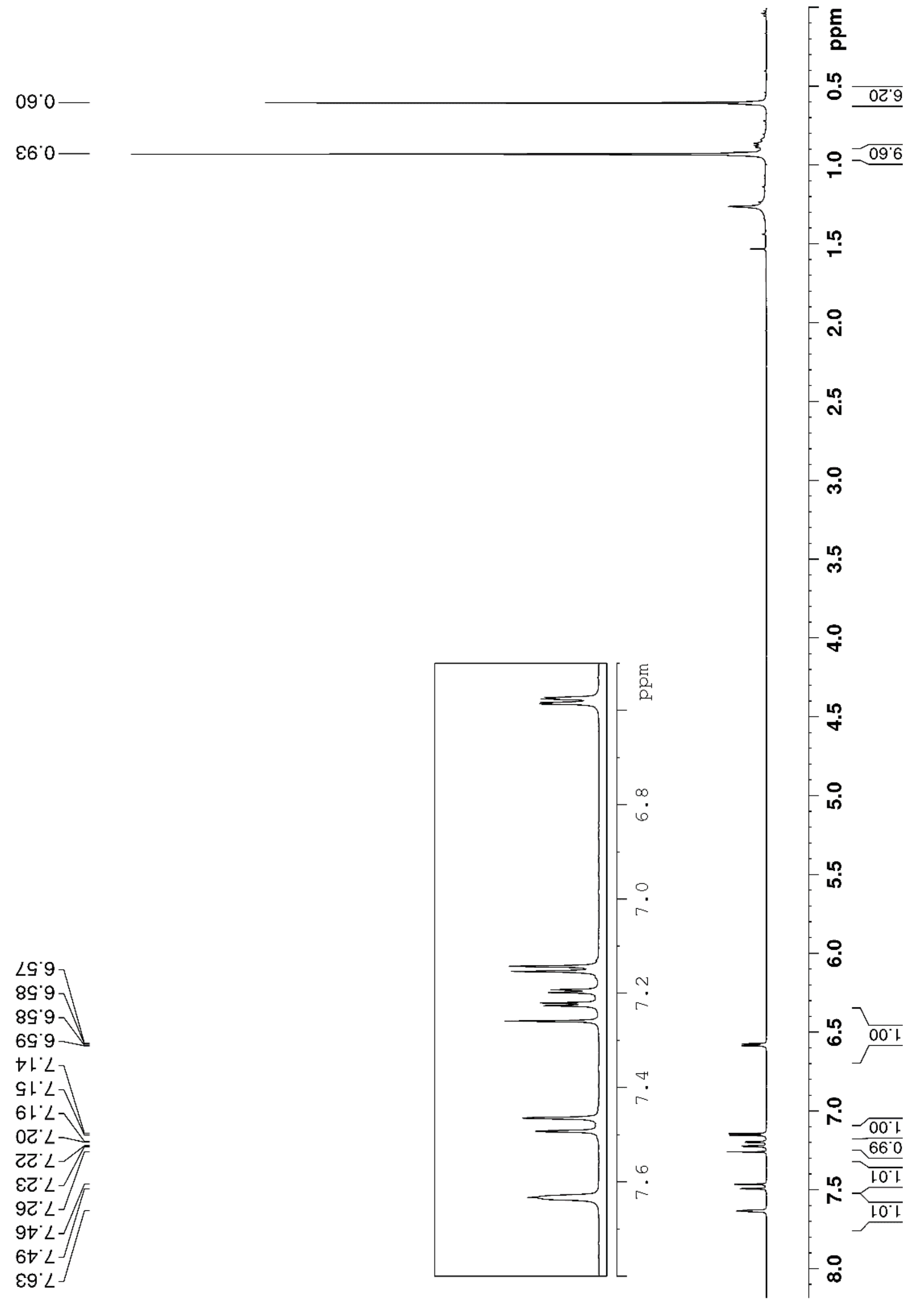

Figure A69. ^{1}H NMR (300 MHz, $CDCl_3$) spectrum of compound **4.15b**.

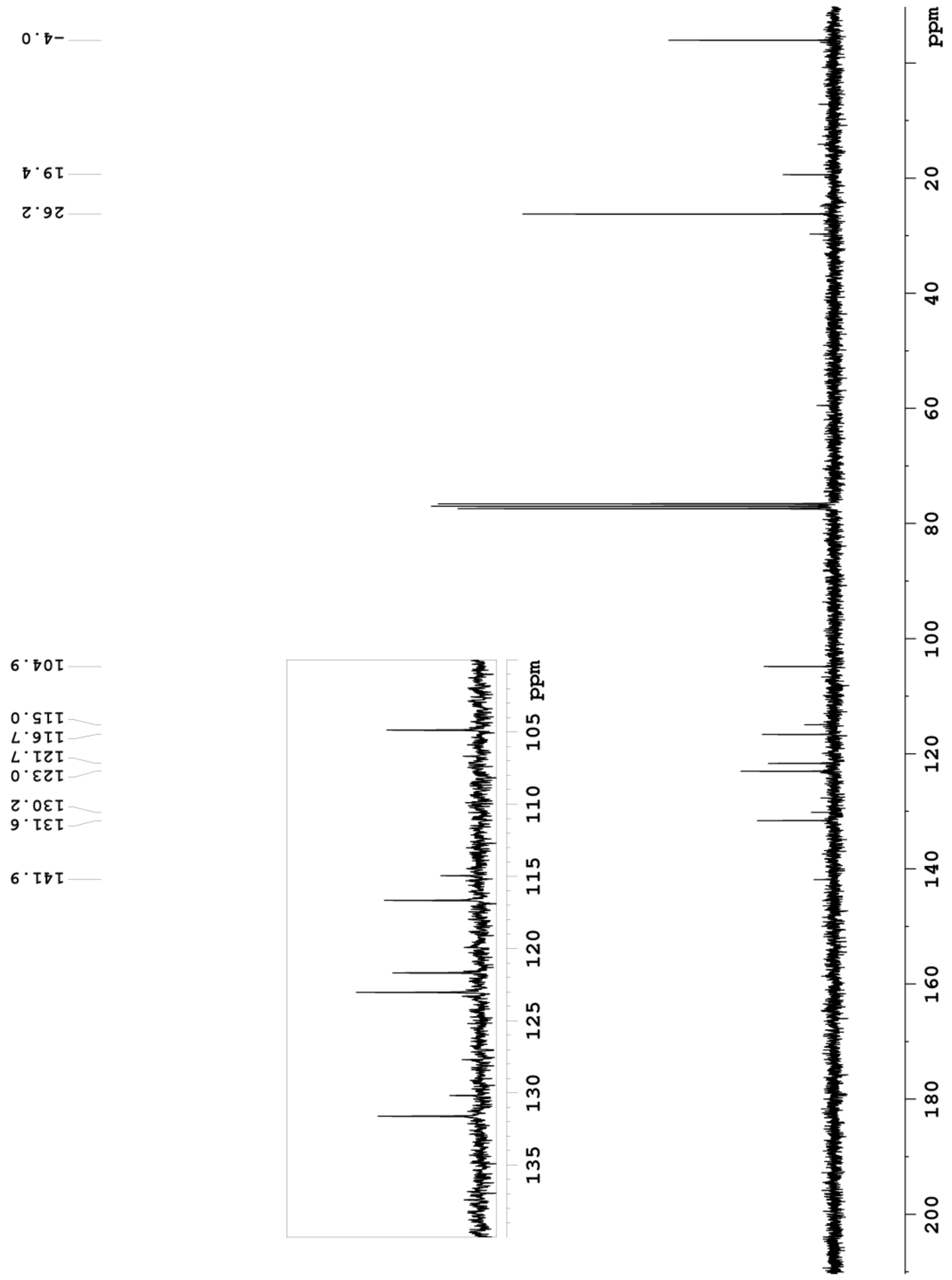

Figure A70. ^{13}C NMR (75 MHz, $CDCl_3$) spectrum of compound **4.15b**.

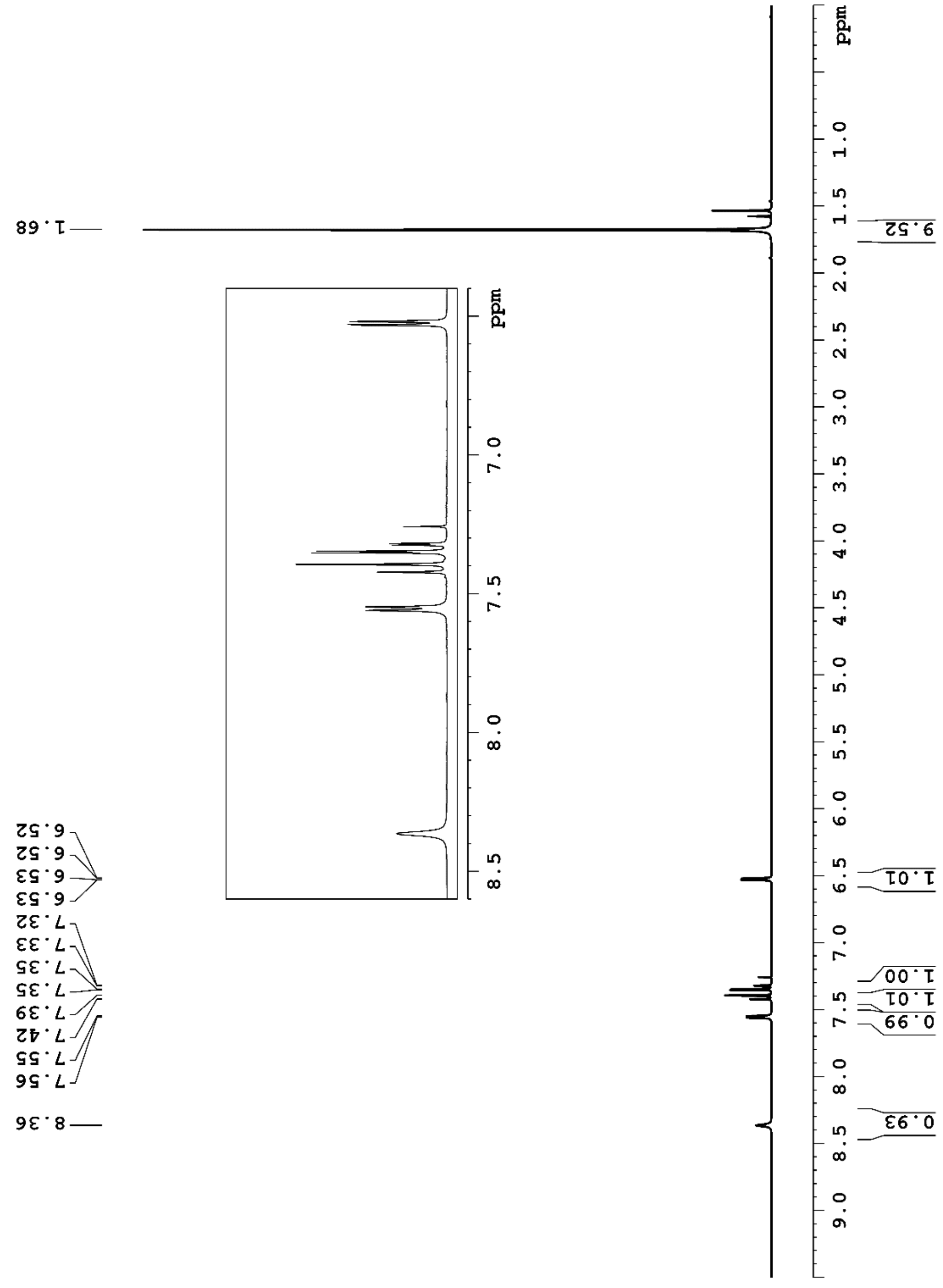

Figure A71. ^{1}H NMR (300 MHz, $CDCl_3$) spectrum of compound **4.15c**.

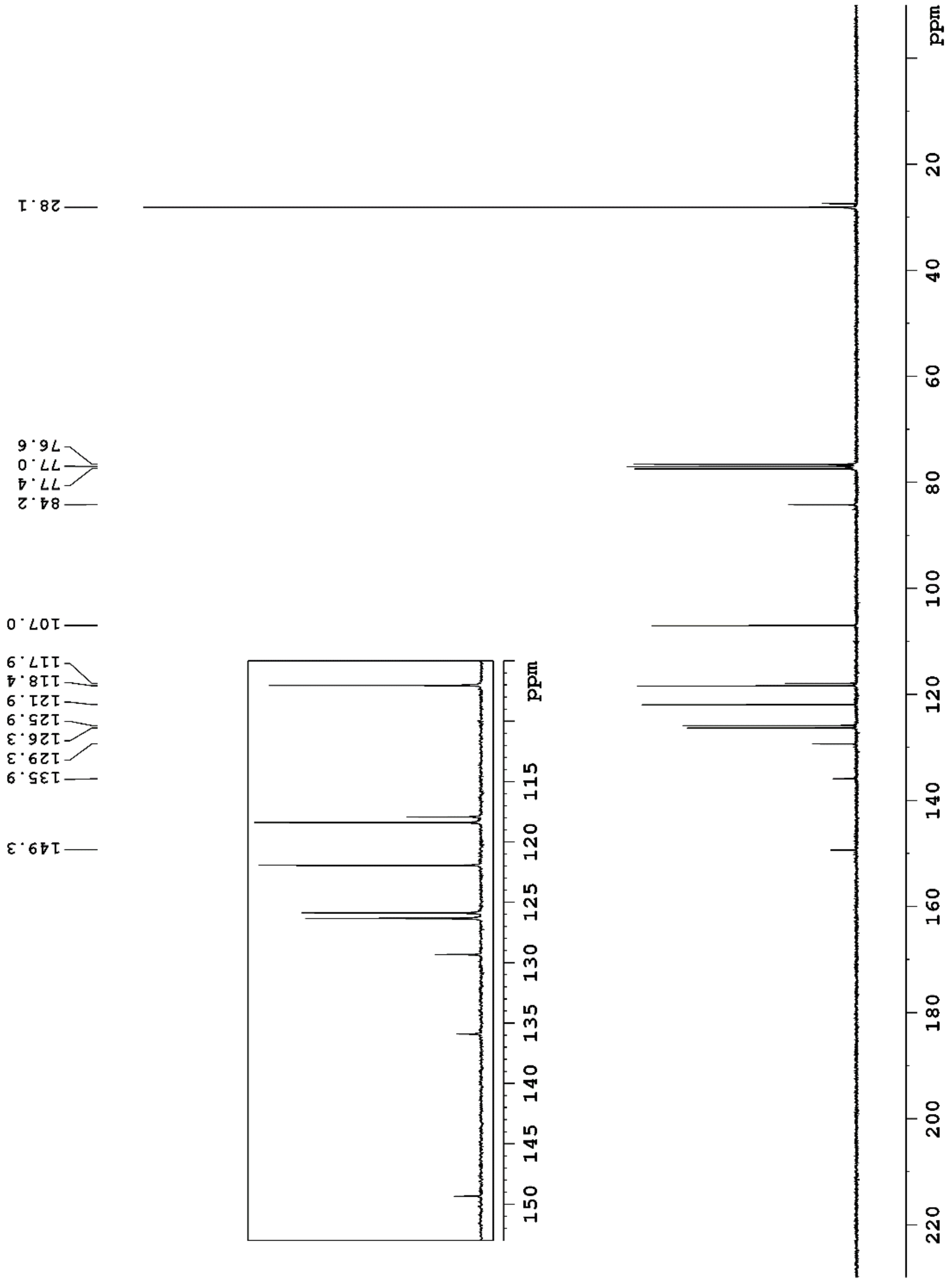

Figure A72. ^{13}C NMR (75 MHz, CDCl$_3$) spectrum of compound **4.15c**.

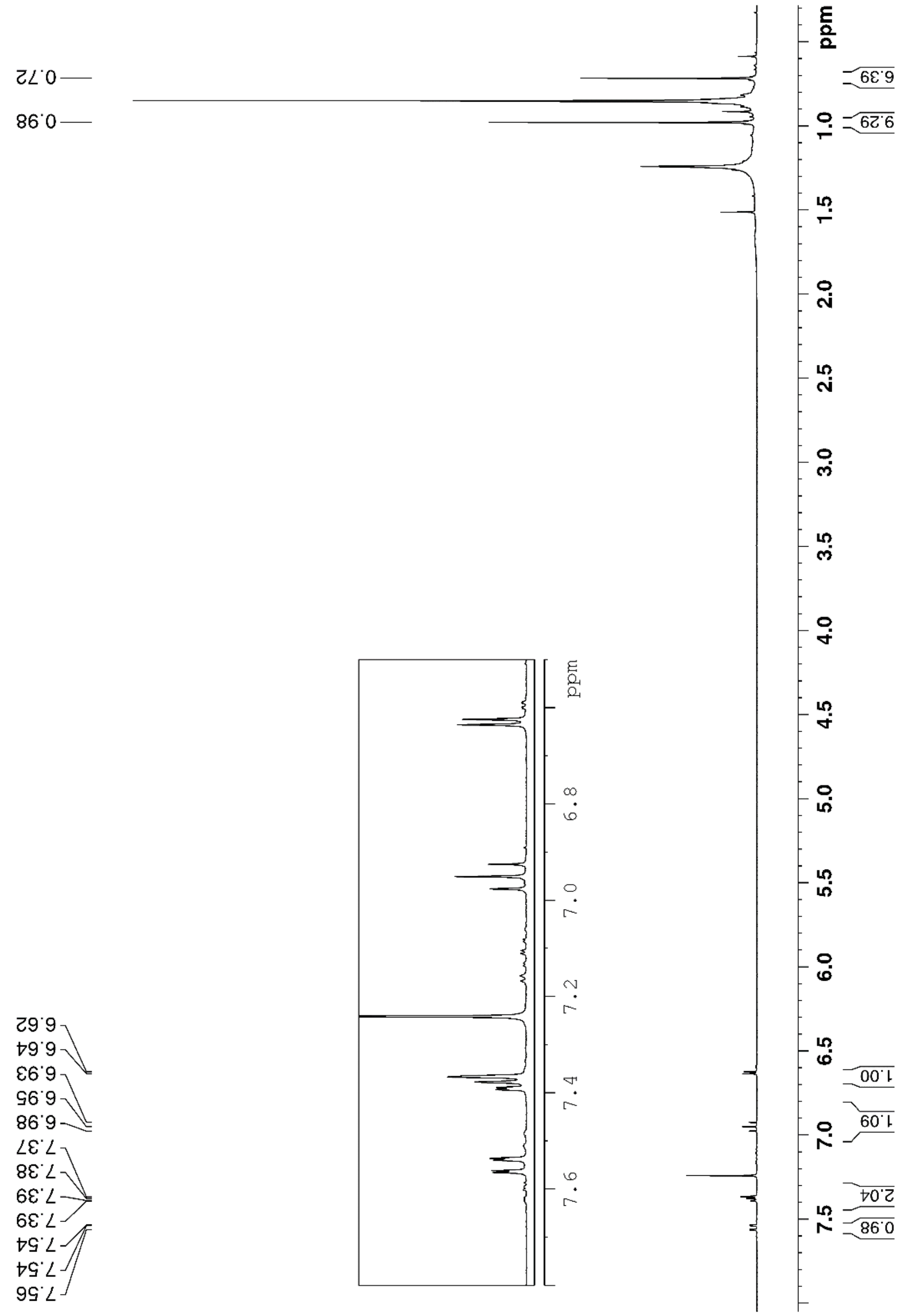

Figure A73. ^{1}H NMR (300 MHz, $CDCl_3$) spectrum of compound **4.16b**.

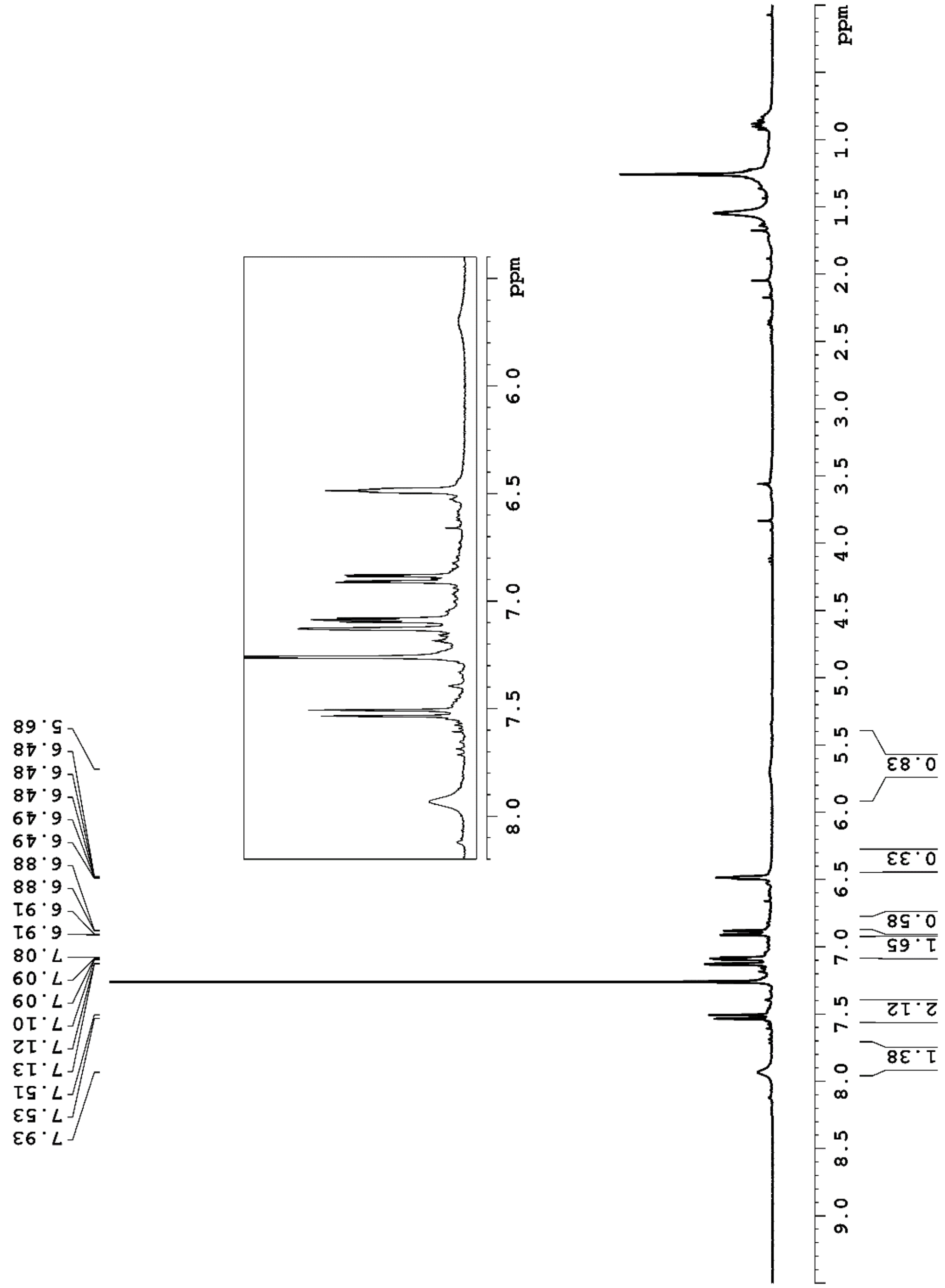

Figure A74. ^{1}H NMR (300 MHz, $CDCl_3$) spectrum of compound **4.20a**.

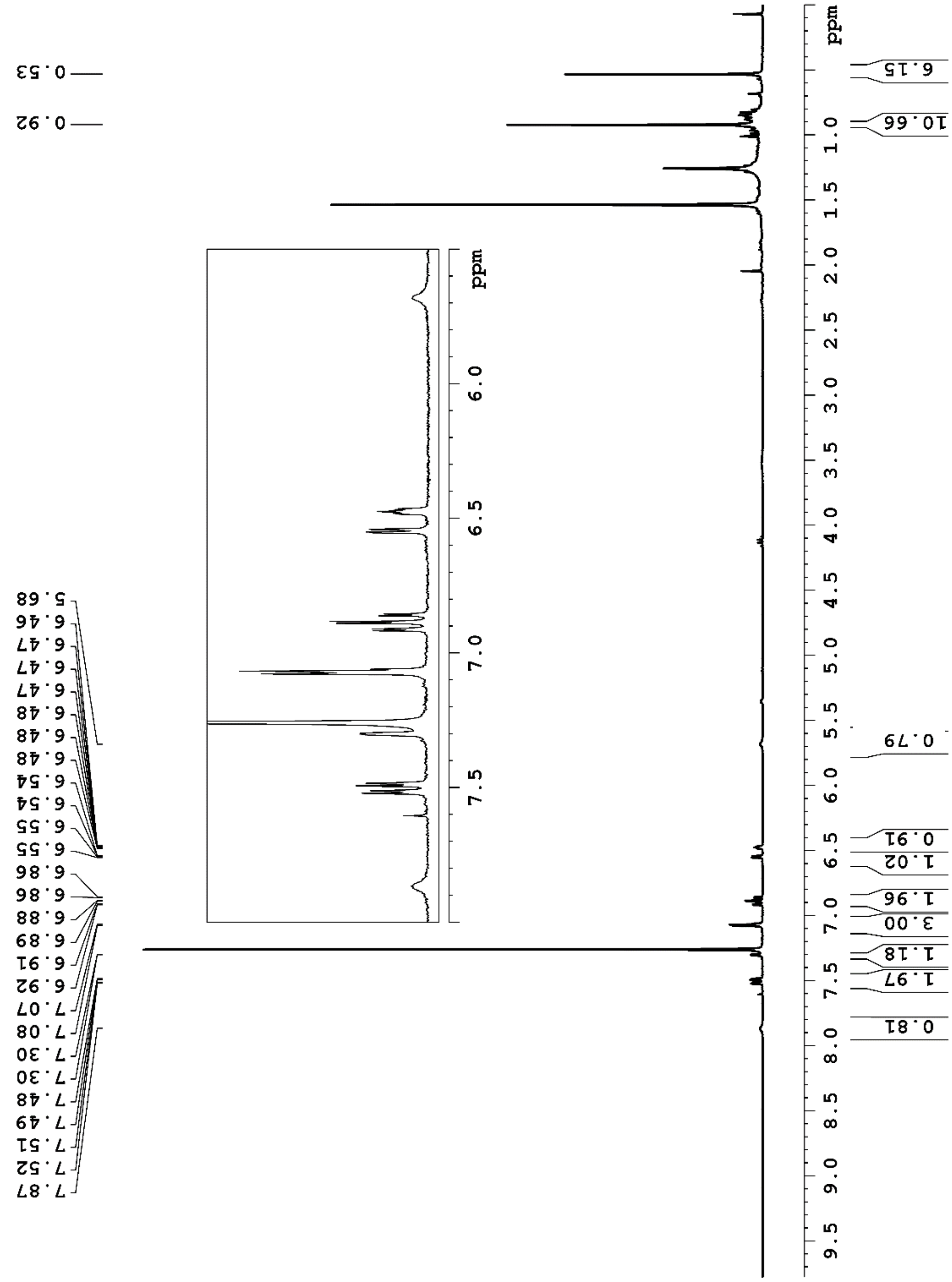

Figure A75. ^{1}H NMR (300 MHz, $CDCl_3$) spectrum of compound **4.20b**.

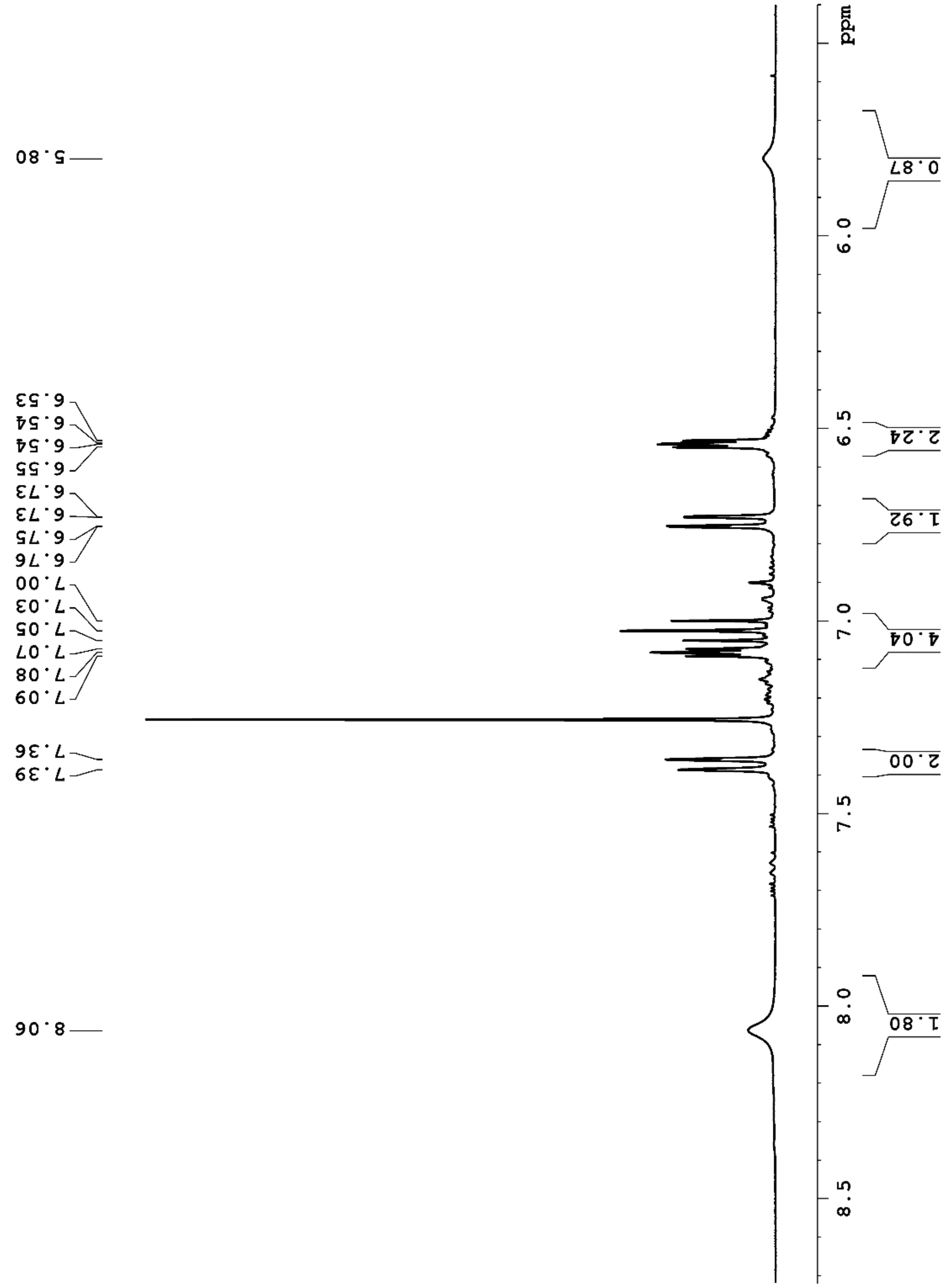

Figure A76. ¹H NMR (300 MHz, $CDCl_3$) spectrum of compound **4.21a**.

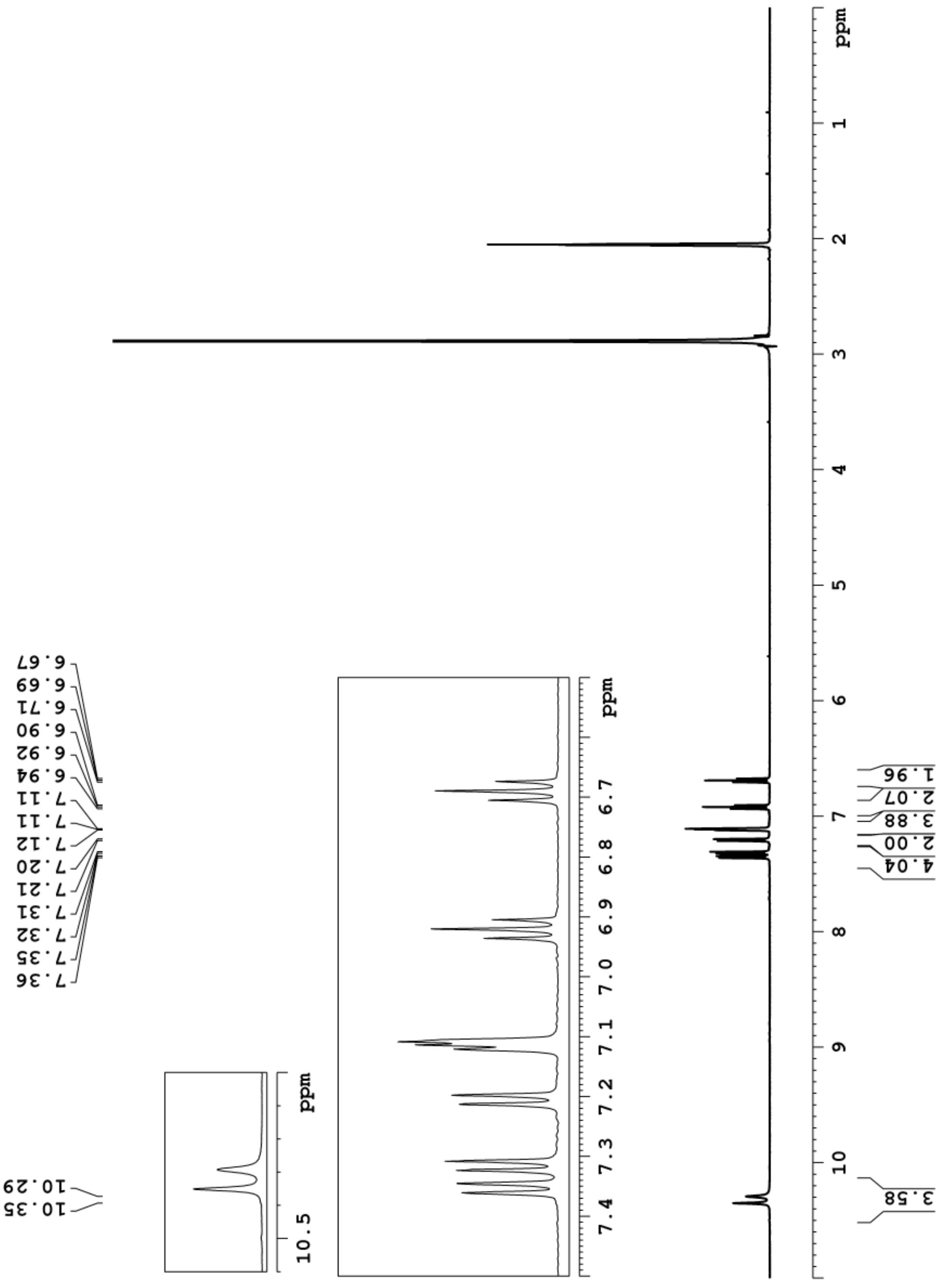

Figure A77. ^{1}H NMR (500 MHz, acetone-*d6*) spectrum of compound **4.24**.

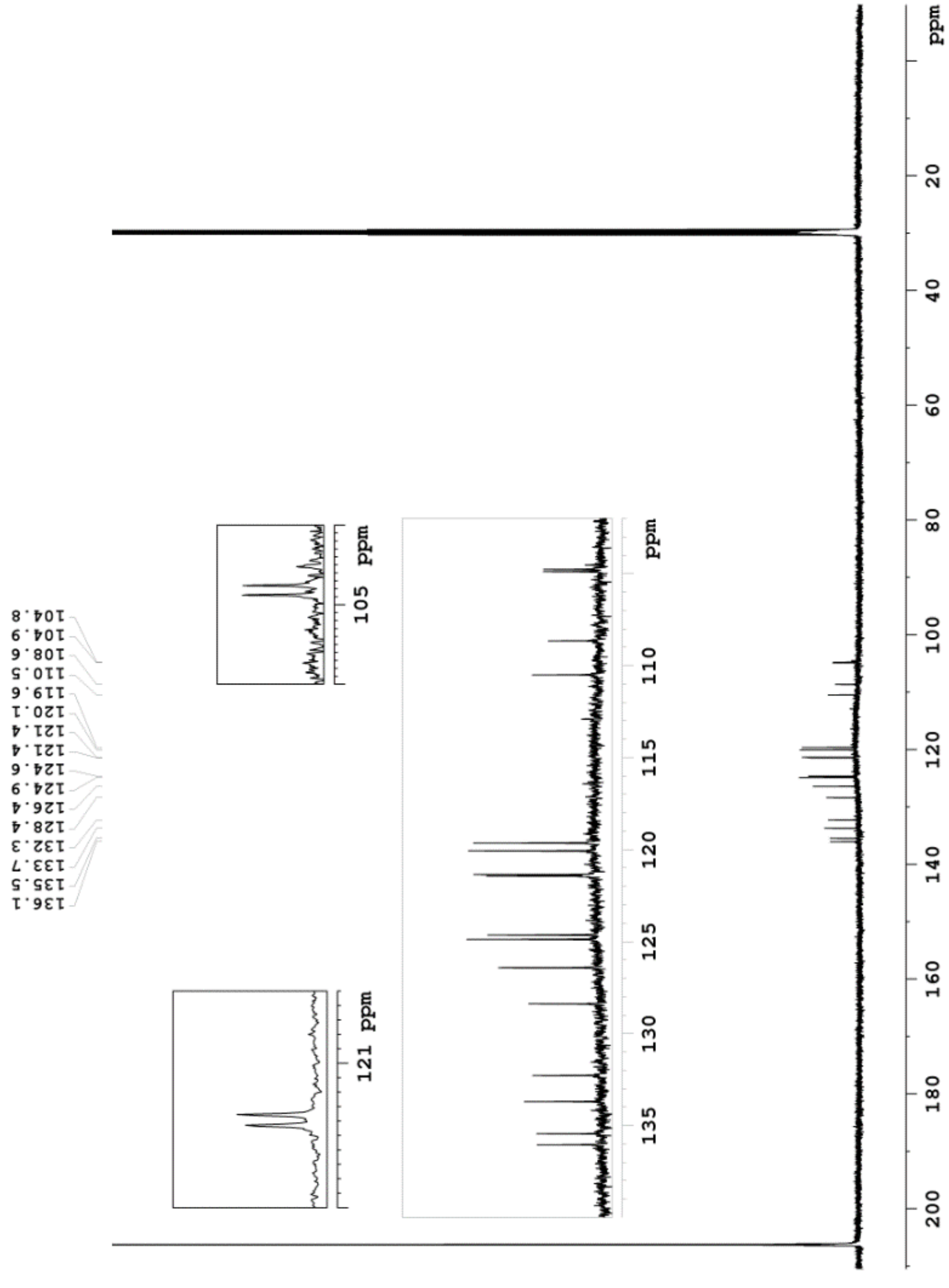

Figure A78. ^{13}C NMR (125 MHz, acetone-*d6*) spectrum of compound **4.24**.

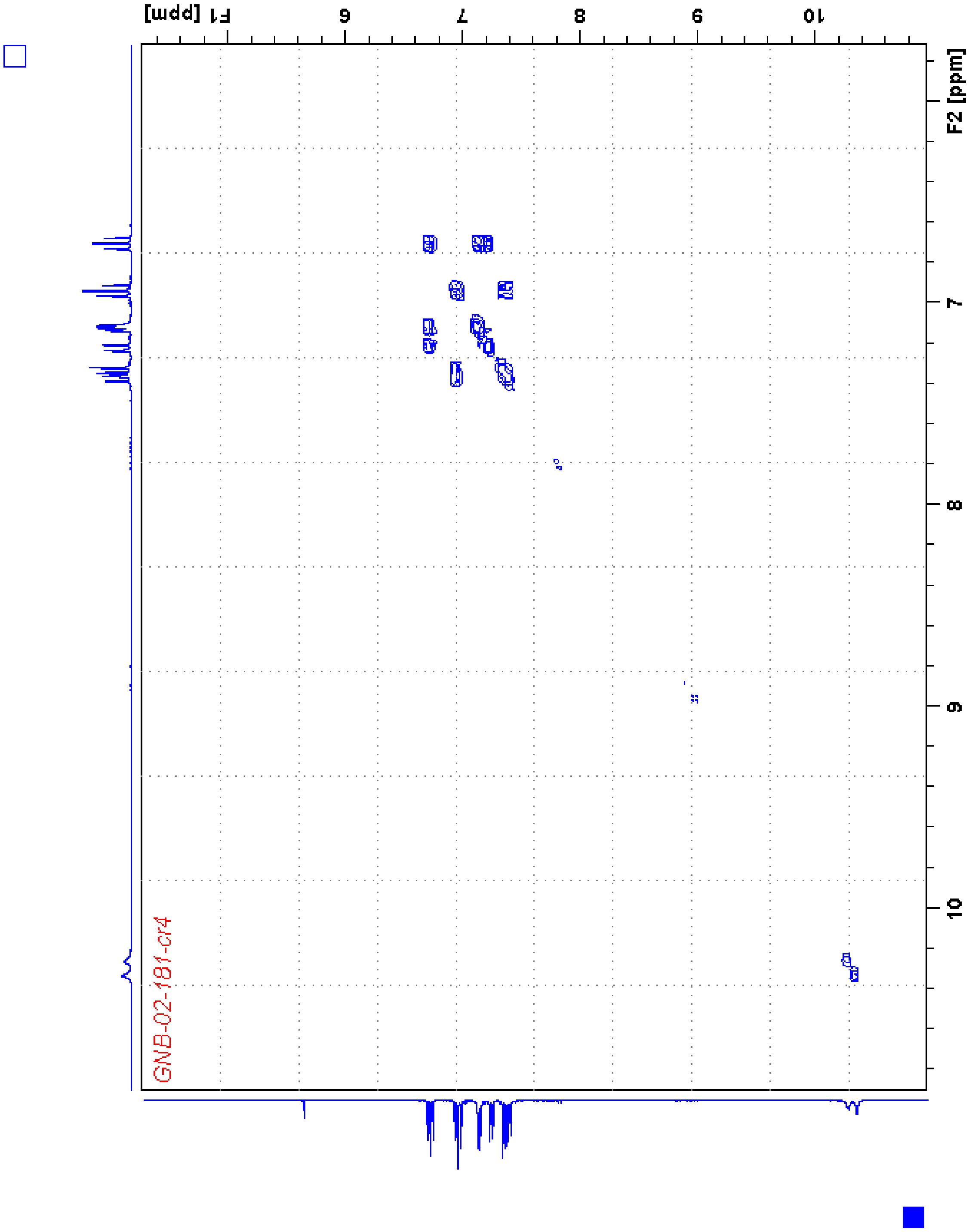

Figure A79. COSY NMR (300 MHz, CDCl$_3$) spectrum of compound **4.24**.

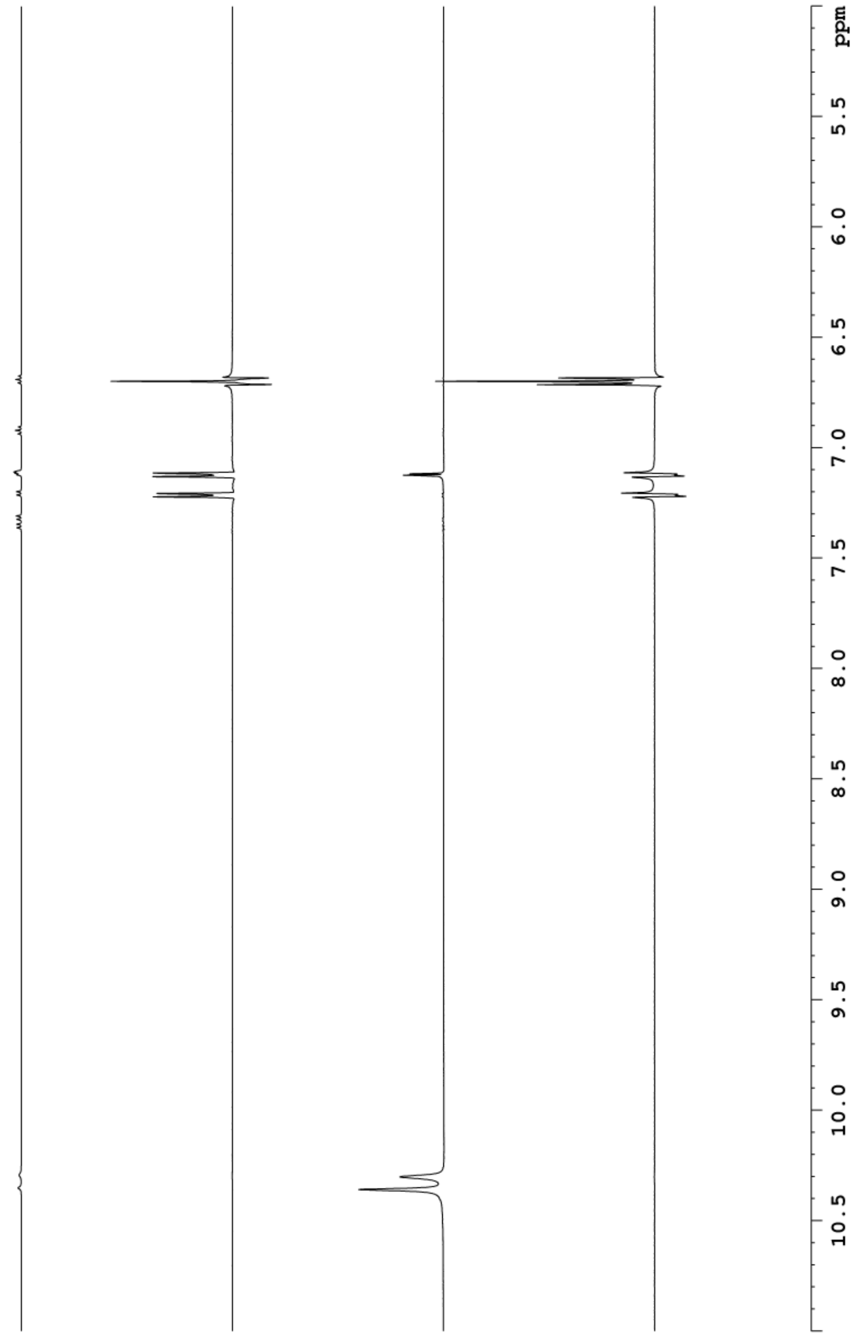

Figure A80. TOCSY NMR (500 MHz, acetone-*d6*) spectrum of compound **4.24**.

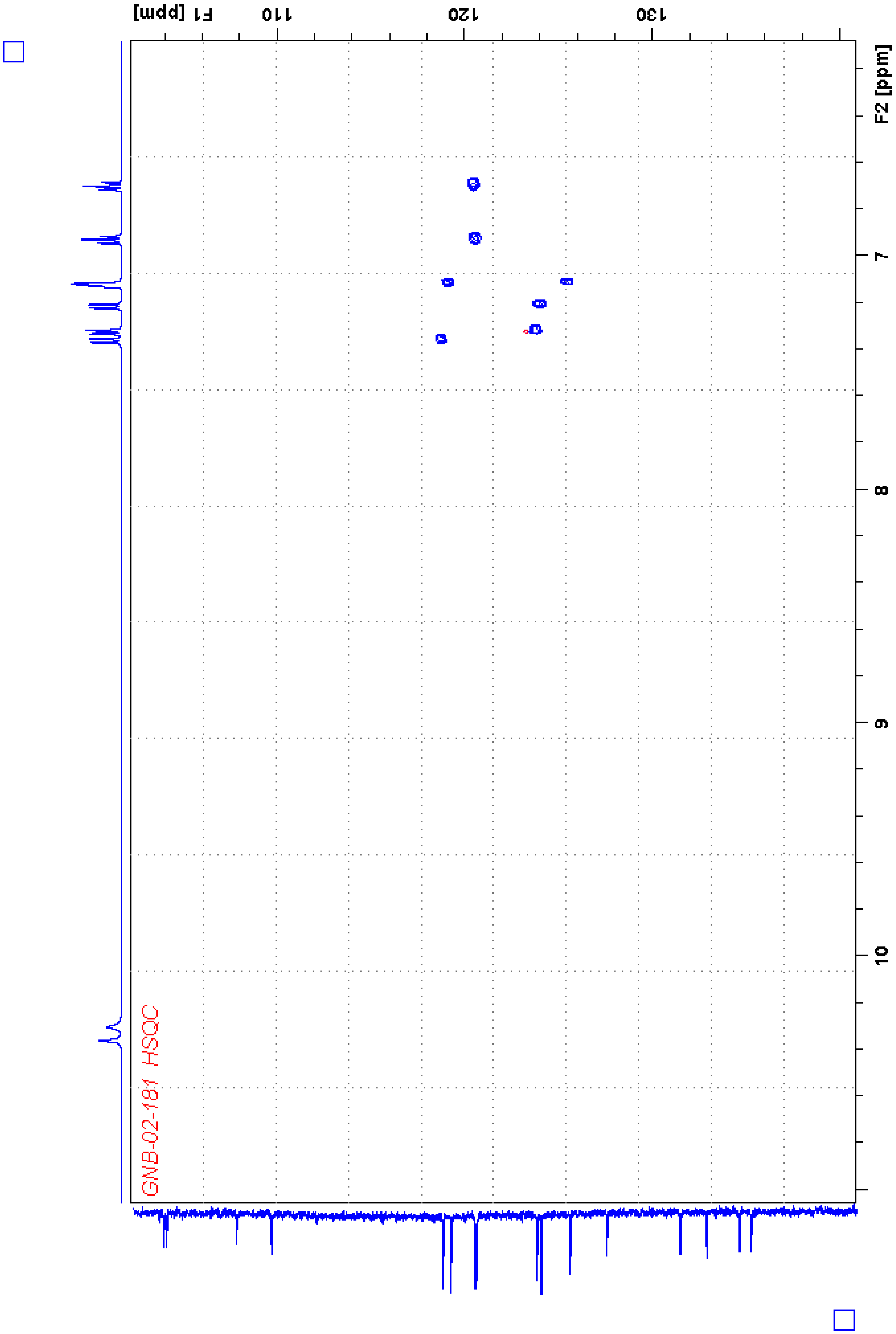

Figure A81. HSQC NMR (500 MHz, acetone-*d6*) spectrum of compound **4.24**.

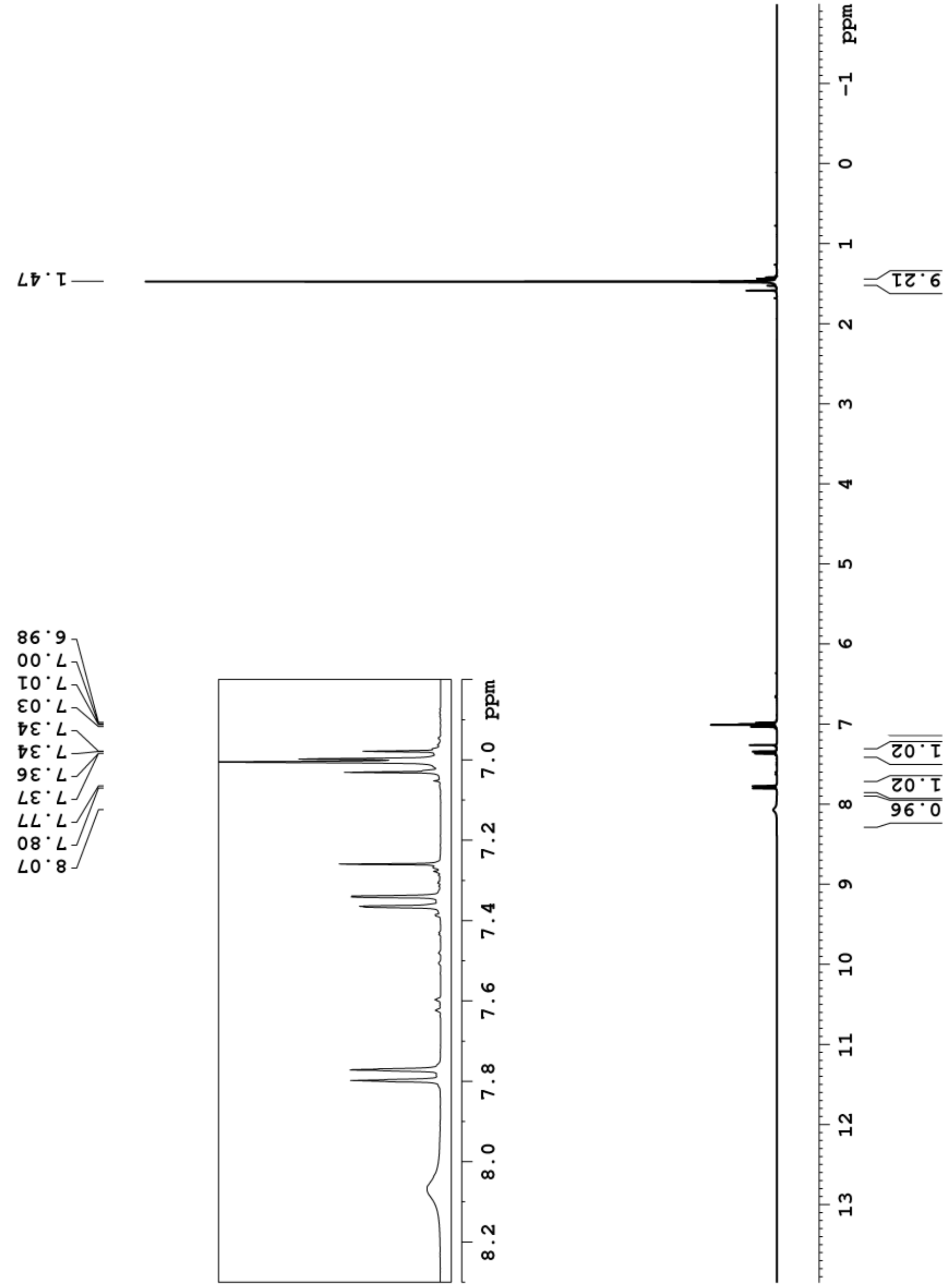

Figure A82. ^{1}H NMR (300 MHz, $CDCl_3$) spectrum of compound **4.25**.

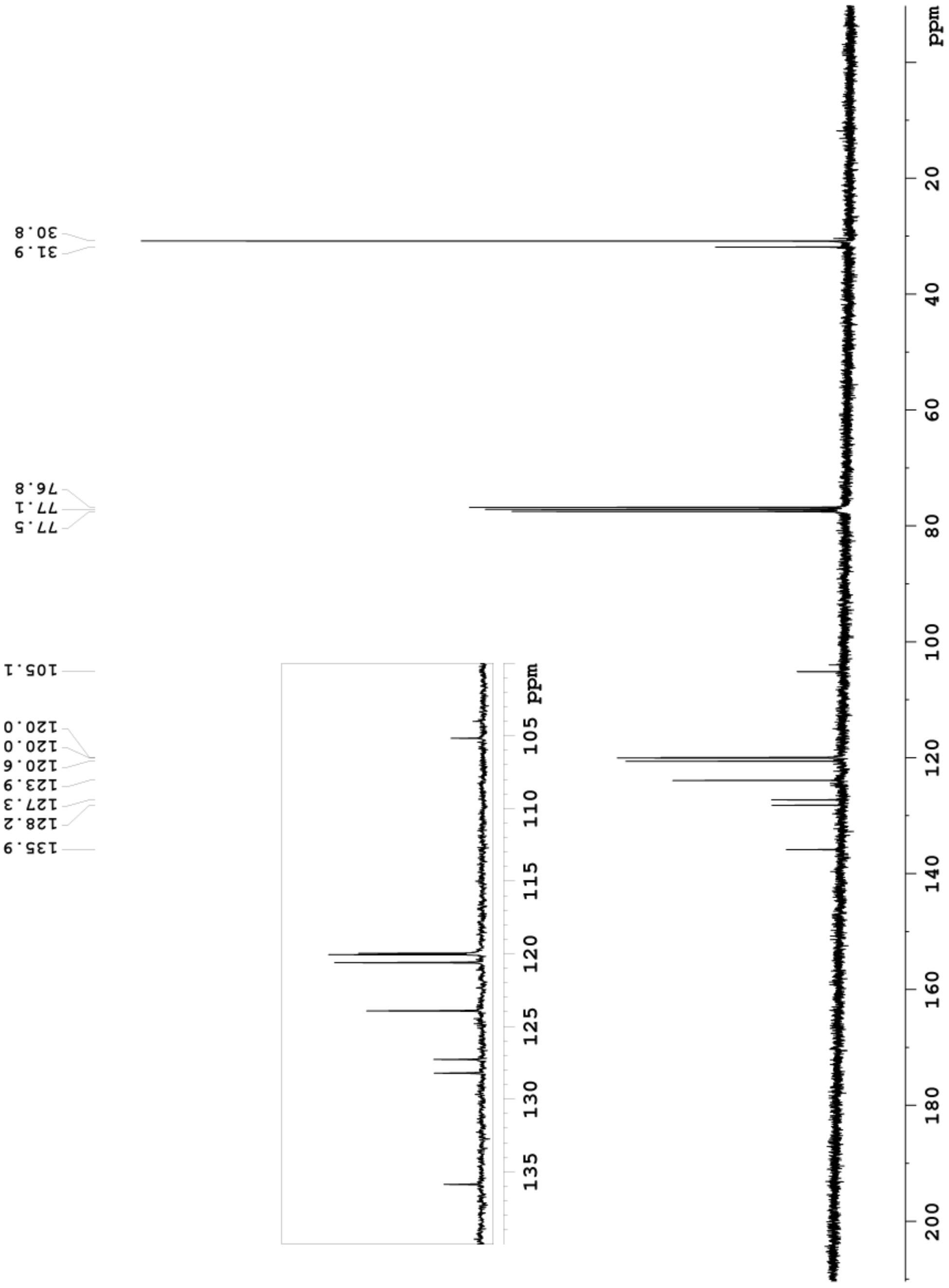

Figure A83. ^{1}13 NMR (90 MHz, CDCl$_3$) spectrum of compound **4.25**.

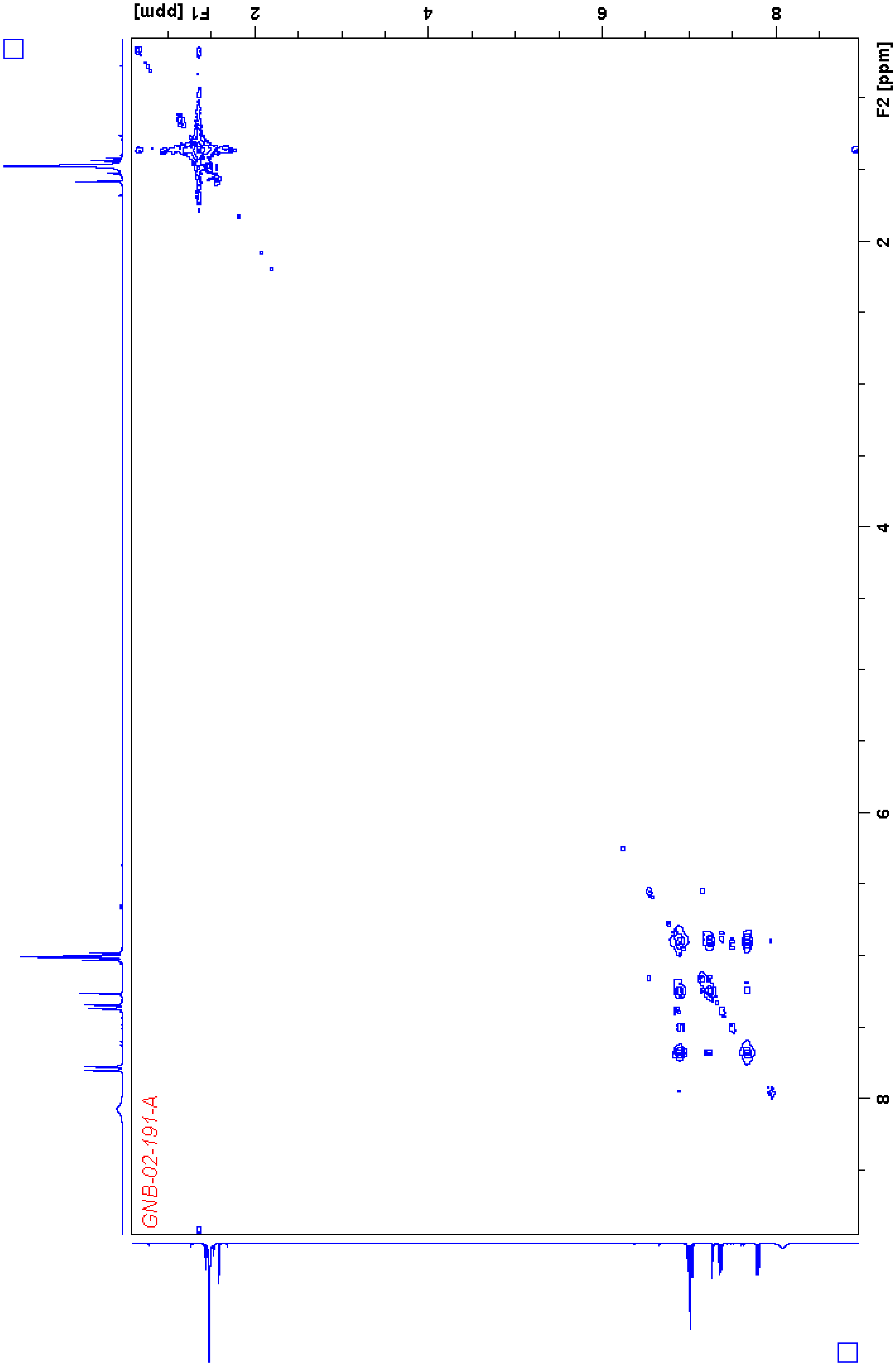

Figure A84. COSY NMR (300 MHz, $CDCl_3$) spectrum of compound **4.25**.

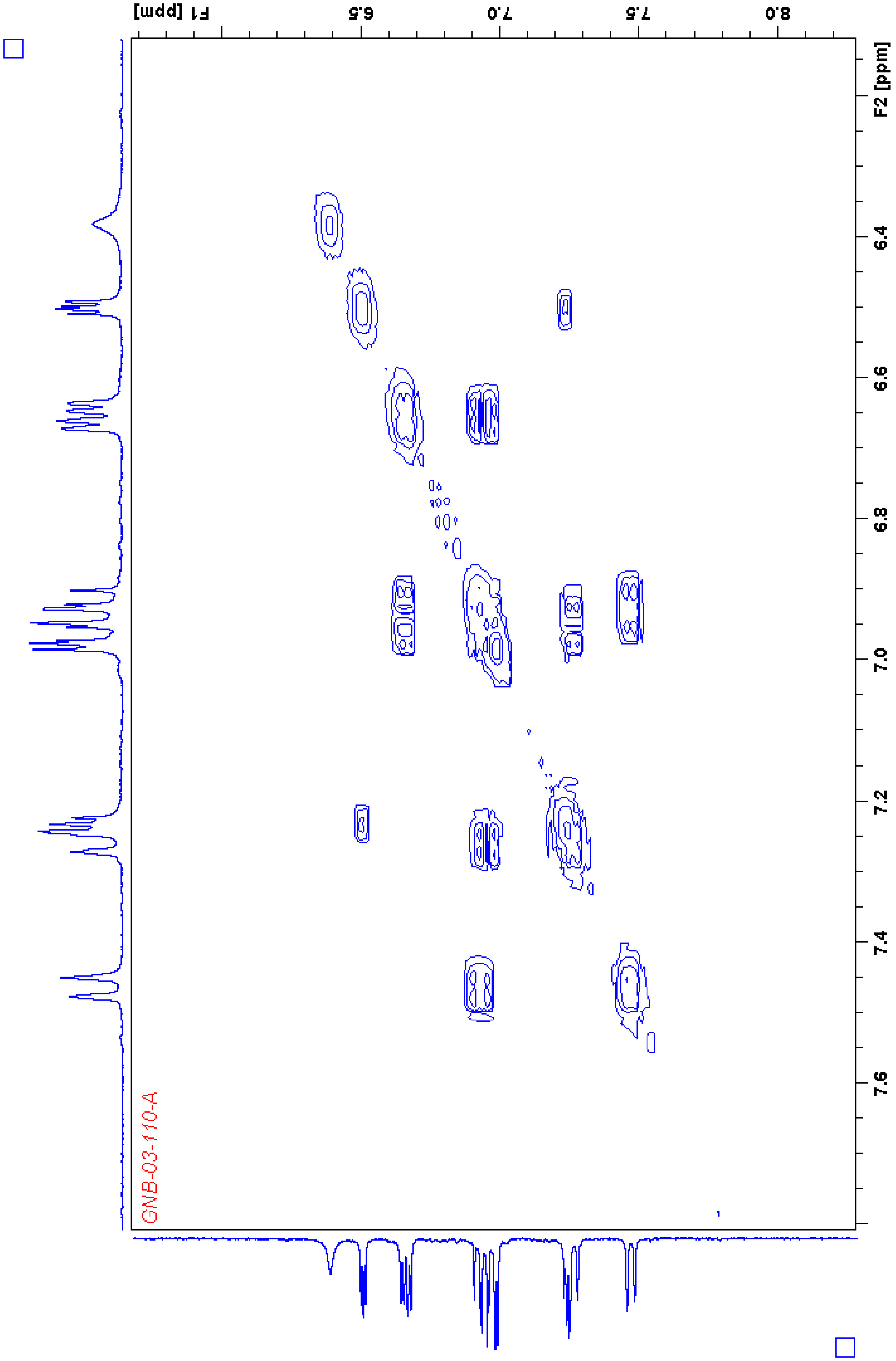

Figure A5. COSY NMR (300 MHz, $CDCl_3$) spectrum of compound **4.25**.

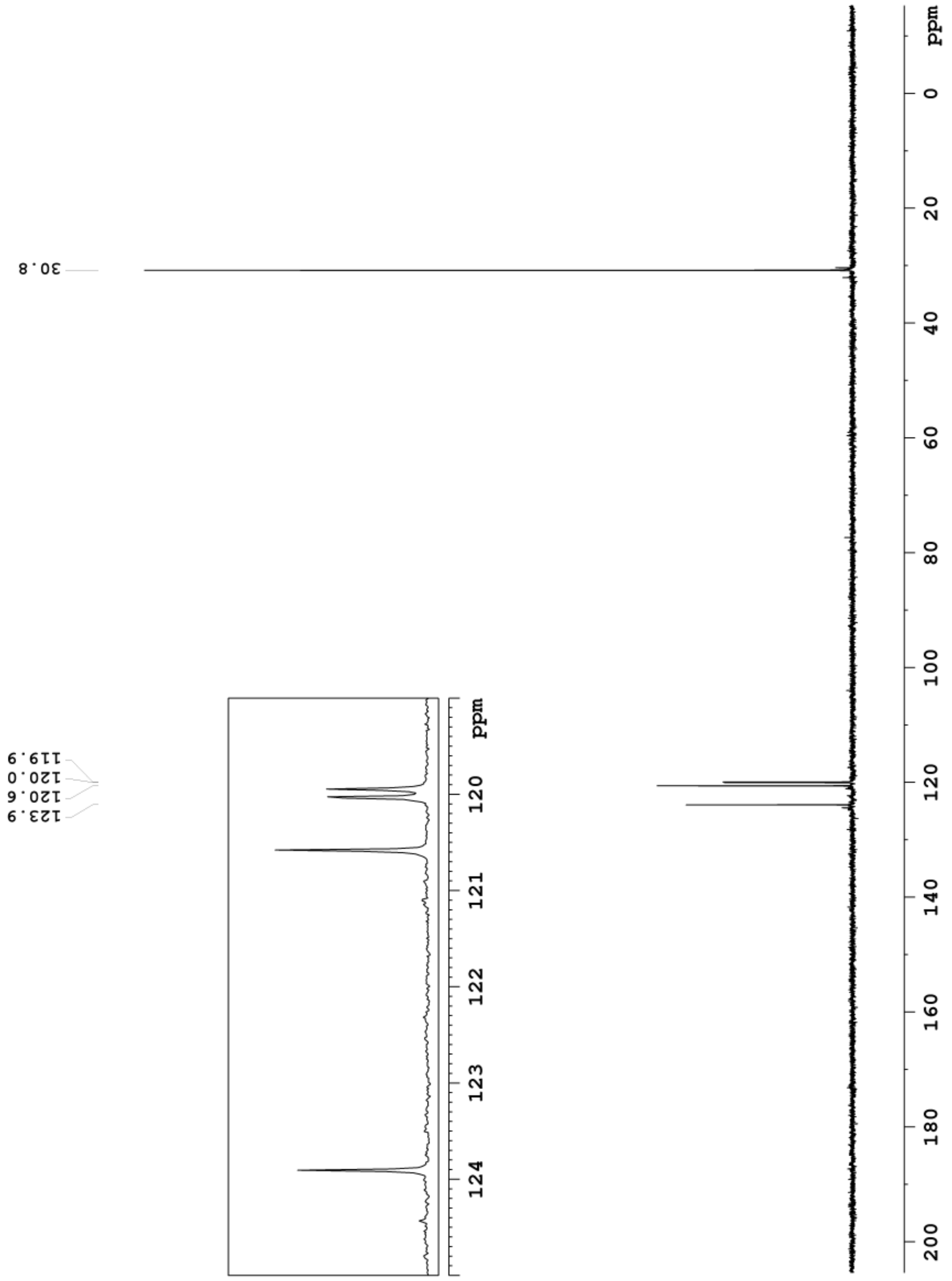

Figure A86. DEPT135 NMR (75 MHz, $CDCl_3$) spectrum of compound **4.25**.

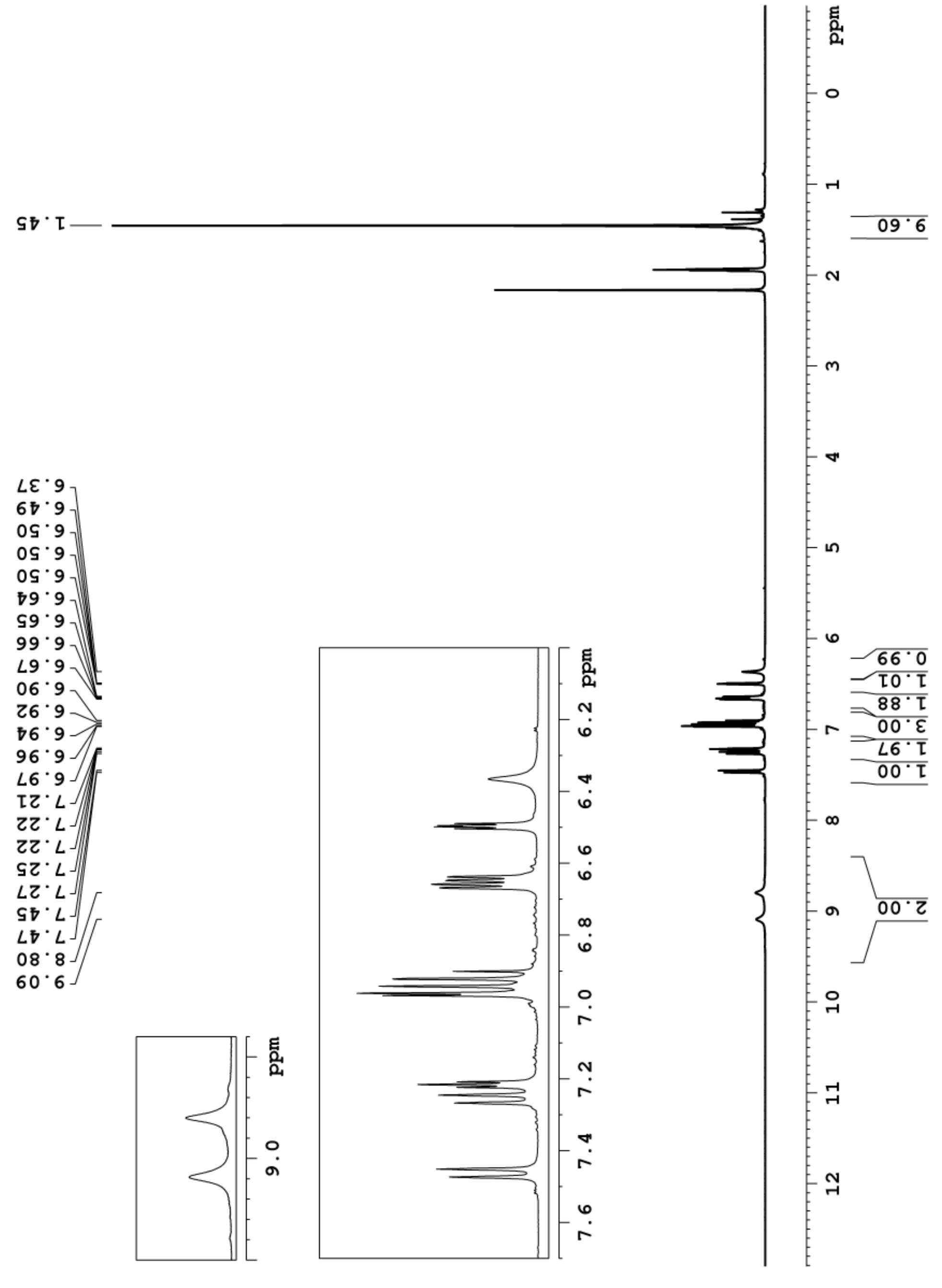

Figure A87. ^{1}H NMR (360 MHz, CD_3CN) spectrum of compound **4.26**.

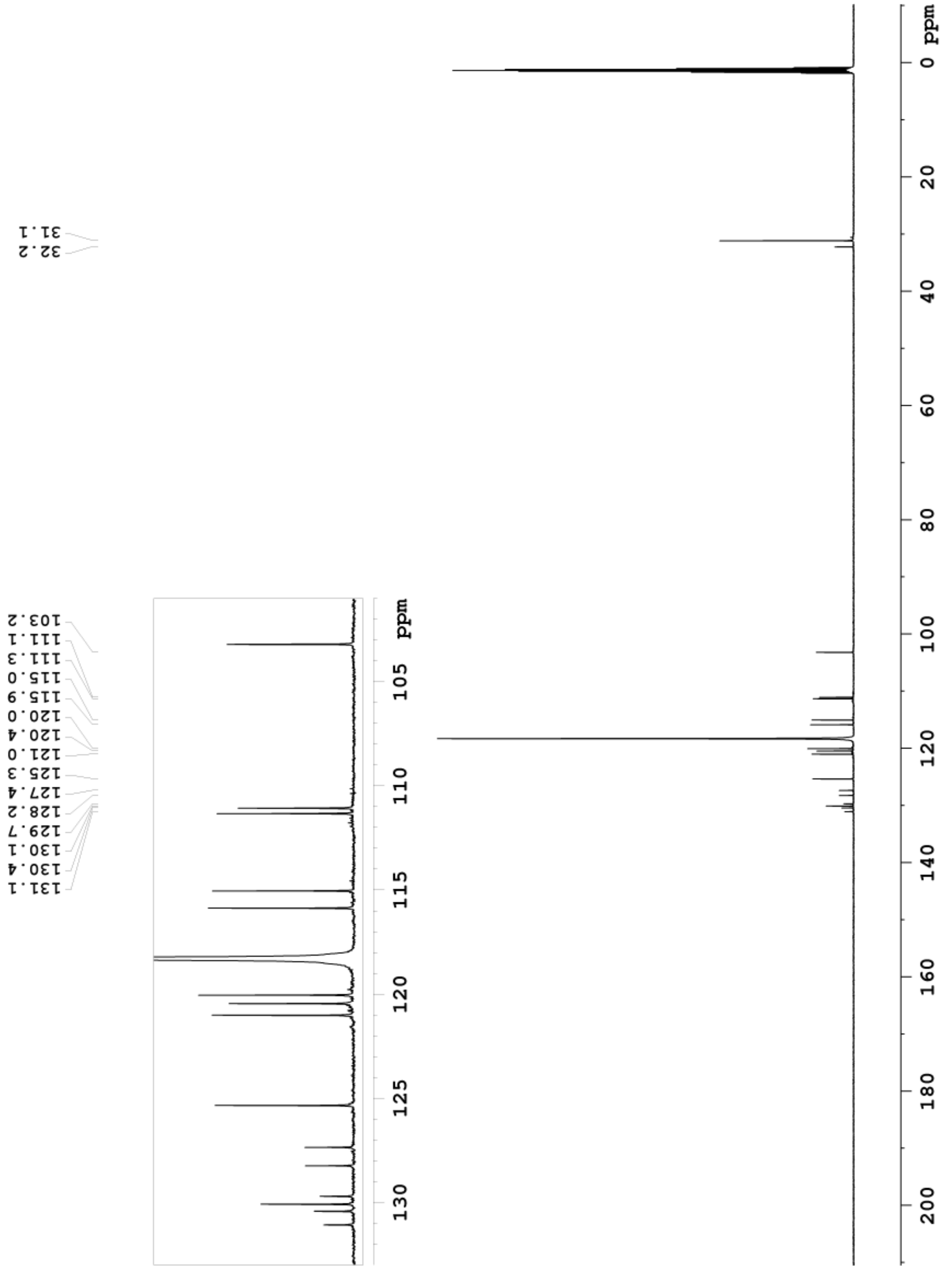

Figure A88. ^{1}13 NMR (125 MHz, CD_3CN) spectrum of compound **4.26**.

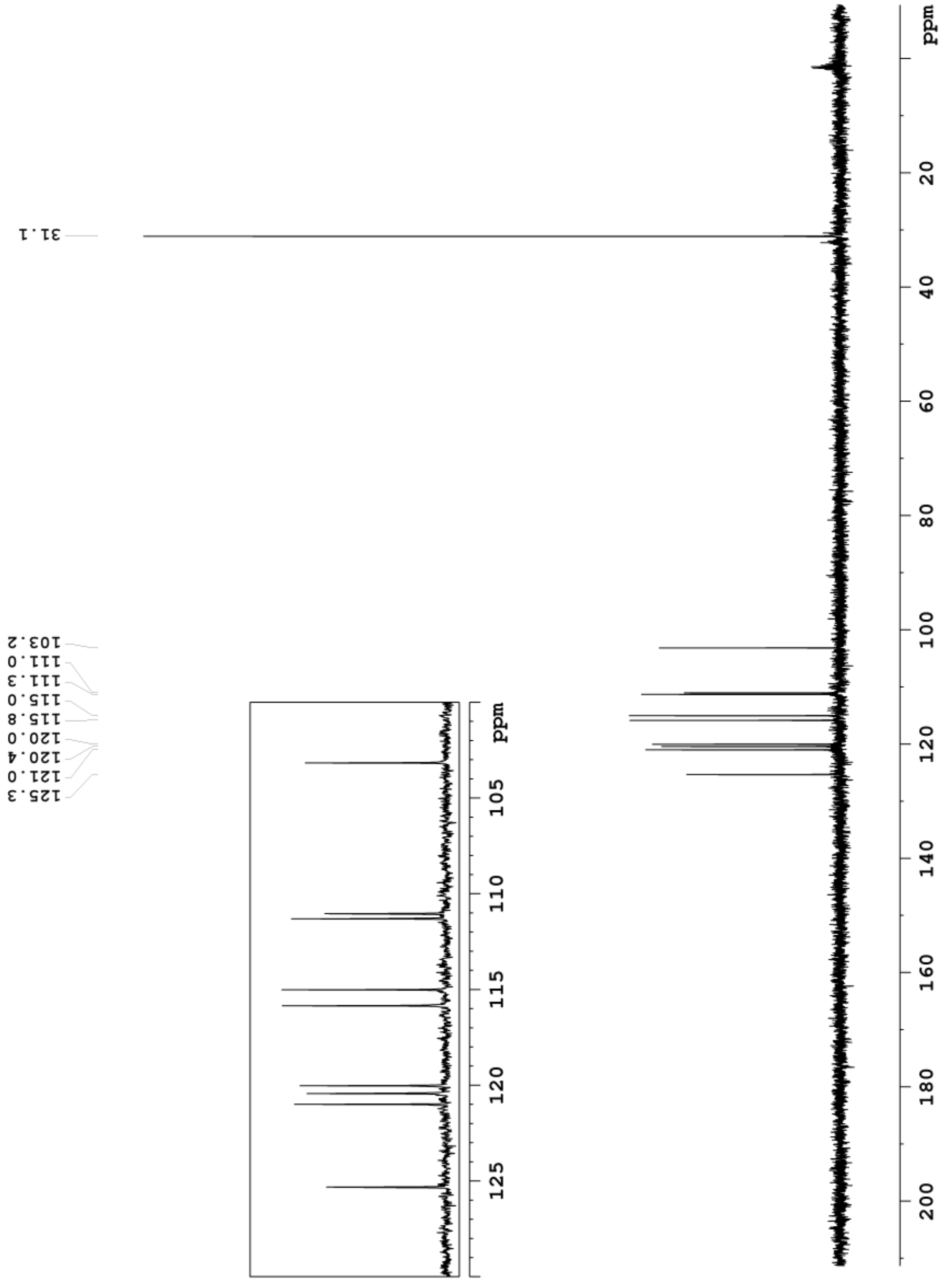

Figure A89 DEPT135 NMR (90 MHz, CD_3CN) spectrum of compound **4.26**

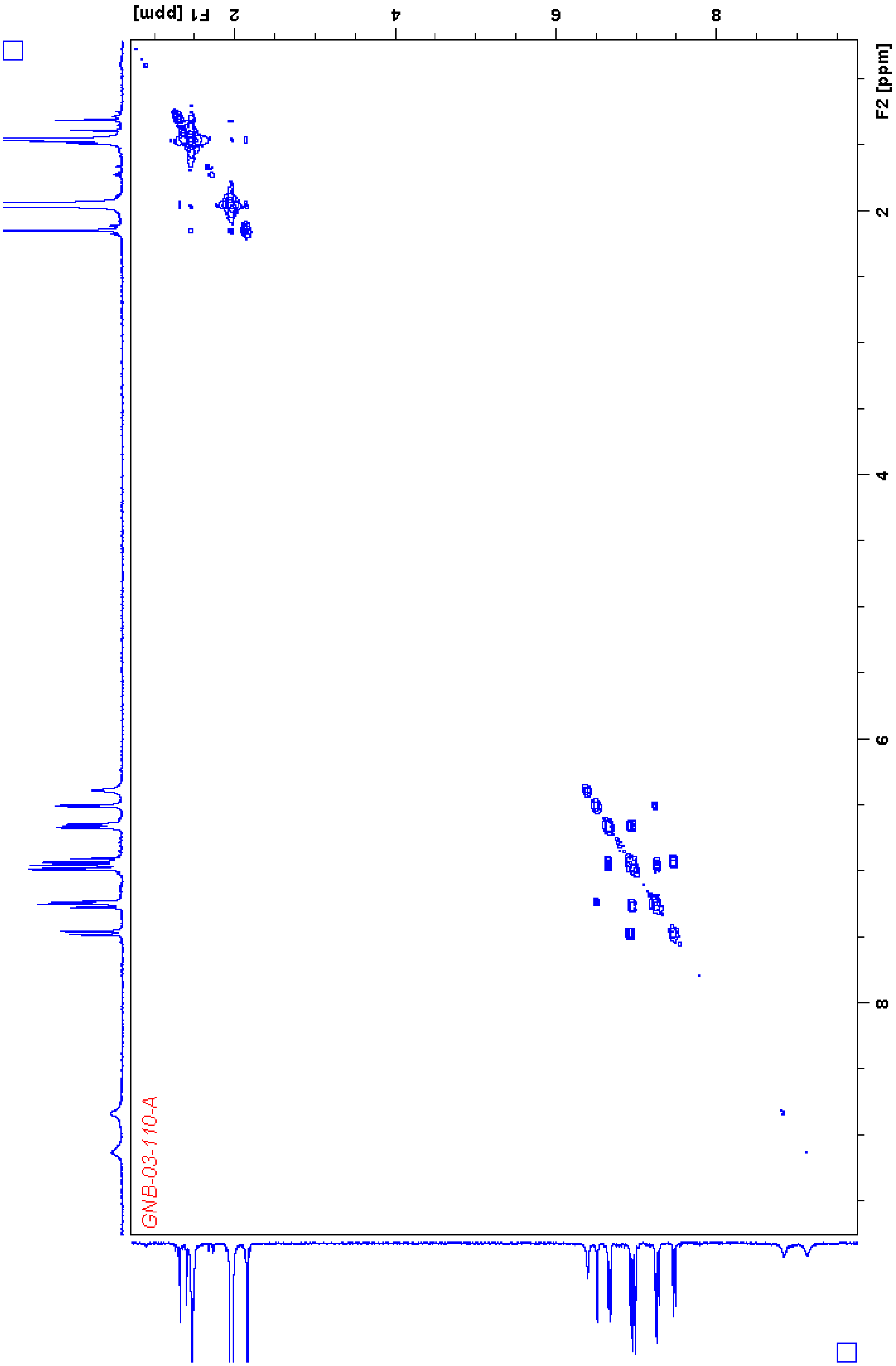

Figure A90. COSY NMR (300 MHz, $CDCl_3$) spectrum of compound **4.26**.

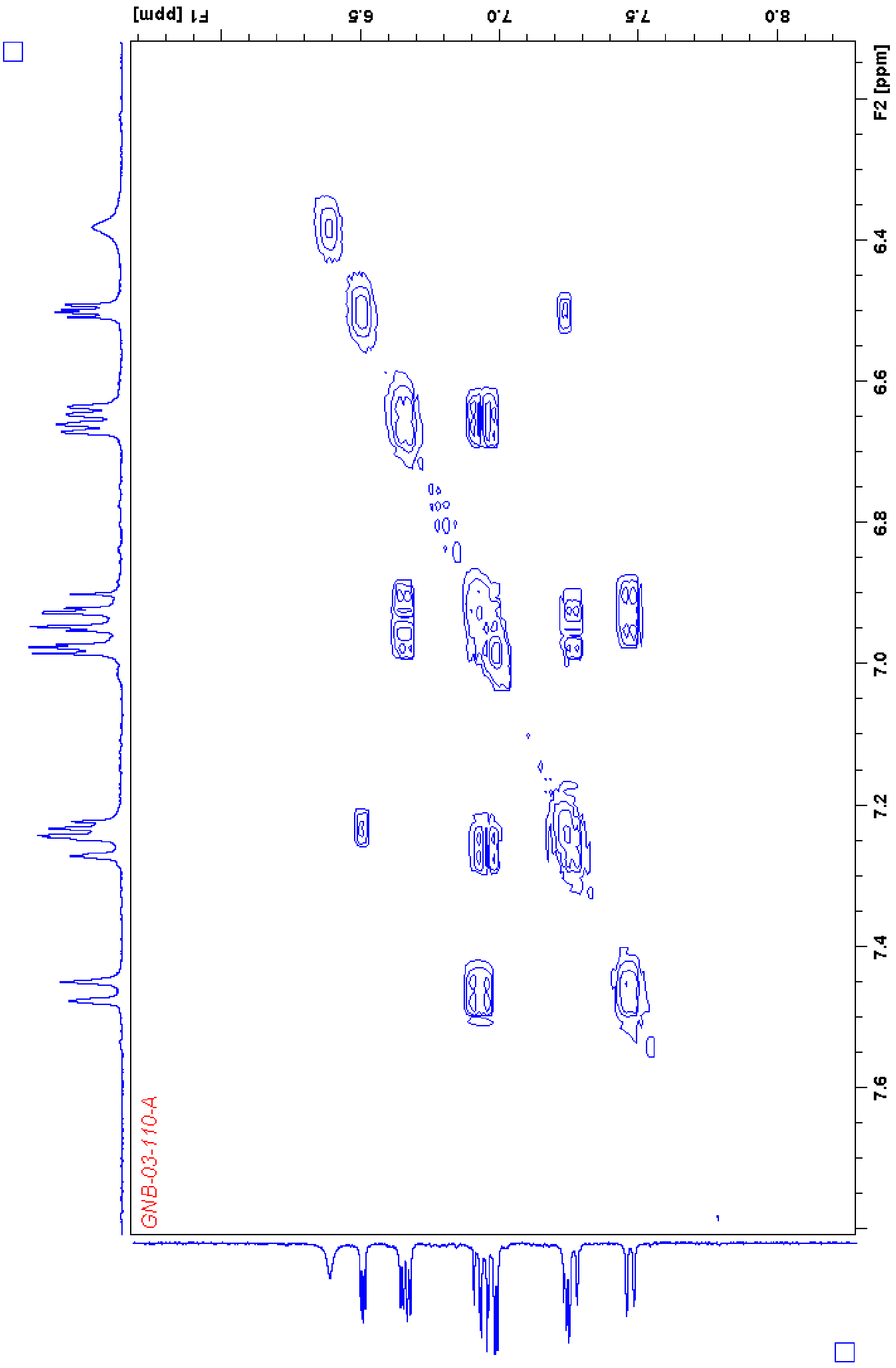

Figure A91. COSY NMR (300 MHz, $CDCl_3$) spectrum of compound **4.26**.

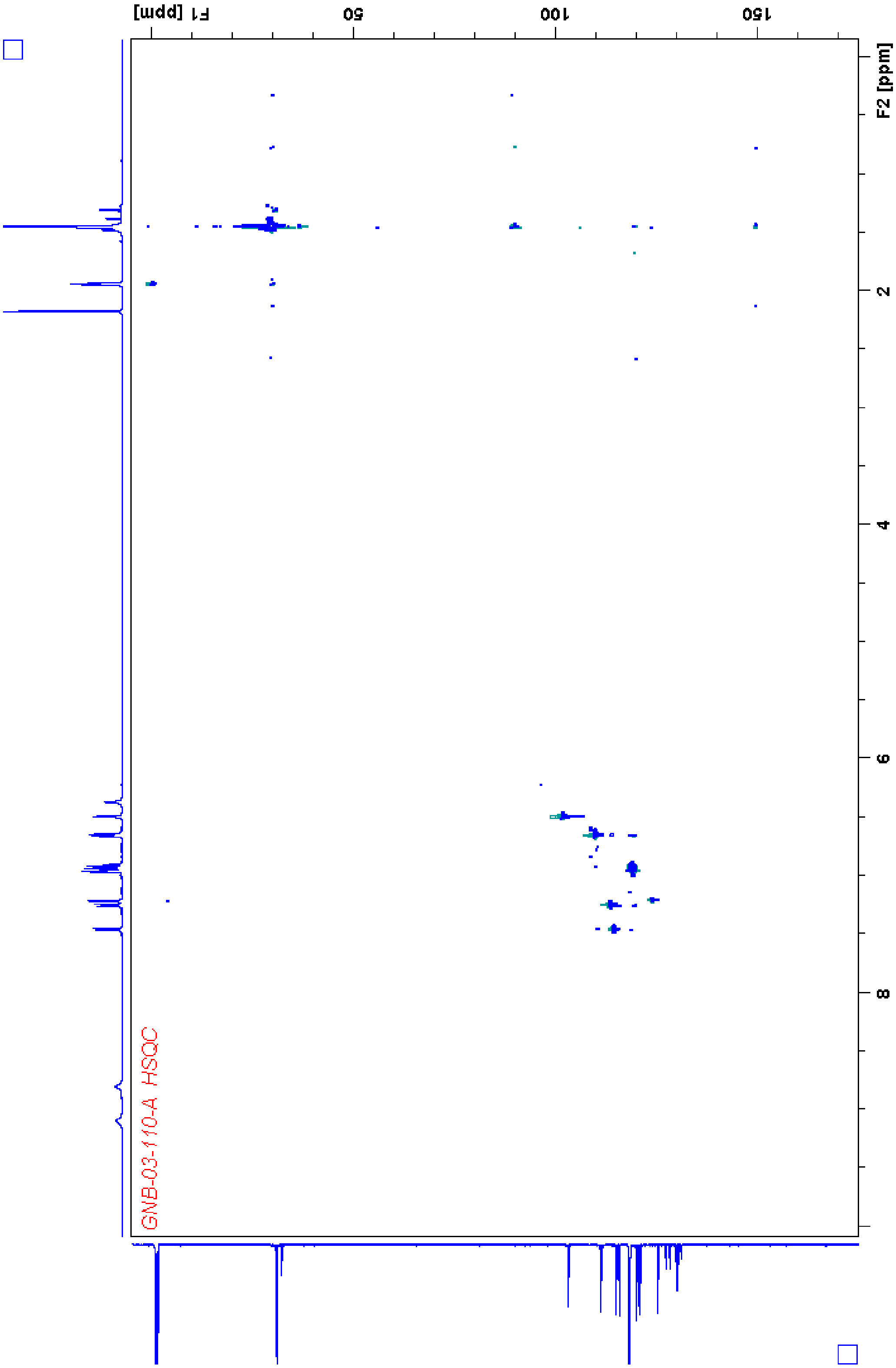

Figure A92. HSQC NMR (500 MHz, CD_3CN) spectrum of compound **4.26**.

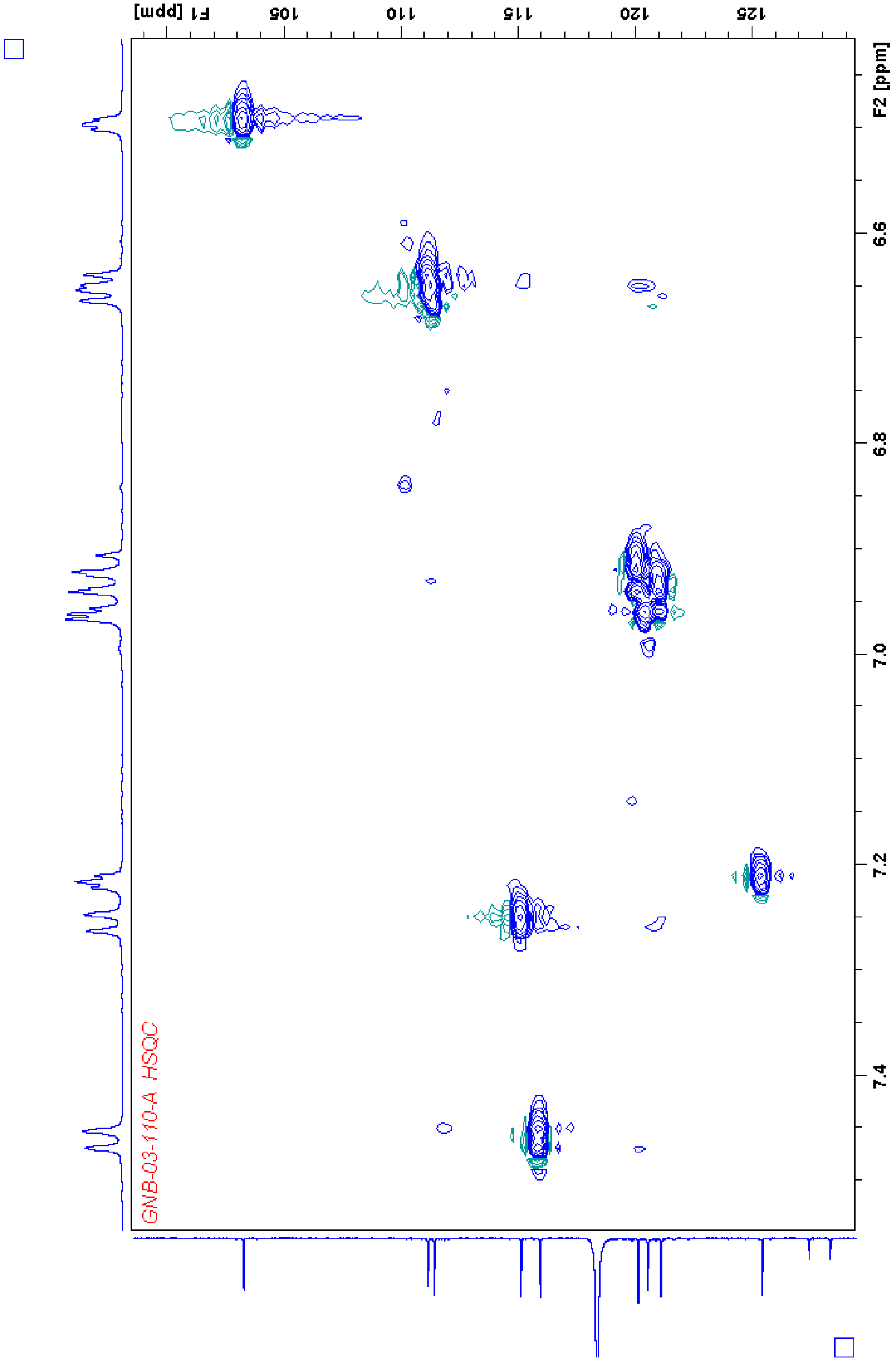

Figure A93. HSQC NMR (500 MHz, CD_3CN) expanded spectrum (6.5–7.5 ppm) of compound **4.26**.

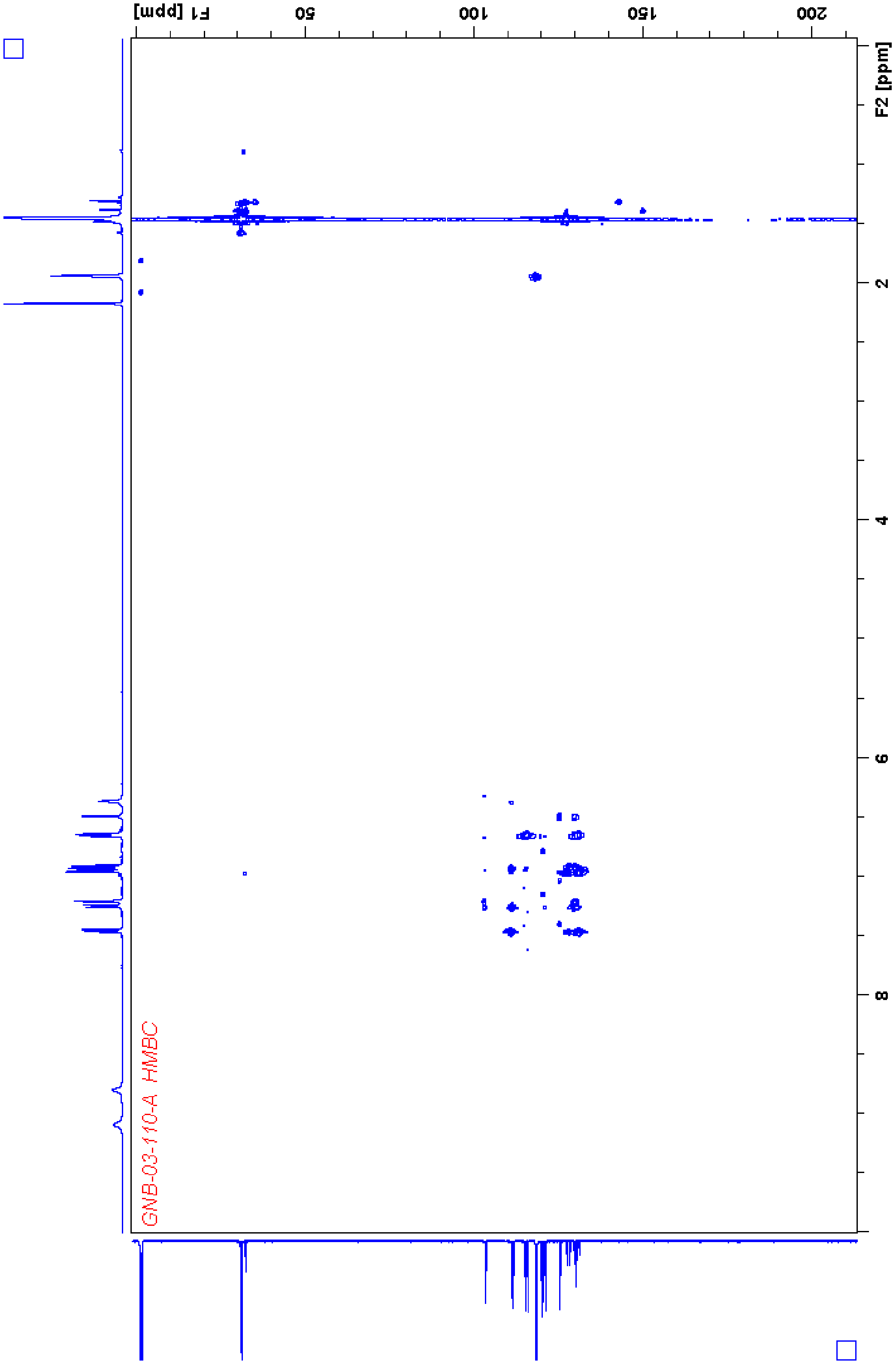

Figure A94. HMBC NMR (500 MHz, CD_3CN) spectrum of compoud **4.26**.

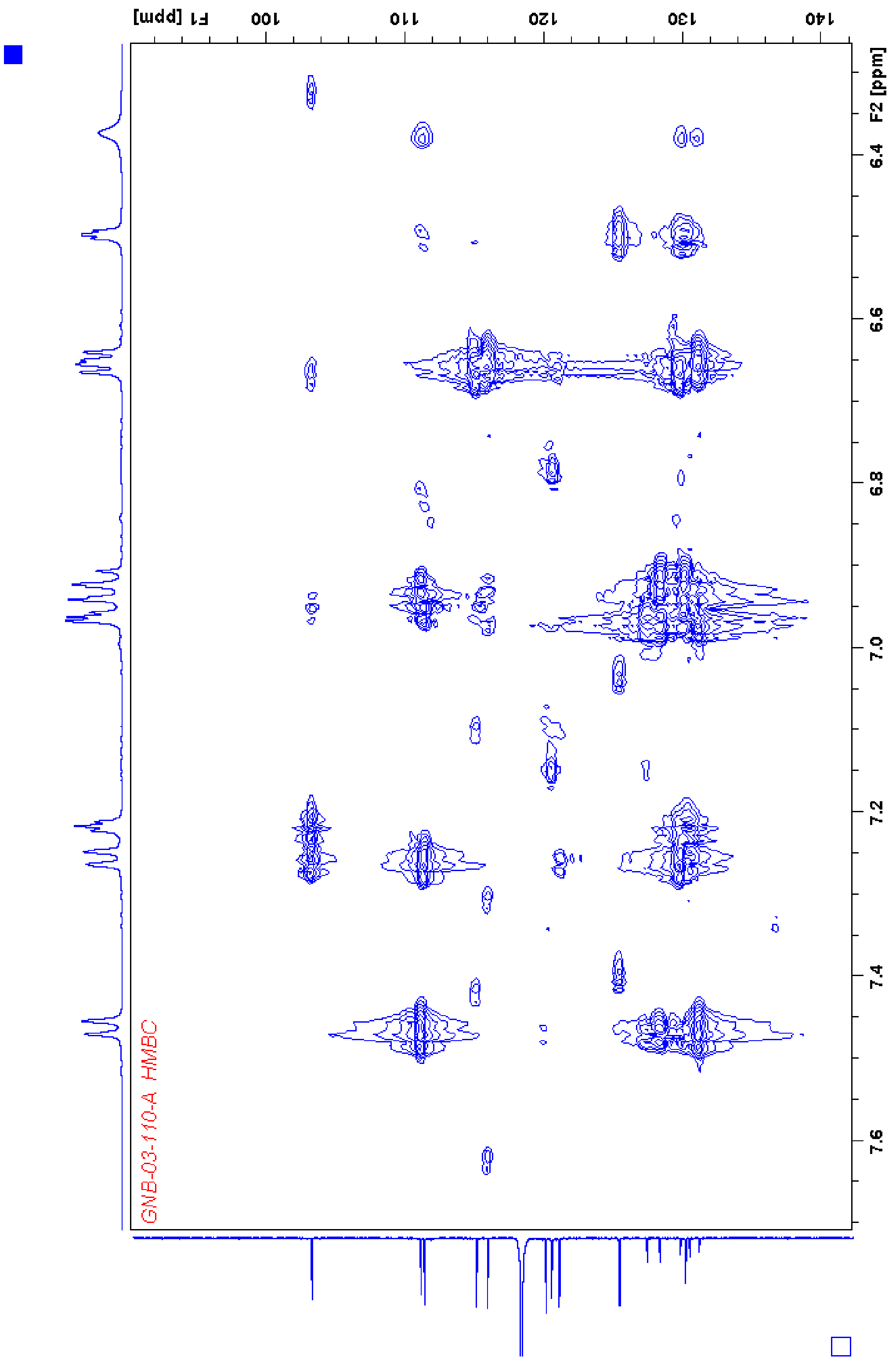

Figure A95. HMBC NMR (500 MHz, CD_3CN) expanded spectrum (6.3–7.7 ppm) of compound **4.26**.

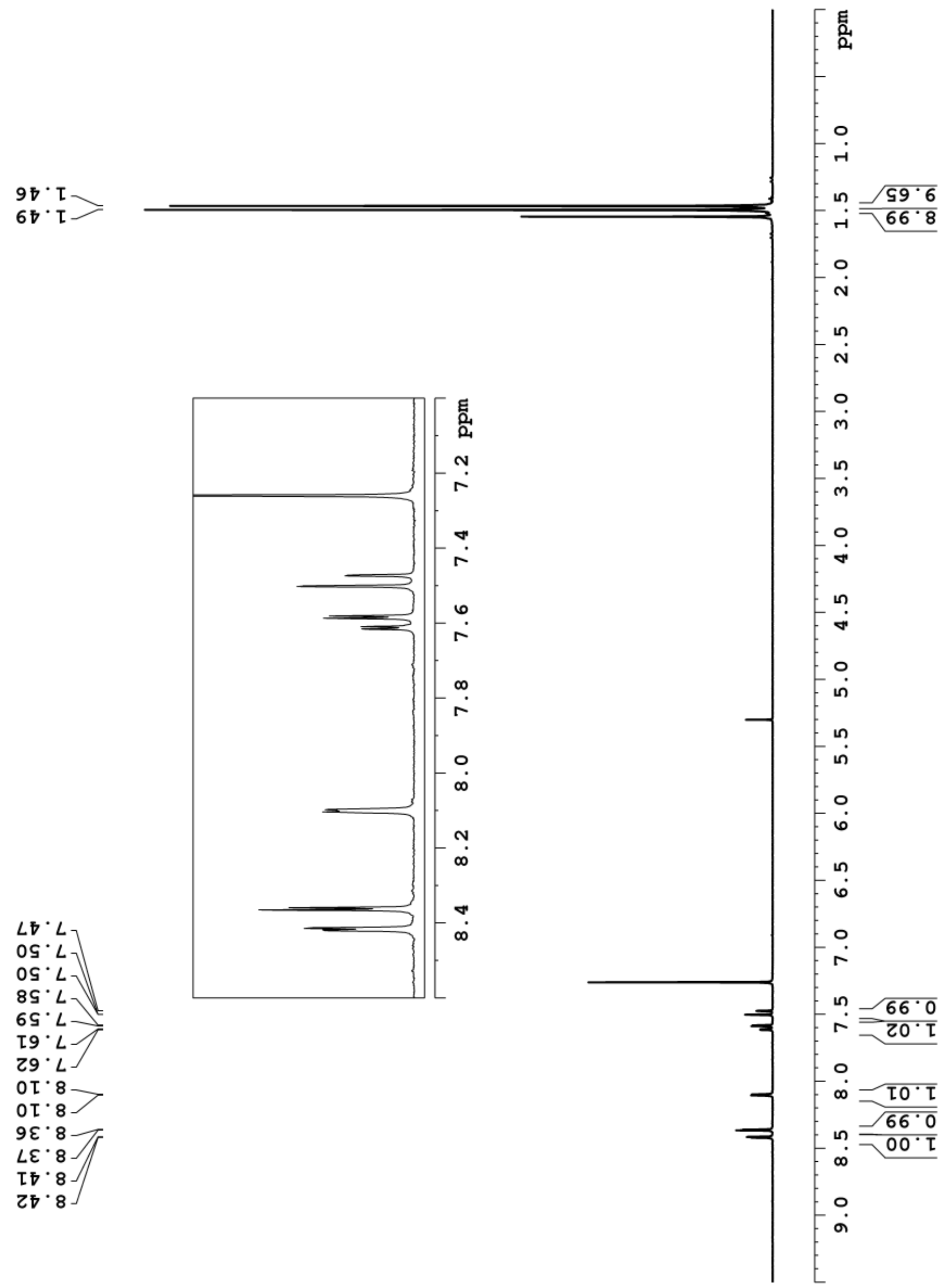

Figure A96. ^{1}H NMR (300 MHz, CDCl$_3$) spectrum of compound **4.36**.

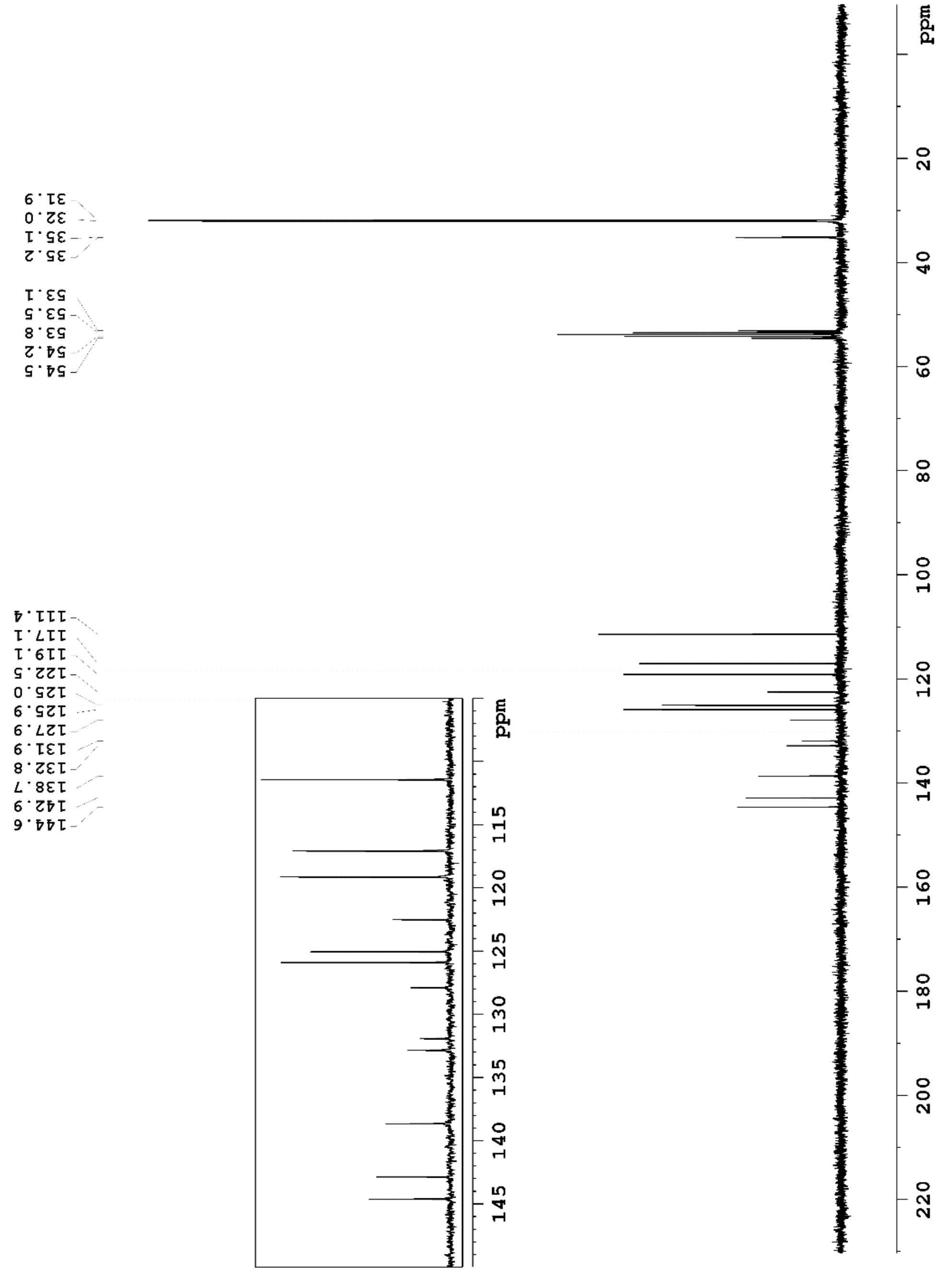

Figure A97. ^{13}C NMR (75 MHz, CD_2Cl_2) spectrum of compound **4.36**.

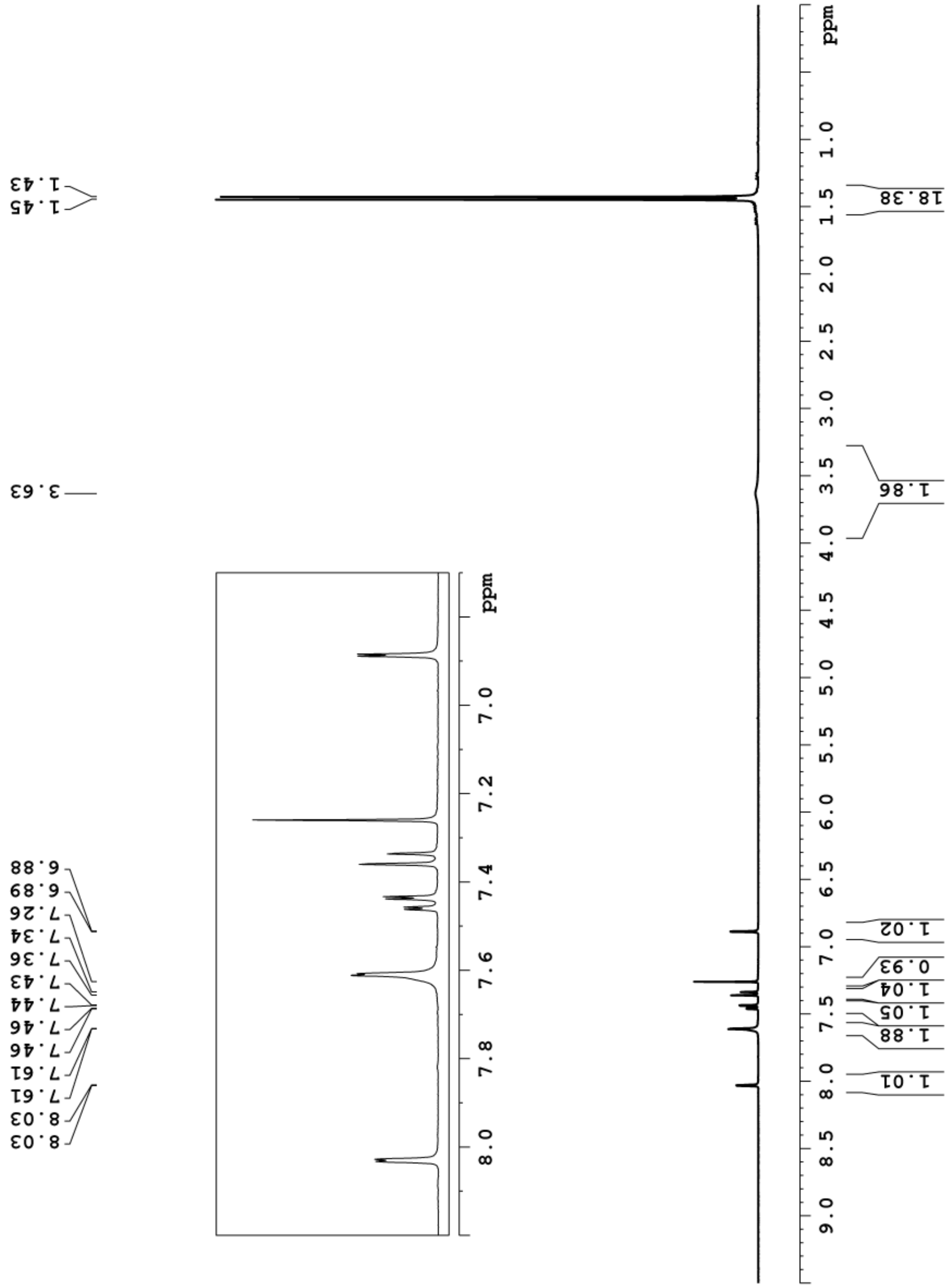

Figure A98. ^{1}H NMR (360 MHz, $CDCl_3$) spectrum of compound **4.37**.

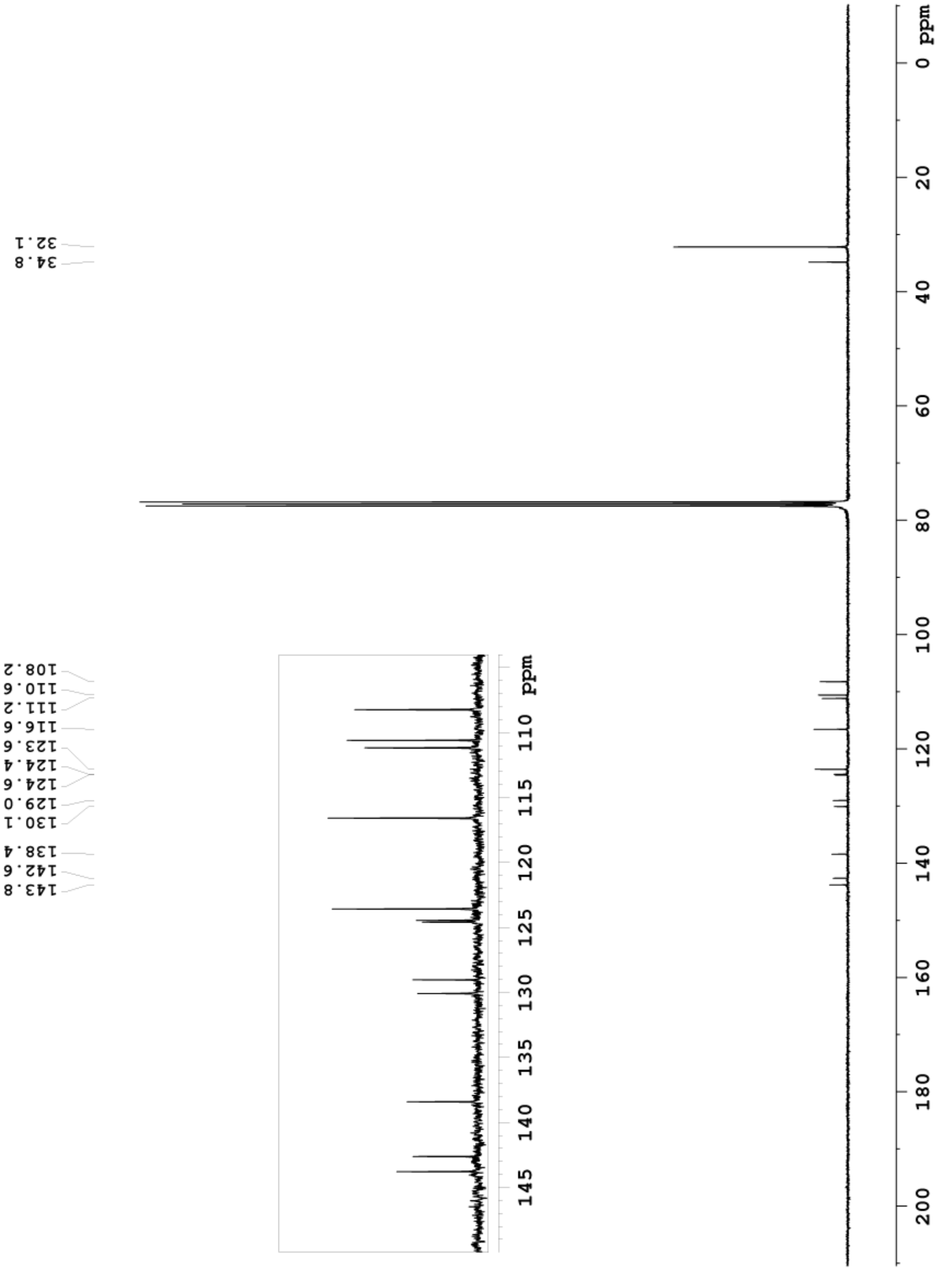

Figure A99. ^{13}C NMR (90 MHz, CDCl$_3$) spectrum of compound **4.37**.

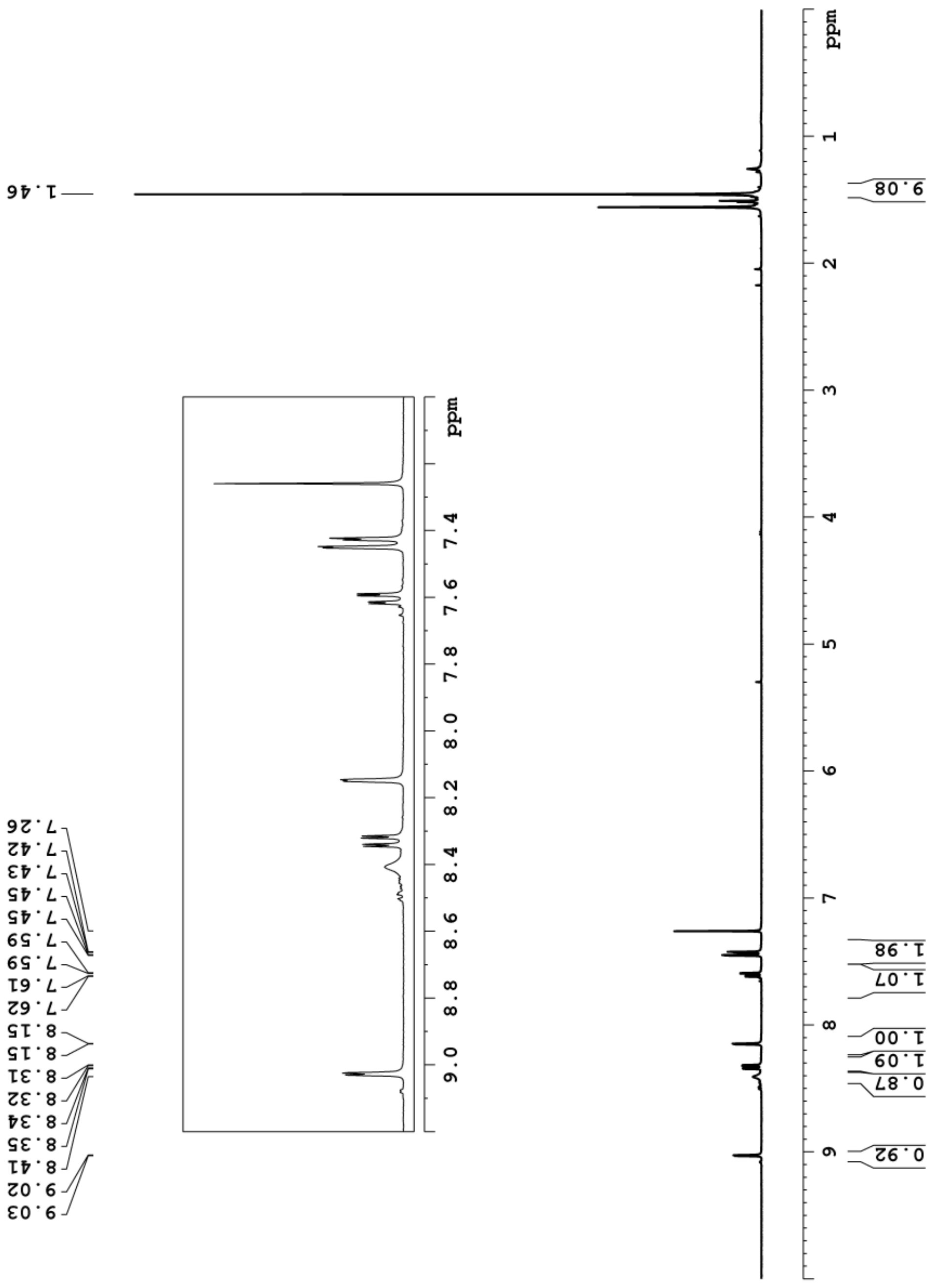

Figure A100. ^{1}H NMR (360 MHz, $CDCl_3$) spectrum of compound **4.40**.

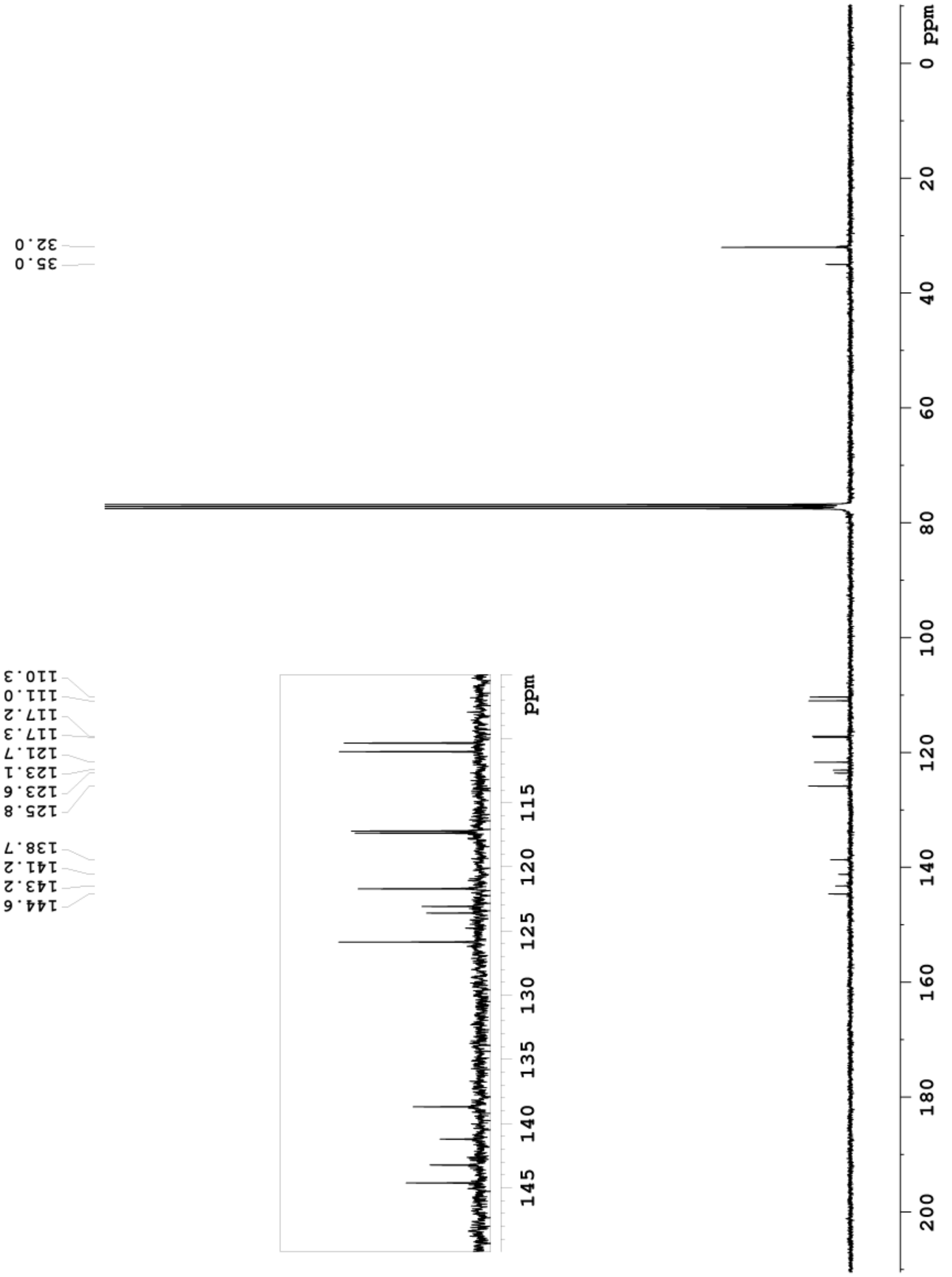

Figure A101. ^{13}C NMR (90 MHz, $CDCl_3$) spectrum of compound **4.40**.

Appendix C. X-ray Crystal Structures and Crystallographic Data

Table C1. Crystallographic data for thioindigo diimines and related chapter 2 compounds.

	2.2a	**2.2b**	**2.3a**	**2.3b**	**2.4b**	**2.5c**	**2.6c**
Empirical Formula	$C_{24}H_{28}N_2S_2$	$C_{28}H_{20}N_2S_2$	$C_{24}H_{26}N_2S_2$	$C_{28}H_{18}N_2S_2$	$C_{28}H_{18}N_2S_2$	$C_{25}H_{19}NOS_2$	$C_{25}H_{19}NOS_2$
Formula Weight	408.62	448.60	406.61	446.59	446.59	413.55	413.55
a (Å)	11.6513 (2)	5.516(2)	6.5738 (6)	20.5364(8)	17.0709(1)	17.4801 (2)	13.1978 (16)
b (Å)	12.2564 (2)	9.667(4)	8.9116 (8)	5.4027(2)	10.6332(9)	24.8084 (3)	22.799 (3)
c (Å)	15.2898 (3)	9.667(4)	17.2370 (15)	18.7745(9)	11.963(1)	10.8082 (2)	6.8177 (8)
α (deg)	90	72.675(7)	90	90	90	90	90
β (deg)	90	86.768(8)	97.4332 (13)	90	106.038(6)	105.8700 (6)	98.9986 (16)
γ (deg)	90	88.228(8)	90	90	90	90	90
V (Å^3)	2183.43 (7)	559.8(4)	1001.31 (15)	2083.1(2)	2086.9(3)	4508.36 (11)	2026.2 (4)
Z	4	1	2	4	4	8	4
space group	$Pbcn$ (# 60)	P -1 (#2)	$P2_1/n$	$Pca2_1$ (#29)	$P\ 2_1/c$ (#14)	$P\ 2_1/c$ (#14)	$P\ 2_1/c$ (#14)
T (°C)	-100	-183.0 ± 0.1	-100	-183 ± 2	-183.0 ± 0.1	-100	-100
λ (Å)	1.54178	0.71073	0.71073	1.54178	1.54178	1.54178	0.71073
D_{calcd} (g cm^{-3})	1.243	1.331	1.349	1.424	1.421	1.394	1.356
μ (cm^{-1})	2.283	2.57	0.279	24.61	24.56	3.918	0.279
R_1 [all data] [a]	0.0489	0.096	0.0388	0.0360	0.123	0.0533	0.0413
wR_2 [all data] [b]	0.1408	0.204	0.0922	0.0879	0.205	0.1590	0.1112
CCDC#	1053903	1053897	1053898	1053899	1053900	1053901	1053902

[a] $R_1 = \sum|F_{obs}-F_{calc}|/\sum|F_{obs}|$. [b] $wR_2 = [\sum(|w||F_{obs}-F_{calc}|)^2/\sum|wF_{obs}^2|]^{1/2}$.

Table C2. Crystallographic data for ruthenium thioindigo diimine complexes, indole tetramer **4.24** and carbazole **4.40**.

	3.5a	**3.5b**	**3.4**	**4.24**	**4.40**
Empirical Formula	$C_{48}H_{22}F_{24}N_2O_8Ru_2S_2$	$C_{48}H_{22}F_{24}N_2O_8Ru_2S_2$	$C_{38}H_{20}F_{12}N_2O_4RuS_2$	$C_{32}H_{18}Br_4N_4$	$C_{16}H_{16}N_2O_2$
Formula Weight	1476.93	1476.93	961.75	778.14	268.32
a (Å)	9.188(3)	29.613(6)	8.5769(7)	12.6185(8)	5.9597(4)
b (Å)	12.530(4)	9.667(2)	13.7143(14)	12.3442(7)	23.7698(12)
c (Å)	23.373(8)	37.632(8)	16.8117(16)	17.9746(10)	9.6328(5)
α (deg)	78.561(6)	90	66.471(5)	90	90
β (deg)	87.404(7)	98.402 (4)	89.755(4)	103.4000(10)	104.572(3)
γ (deg)	87.711(6)	90	88.118(5)	90	90
V (Å^3)	2633.4(15)	10657(4)	1812.0(3)	2723.6(3)	1320.69(13)
Z	2	16	2	4	4
space group	*P*-1	C2/c	*P* -1 (#2)	$P2_1/c$	$P2_1$
T (°C)	-183	-183	-173.0 ± 2	-183	-183
λ (Å)	0.71073	0.71073	0.71073	0.71073	0.71073
D_{calcd} (g cm^{-3})	1.863	1.841	1.763	1.898	1.349
μ (cm^{-1})	7.93	7.84	6.56	5.942	0.090
R_1 [all data] [a]	0.0782	0.0667	0.066	0.0759	0.0501
wR_2 [all data] [b]	0.1541	0.1371	0.165	0.0895	0.1074
CCDC#	1548434	1548435	1548433	N/A	N/A

[a] $R_1 = \sum|F_{obs}-F_{calc}|/\sum|F_{obs}|$. [b] $wR_2 = [\sum(|w||F_{obs}-F_{calc}|)^2/\sum|wF_{obs}^2|]^{1/2}$.

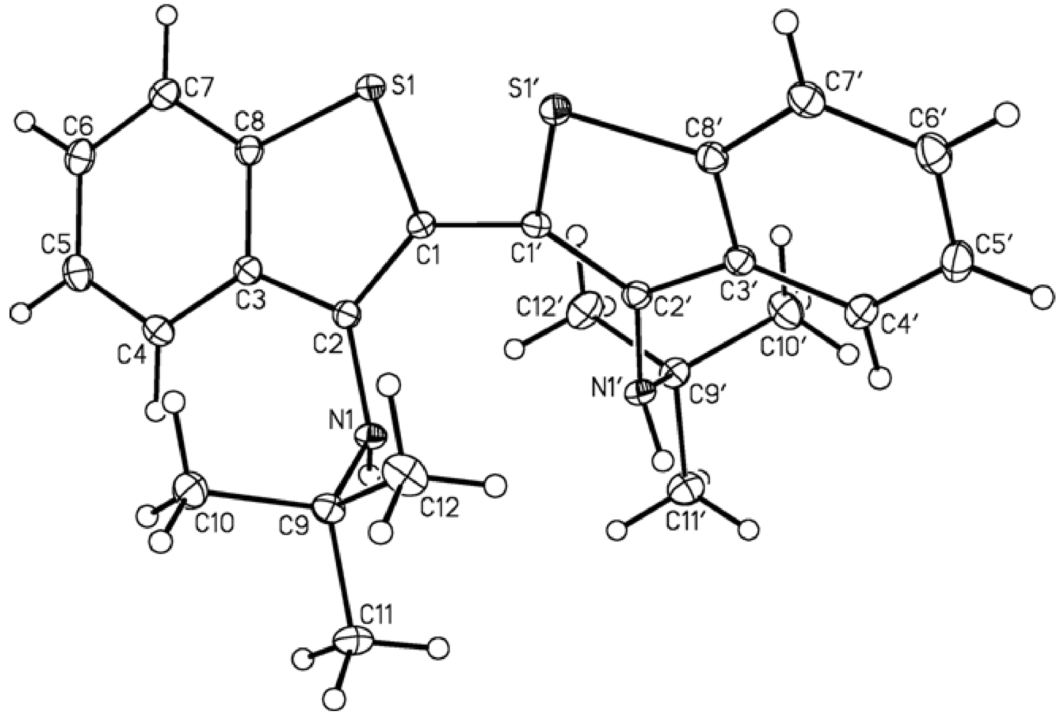

Figure C1. ORTEP diagram of diamine **2.2a** with thermal elipsoids represented at 50% probability.

Table C1. Bond Lengths of diamine **2.2a**.

Atom 1	**Atom 2**	**Length/Å**	**Atom 1**	**Atom 2**	**Length/Å**
S1	C1	1.753(2)	S1′	C1′	1.753(2)
S1	C8	1.734(2)	S1′	C8′	1.734(2)
N1	C2	1.416(2)	N1′	C2′	1.416(2)
N1	C9	1.499(2)	N1′	C9′	1.499(2)
C1	C2	1.371(2)	C1′	C2′	1.371(2)
C1	C1′	1.460(2)	C2′	C3′	1.449(2)
C2	C3	1.449(2)	C3′	C4′	1.406(2)
C3	C4	1.406(2)	C3′	C8′	1.404(2)
C3	C8	1.404(2)	C4′	C5′	1.375(3)
C4	C5	1.375(3)	C5′	C6′	1.401(3)
C5	C6	1.401(3)	C6′	C7′	1.381(3)
C6	C7	1.381(3)	C7′	C8′	1.395(2)
C7	C8	1.395(2)	C9′	C10′	1.522(3)
C9	C10	1.522(3)	C9′	C11′	1.527(3)

C9	C11	1.527(3)	C9′	C12′	1.526(3)
C9	C12	1.526(3)			

Table C2. Bond Angles for diamine **2.2a**.

Atom 1	**Atom 2**	**Atom 3**	**Angle / °**
C1	S1	C8	91.76(8)
C2	N1	C9	120.5(1)
S1	C1	C2	112.5(1)
S1	C1	C1′	115.8(1)
C2	C1	C1′	131.7(1)
N1	C2	C1	124.5(1)
N1	C2	C3	123.5(1)
C1	C2	C3	111.8(1)
C2	C3	C4	129.1(2)
C2	C3	C8	112.8(1)
C4	C3	C8	118.1(2)
C3	C4	C5	119.7(2)
C4	C5	C6	121.4(2)
C5	C6	C7	120.2(2)
C6	C7	C8	118.4(2)
S1	C8	C3	111.1(1)
S1	C8	C7	126.6(1)
C3	C8	C7	122.3(2)
N1	C9	C10	111.9(1)
N1	C9	C11	105.2(1)
N1	C9	C12	110.2(1)
C10	C9	C11	110.1(2)
C10	C9	C12	109.7(2)
C11	C9	C12	109.7(2)
C1′	S1′	C8′	91.76(8)
C2′	N1′	C9′	120.5(1)
S1′	C1′	C2′	112.5(1)
S1′	C1′	C1	115.8(1)
C2′	C1′	C1	131.7(1)
N1′	C2′	C1′	124.5(1)
N1′	C2′	C3′	123.5(1)
C1′	C2′	C3′	111.8(1)
C2′	C3′	C4′	129.1(2)

C2′	C3′	C8′	112.8(1)
C4′	C3′	C8′	118.1(2)
C3′	C4′	C5′	119.7(2)
C4′	C5′	C6′	121.4(2)
C5′	C6′	C7′	120.2(2)
C6′	C7′	C8′	118.4(2)
S1′	C8′	C3′	111.1(1)
S1′	C8′	C7′	126.6(1)
C3′	C8′	C7′	122.3(2)
N1′	C9′	C10′	111.9(1)
N1′	C9′	C11′	105.2(1)
N1′	C9′	C12′	110.2(1)
C10′	C9′	C11′	110.1(2)
C10′	C9′	C12′	109.7(2)
C11′	C9′	C12′	109.7(2)

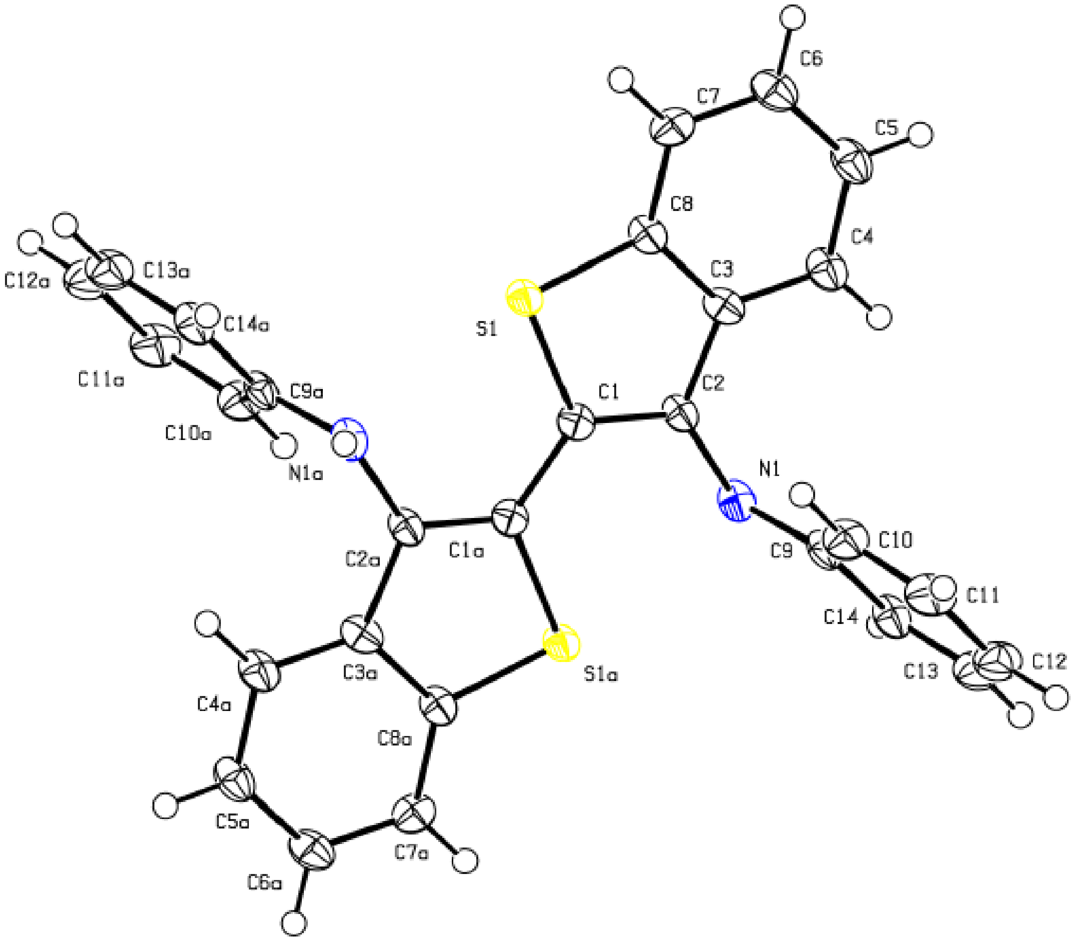

Figure C2. ORTEP diagram of diamine **2.2b** with thermal ellipsoids represented at 50% probability.

Table C3. Bond Lengths of diamine **2.2b**.

Atom 1	Atom 2	Length/Å	Atom 1	Atom 2	Length/Å
S1	C1	1.766(5)	S1a	C1a	1.766(5)
S1	C8	1.753(5)	S1a	C8a	1.753(5)
N1	H1	0.72(7)	N1a	H1a	0.72(7)
N1	C2	1.416(7)	N1a	C2a	1.416(7)
N1	C9	1.394(8)	N1a	C9a	1.394(8)
C1	C2	1.369(8)	C1a	C2a	1.369(8)
C1	C1a	1.454(6)	C2a	C3a	1.454(6)
C2	C3	1.454(6)	C3a	C4a	1.405(8)
C3	C4	1.405(8)	C3a	C8a	1.409(8)

C3	C8	1.409(8)	C4a	C5a	1.400(7)
C4	C5	1.400(7)	C5a	C6a	1.412(9)
C5	C6	1.412(9)	C6a	C7a	1.397(8)
C6	C7	1.397(8)	C7a	C8a	1.396(6)
C7	C8	1.396(6)	C9a	C10a	1.415(7)
C9	C10	1.415(7)	C9a	C14a	1.404(8)
C9	C14	1.404(8)	C10a	C11a	1.387(9)
C10	C11	1.387(9)	C11a	C12a	1.399(9)
C11	C12	1.399(9)	C12a	C13a	1.400(7)
C12	C13	1.400(7)	C13a	C14a	1.382(9)
C13	C14	1.382(9)			

Table C4. Bond Angles for diamine **2.2b**.

Atom 1	**Atom 2**	**Atom 3**	**Angle / °**
C1	S1	C8	91.2(2)
H1	N1	C2	113(6)
H1	N1	C9	113(6)
C2	N1	C9	124.1(4)
S1	C1	C2	111.6(4)
S1	C1	C1a	121.1(4)
C2	C1	C1	127.3(4)
N1	C2	C1	122.3(4)
N1	C2	C3	123.6(4)
C1	C2	C3	114.1(4)
C2	C3	C4	128.8(5)
C2	C3	C8	110.8(4)
C4	C3	C8	120.4(4)
C3	C4	C5	118.6(5)
C4	C5	C6	120.6(5)
C5	C6	C7	120.9(5)
C6	C7	C8	118.5(5)
S1	C8	C3	112.2(3)
S1	C8	C7	126.7(4)
C3	C8	C7	121.1(4)
N1	C9	C10	122.0(5)
N1	C9	C14	119.9(4)

C10	C9	C14	118.0(5)
C9	C10	C11	120.1(5)
C10	C11	C12	121.6(5)
C11	C12	C13	118.1(5)
C12	C13	C14	120.9(5)
C9	C14	C13	121.3(5)
C1a	S1a	C8a	91.2(2)
H1a	N1a	C2a	113(6)
H1a	N1a	C9a	113(6)
C2a	N1a	C9a	124.1(4)
C1a	C1a	S1a	121.1(4)
C1a	C1a	C2a	127.3(4)
S1a	C1a	C2a	111.6(4)
N1a	C2a	C1a	122.3(4)
N1a	C2a	C3a	123.6(4)
C1a	C2a	C3a	114.1(4)
C2a	C3a	C4a	128.8(5)
C2a	C3a	C8a	110.8(4)
C4a	C3a	C8a	120.4(4)
C3a	C4a	C5a	118.6(5)
C4a	C5a	C6a	120.6(5)
C5a	C6a	C7a	120.9(5)
C6a	C7a	C8a	118.5(5)
S1a	C8a	C3a	112.2(3)
S1a	C8a	C7a	126.7(4)
C3a	C8a	C7a	121.1(4)
N1a	C9a	C10a	122.0(5)
N1a	C9a	C14a	119.9(4)
C10a	C9a	C14a	118.0(5)
C11a	C12a	C13a	118.1(5)
C12a	C13a	C14a	120.9(5)
C9a	C14a	C13a	121.3(5)

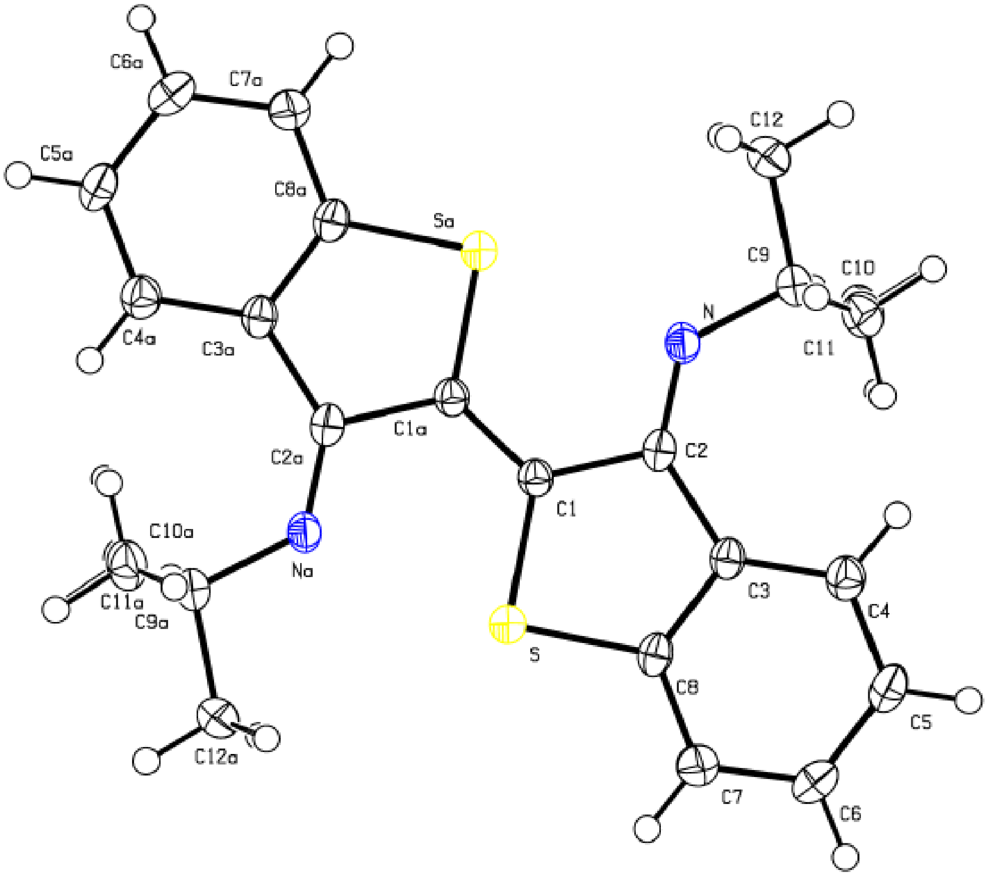

Figure C3. ORTEP diagram of thioindigo diimine **2.3a** with thermal ellipsoids represented at 50% probability.

Table C5. Bond Lengths of thioindigo diimine **2.3a**.

Atom 1	**Atom 2**	**Length/Å**	**Atom 1**	**Atom 2**	**Length/Å**
S	C1	1.7427(19)	S′	C1′	1.7427(19)
S	C8	1.762(2)	S′	C8′	1.762(2)
N	C2	1.280(2)	N′	C2′	1.280(2)
N	C9	1.469(2)	N′	C9′	1.469(2)
C1	C1′	1.361(4)	C1′	C2′	1.486(3)
C1	C2	1.486(3)	C2′	C3′	1.495(3)
C2	C3	1.495(3)	C3′	C4′	1.403(3)
C3	C4	1.403(3)	C3′	C8′	1.403(3)
C3	C8	1.403(3)	C4′	C5′	1.381(3)
C4	C5	1.381(3)	C5′	C6′	1.386(3)
C5	C6	1.386(3)	C6′	C7′	1.385(3)

C6	C7	1.385(3)	C7′	C8′	1.388(3)
C7	C8	1.388(3)	C9′	C10′	1.533(3)
C9	C10	1.533(3)	C9′	C11′	1.547(3)
C9	C11	1.547(3)	C9′	C12′	1.529(3)
C9	C12	1.529(3)			

Table C6. Bond Angles for thioindigo diimine **2.3a**.

Atom 1	**Atom 2**	**Atom 3**	**Angle / °**
C1	S	C8	90.76(9)
C2	N	C9	129.30(17)
S	C1	C1′	123.1(2)
S	C1	C2	113.36(13)
C1′	C1	C2	123.5(2)
N	C2	C1	114.71(16)
N	C2	C3	135.86(17)
C1	C2	C3	109.43(16)
C2	C3	C4	131.41(18)
C2	C3	C8	111.03(17)
C4	C3	C8	117.55(19)
C3	C4	C5	120.5(2)
C4	C5	C6	120.8(2)
C5	C6	C7	120.3(2)
C6	C7	C8	118.78(19)
S	C8	C3	115.38(15)
S	C8	C7	122.47(16)
C3	C8	C7	122.12(19)
N	C9	C10	110.63(17)
N	C9	C11	111.53(17)
N	C9	C12	105.95(16)
C10	C9	C11	113.46(18)
C10	C9	C12	107.81(18)
C11	C9	C12	107.05(18)
C1′	S′	C8′	90.76(9)
C2′	N′	C9′	129.30(17)
S′	C1′	C1	123.1(2)
S′	C1′	C2′	113.36(13)
C1	C1′	C2′	123.5(2)
N′	C2′	C1′	114.71(16)
N′	C2′	C3′	135.86(17)
C1′	C2′	C3′	109.43(16)

C2′	C3′	C4′	131.41(18)
C2′	C3′	C8′	111.03(17)
C4′	C3′	C8′	117.55(19)
C3′	C4′	C5′	120.5(2)
C4′	C5′	C6′	120.8(2)
C5′	C6′	C7′	120.3(2)
C6′	C7′	C8′	118.78(19)
S′	C8′	C3′	115.38(15)
S′	C8′	C7′	122.47(16)
C3′	C8′	C7′	122.12(19)
N′	C9′	C10′	110.63(17)
N′	C9′	C11′	111.53(17)
N′	C9′	C12′	105.95(16)
C10′	C9′	C11′	113.46(18)
C10′	C9′	C12′	107.81(18)
C11′	C9′	C12′	107.05(18)

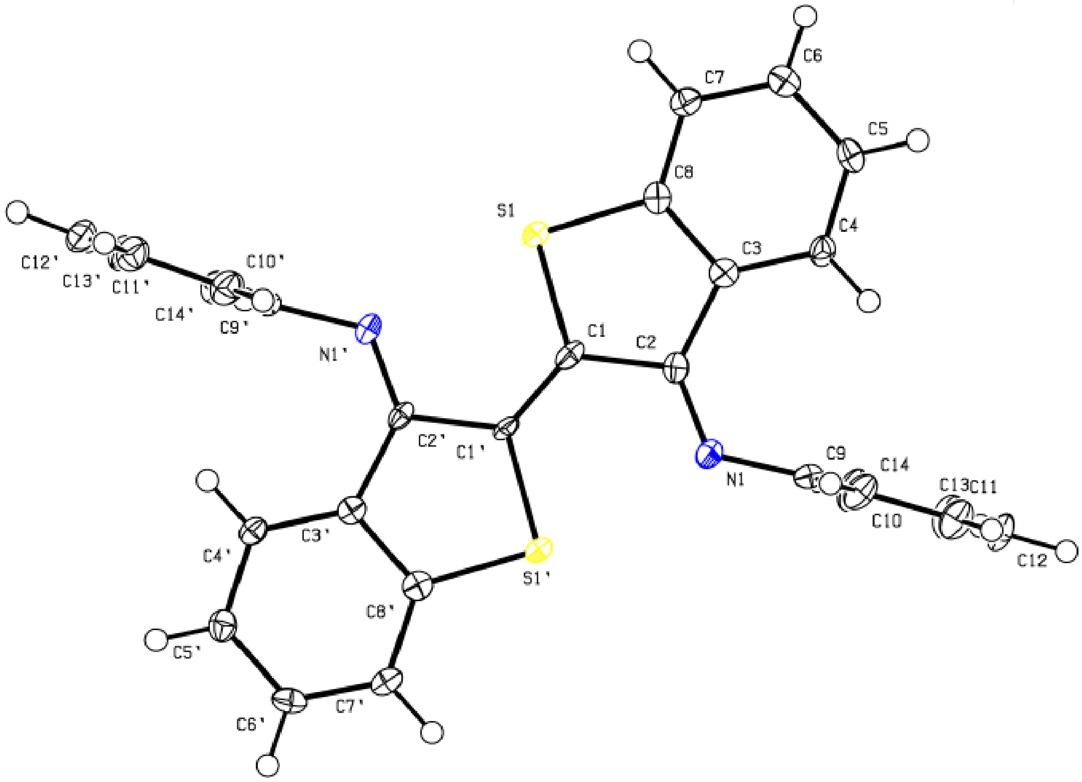

Figure C4. ORTEP diagram of thioindigo diimine **2.3b** with thermal ellipsoids represented at 50% probability.

Table C7. Bond Lengths of thioindigo diimine **2.3b**.

Atom 1	Atom 2	Length/Å	Atom 1	Atom 2	Length/Å
S1	C1	1.752(4)	C5	C6	1.390(6)
S1	C8	1.754(4)	C5'	C6'	1.393(6)
S1'	C1'	1.747(3)	C6	C7	1.390(5)
S1'	C8'	1.762(4)	C6'	C7'	1.376(5)
N1	C2	1.286(5)	C7	C8	1.395(5)
N1	C9	1.415(5)	C7'	C8'	1.394(5)
N1'	C2'	1.291(5)	C9	C10	1.377(5)
N1'	C9'	1.427(5)	C9	C14	1.401(5)
C1	C1'	1.350(5)	C9'	C10'	1.384(5)
C1	C2	1.481(5)	C9'	C14'	1.395(5)
C1'	C2'	1.468(5)	C10	C11	1.393(6)
C2	C3	1.476(5)	C10'	C11'	1.393(5)
C2'	C3'	1.479(5)	C11	C12	1.374(6)
C3	C4	1.400(5)	C11'	C12'	1.389(6)
C3	C8	1.397(5)	C12	C13	1.385(5)
C3'	C4'	1.401(5)	C12'	C13'	1.385(5)
C3'	C8'	1.393(5)	C13	C14	1.384(5)
C4	C5	1.384(5)	C13'	C14'	1.383(5)
C4'	C5'	1.379(5)			

Table C8. Bond Angles for thioindigo diimine **2.3b**.

Atom 1	Atom 2	Atom 3	Angle / °
C1	S1	C8	90.9(2)
C1'	S1'	C8'	91.1(2)
C2	N1	C9	123.5(3)
C2'	N1'	C9'	124.1(3)
S1	C1	C1'	123.2(3)
S1	C1	C2	112.3(3)
C1'	C1	C2	124.5(3)
S1'	C1'	C1	123.5(3)
S1'	C1'	C2'	112.3(3)
C1	C1'	C2'	124.2(3)

N1	C2	C1	117.8(3)
N1	C2	C3	131.9(3)
C1	C2	C3	110.2(3)
N1'	C2'	C1'	117.5(3)
N1'	C2'	C3'	131.9(3)
C1'	C2'	C3'	110.6(3)
C2	C3	C4	129.4(3)
C2	C3	C8	111.3(3)
C4	C3	C8	119.2(3)
C2'	C3'	C4'	129.3(3)
C2'	C3'	C8'	111.4(3)
C4'	C3'	C8'	119.2(3)
C3	C4	C5	119.4(3)
C3'	C4'	C5'	119.6(3)
C4	C5	C6	121.0(4)
C4'	C5'	C6'	120.5(4)
C5	C6	C7	120.5(4)
C5'	C6'	C7'	120.8(4)
C6	C7	C8	118.5(3)
C6'	C7'	C8'	118.8(3)
S1	C8	C3	115.2(3)
S1	C8	C7	123.3(3)
C3	C8	C7	121.5(3)
S1'	C8'	C3'	114.5(3)
S1'	C8'	C7'	124.3(3)
C3'	C8'	C7'	121.1(3)
N1	C9	C10	120.2(3)
N1	C9	C14	120.3(3)
C10	C9	C14	119.3(3)
N1'	C9'	C10'	119.5(3)
N1'	C9'	C14'	120.3(3)
C10'	C9'	C14'	119.9(3)
C9	C10	C11	120.6(4)
C9'	C10'	C11'	120.3(4)
C10	C11	C12	120.1(4)
C10'	C11'	C12'	119.7(4)
C11	C12	C13	119.7(4)
C11'	C12'	C13'	119.7(4)
C12	C13	C14	120.7(4)

C12'	C13'	C14'	120.8(3)
C9	C14	C13	119.6(3)
C9'	C14'	C13'	119.5(3)

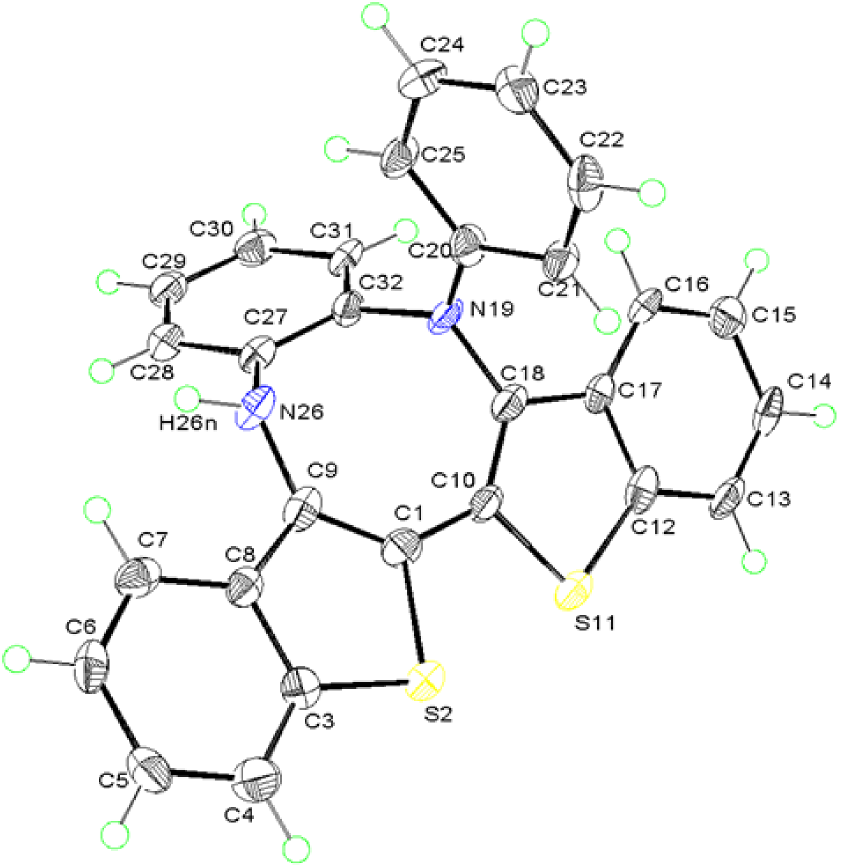

Figure C5. ORTEP diagram of diazocine **2.4b** with thermal elipsoids represented at 50% probability.

Table 9. Bond Lengths of diazocine **2.4b**.

Atom 1	Atom 2	Length/Å	Atom 1	Atom 2	Length/Å
C1	C9	1.39(1)	C16	C17	1.40(1)
C1	C10	1.45(1)	C17	C18	1.43(1)
C1	S2	1.752(8)	C18	N19	1.422(8)
C3	C4	1.38(1)	C20	C21	1.405(9)
C3	C8	1.40(1)	C20	C25	1.401(9)

C3	S2	1.724(8)
C4	C5	1.39(1)
C5	C6	1.39(1)
C6	C7	1.37(1)
C7	C8	1.42(1)
C8	C9	1.43(1)
C9	N26	1.409(9)
C10	C18	1.36(1)
C10	S11	1.754(7)
C12	C13	1.41(1)
C12	C17	1.412(9)
C12	S11	1.733(9)
C13	C14	1.37(1)
C14	C15	1.41(1)
C15	C16	1.35(1)
C20	N19	1.388(8)
C21	C22	1.393(9)
C22	C23	1.39(1)
C23	C24	1.39(1)
C24	C25	1.367(9)
C27	C28	1.40(1)
C27	C32	1.40(1)
C27	N26	1.42(1)
C28	C29	1.38(1)
C29	C30	1.38(1)
C30	C31	1.40(1)
C31	C32	1.38(1)
C32	N19	1.445(8)
N26	H26N	0.93(8)

Table C10. Bond Angles for diazocine **2.4b**.

Atom 1	**Atom 2**	**Atom 3**	**Angle / °**
C9	C1	C10	134.1(7)
C9	C1	S2	110.9(5)
C10	C1	S2	114.9(5)
C4	C3	C8	121.9(7)
C4	C3	S2	127.3(6)
C8	C3	S2	110.8(5)
C3	C4	C5	119.2(7)
C4	C5	C6	119.7(7)
C5	C6	C7	121.2(7)
C6	C7	C8	120.6(7)
C3	C8	C7	117.3(6)
C3	C8	C9	113.3(6)
C7	C8	C9	129.4(6)
C1	C9	C8	112.4(6)
C1	C9	N26	129.1(6)
C8	C9	N26	118.5(6)
C1	C10	C18	131.4(6)
C1	C10	S11	117.6(5)

C18	C10	S11	110.9(5)
C13	C12	C17	121.1(7)
C13	C12	S11	127.5(6)
C17	C12	S11	111.5(5)
C12	C13	C14	118.1(7)
C13	C14	C15	120.7(7)
C14	C15	C16	121.7(7)
C15	C16	C17	119.3(7)
C12	C17	C16	119.1(6)
C12	C17	C18	111.0(6)
C16	C17	C18	129.9(6)
C10	C18	C17	114.7(6)
C10	C18	N19	122.7(6)
C17	C18	N19	122.6(6)
C21	C20	C25	118.8(6)
C21	C20	N19	120.4(6)
C25	C20	N19	120.7(6)
C20	C21	C22	119.2(6)
C21	C22	C23	121.3(7)
C22	C23	C24	118.9(7)
C23	C24	C25	120.5(7)
C20	C25	C24	121.2(7)
C28	C27	C32	118.9(6)
C28	C27	N26	119.4(6)
C32	C27	N26	121.4(6)
C27	C28	C29	119.7(7)
C28	C29	C30	121.7(7)
C29	C30	C31	119.1(7)
C30	C31	C32	119.5(6)
C27	C32	C31	120.8(6)
C27	C32	N19	119.3(6)
C31	C32	N19	119.8(6)
C18	N19	C20	122.9(6)
C18	N19	C32	116.6(5)
C20	N19	C32	120.0(5)
C9	N26	C27	126.0(6)
C9	N26	H26N	113(5)
C27	N26	H26N	109(5)
C1	S2	C3	92.6(3)

C10	S11	C12	91.9(3)

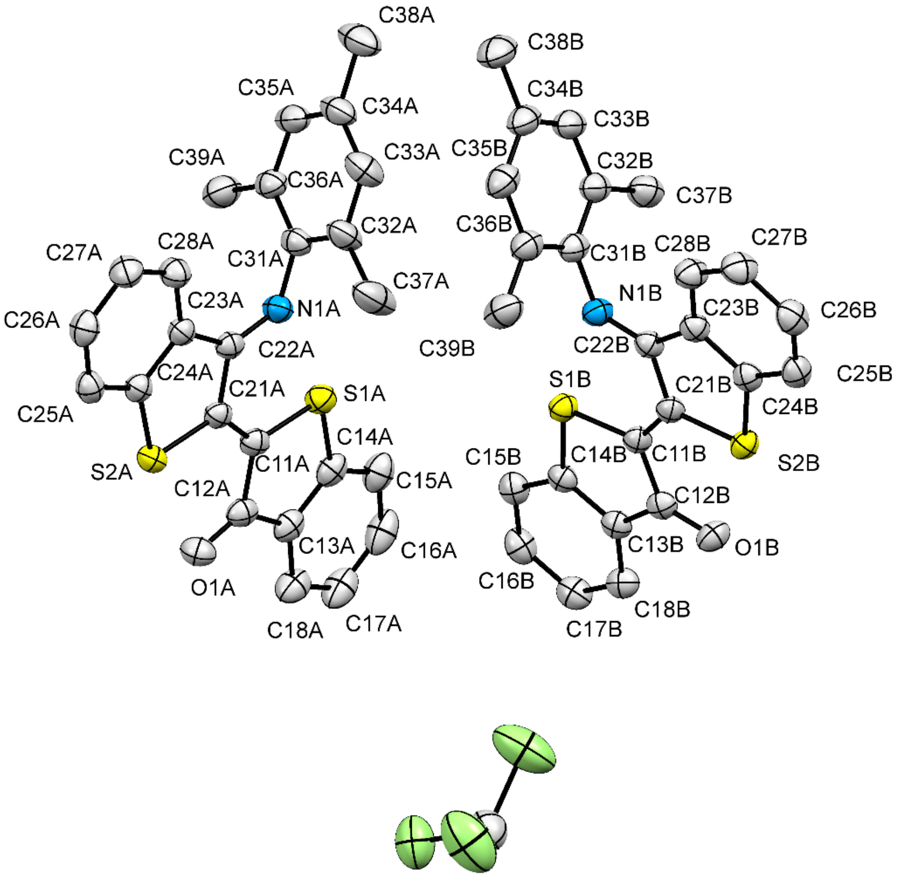

Figure C6. ORTEP diagram of thioindigo monoimine compound **2.5c.** with thermal ellipsoids represented at 50% probability. Hydrogen atoms are removed for clarity. CHCl3 is present in the crystal structure.

Table C11. Bond Lengths of thioindigo monoimine compound **2.5c**.

	Molecule A			**Molecule B**	
Atom 1	**Atom 2**	**Length/Å**	**Atom 1**	**Atom 2**	**Length/Å**
S1	C11	1.747(3)	S1	C11	1.751(2)
S1	C14	1.764(3)	S1	C14	1.772(2)

S2	C21	1.746(2)	S2	C21	1.748(2)
S2	C24	1.766(3)	S2	C24	1.760(3)
O1	C12	1.225(3)	O1	C12	1.227(3)
N1	C22	1.285(3)	N1	C22	1.283(3)
N1	C31	1.425(3)	N1	C31	1.426(3)
C11	C12	1.483(3)	C11	C12	1.488(3)
C11	C21	1.358(4)	C11	C21	1.354(4)
C12	C13	1.466(4)	C12	C13	1.462(3)
C13	C14	1.393(4)	C13	C14	1.391(3)
C13	C18	1.400(4)	C13	C18	1.402(4)
C14	C15	1.392(4)	C14	C15	1.390(4)
C15	C16	1.381(5)	C15	C16	1.383(4)
C16	C17	1.385(5)	C16	C17	1.399(4)
C17	C18	1.386(5)	C17	C18	1.382(4)
C21	C22	1.480(3)	C21	C22	1.482(3)
C22	C23	1.473(4)	C22	C23	1.474(3)
C23	C24	1.400(3)	C23	C24	1.403(3)
C23	C28	1.394(4)	C23	C28	1.391(4)
C24	C25	1.387(4)	C24	C25	1.391(3)
C25	C26	1.382(4)	C25	C26	1.376(4)
C26	C27	1.389(4)	C26	C27	1.404(4)
C27	C28	1.383(4)	C27	C28	1.386(4)
C31	C32	1.392(4)	C31	C32	1.400(4)
C31	C36	1.406(4)	C31	C36	1.395(4)
C32	C33	1.392(4)	C32	C33	1.398(4)
C32	C37	1.505(4)	C32	C37	1.499(4)
C33	C34	1.386(5)	C33	C34	1.380(5)
C34	C35	1.374(5)	C34	C35	1.392(4)
C34	C38	1.517(4)	C34	C38	1.516(4)
C35	C36	1.399(4)	C35	C36	1.400(4)
C36	C39	1.491(4)	C36	C39	1.507(4)

Table C12. Bond Angles for thioindigo monoimine **2.5c**.

		Molecule A	
Atom 1	**Atom 2**	**Atom 3**	**Angle / °**
C11	S1	C14	90.84(12)
C21	S2	C24	91.11(11)
C22	N1	C31	123.1(2)

S1	C11	C12	112.70(19)
S1	C11	C21	124.24(19)
C12	C11	C21	123.1(2)
O1	C12	C11	123.2(2)
O1	C12	C13	127.2(2)
C11	C12	C13	109.6(2)
C12	C13	C14	112.6(2)
C12	C13	C18	127.1(3)
C14	C13	C18	120.3(3)
S1	C14	C13	114.2(2)
S1	C14	C15	124.9(2)
C13	C14	C15	120.8(3)
C14	C15	C16	118.2(3)
C15	C16	C17	121.5(3)
C16	C17	C18	120.7(3)
C13	C18	C17	118.4(3)
S2	C21	C11	123.43(19)
S2	C21	C22	112.41(18)
C11	C21	C22	124.2(2)
N1	C22	C21	117.1(2)
N1	C22	C23	132.5(2)
C21	C22	C23	110.4(2)
C22	C23	C24	111.7(2)
C22	C23	C28	129.2(2)
C24	C23	C28	119.1(2)
S2	C24	C23	114.41(19)
S2	C24	C25	124.15(19)
C23	C24	C25	121.4(2)
C24	C25	C26	118.5(2)
C25	C26	C27	120.9(3)
C26	C27	C28	120.6(3)
C23	C28	C27	119.5(2)
N1	C31	C32	119.7(2)
N1	C31	C36	118.9(2)
C32	C31	C36	121.1(2)
C31	C32	C33	118.3(3)
C31	C32	C37	120.7(3)
C33	C32	C37	121.0(3)
C32	C33	C34	122.0(3)

C33	C34	C35	118.6(3)
C33	C34	C38	120.3(3)
C35	C34	C38	121.1(3)
C34	C35	C36	122.1(3)
C31	C36	C35	117.9(3)
C31	C36	C39	120.8(2)
C35	C36	C39	121.3(3)
C31	C32	C33	118.3(3)
C31	C32	C37	120.7(3)
C33	C32	C37	121.0(3)
C32	C33	C34	122.0(3)
C33	C34	C35	118.6(3)
C33	C34	C38	120.3(3)
C35	C34	C38	121.1(3)
C34	C35	C36	122.1(3)
C31	C36	C35	117.9(3)
C31	C36	C39	120.8(2)
C35	C36	C39	121.3(3)

Molecule B

Atom 1	**Atom 2**	**Atom 3**	**Angle / °**
C11	S1	C14	90.83(11)
C21	S2	C24	91.16(11)
C22	N1	C31	122.5(2)
S1	C11	C12	112.33(17)
S1	C11	C21	125.22(19)
C12	C11	C21	122.5(2)
O1	C12	C11	122.9(2)
O1	C12	C13	127.2(2)
C11	C12	C13	109.9(2)
C12	C13	C14	112.7(2)
C12	C13	C18	126.5(2)
C14	C13	C18	120.8(2)
S1	C14	C13	114.20(18)
S1	C14	C15	125.0(2)
C13	C14	C15	120.8(2)
C14	C15	C16	118.2(2)
C15	C16	C17	121.4(2)

C16	C17	C18	120.5(3)
C13	C18	C17	118.3(2)
S2	C21	C11	123.00(19)
S2	C21	C22	112.27(17)
C11	C21	C22	124.7(2)
N1	C22	C21	117.7(2)
N1	C22	C23	131.9(2)
C21	C22	C23	110.4(2)
C22	C23	C24	111.4(2)
C22	C23	C28	129.3(2)
C24	C23	C28	119.3(2)
S2	C24	C23	114.67(18)
S2	C24	C25	124.2(2)
C23	C24	C25	121.1(2)
C24	C25	C26	118.9(2)
C25	C26	C27	120.9(2)
C26	C27	C28	120.0(3)
C23	C28	C27	119.9(3)
N1	C31	C32	118.1(3)
N1	C31	C36	120.2(2)
C32	C31	C36	121.6(2)
C31	C32	C33	118.1(3)
C31	C32	C37	120.3(2)
C33	C32	C37	121.7(3)
C32	C33	C34	122.1(3)
C33	C34	C35	118.4(3)
C33	C34	C38	121.6(3)
C35	C34	C38	120.0(3)
C34	C35	C36	121.9(3)
C31	C36	C35	118.0(3)
C31	C36	C39	120.8(2)
C35	C36	C39	121.3(3)

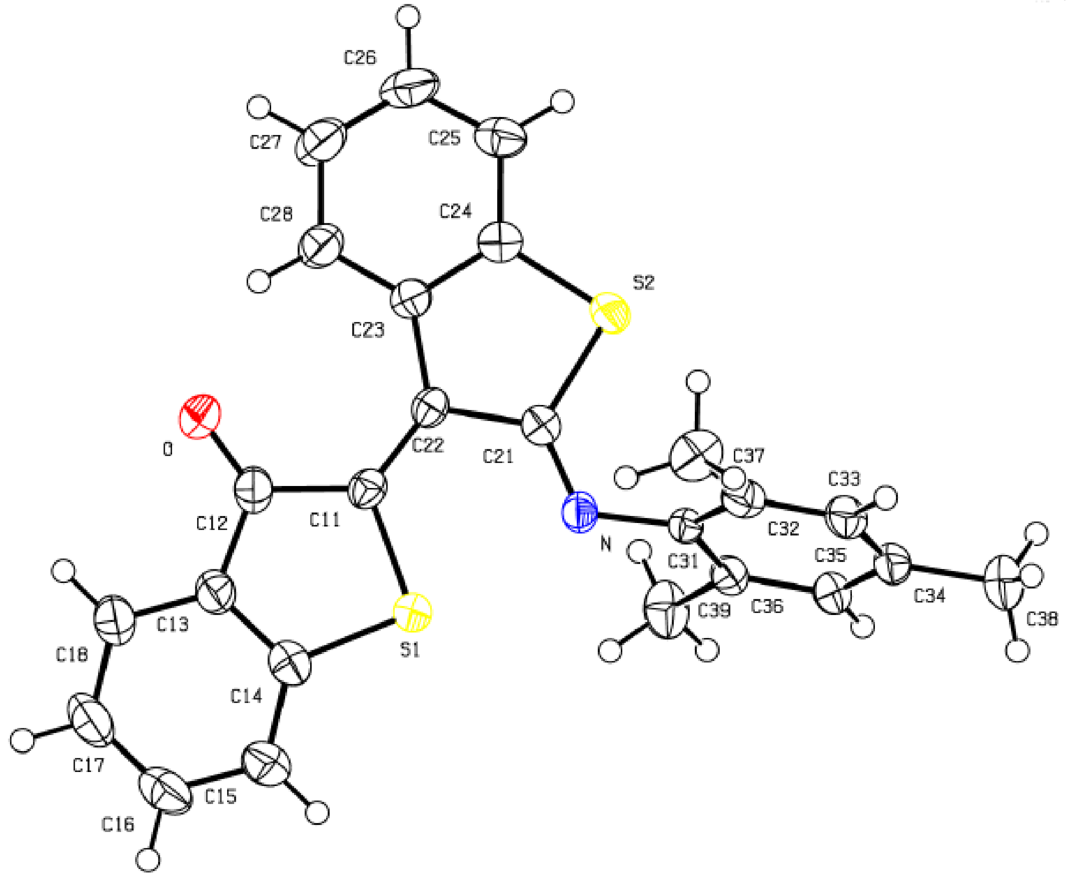

Figure C7. ORTEP diagram of thioindirubin compound **2.6c** with thermal ellipsoids represented at 50% probability.

Table C13. Bond Lengths of thioindirubin compound **2.6c**.

Atom 1	**Atom 2**	**Length/Å**	**Atom 1**	**Atom 2**	**Length/Å**
S1	C11	1.760(2)	C22	C23	1.474(3)
S1	C14	1.768(3)	C23	C24	1.407(3)
S2	C21	1.764(2)	C23	C28	1.395(3)
S2	C24	1.746(2)	C24	C25	1.386(3)
O	C12	1.206(3)	C25	C26	1.380(4)
N	C21	1.269(3)	C26	C27	1.380(4)
N	C31	1.422(3)	C27	C28	1.384(4)
C11	C12	1.515(3)	C31	C32	1.400(3)
C11	C22	1.373(3)	C31	C36	1.396(3)
C12	C13	1.455(4)	C32	C33	1.388(3)
C13	C14	1.377(3)	C32	C37	1.507(3)

C13	C18	1.390(4)	C33	C34	1.383(3)
C14	C15	1.383(4)	C34	C35	1.392(4)
C15	C16	1.382(4)	C34	C38	1.509(4)
C16	C17	1.380(4)	C35	C36	1.387(3)
C17	C18	1.375(4)	C36	C39	1.504(4)
C21	C22	1.491(3)			

Table C14. Bond Angles for thioindirubin compound **2.6c**.

Atom 1	**Atom 2**	**Atom 3**	**Angle / °**
C11	S1	C14	92.7(1)
C21	S2	C24	91.1(1)
C21	N	C31	121.2(2)
S1	C11	C12	109.3(2)
S1	C11	C22	122.5(2)
C12	C11	C22	128.2(2)
O	C12	C11	125.8(2)
O	C12	C13	123.2(3)
C11	C12	C13	111.0(2)
C12	C13	C14	113.4(2)
C12	C13	C18	126.0(2)
C14	C13	C18	120.6(2)
S1	C14	C13	113.5(2)
S1	C14	C15	125.9(2)
C13	C14	C15	120.6(2)
C14	C15	C16	118.4(2)
C15	C16	C17	121.2(3)
C16	C17	C18	120.3(3)
C13	C18	C17	118.9(2)
S2	C21	N	124.4(2)
S2	C21	C22	112.3(1)
N	C21	C22	123.3(2)
C11	C22	C21	118.3(2)
C11	C22	C23	132.3(2)
C21	C22	C23	109.4(2)
C22	C23	C24	112.3(2)
C22	C23	C28	130.8(2)
C24	C23	C28	116.9(2)
S2	C24	C23	114.7(2)

S2	C24	C25	122.6(2)
C23	C24	C25	122.7(2)
C24	C25	C26	118.5(2)
C25	C26	C27	120.1(3)
C26	C27	C28	121.2(3)
C23	C28	C27	120.4(2)
N	C31	C32	121.2(2)
N	C31	C36	117.9(2)
C32	C31	C36	120.7(2)
C31	C32	C33	118.3(2)
C31	C32	C37	121.7(2)
C33	C32	C37	119.8(2)
C32	C33	C34	122.4(2)
C33	C34	C35	117.9(2)
C33	C34	C38	121.6(2)
C35	C34	C38	120.5(2)
C34	C35	C36	121.9(2)
C31	C36	C35	118.7(2)
C31	C36	C39	120.5(2)
C35	C36	C39	120.8(2)

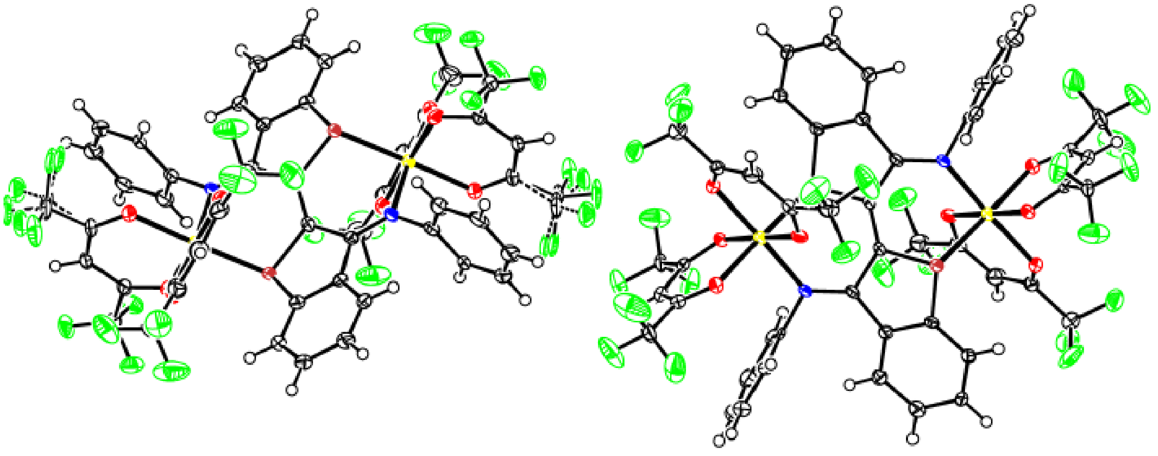

Figure C8. ORTEP diagram of *meso* diruthenium complex **3.5a** with thermal ellipsoids represented at 50% probability.

Table C15. Bond Lengths for *meso* diruthenium complex **3.5a**.

Atom 1	**Atom 2**	**Length/Å**	**Atom 1**	**Atom 2**	**Length/Å**
C25	C25^1	1.350(15)	Ru2	S2^1	2.282(2)
C25	C26	1.488(10)	S2	Ru2^1	2.282(2)
C25	S2	1.774(8)	C1	C1^2	1.351(14)
C26	C27	1.488(11)	C1	C2	1.477(10)
C26	N2	1.308(10)	C1	S1	1.784(7)
C27	C28	1.402(11)	C2	C3	1.495(10)
C27	C32	1.417(11)	C2	N1	1.312(9)
C28	C29	1.371(11)	C3	C4	1.413(10)
C29	C30	1.403(11)	C3	C8	1.402(10)
C30	C31	1.382(11)	C4	C5	1.388(11)
C31	C32	1.396(11)	C5	C6	1.397(11)
C32	S2	1.777(8)	C6	C7	1.385(11)
C33	C34	1.407(11)	C7	C8	1.400(10)
C33	C38	1.384(11)	C8	S1	1.777(7)
C33	N2	1.449(10)	C9	C10	1.374(11)
C34	C35	1.396(11)	C9	C14	1.379(11)
C35	C36	1.373(13)	C9	N1	1.472(9)
C36	C37	1.375(12)	C10	C11	1.404(11)
C37	C38	1.403(11)	C11	C12	1.368(13)
C39	C40	1.531(10)	C12	C13	1.384(14)
C39	F13	1.341(9)	C13	C14	1.427(12)
C39	F14	1.346(9)	C15	C16	1.528(11)
C39	F15	1.342(9)	C15	F1	1.337(9)
C40	C41	1.403(10)	C15	F2	1.363(10)
C40	O5	1.279(9)	C15	F3	1.304(9)
C41	C42	1.393(11)	C16	C17	1.392(11)
C42	C43	1.518(13)	C16	O1	1.271(9)
C42	C44	1.522(17)	C17	C18	1.400(11)
C42	O6	1.271(9)	C18	C19	1.548(11)
C43	F17	1.343(12)	C18	O2	1.253(9)
C43	F18	1.343(12)	C19	F4	1.332(10)
C43	F21	1.334(12)	C19	F5	1.348(10)
C44	F16	1.336(15)	C19	F6	1.333(10)
C44	F19	1.341(15)	C20	C21	1.549(11)
C44	F20	1.335(15)	C20	F7	1.312(10)

C45	C46	1.523(11)	C20	F8	1.321(10)
C45	F22	1.345(11)	C20	F9	1.294(10)
C45	F23	1.337(10)	C21	C22	1.373(11)
C45	F24	1.299(11)	C21	O3	1.280(9)
C46	C47	1.406(12)	C22	C23	1.397(11)
C46	O7	1.273(10)	C23	C24	1.534(11)
C47	C48	1.394(12)	C23	O4	1.281(9)
C48	C49	1.547(12)	C24	F10	1.328(9)
C48	O8	1.263(10)	C24	F11	1.326(9)
C49	F25	1.317(11)	C24	F12	1.328(9)
C49	F26	1.337(11)	N1	Ru1	2.050(6)
C49	F27	1.328(12)	O1	Ru1	2.035(5)
N2	Ru2	2.067(6)	O2	Ru1	2.067(5)
O5	Ru2	2.050(5)	O3	Ru1	2.055(5)
O6	Ru2	2.055(5)	O4	Ru1	2.048(5)
O7	Ru2	2.039(5)	Ru1	S1^{2}	2.285(2)
O8	Ru2	2.059(5)	S1	Ru1^{2}	2.285(2)

Table C16. Bond Angles for *meso* diruthenium complex **3.5a**.

Atom 1	**Atom 2**	**Atom 3**	**Angle / °**
C25^{1}	C25	C26	128.3(9)
C25^{1}	C25	S2	120.7(8)
C26	C25	S2	110.5(5)
C25	C26	C27	109.7(6)
N2	C26	C25	121.6(7)
N2	C26	C27	128.7(7)
C28	C27	C26	132.0(7)
C28	C27	C32	117.1(7)
C32	C27	C26	110.9(7)
C29	C28	C27	120.5(7)
C28	C29	C30	121.2(8)
C31	C30	C29	120.5(8)
C30	C31	C32	117.7(7)
C27	C32	S2	114.2(6)
C31	C32	C27	122.9(7)
C31	C32	S2	122.9(6)

C34	C33	N2	119.0(7)
C38	C33	C34	121.5(7)
C38	C33	N2	119.4(7)
C35	C34	C33	118.3(8)
C36	C35	C34	120.4(8)
C35	C36	C37	121.0(8)
C36	C37	C38	120.4(8)
C33	C38	C37	118.4(8)
F13	C39	C40	114.0(6)
F13	C39	F14	106.3(6)
F13	C39	F15	107.6(6)
F14	C39	C40	109.7(6)
F15	C39	C40	112.4(6)
F15	C39	F14	106.4(6)
C41	C40	C39	118.0(6)
O5	C40	C39	111.8(6)
O5	C40	C41	130.2(7)
C42	C41	C40	124.1(7)
C41	C42	C43	116.9(8)
C41	C42	C44	117.7(11)
O6	C42	C41	129.4(7)
O6	C42	C43	113.6(8)
O6	C42	C44	112.6(12)
F17	C43	C42	110.2(10)
F17	C43	F18	105.9(11)
F18	C43	C42	114.0(10)
F21	C43	C42	111.7(15)
F21	C43	F17	108.2(19)
F21	C43	F18	106.6(12)
F16	C44	C42	111.8(18)
F16	C44	F19	103.6(19)
F19	C44	C42	113.6(17)
F20	C44	C42	112(3)
F20	C44	F16	104(3)
F20	C44	F19	111(3)
F22	C45	C46	109.4(7)
F23	C45	C46	111.2(7)
F23	C45	F22	105.8(8)
F24	C45	C46	114.6(8)

F24	C45	F22	107.5(8)
F24	C45	F23	107.8(8)
C47	C46	C45	118.5(8)
O7	C46	C45	112.7(8)
O7	C46	C47	128.8(8)
C48	C47	C46	124.2(8)
C47	C48	C49	118.2(8)
O8	C48	C47	129.4(8)
O8	C48	C49	112.4(7)
F25	C49	C48	113.0(8)
F25	C49	F26	106.5(8)
F25	C49	F27	108.7(8)
F26	C49	C48	109.9(7)
F27	C49	C48	109.9(8)
F27	C49	F26	108.6(8)
C26	N2	C33	118.9(6)
C26	N2	Ru2	128.0(5)
C33	N2	Ru2	112.9(5)
C40	O5	Ru2	120.7(5)
C42	O6	Ru2	121.6(5)
C46	O7	Ru2	122.5(5)
C48	O8	Ru2	122.0(5)
N2	Ru2	S2[1]	86.57(18)
O5	Ru2	N2	92.4(2)
O5	Ru2	O6	93.8(2)
O5	Ru2	O8	87.3(2)
O5	Ru2	S2[1]	88.49(15)
O6	Ru2	N2	92.6(2)
O6	Ru2	O8	83.6(2)
O6	Ru2	S2[1]	177.61(15)
O7	Ru2	N2	87.4(2)
O7	Ru2	O5	179.8(2)
O7	Ru2	O6	86.1(2)
O7	Ru2	O8	92.9(2)
O7	Ru2	S2[1]	91.66(15)
O8	Ru2	N2	176.1(2)
O8	Ru2	S2[1]	97.27(16)
C25	S2	C32	90.2(3)
C25	S2	Ru2[1]	104.8(2)

C32	S2	Ru2^{1}	115.3(3)
C1^{2}	C1	C2	128.4(9)
C1^{2}	C1	S1	119.9(7)
C2	C1	S1	111.3(5)
C1	C2	C3	109.1(6)
N1	C2	C1	120.9(6)
N1	C2	C3	130.0(6)
C4	C3	C2	131.0(7)
C8	C3	C2	111.3(6)
C8	C3	C4	117.7(7)
C5	C4	C3	119.7(7)
C4	C5	C6	121.4(7)
C7	C6	C5	119.9(7)
C6	C7	C8	118.7(7)
C3	C8	S1	114.7(5)
C7	C8	C3	122.4(7)
C7	C8	S1	122.8(6)
C10	C9	C14	122.2(7)
C10	C9	N1	118.8(7)
C14	C9	N1	118.9(7)
C9	C10	C11	119.7(8)
C12	C11	C10	119.5(9)
C11	C12	C13	121.0(8)
C12	C13	C14	120.1(9)
C9	C14	C13	117.4(8)
F1	C15	C16	112.9(6)
F1	C15	F2	104.8(7)
F2	C15	C16	109.0(6)
F3	C15	C16	114.9(7)
F3	C15	F1	107.6(7)
F3	C15	F2	107.0(7)
C17	C16	C15	118.3(7)
O1	C16	C15	111.8(7)
O1	C16	C17	129.8(7)
C16	C17	C18	123.5(7)
C17	C18	C19	117.7(7)
O2	C18	C17	130.1(7)
O2	C18	C19	112.1(7)
F4	C19	C18	113.9(7)

F4	C19	F5	106.0(7)
F4	C19	F6	107.0(7)
F5	C19	C18	110.8(6)
F6	C19	C18	111.6(7)
F6	C19	F5	107.1(7)
F7	C20	C21	111.1(7)
F7	C20	F8	107.5(7)
F8	C20	C21	112.5(7)
F9	C20	C21	111.0(7)
F9	C20	F7	109.0(8)
F9	C20	F8	105.5(8)
C22	C21	C20	119.0(7)
O3	C21	C20	111.5(7)
O3	C21	C22	129.5(8)
C21	C22	C23	124.8(7)
C22	C23	C24	119.0(7)
O4	C23	C22	129.6(7)
O4	C23	C24	111.4(6)
F10	C24	C23	113.8(6)
F10	C24	F12	106.8(6)
F11	C24	C23	111.9(6)
F11	C24	F10	106.5(6)
F11	C24	F12	107.1(7)
F12	C24	C23	110.4(6)
C2	N1	C9	117.2(6)
C2	N1	Ru1	127.9(5)
C9	N1	Ru1	114.7(4)
C16	O1	Ru1	122.0(5)
C18	O2	Ru1	121.5(5)
C21	O3	Ru1	121.5(5)
C23	O4	Ru1	121.1(5)
N1	Ru1	O2	177.9(2)
N1	Ru1	O3	93.3(2)
N1	Ru1	S1^2	85.56(17)
O1	Ru1	N1	87.5(2)
O1	Ru1	O2	93.0(2)
O1	Ru1	O3	86.4(2)
O1	Ru1	O4	179.5(2)
O1	Ru1	S1^2	91.02(15)

O2	Ru1	S1^2	96.49(16)
O3	Ru1	O2	84.6(2)
O3	Ru1	S1^2	177.23(15)
O4	Ru1	N1	92.1(2)
O4	Ru1	O2	87.5(2)
O4	Ru1	O3	93.4(2)
O4	Ru1	S1^2	89.21(14)
C1	S1	Ru1^2	103.7(2)
C8	S1	C1	89.6(3)
C8	S1	Ru1^2	114.5(3)

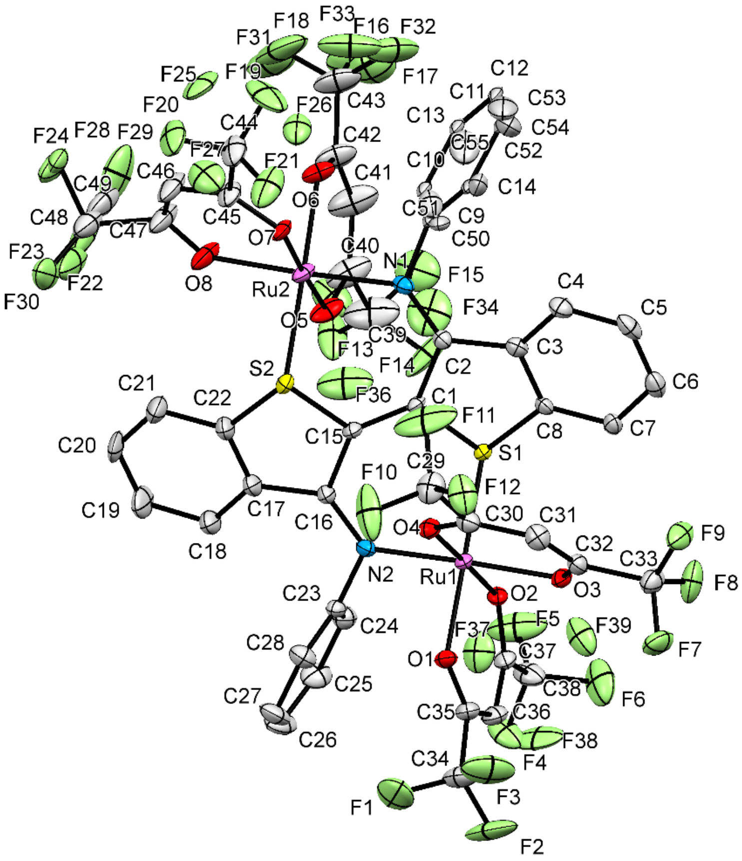

Figure C9. ORTEP diagram of *rac* diruthenium complex **3.5b** with thermal ellipsoids represented at 50% probability. Hydrogen atoms have been removed for clarity.

Table C17. Bond Lengths for *rac* diruthenium complex **3.5b**.

Atom 1	**Atom 2**	**Length/Å**	**Atom 1**	**Atom 2**	**Length/Å**
Ru1	S1	2.2752(9)	C6	C7	1.388(5)
Ru1	O1	2.065(2)	C7	C8	1.383(4)
Ru1	O2	2.046(2)	C11	C10	1.3945
Ru1	O3	2.056(2)	C11	C12	1.3945
Ru1	O4	2.013(2)	C9	C10	1.3937
Ru1	N2	2.043(3)	C9	C14	1.3944
Ru2	S2	2.2860(10)	C12	C13	1.3940
Ru2	O5	2.014(2)	C13	C14	1.3942
Ru2	O6	2.068(3)	C48	C47	1.516(4)
Ru2	O7	2.042(2)	F36	C39	1.464(6)
Ru2	O8	2.053(3)	F28	C49	1.3478
Ru2	N1	2.039(3)	C53	C52	1.3723
S1	C1	1.775(3)	C53	C54	1.3706
S1	C8	1.781(3)	F32	C43	1.303(5)
S2	C15	1.770(3)	C49	F30	1.3441
S2	C22	1.783(4)	C49	F29	1.3390
F1	C34	1.322(5)	C49	C47	1.520(4)
F2	C34	1.334(5)	F34	C39	1.161(6)
F3	C34	1.320(5)	F38	C38	1.307(4)
F4	C38	1.316(6)	C51	C50	1.3605
F5	C38	1.259(6)	C51	C52	1.3694
F6	C38	1.394(6)	C55	C50	1.3913
F7	C33	1.331(4)	C55	C54	1.3814
F8	C33	1.328(5)	F31	C43	1.394(6)
F9	C33	1.334(4)	F33	C43	1.266(5)
F10	C29	1.309(5)	F35	C39	1.407(6)
F11	C29	1.334(5)	F37	C38	1.424(5)
F12	C29	1.325(4)	F39	C38	1.317(5)
F13	C39	1.136(7)	F25	C44	1.447(5)
F14	C39	1.395(7)	F26	C44	1.337(5)
F15	C39	1.505(7)	F27	C44	1.177(5)
F16	C43	1.328(6)	C15	C16	1.489(4)
F17	C43	1.394(7)	C16	C17	1.484(4)
F18	C43	1.319(6)	C17	C18	1.402(5)
F19	C44	1.267(6)	C17	C22	1.398(5)

F20	C44	1.344(5)	C18	C19	1.393(5)
F21	C44	1.378(6)	C19	C20	1.387(7)
F22	C48	1.359(8)	C20	C21	1.379(6)
F23	C48	1.369(7)	C21	C22	1.391(5)
F24	C48	1.387(8)	C23	C24	1.389(5)
O1	C35	1.264(4)	C23	C28	1.383(5)
O2	C37	1.269(4)	C24	C25	1.394(5)
O3	C32	1.262(4)	C25	C26	1.389(6)
O4	C30	1.262(4)	C26	C27	1.384(6)
O5	C40	1.266(5)	C27	C28	1.393(5)
O6	C42	1.252(5)	C29	C30	1.532(5)
O7	C45	1.257(4)	C30	C31	1.390(5)
O8	C47	1.269(5)	C31	C32	1.395(5)
N1	C2	1.315(4)	C32	C33	1.529(5)
N1	C9	1.412(3)	C34	C35	1.536(5)
N1	C50	1.492(3)	C35	C36	1.396(5)
N2	C16	1.308(4)	C36	C37	1.396(5)
N2	C23	1.454(4)	C37	C38	1.507(5)
C1	C2	1.471(4)	C39	C40	1.497(6)
C1	C15	1.344(5)	C40	C41	1.398(7)
C2	C3	1.487(4)	C41	C42	1.400(6)
C3	C4	1.408(5)	C42	C43	1.497(5)
C3	C8	1.411(4)	C44	C45	1.530(5)
C4	C5	1.383(5)	C45	C46	1.393(5)
C5	C6	1.389(5)	C46	C47	1.399(6)

Table C18. Bond Angles for *rac* diruthenium complex **3.5b**.

Atom 1	**Atom 2**	**Atom 3**	**Angle / °**
O1	Ru1	S1	177.62(7)
O2	Ru1	S1	89.08(7)
O2	Ru1	O1	93.25(9)
O2	Ru1	O3	86.85(9)
O3	Ru1	S1	95.64(7)
O3	Ru1	O1	83.98(9)
O4	Ru1	S1	91.68(7)
O4	Ru1	O1	86.00(9)

O4	Ru1	O2	179.07(9)
O4	Ru1	O3	93.61(9)
O4	Ru1	N2	86.36(10)
N2	Ru1	S1	86.17(8)
N2	Ru1	O1	94.21(10)
N2	Ru1	O2	93.15(10)
N2	Ru1	O3	178.19(10)
O5	Ru2	S2	87.20(8)
O5	Ru2	O6	93.57(11)
O5	Ru2	O7	177.07(11)
O5	Ru2	O8	88.83(11)
O5	Ru2	N1	88.12(11)
O6	Ru2	S2	178.98(8)
O7	Ru2	S2	95.63(7)
O7	Ru2	O6	83.61(10)
O7	Ru2	O8	91.65(10)
O8	Ru2	S2	95.59(9)
O8	Ru2	O6	83.76(11)
N1	Ru2	S2	88.34(8)
N1	Ru2	O6	92.35(11)
N1	Ru2	O7	91.20(10)
N1	Ru2	O8	174.90(12)
C1	S1	Ru1	104.16(11)
C1	S1	C8	90.12(15)
C8	S1	Ru1	114.71(11)
C15	S2	Ru2	104.06(12)
C15	S2	C22	89.47(17)
C22	S2	Ru2	113.50(14)
C35	O1	Ru1	120.9(2)
C37	O2	Ru1	121.7(2)
C32	O3	Ru1	120.9(2)
C30	O4	Ru1	122.5(2)
C40	O5	Ru2	121.8(3)
C42	O6	Ru2	121.9(2)
C45	O7	Ru2	122.6(2)
C47	O8	Ru2	122.6(2)
C2	N1	Ru2	128.6(2)
C2	N1	C9	123.3(2)
C2	N1	C50	114.6(2)

C9	N1	Ru2	106.49(17)
C50	N1	Ru2	116.79(17)
C16	N2	Ru1	128.0(2)
C16	N2	C23	117.9(3)
C23	N2	Ru1	113.9(2)
C2	C1	S1	110.7(2)
C15	C1	S1	120.2(2)
C15	C1	C2	129.0(3)
N1	C2	C1	121.8(3)
N1	C2	C3	129.0(3)
C1	C2	C3	109.1(3)
C4	C3	C2	130.6(3)
C4	C3	C8	117.5(3)
C8	C3	C2	111.9(3)
C5	C4	C3	119.3(3)
C4	C5	C6	122.0(3)
C7	C6	C5	119.8(3)
C8	C7	C6	118.4(3)
C3	C8	S1	113.1(2)
C7	C8	S1	124.0(3)
C7	C8	C3	122.9(3)
C12	C11	C10	120.0
C10	C9	N1	120.23(13)
C10	C9	C14	120.0
C14	C9	N1	119.31(13)
C9	C10	C11	120.0
C13	C12	C11	120.0
C12	C13	C14	120.0
C13	C14	C9	120.0
F22	C48	F23	104.9(6)
F22	C48	F24	103.7(6)
F22	C48	C47	105.9(4)
F23	C48	F24	109.0(5)
F23	C48	C47	123.3(4)
F24	C48	C47	108.4(5)
C54	C53	C52	121.0
F28	C49	C47	113.17(18)
F30	C49	F28	102.7
F30	C49	C47	107.5(2)

F29	C49	F28	108.1
F29	C49	F30	106.8
F29	C49	C47	117.3(2)
C50	C51	C52	118.0
C54	C55	C50	117.8
C51	C50	N1	119.96(12)
C51	C50	C55	122.9
C55	C50	N1	117.05(12)
C51	C52	C53	120.5
C53	C54	C55	119.6
C1	C15	S2	121.1(2)
C1	C15	C16	127.8(3)
C16	C15	S2	110.8(2)
N2	C16	C15	121.5(3)
N2	C16	C17	130.0(3)
C17	C16	C15	108.5(3)
C18	C17	C16	129.6(3)
C22	C17	C16	111.7(3)
C22	C17	C18	118.6(3)
C19	C18	C17	118.9(4)
C20	C19	C18	121.4(4)
C21	C20	C19	120.4(4)
C20	C21	C22	118.5(4)
C17	C22	S2	114.1(3)
C21	C22	S2	123.7(3)
C21	C22	C17	122.1(4)
C24	C23	N2	118.9(3)
C28	C23	N2	119.7(3)
C28	C23	C24	121.3(3)
C23	C24	C25	118.9(3)
C26	C25	C24	120.2(4)
C27	C26	C25	120.0(3)
C26	C27	C28	120.3(4)
C23	C28	C27	119.1(3)
F10	C29	F11	108.3(4)
F10	C29	F12	106.4(3)
F10	C29	C30	112.0(3)
F11	C29	C30	108.8(3)
F12	C29	F11	107.3(3)

F12	C29	C30	113.8(3)
O4	C30	C29	111.4(3)
O4	C30	C31	128.8(3)
C31	C30	C29	119.7(3)
C30	C31	C32	124.7(3)
O3	C32	C31	129.3(3)
O3	C32	C33	113.4(3)
C31	C32	C33	117.4(3)
F7	C33	F9	107.4(3)
F7	C33	C32	111.1(3)
F8	C33	F7	106.6(3)
F8	C33	F9	107.1(3)
F8	C33	C32	112.1(3)
F9	C33	C32	112.2(3)
F1	C34	F2	106.7(4)
F1	C34	C35	110.6(3)
F2	C34	C35	112.4(3)
F3	C34	F1	107.9(4)
F3	C34	F2	107.4(4)
F3	C34	C35	111.4(3)
O1	C35	C34	112.2(3)
O1	C35	C36	128.9(3)
C36	C35	C34	118.9(3)
C37	C36	C35	125.2(3)
O2	C37	C36	128.9(3)
O2	C37	C38	113.3(3)
C36	C37	C38	117.9(3)
F4	C38	F6	104.7(4)
F4	C38	C37	111.5(4)
F5	C38	F4	110.9(5)
F5	C38	F6	106.8(5)
F5	C38	C37	114.4(4)
F6	C38	C37	107.9(4)
F38	C38	F37	101.9(3)
F38	C38	F39	110.6(3)
F38	C38	C37	118.1(3)
F37	C38	C37	109.7(3)
F39	C38	F37	99.6(3)
F39	C38	C37	114.5(3)

F13	C39	F14	118.2(6)
F13	C39	F15	104.9(6)
F13	C39	C40	120.3(6)
F14	C39	F15	90.6(6)
F14	C39	C40	108.3(4)
F36	C39	C40	110.3(4)
F34	C39	F36	111.9(4)
F34	C39	F35	110.0(4)
F34	C39	C40	117.6(5)
F35	C39	F36	92.9(3)
F35	C39	C40	111.5(4)
C40	C39	F15	109.9(4)
O5	C40	C39	111.7(4)
O5	C40	C41	128.8(4)
C41	C40	C39	119.5(4)
C40	C41	C42	125.5(4)
O6	C42	C41	127.8(4)
O6	C42	C43	113.5(4)
C41	C42	C43	118.7(4)
F16	C43	F17	101.5(5)
F16	C43	C42	117.0(4)
F17	C43	C42	111.3(4)
F18	C43	F16	107.6(5)
F18	C43	F17	105.3(5)
F18	C43	C42	113.0(5)
F32	C43	F31	102.1(3)
F32	C43	C42	111.7(4)
F31	C43	C42	106.0(4)
F33	C43	F32	116.8(4)
F33	C43	F31	104.5(3)
F33	C43	C42	114.0(3)
F19	C44	F20	111.3(4)
F19	C44	F21	108.8(4)
F19	C44	C45	110.3(4)
F20	C44	F21	102.8(4)
F20	C44	C45	113.4(3)
F21	C44	C45	109.9(3)
F25	C44	C45	110.4(3)
F26	C44	F25	99.8(3)

F26	C44	C45	114.4(3)
F27	C44	F25	106.4(3)
F27	C44	F26	112.4(4)
F27	C44	C45	112.4(4)
O7	C45	C44	113.2(3)
O7	C45	C46	128.4(3)
C46	C45	C44	118.3(3)
C45	C46	C47	124.6(4)
O8	C47	C48	118.6(3)
O8	C47	C49	108.4(3)
O8	C47	C46	128.1(4)
C46	C47	C48	110.2(4)
C46	C47	C49	123.0(3)

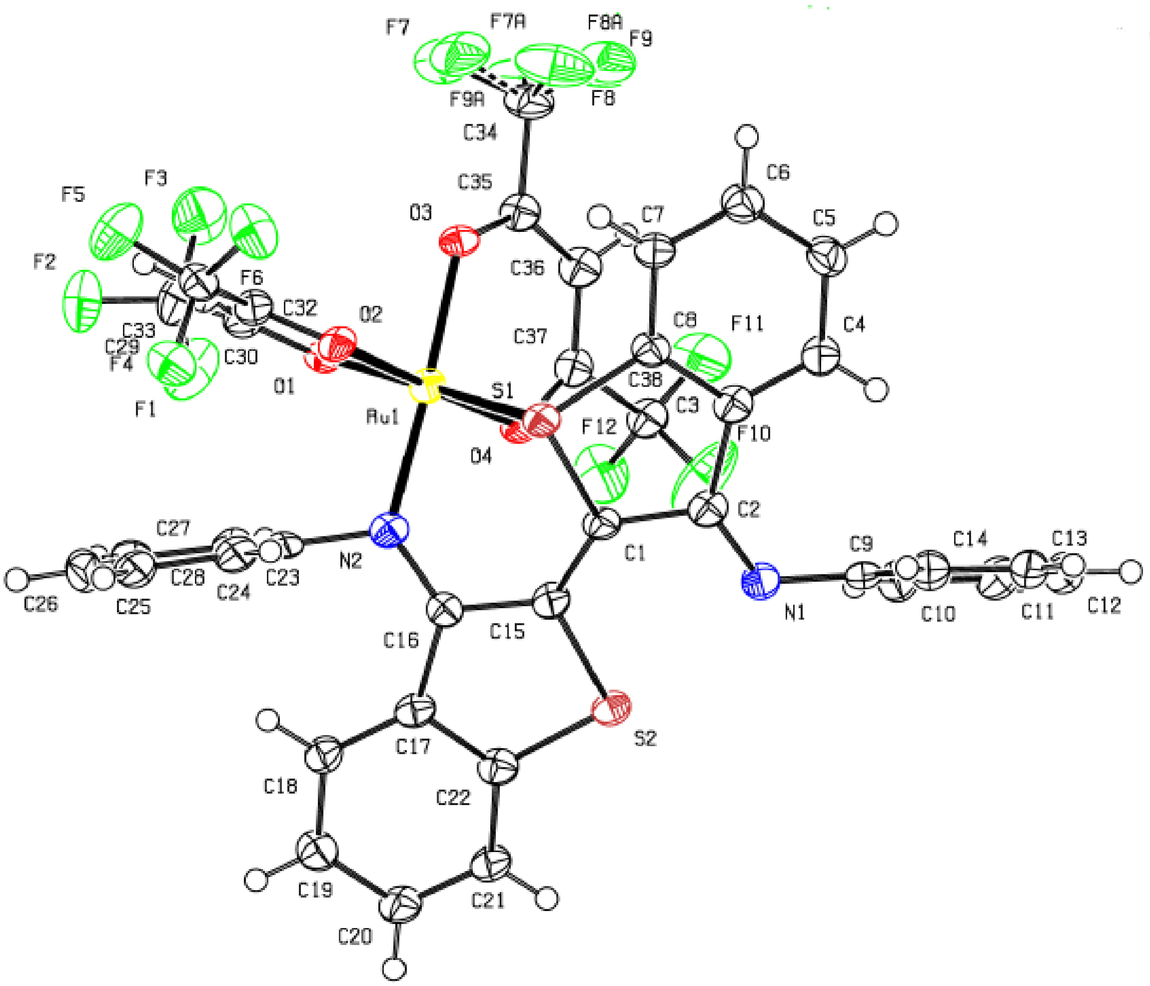

Figure C10. ORTEP diagram of monoruthenium complex **3.4** with thermal elipsoids represented at 50% probability.

Table C19. Bond Lengths for monoruthenium complex **3.4**.

Atom 1	**Atom 2**	**Length/Å**	**Atom 1**	**Atom 2**	**Length/Å**
Ru1	S1	2.262(2)	C6	C7	1.37(1)
Ru1	O1	2.082(5)	C7	C8	1.38(1)
Ru1	O2	2.038(5)	C9	C10	1.38(1)
Ru1	O3	2.050(5)	C9	C14	1.39(1)
Ru1	O4	2.040(5)	C10	C11	1.38(1)
Ru1	N2	2.054(7)	C11	C12	1.40(1)
S1	C1	1.769(7)	C12	C13	1.37(1)
S1	C8	1.79(1)	C13	C14	1.39(1)
S2	C15	1.760(7)	C15	C16	1.47(1)

S2	C22	1.76(1)	C16	C17	1.46(1)
F1	C29	1.33(1)	C17	C18	1.39(1)
F2	C29	1.34(1)	C17	C22	1.40(1)
F3	C29	1.31(1)	C18	C19	1.39(1)
F4	C33	1.33(1)	C19	C20	1.40(1)
F5	C33	1.343(8)	C20	C21	1.37(1)
F6	C33	1.32(1)	C21	C22	1.40(1)
F10	C38	1.313(8)	C23	C24	1.38(1)
F11	C38	1.30(1)	C23	C28	1.38(1)
F12	C38	1.33(1)	C24	C25	1.38(1)
O1	C30	1.239(9)	C25	C26	1.37(1)
O2	C32	1.268(9)	C26	C27	1.40(1)
O3	C35	1.25(1)	C27	C28	1.37(1)
O4	C37	1.24(1)	C29	C30	1.54(1)
N1	C2	1.285(9)	C30	C31	1.41(1)
N1	C9	1.42(1)	C31	C32	1.389(9)
N2	C16	1.329(8)	C32	C33	1.54(1)
N2	C23	1.44(1)	C34	C35	1.52(1)
C1	C2	1.47(1)	C34	F7	1.32(1)
C1	C15	1.35(1)	C34	F8	1.33(1)
C2	C3	1.49(1)	C34	F9	1.30(2)
C3	C4	1.38(1)	C35	C36	1.40(1)
C3	C8	1.40(1)	C36	C37	1.38(1)
C4	C5	1.39(1)	C37	C38	1.55(1)
C5	C6	1.42(1)			

Table C20. Bond Angles for monoruthenium complex **3.4**.

Atom 1	**Atom 2**	**Atom 3**	**Angle / °**
S1	Ru1	O1	178.7(1)
S1	Ru1	O2	87.7(1)
S1	Ru1	O3	98.0(1)
S1	Ru1	O4	91.3(1)
S1	Ru1	N2	84.6(2)
O1	Ru1	O2	93.2(2)
O1	Ru1	O3	82.9(2)
O1	Ru1	O4	87.8(2)

O1	Ru1	N2	94.5(2)
O2	Ru1	O3	87.3(2)
O2	Ru1	O4	178.8(2)
O2	Ru1	N2	92.4(2)
O3	Ru1	O4	92.1(2)
O3	Ru1	N2	177.4(2)
O4	Ru1	N2	88.2(2)
Ru1	S1	C1	103.4(3)
Ru1	S1	C8	114.9(3)
C1	S1	C8	90.8(4)
C15	S2	C22	90.4(4)
Ru1	O1	C30	121.0(5)
Ru1	O2	C32	121.1(5)
Ru1	O3	C35	122.1(5)
Ru1	O4	C37	122.7(5)
C2	N1	C9	123.9(7)
Ru1	N2	C16	130.5(5)
Ru1	N2	C23	112.7(5)
C16	N2	C23	116.7(6)
S1	C1	C2	112.0(6)
S1	C1	C15	120.9(6)
C2	C1	C15	126.8(7)
N1	C2	C1	117.9(7)
N1	C2	C3	131.2(7)
C1	C2	C3	110.7(7)
C2	C3	C4	130.3(7)
C2	C3	C8	111.9(7)
C4	C3	C8	117.7(7)
C3	C4	C5	120.3(7)
C4	C5	C6	120.6(7)
C5	C6	C7	119.8(7)
C6	C7	C8	118.5(7)
S1	C8	C3	113.6(6)
S1	C8	C7	123.3(6)
C3	C8	C7	123.1(7)
N1	C9	C10	118.7(7)
N1	C9	C14	121.9(7)
C10	C9	C14	119.3(7)
C9	C10	C11	120.1(8)

C10	C11	C12	120.7(8)
C11	C12	C13	119.1(9)
C12	C13	C14	120.4(8)
C9	C14	C13	120.5(8)
S2	C15	C1	120.6(6)
S2	C15	C16	111.2(6)
C1	C15	C16	128.1(7)
N2	C16	C15	120.0(7)
N2	C16	C17	127.2(7)
C15	C16	C17	111.9(7)
C16	C17	C18	132.0(7)
C16	C17	C22	109.9(7)
C18	C17	C22	118.1(7)
C17	C18	C19	119.6(7)
C18	C19	C20	121.6(7)
C19	C20	C21	119.6(7)
C20	C21	C22	119.0(7)
S2	C22	C17	115.6(6)
S2	C22	C21	122.4(6)
C17	C22	C21	122.0(7)
N2	C23	C24	119.3(7)
N2	C23	C28	121.7(7)
C24	C23	C28	118.9(7)
C23	C24	C25	120.9(8)
C24	C25	C26	119.4(8)
C25	C26	C27	120.2(9)
C26	C27	C28	119.3(8)
C23	C28	C27	121.2(8)
F1	C29	F2	105.5(7)
F1	C29	F3	107.8(7)
F1	C29	C30	110.4(7)
F2	C29	F3	108.7(7)
F2	C29	C30	112.7(7)
F3	C29	C30	111.5(7)
O1	C30	C29	113.1(7)
O1	C30	C31	130.3(7)
C29	C30	C31	116.6(7)
C30	C31	C32	123.6(7)
O2	C32	C31	130.6(7)

O2	C32	C33	111.8(7)
C31	C32	C33	117.5(7)
F4	C33	F5	106.2(6)
F4	C33	F6	107.3(6)
F4	C33	C32	110.8(6)
F5	C33	F6	108.0(7)
F5	C33	C32	112.8(7)
F6	C33	C32	111.6(7)
C35	C34	F7	111.1(8)
C35	C34	F8	110.6(8)
C35	C34	F9	115.8(8)
F7	C34	F8	104.5(9)
F7	C34	F9	109.4(9)
F8	C34	F9	104.7(9)
O3	C35	C34	113.5(7)
O3	C35	C36	129.4(7)
C34	C35	C36	117.1(7)
C35	C36	C37	123.3(7)
O4	C37	C36	130.0(7)
O4	C37	C38	112.8(7)
C36	C37	C38	117.2(7)
F10	C38	F11	109.1(7)
F10	C38	F12	106.5(7)
F10	C38	C37	109.7(7)
F11	C38	F12	106.2(7)
F11	C38	C37	114.3(7)
F12	C38	C37	110.9(7)

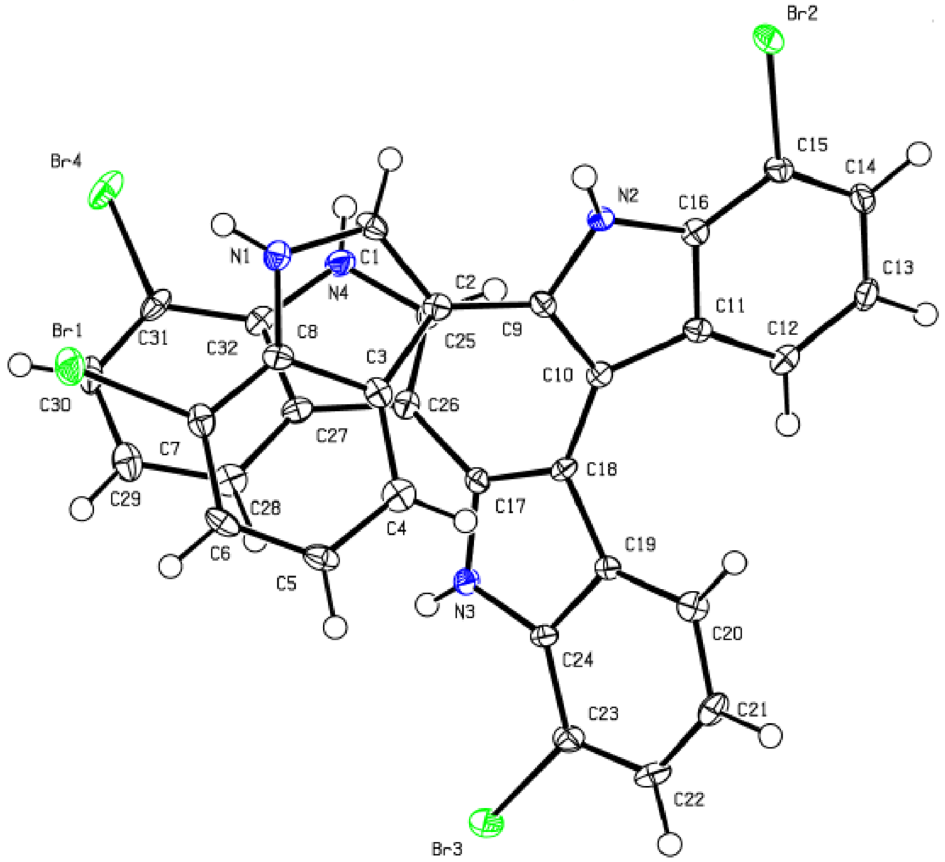

Figure C11. ORTEP diagram of indole tetramer **4.24** with thermal elipsoids represented at 50% probability.

Table C21. Bond Lengths for indole tetramer **4.24**.

Atom 1	**Atom 2**	**Length/Å**
Br1	C7	1.900(4)
Br2	C15	1.909(4)
Br3	C23	1.901(4)
Br4	C31	1.899(4)
N1	C1	1.369(5)
N1	C8	1.371(5)
N2	C9	1.377(5)
N2	C16	1.368(5)
N3	C17	1.382(5)
C11	C12	1.398(5)
C11	C16	1.423(5)
C12	C13	1.385(6)
C13	C14	1.411(6)
C14	C15	1.352(6)
C15	C16	1.389(5)
C17	C18	1.383(5)
C17	C26	1.460(5)
C18	C19	1.440(5)

N3	C24	1.362(5)	C19	C20	1.408(5)
N4	C25	1.383(5)	C19	C24	1.423(5)
N4	C32	1.369(5)	C20	C21	1.391(6)
C1	C2	1.373(5)	C21	C22	1.398(6)
C2	C3	1.447(5)	C22	C23	1.376(5)
C2	C9	1.464(5)	C23	C24	1.397(5)
C3	C4	1.404(6)	C25	C26	1.365(6)
C3	C8	1.422(5)	C26	C27	1.447(5)
C4	C5	1.376(6)	C27	C28	1.399(6)
C5	C6	1.401(6)	C27	C32	1.413(5)
C6	C7	1.384(6)	C28	C29	1.383(6)
C7	C8	1.383(5)	C29	C30	1.398(6)
C9	C10	1.387(5)	C30	C31	1.374(6)
C10	C11	1.443(5)	C31	C32	1.394(5)
C10	C18	1.460(5)			

Table C22. Bond Angles for indole tetramer **4.24**.

Atom 1	**Atom 2**	**Atom 3**	**Angle / °**
C1	N1	C8	109.2(3)
C16	N2	C9	109.8(3)
C24	N3	C17	109.7(3)
C32	N4	C25	108.8(3)
N1	C1	C2	110.2(4)
C1	C2	C3	106.5(3)
C1	C2	C9	124.8(4)
C3	C2	C9	128.5(3)
C4	C3	C2	135.3(4)
C4	C3	C8	118.5(4)
C8	C3	C2	106.2(3)
C5	C4	C3	119.3(4)
C4	C5	C6	121.7(4)
C7	C6	C5	119.8(4)
C6	C7	Br1	122.0(3)
C8	C7	Br1	118.8(3)
C8	C7	C6	119.3(4)
N1	C8	C3	107.9(3)

N1	C8	C7	130.7(4)
C7	C8	C3	121.3(4)
N2	C9	C2	120.5(3)
N2	C9	C10	109.3(3)
C10	C9	C2	130.1(4)
C9	C10	C11	106.5(3)
C9	C10	C18	127.3(3)
C11	C10	C18	125.6(3)
C12	C11	C10	134.4(4)
C12	C11	C16	118.9(4)
C16	C11	C10	106.7(3)
C13	C12	C11	119.6(4)
C12	C13	C14	120.6(4)
C15	C14	C13	120.1(4)
C14	C15	Br2	121.8(3)
C14	C15	C16	120.7(4)
C16	C15	Br2	117.5(3)
N2	C16	C11	107.7(3)
N2	C16	C15	132.2(4)
C15	C16	C11	120.1(4)
N3	C17	C18	109.3(3)
N3	C17	C26	120.8(3)
C18	C17	C26	129.9(4)
C17	C18	C10	125.7(3)
C17	C18	C19	106.4(3)
C19	C18	C10	127.8(3)
C20	C19	C18	134.0(4)
C20	C19	C24	119.2(3)
C24	C19	C18	106.8(3)
C21	C20	C19	118.6(4)
C20	C21	C22	121.6(4)
C23	C22	C21	120.4(4)
C22	C23	Br3	122.2(3)
C22	C23	C24	119.3(4)
C24	C23	Br3	118.5(3)
N3	C24	C19	107.7(3)
N3	C24	C23	131.5(4)
C23	C24	C19	120.8(3)
C26	C25	N4	110.0(4)

C25	C26	C17	127.3(4)
C25	C26	C27	106.6(3)
C27	C26	C17	126.0(4)
C28	C27	C26	134.0(4)
C28	C27	C32	119.6(4)
C32	C27	C26	106.4(3)
C29	C28	C27	119.2(4)
C28	C29	C30	120.7(4)
C31	C30	C29	120.9(4)
C30	C31	Br4	120.9(3)
C30	C31	C32	119.2(4)
C32	C31	Br4	119.9(3)
N4	C32	C27	108.2(3)
N4	C32	C31	131.4(4)
C31	C32	C27	120.4(4)

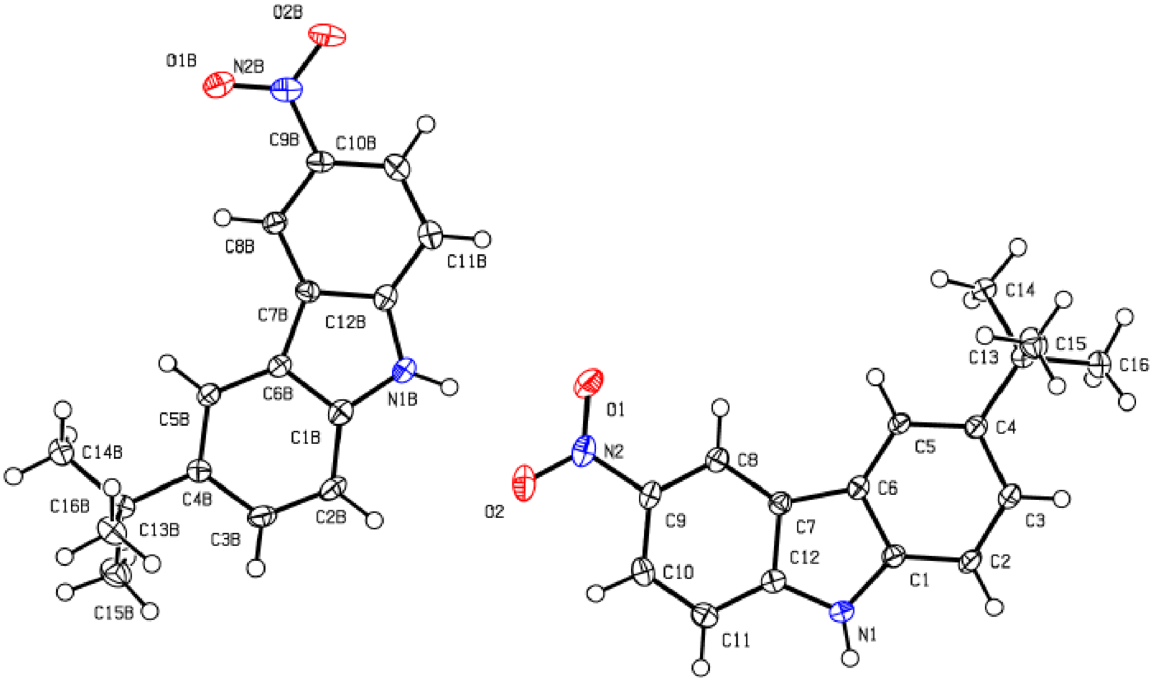

Figure C12. ORTEP diagram of carbazole **4.40** with thermal elipsoids represented at 50% probability.

Table C23. Bond Lengths for carbazole **4.40**.

Atom 1	Atom 2	Length/Å	Atom 1	Atom 2	Length/Å
O1	N2	1.231(3)	O1B	N2B	1.231(3)
O2	N2	1.237(3)	O2B	N2B	1.239(3)
N1	C1	1.388(3)	N1B	C1B	1.394(3)
N1	C12	1.367(3)	N1B	C12B	1.365(3)
N2	C9	1.454(3)	N2B	C9B	1.454(3)
C1	C2	1.388(3)	C1B	C2B	1.387(3)
C1	C6	1.406(3)	C1B	C6B	1.401(3)
C2	C3	1.385(3)	C2B	C3B	1.381(3)
C3	C4	1.408(3)	C3B	C4B	1.416(3)
C4	C5	1.394(3)	C4B	C5B	1.392(3)
C4	C13	1.538(3)	C4B	C13B	1.535(3)
C5	C6	1.395(3)	C5B	C6B	1.393(3)
C6	C7	1.449(3)	C6B	C7B	1.450(3)
C7	C8	1.387(3)	C7B	C8B	1.382(3)
C7	C12	1.424(3)	C7B	C12B	1.421(3)
C8	C9	1.378(3)	C8B	C9B	1.389(3)
C9	C10	1.399(3)	C9B	C10B	1.396(3)
C10	C11	1.375(4)	C10B	C11B	1.375(4)
C11	C12	1.399(3)	C11B	C12B	1.400(3)
C13	C14	1.531(3)	C13B	C14B	1.526(3)
C13	C15	1.533(3)	C13B	C15B	1.539(3)
C13	C16	1.537(3)	C13B	C16B	1.537(3)

Table C24 Bond Angles for carbazole **4.40**.

Atom 1	Atom 2	Atom 3	Angle / °
C12	N1	C1	109.06(19)
O1	N2	O2	122.3(2)
O1	N2	C9	119.35(19)
O2	N2	C9	118.4(2)
N1	C1	C6	109.2(2)
C2	C1	N1	129.3(2)
C2	C1	C6	121.4(2)
C3	C2	C1	117.4(2)

C2	C3	C4	123.1(2)
C3	C4	C13	121.05(19)
C5	C4	C3	118.1(2)
C5	C4	C13	120.8(2)
C4	C5	C6	120.2(2)
C1	C6	C7	106.37(19)
C5	C6	C1	119.7(2)
C5	C6	C7	133.9(2)
C8	C7	C6	134.2(2)
C8	C7	C12	119.5(2)
C12	C7	C6	106.26(19)
C9	C8	C7	117.5(2)
C8	C9	N2	118.5(2)
C8	C9	C10	123.4(2)
C10	C9	N2	118.0(2)
C11	C10	C9	119.9(2)
C10	C11	C12	117.7(2)
N1	C12	C7	109.08(18)
N1	C12	C11	129.1(2)
C11	C12	C7	121.9(2)
C14	C13	C4	110.93(18)
C14	C13	C15	108.8(2)
C14	C13	C16	108.0(2)
C15	C13	C4	109.33(19)
C15	C13	C16	108.3(2)
C16	C13	C4	111.42(19)
C12B	N1B	C1B	108.9(2)
O1B	N2B	O2B	122.4(2)
O1B	N2B	C9B	119.62(19)
O2B	N2B	C9B	118.0(2)
N1B	C1B	C6B	109.3(2)
C2B	C1B	N1B	129.5(2)
C2B	C1B	C6B	121.2(2)
C3B	C2B	C1B	117.4(2)
C2B	C3B	C4B	123.1(2)
C3B	C4B	C13B	119.9(2)
C5B	C4B	C3B	118.0(2)
C5B	C4B	C13B	122.1(2)
C4B	C5B	C6B	119.9(2)

C1B	C6B	C7B	106.34(19)
C5B	C6B	C1B	120.4(2)
C5B	C6B	C7B	133.3(2)
C8B	C7B	C6B	133.3(2)
C8B	C7B	C12B	120.3(2)
C12B	C7B	C6B	106.37(19)
C7B	C8B	C9B	117.1(2)
C8B	C9B	N2B	117.6(2)
C8B	C9B	C10B	123.2(2)
C10B	C9B	N2B	119.2(2)
C11B	C10B	C9B	120.2(2)
C10B	C11B	C12B	117.8(2)
N1B	C12B	C7B	109.1(2)
N1B	C12B	C11B	129.5(2)
C11B	C12B	C7B	121.4(2)
C4B	C13B	C15B	110.9(2)
C4B	C13B	C16B	107.48(18)
C14B	C13B	C4B	111.95(18)
C14B	C13B	C15B	107.6(2)
C14B	C13B	C16B	109.0(2)
C16B	C13B	C15B	109.9(2)